A combined experimental and theoretical investigation of the damage process in hard rock with application to rockburst

By

Thomas Daniel Bruning

The School of Civil, Environmental and Mining Engineering

This thesis is submitted in fulfilment of the requirements for the degree of

Doctor of Philosophy

Faculty of Engineering, Computer and Mathematical Sciences

10 August 2018


rock
rockburst
energy
damage
material
failure
stress
strain
model
behaviour
modelling
evolution
loading
elastic
rocks
brittle
research
models
evolution
testing
stiffness
test
study
excavation
Ortlepp
Axial
conducted
phenomenon
prediction
numerical
compressive
crack
method
variable
constitutive
mining
plastic
data
tests
yield
burst
initiation
threshold
strength
Granite
mechanics
strainburst
release
Although
seismic
However
thresholds
researchers
calibration
important
applied
microcracks
Chen
Disp
Jiang
hard
mechanisms
specimen
compression
hardening
rockbursts
modulus
criterion
index
proposed
Equation
accumulated
classification
deformation
mechanism
calculated
Tarasov
predict
violent
stored
process
Class
mine
depth
high
relationship
understanding
results
surface

ABSTRACT

Modern day mining operations are being forced deeper due to the depletion of near surface deposits. As such, more rock stability problems are being encountered due to the higher stress and temperature conditions found at depth. Some of these problems can be dealt with using current knowledge and conventional rock mechanics, however, the rockburst phenomenon proves hard to predict and mitigate. As a result it is necessary to develop more focussed strategies to address rockburst and provide a means to test and model the mechanism. It was clear in the literature that the controlling factors in rockburst is the elastic strain energy stored in the rock prior to failure and the accumulated damage in the ‘skin’ layer of an excavation. Therefore, this study focussed on the formation of a strategy to better understand the damage processes in hard, burst prone rocks and hence provide a better testing and modelling platform for further rockburst research.

Initial review of literature test data revealed a need for the implementation of a thorough testing methodology to measure the full stress-strain and damage evolution of conventional, compressive rock tests. As such, this dissertation proposes a coupled full circumferential control (FCC) and acoustic emission methodology to provide linked stress-strain-damage results. It is shown that the circumferential strain control method of testing provides a more comprehensive data set for the calibration of constitutive models. It also postulates that crack damage thresholds are very reliant on the load control method used during testing. Therefore, rocks that exhibit snap back behaviour should be controlled using circumferential strain rate. Using the proposed testing methodology this research was able to obtain a complete data set for granite under multiple confinement levels.

After conventional testing, the gathered data should be incorporated into a theoretical model to enable the numerical analysis of rock failure. Most models in the literature calibrate using stress-strain and damage, however, they are dealt with separately or via the use of complex hardening and softening functions. Therefore, development of a flexible unified yield-failure criterion is given along with a new calibration procedure to allow more physicality to be maintained in a simple, phenomenological damage-plasticity model. The enhanced yield-failure criterion enables the simple calibration of damage state with stress evolution and therefore, when subjected to unloading or to a load path change the model can correctly measure the level of accumulated damage in the material. Other phenomenological enhancements allowing pre-peak hardening and damage evolution law calibration are also presented.

Generally, once a constitutive model has been calibrated using conventional experiments it is applied numerically to simulate engineering problems. However, as little is known about rockburst mechanisms, it is vital to provide the model with a relevant data set to validate the effectiveness of predicting the phenomenon. Existing research in rockburst testing is expensive and has inherent limitations. Therefore, to easily and consistently replicate the mechanisms in the laboratory an innovative method for small scale rockburst testing is proposed. The test was centred on a standard Hoek triaxial cell, utilising the three dimensional stress state of a thick walled hollow cylinder to replicate in-situ ground conditions. Internal pressure was then imparted, maintained and released using a new platen design to simulate the excavation of a tunnel during the loading phase of the test. The proposed method successfully predicted and replicated the conditions of rockburst in the internal bore of the specimen. Characteristic acoustic emission response and stress states were also identified to provide some indication of the propensity of burst under varying in-situ pressure. Due to the success of the experimental apparatus, the data at bursting coupled with the acoustic emission response from inventive platen sensor housings gave a good indication that the apparatus has the potential for patent.

DECLARATION

I certify that this work contains no material which has been accepted for the award of any other degree or diploma in my name, in any university or other tertiary institution and, to the best of my knowledge and belief, contains no material previously published or written by another person, except where due reference has been made in the text. In addition, I certify that no part of this work will, in the future, be used in a submission in my name, for any other degree or diploma in any university or other tertiary institution without the prior approval of the University of Adelaide and where applicable, any partner institution responsible for the joint-award of this degree.

I acknowledge that copyright of published works contained within this thesis resides with the copyright holder(s) of those works.

I also give permission for the digital version of my thesis to be made available on the web, via the University's digital research repository, the Library Search and also through web search engines, unless permission has been granted by the University to restrict access for a period of time.

I acknowledge the support I have received for my research through the provision of an Australian Government Research Training Program Scholarship.

Thomas Daniel Bruning

10 August 2018

ACKNOWLEDGEMENTS

I would like to begin by thanking my supervisors, A/Prof. Murat Karakus, A/Prof. Giang D. Nguyen and David Goodchild for the support and knowledge they have given me over the duration of my PhD candidature. A special thanks is extended to Prof. Martin Lambert, who as head of school, provided me with fantastic opportunities in teaching. I would also like to extend a special thanks to the laboratory technicians that assisted with the experiments, namely Adam Ryntjes and Simon Golding.

Financial support for this research was supplied by OZ Minerals and the ARC linkage project (LP150100539), without which this opportunity would never have been possible.

I would like to give special thanks to the colleagues that have become my friends throughout this period of my life. To Dr. Arash Mir, Dr. Adam Schwartzkopff and Selahattin Akdag for our many interesting, often philosophical discussions and support.

Finally, the time has come to dedicate this thesis. To this end I would like to dedicate it to my family as a whole, as without any one of their support this would not have been possible. A special mention to my parents Mark and Jennifer Bruning, who have always driven me towards becoming the best version of myself, despite my resistance at times. Finally, but by far most importantly, to my wife Brooke, you have supported me throughout the entire process and inspired me to work hard every day. Coming home to you on even the hardest, most challenging days, keeps me striving to achieve the highest of goals.

PUBLICATIONS RELATED TO THIS THESIS

Chapter 3

- Bruning T, Karakus M, Nguyen G, Goodchild D (2018) ‘Experimental study on the damage evolution of brittle rock under triaxial confinement with full circumferential strain control.’ Rock Mechanics and Rock Engineering, doi:10.1007/s00603-018-1537-7

Chapter 4

- Bruning T, Karakus M, Nguyen G, Goodchild D ‘Development of a unified yield-failure criterion for the modelling of hard rocks.’ In: International Conference on Geomechanics, Geo-energy and Geo-resources (IC3G), Melbourne, Australia, 2016.
- Bruning T, Karakus M, Nguyen G, Goodchild D (2018) ‘Damage-plasticity model calibration for hard rock with a unified yield-failure function.’ International Journal of Rock Mechanics and Mining Sciences (Prepared for Submission)

Chapter 5

- Bruning T, Karakus M, Nguyen G, Goodchild D (2018) ‘An innovative hollow cylinder testing apparatus for small scale rockburst investigation.’ International Journal of Rock Mechanics and Mining Sciences (Submitted)
- Bruning T, Karakus M, Nguyen G, Goodchild D (2018) ‘Influence of deviatoric stress on rockburst occurrence: an experimental study’ International Journal of Mining Science and Technology, Rockburst special edition paper (Accepted)

TABLE OF CONTENTS

LIST OF SYMBOLS

E	Elastic modulus
ν	Poisson’s ratio
σ_c	Uniaxial Compressive Strength (UCS)
σ_1	Axial stress (Major Principal Stress)
σ_3	Lateral stress (Minor Principle Stress)
ε_1	Axial strain (Major Principal Strain)
ε_3	Lateral strain (Minor Principal Strain)
ε_v	Total volumetric strain
ε_s	Total shear strain
D	Damage variable
Ω	Accumulated acoustic emission energy
Ω_{total}	Total accumulated acoustic emission energy
σ_y	Initial yield stress
σ_p	Peak failure stress
σ_{res}	Residual stress
ε_v^{in}	Inelastic volumetric strain
ε_s^{in}	Inelastic shear strain
p	Hydrostatic stress
q	Deviatoric stress
K	Bulk modulus
G	Shear modulus
σ_{cc}	Crack closure stress threshold
σ_{ci}	Crack initiation stress threshold
σ_{cd}	Crack damage stress threshold
σ_{ij}	Cauchy stress tensor
ε_{kl}	Strain tensor
I_1	First invariant of the stress tensor
s_{ij}	Deviatoric stress tensor
J_2	Second invariant of the deviatoric stress tensor
θ	Lode angle
C_{ijkl}	Stiffness tensor
ε_{kl}^p	Plastic strain tensor
y	Unified yield-failure function

M	Frictional failure slope
p_c	Isotropic compression yield stress
c	Isotropic tensile yield stress
α	Material parameter controlling skew direction of initial yield
m	Material parameter controlling magnitude of yield curve skew
ω	Function of hydrostatic stress and tensile strength
γ	Dilation control parameter
g	Damage-plastic potential function
$\Delta\varepsilon_s^p$	Incremental plastic shear strain
$\Delta\varepsilon_v^p$	Incremental plastic volumetric strain
$\Delta\lambda$	Damage plastic multiplier
ϵ_p	Accumulated plastic strain
A, B	Damage evolution control parameters
M_0	Initial frictional failure slope
M_u	Final frictional failure slope
a	Parameter controlling magnitude of hardening
b	Parameter controlling extent of hardening
c_1	Pressure dependent damage evolution parameter
c_2	Pressure dependent damage evolution parameter
β	Tensile diminishment control parameter
D_i	Damage pivot
Γ, Υ	Damage evolution parameters
σ_z	Axial stress
σ_r	Radial stress
σ_θ	Tangential stress
R_i , R_o	Inner and outer cylinder radii
P_i	Internal borehole pressure
P_o	External Hoek cell pressure
F	Axial force
σ_{RB}	Rockburst stress
q_{RB}	Rockburst deviatoric stress

LIST OF FIGURES

LIST OF TABLES

Chapter 1 – INTRODUCTION

1.1 Background

Due to the depletion of near surface deposits, mining operations are being forced deeper. As a result more problems associated with rock mechanics are being realised due to the increased stresses and temperatures associated with depth. One such problem being encountered more frequently is rockburst which is observed in deep excavations as a sudden brittle failure causing fragments to eject from the excavation face. This section details the industrial impact that such violent events have on safety of an operation.

The first recorded rockburst event occurred in the year 1640 at the Altenberg tin mine located in Germany. The seismic event was felt up to 45 km away and the damage to excavation was so severe that the mine was not reopened until some two hundred years later (Ortlepp 2005).

Rockbursts have proved to be a major problem all around the world and it seems that no deep mine setting can be completely excluded from this hazard. In Australia, rockburst was first discovered to be a problem in the early 20th century as the mines in the Kalgoorlie district began to venture deeper into the crust. More recently at the Mt. Charlotte mine, several very large seismic events were caused by mining. These measured 2.5 and 4.3 on the Richter scale (Ortlepp 2005).

The very deep tabular ore bodies of South Africa experience far more severe and frequent rockburst events than anywhere else in the world. As a result, South Africa perhaps exhibits the most alarming and important statistics about rockburst consequences. The country displays the most severe and prevalent rockbursting in the world due to the greater depths at which mining is being undertaken and as a result industry-wide research has been established for around 50 years. Over that time fatality statistics have been kept and the trend of rockburst severity has been logged. Twenty years ago there were 129 deaths due to rockbursts out of a total workforce of 477,000 people. This corresponds to an annual rate of 0.27 fatalities per 1000 workers. When compared with data from 2003 where there was an annual rate observed of 0.2 per 1000 workers the trend is seen to be decreasing with the greater understanding that research is providing when designing underground support for rockburst. Despite this slight improvement, mines continue to get deeper and rock support systems need to keep evolving to ensure this trend quickly decreases towards zero fatalities. This can only be achieved if the mechanism for rockburst can be understood and described thoroughly to enable the advance prediction of events so there are no workers in the area when bursting occurs (Ortlepp 2005).

The severity of the rockburst problem all around the world keeps becoming more apparent as mines delve deeper and accident statistics emerge. In central Europe there have been approximately 190 rockbursts in the last 20 years which have sadly caused the deaths of 122 workers in the mines. These shocking numbers were only sourced from 42 mines across central Europe which log over a thousand seismic events each year (Ortlepp 2005). Perhaps more shocking is that in China, since the first recorded rockburst event in 1933 at Shengli Mine, events have numbered in the thousands and continue to increase in frequency due to the deeper excavations being attempted. For example from 2001 to 2007 in metal mines alone, 13,000 accidents accompanied by 16,000 casualties were attributed to rockbursts (Adoko *et al.* 2013). Other significant damage to mine operations and life caused by rockbursts has also occurred in Russia, the USA, and Canada with mines becoming deeper and more ambitious civil projects are being undertaken (Ortlepp 2005).

The significance in Australia is also first and foremost as mines are becoming deeper and rockbursting becomes more frequent. Although rockbursts had been documented in the Kalgoorlie district since the early 1900’s it has only been more recently in the 1990’s that seismic monitoring and rockburst research is thought to be important for Australian mines. Since that time although seismic monitoring has been installed at some mine locations there have still been deaths and injuries as a result of rockburst in Australia (Ortlepp 2005).

More recently Daniell and Love (2010) reported that from 1996-2006 there have been 4 deaths and 2 serious injuries resulting from rockburst events. Three of the fatalities occurred in the deep gold fields in Western Australia and one from the Beaconsfield mine in Tasmania. Although the Beaconsfield incident is still under debate regarding the mechanism the study assumed with good reason that the death was caused by a rockburst event.

Although the focus of this research, the rockburst phenomenon is not only restricted to mining operations. More ambitious civil tunnelling projects are being conducted and as a result the problem has been recorded in tunnels situated under large amounts of overburden, due not only to depth from surface but also overlying mountain ranges. Table 1-1 shows some conditions for tunnels constructed around the world. As can be seen there is not always a linear or intuitive relationship between the depth, stress and temperature, so each parameter should be investigated in relation to rockburst systematically (Chen *et al.* 2014a).

Table 1-1: Deep tunnel data (Chen *et al.* 2014a)

No.	Country	Tunnel	Max. Depth (m)	Vertical Stress (MPa)	Ground Temperature (°C)
1	Italy	Lyon-Turin	2000	15	40
2	Japan	Anfang	700	10	75
3	Switzerland	Simplon	2140	20	55
4	France	Mont Blanc	2480	25	37
5	Italy	Apennines	2000	30	64
6	China	Gaoligong	1167	25	60
7	China	Motuo	4000	108	90
8	China	Kongur	1500	15	90
9	China	Galongla	821	28	50
10	Japan	New Black	1000	13	170

Given the potential damage that rockbursts can cause, it is extremely important to understand this phenomenon. However, the prediction of rockbursts has only recently become an explicit goal of researchers on a whole to this point. More so the understanding, monitoring and to a lesser extent the mechanism derivation of rockburst events have taken precedence over the studies conducted thus far. Therefore it is apparent that there is a necessity to conduct investigation in to the behaviour of brittle rocks under the high stresses associated with deep mining. The following section provides an outline of the research conducted in this dissertation to address the need for deeper understanding of such an environment.

1.2 Thesis Outline

The structure of this thesis is such to provide a thorough investigation of the experimental and theoretical damage process in rocks during quasi-static loading prior to burst. This is focussed toward a future application to rockburst numerical modelling which is consistent with real mechanisms rather than empirical laws. In particular, the stress states leading up until burst are considered in this study. Therefore, the dynamic nature of rockburst itself is a focus of future research. As such, the dissertation begins with a discussion on the current literature available for rockburst and damage in hard rocks. The section outlines the key aspects of rockburst prediction to be the damage accumulation and energy storage in rock. Therefore, it is expanded to include studies on the damage modelling and testing of hard rock to identify the gaps in knowledge to be addressed.

Chapter 3 presents an experimental study on the testing of hard rocks to obtain the full load-displacement and damage behaviour. The proposed method utilises the full circumferential control (FCC) method to enable the full post-peak reaction to be recorded. This in turn enabled snap-back behaviour at low confinements. To highlight the importance of control method, the crack damage thresholds of each test were calculated using several existing methods as well as two new methods incorporating an experimentally obtained damage variable from acoustic emissions.

Chapter 4 is devoted to the development of a theoretical model based on damage mechanics and plasticity theory to accommodate the experimental findings in Chapter 3. The section proposes a generic framework coupling damage with plasticity for modelling rock failure under a wide range of confining pressures. The proposed unified yield-failure function makes better use of the concepts of initial inelastic behaviour (yielding) and the remaining residual strength mostly due to friction (failure) by allowing constant evolution between the two states. Hardening or softening is then related to how the yield surface evolves to the ultimate failure surface. This eliminates the need for separate loading surfaces and individually defined hardening and softening laws. This function is also able to automatically describe the brittle-ductile transition of rock under increasing confinement. It is shown that the proposed model is able to replicate a wide range of hard rock behaviour. In addition, the novel calibration procedure ensures that changing stress paths can be accounted for and experimentally derived damage evolution laws can be used directly without need for generalisation.

Chapter 5 then proposes a new apparatus for the small scale testing of rockburst to provide a validation data set for the future application of the constitutive model to rockburst numerical analysis. The design and implementation of innovative test platens are displayed along with the methodology to replicate the conditions for rockburst in the laboratory. The new method is shown to successfully replicate rockburst conditions on the inner free face. The stress state at burst and characteristic acoustic responses ae also presented and discussed. The importance in constitutive modelling is highlighted by analysing the results and specific stress redistribution characteristics unique to the rockburst mechanism.

The final chapter concludes the study and provides insight into the future works to be conducted and recommended. Specific conclusions on the testing and constitutive modelling of rockburst lead to continuing research in experimental method and numerical modelling.

Chapter 2 – A REVIEW ON ROCKBURST AND DAMAGE MODELLING IN HARD ROCK

Although some problems are manageable under the current understanding and monitoring of rock mechanics, rockburst cannot be predicted or mitigated accurately and confidently. As a result, a deeper understanding of the damage processes in rock needs to be established and strategies developed to model and test for rockburst. This chapter will review the rockburst phenomenon and the current research in rock damage testing and modelling. The motivation for the research in this dissertation will then be presented.

2.1 The rockburst phenomenon

Firstly it is necessary to define what is meant by the term 'Rockburst'. Several researchers have given definitions for the rockburst phenomenon. Ortlepp and Stacey (1994) described it as the 'violent ejection of rock' from the excavated face of the tunnel or mine opening. Ortlepp (2005) elaborated on this observation concluding, 'A rockburst is the significant damage caused to underground excavations by a seismic event.' The research also described a seismic event as 'the transient energy released by a sudden fracture or failure in the rock mass which results in the emission of a seismic vibration transmitted through the rock.' Another definition by He *et al.* (2010a) characterised rockburst as 'a non-linear dynamic phenomenon that may be defined as any sudden and/or violent expulsion of rock pieces from a temporarily stable opening.'

Although there have been many other definitions including those mentioned, the most complete description has been set out by He *et al.* (2010a), where it was postulated that, ‘rock burst often occurs in a sudden or violent way in the excavation surface of underground rock masses. Such a failure process of rocks is usually characterised by crack initiation, propagation and coalescence with associated damage evolution.’ This implies that cracks within the rock mass at all scales are extremely important in understanding the development of the failure process.

This section will give a brief overview of the rockburst phenomenon observed in the civil and mining industries. The initial research attempts will be presented followed by the current research being conducted to understand and mitigate the problem.

2.1.1 Rockburst mechanisms and empirical research

Several researchers have studied the behaviour of rockburst events and put forward mechanisms to describe and predict them. The first such study was conducted by Cook (1964) where it was postulated that the main source of energy for rockbursts is the gravitational elastic strain energy made available when the stiffness of the loading system was less than that of the failing portion of the rock mass (Cook 1964; Cook 1976).

Ortlepp and Stacey (1994) went on to say that the most probable cause of rockbursting in massive intact rock is strainburst (refer to Figure 2-1). This is due to hard, intact rocks being able to cope with high stress until brittle failure occurs to facilitate the rockburst phenomenon. It was observed that the mechanism is more likely to occur in a machine excavated tunnel than one mined using drill and blast techniques. This is due to the increased damage to the ‘skin’ layer of rock around the opening due to drill and blast. Therefore, elastic energy cannot be stored as efficiently in the face of the excavation. However, this was expected to be less of a factor when the harder the rock type and the higher the stress field, such is the situation found in ultra-deep mines. The other crucial finding of the paper is that strainbursting does not only occur in brittle, hard rocks. However the effect is amplified with increasing competency of the material (Ortlepp and Stacey 1994).

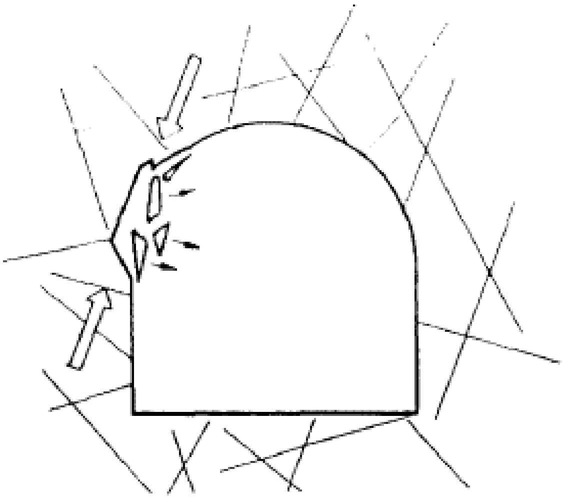

Figure 2-1: Illustrative example of strainburst (Ortlepp and Stacey 1994)

Further investigation of the seismic activity and rockbursts at the East Rand Proprietary Mines (ERPM) in South Africa found that the particularly violent events were a result of large shear ruptures. Observation revealed that these were planar features with displacements up to 100mm in a dip-slip sense (Ortlepp 2000).

Given the different mechanism observed to cause rockburst, Ortlepp (2001) proposed a classification table of the types of seismic event that can be experienced in an underground mine or civil tunnel (Table 2-1). Rockburst was assumed to fall under the first two categories in this classification. This study also postulates that rockburst events can be brought on by mining related stress field disturbances such as blasting and excavation proximity. This is not seen as much in civil excavations where the disturbances are minimal (Ortlepp 2001).

Table 2-1: Seismic event classification in underground excavations (Ortlepp 2001)

Seismic event	Postulated source mechanism	First motion from seismic records	Richter magnitude, M_L
Strainburst	Superficial spalling with violent ejection of fragments	Usually undetected, could be implosive	-0.2 – 1
Buckling	Outward expulsion of large slabs pre-existing parallel to surface of opening	Implosive	0 – 1.5
Face crush/pillar burst	Violent expulsion of rock from stope face or pillar sides	Mostly implosive, complex	1 – 2.5
Shear rupture	Violent propagation of shear fracture through intact rock mass	Double-couple shear	2 – 3.5
Fault-slip	Sudden, renewed movement on existing fault or dyke contact	Double-couple shear	2.5 – 5

He *et al.* (2012) further divided rockburst events into three main types, strainburst, fault-slip burst and pillar burst (see Figure 2-2). All three contribute to the rockburst phenomenon on a whole, however, strainburst was considered by the research team to be the hardest to predict and hence account for. The research pointed out that there are no visible macroscopic signs leading towards a rockburst event. Therefore, the cracking process at a microscopic scale plays a vital part in the energy accumulation and damage of the rock mass and hence contributes significantly to rockburst occurrence and severity.

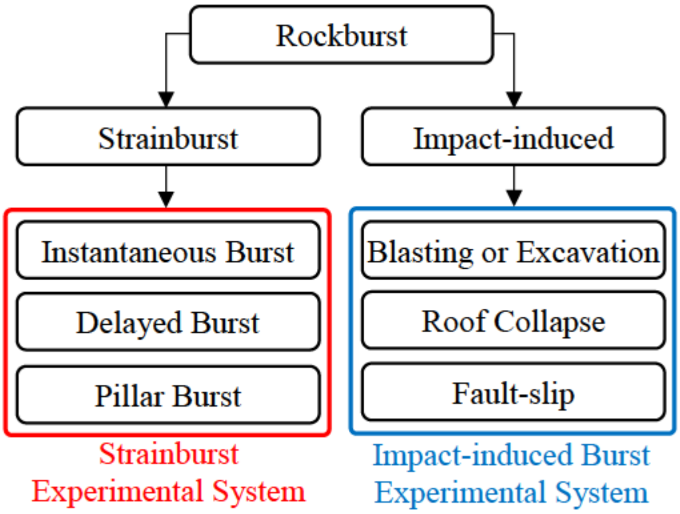

Figure 2-2: Rockburst classification and experimental strategy (modified from He *et al.* (2012))

So far many researchers have used energy balance relationships and brittleness constants to explain the mechanisms of rockburst mentioned. These can be useful in formulating general empirical guidelines for specific mining or civil operations. Wang and Park (2001) first stated that an important factor in rockburst was the accumulation of strain energy in the rock mass and the violent fracture and then expulsion of rock was caused by an excess of available energy during the post-peak stage of deformation. They went on to say that rockburst is induced by a sudden release of elastic energy when the rock is subjected to brittle failure. They in turn studied the effects of cyclic loading on specimens to determine the remaining or residual capacity for stored elastic strain energy. Figure 2-3 shows the analytical relationship they used to study the energy capacity of rock during cyclic testing (Wang and Park 2001).

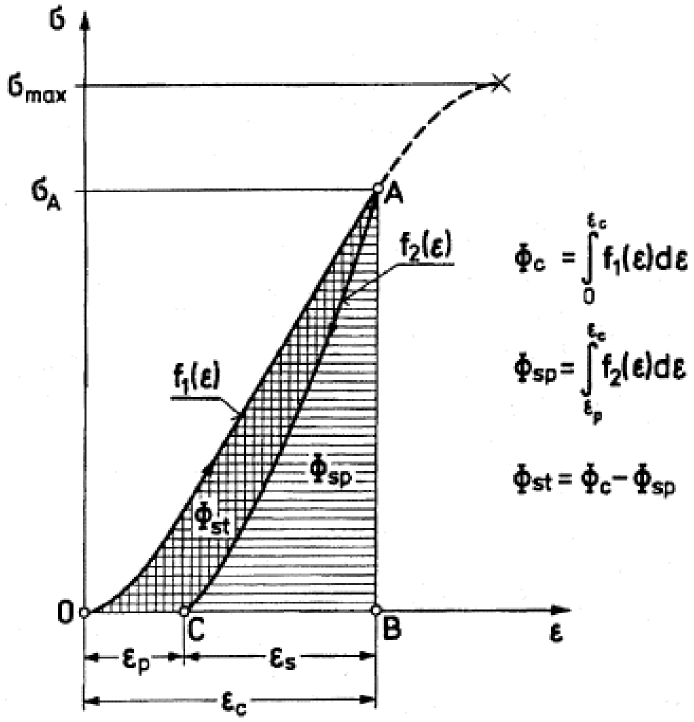

Figure 2-3: Energy calculations for cyclic loading experiments (Wang and Park 2001)

Using the equation for the elastic strain energy in a rock mass the study showed that as the rocks become more brittle, the energy dissipated during plastic deformation and micro-fracture becomes very small. Therefore, the released elastic energy when brittle failure occurs is high and will result in a strong bursting effect. They also found a rockbursts threshold when the stored energy exceeds 1.0 x 105 J/m^3. A rockburst criterion was then proposed which is shown in Equation 2-1, where F is the factor of shock, φ_{sp} is the elastic energy stored in the rock and φ_{st} is the dissipated energy in the creation of microfracture and plastic deformation. Refer to Figure 2-3 for the graphical representation of the energy ratio (Wang and Park 2001).

$$F = \frac{\varphi_{sp}}{\varphi_{st}} \tag{2-1}$$

where calculated value for this ratio is then subjected to comparison with the criteria; $F \leq 2.0$, means no shock, $2.0 \leq F < 5.0$, means weak to medium shock and $F \geq 5.0$, means strong or violent shock (rockburst) (Wang and Park 2001).

Strain energy empirical relations were largely relied upon up until Tarasov (2010) extended the stored energy theory to include the post-peak region of brittle rock failure. They defined a brittleness index, k, which is formulated using the information in Figure 2-4 along with the relationship:

$$\mathrm{k} = \frac{\mathrm{dW_r}}{\mathrm{dW_e}} = \frac{\mathrm{E-M}}{\mathrm{M}} \tag{2-2}$$

where $\mathrm{dW_r} = \frac{\mathrm{d\sigma^2(E-M)}}{\mathrm{2EM}}$ is the rupture energy, $\mathrm{dW_e} = \frac{\mathrm{d\sigma^2}}{\mathrm{2E}}$ is the accumulated elastic energy available for the rupture process, $\mathrm{E} = \frac{\mathrm{d\sigma}}{\mathrm{d\varepsilon}}$ is the unloading elastic modulus and, $\mathrm{M} = \frac{\mathrm{d\sigma}}{\mathrm{d\varepsilon}}$ is the post peak modulus (Tarasov 2010).

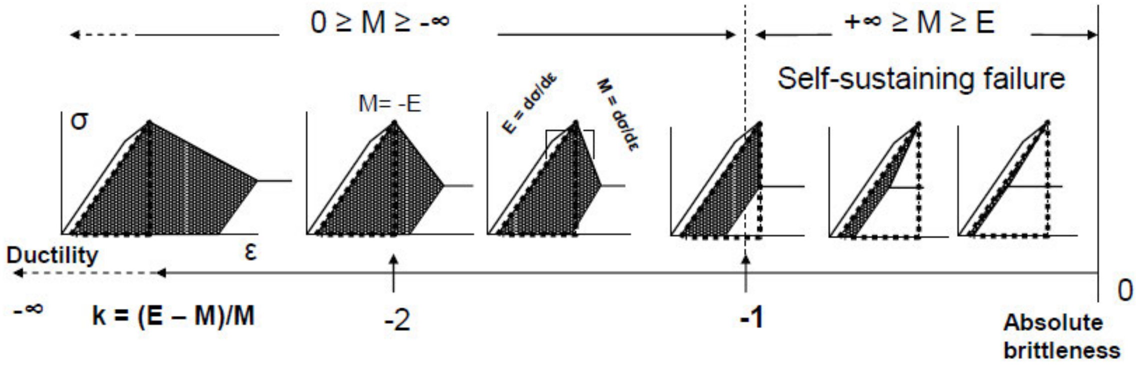

Figure 2-4: Brittleness index stress-strain curve types (Tarasov 2010)

The study then compared the brittleness characteristics of a sandstone, a quartzite, granite and the dolerite (tested by Tarasov and Randolph (2008)). It was found that as confining pressure is increased during triaxial testing, hard rocks experience *embrittlement* (higher k factors) before transitioning to ductile behaviour. This can be seen in Figure 2-5 where the rocks are numbered from 1 (diorite) to 4 (sandstone). Using these results it was proposed that the 'superbrittleness' range is the area which the rock is prone to bursting mechanisms (Tarasov 2010).

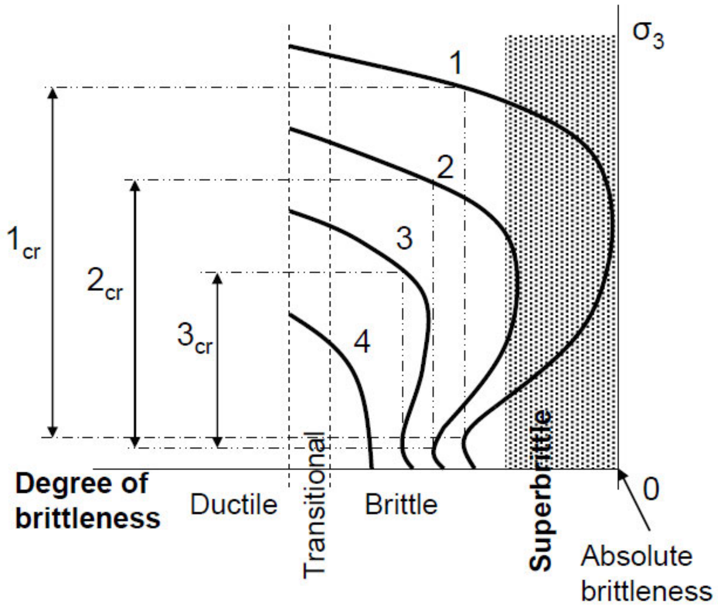

Figure 2-5: Rock embrittlement process (Tarasov 2010)

Following this, He *et al.* (2012) proposed a criterion for strain burst prediction as well as a means to calculate the released energy. For bursting to occur, the following criterion was imposed:

$$\Delta E = E(\sigma_{1c}) - E(\sigma_c) > 0 \tag{2-3}$$

where the energy released during bursting was then described as:

$$\Delta E = E(\sigma_{1c}) - E(\sigma_c) = \frac{1}{2}\sigma_{1c}\varepsilon_c - \int_0^{\varepsilon_c} E\varepsilon d\varepsilon = \frac{1}{2}\sigma_{1c}\varepsilon_c - \frac{1}{2}E{\varepsilon_c}^2 \tag{2-4}$$

where ε_c is the maximum principal strain at the peak stress in the rockburst test and Figure 2-6 illustrates the energy calculation process (He *et al.* 2012).

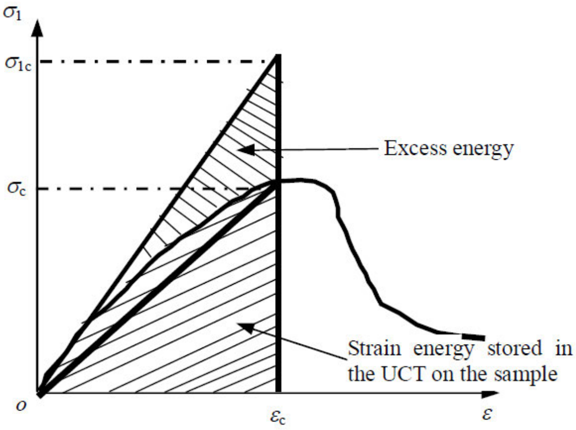

Figure 2-6: Model for energy calculation of strainbursts (He *et al.* 2012)

The research also proposed a graphical representation of the different loading paths that contribute to rockburst. Figure 2-7 presents the proposed loading paths for three types of strain burst. Area Z_1 is the potential zone for instantaneous burst and Z_2 is the burst-prone zone for delayed rock burst. Points A, B and C_1 and C_2 are the initial stress states before unloading (He *et al.* 2012)

For the instantaneous burst criterion shown in Figure 2-7a, the area Z_1 is the potential zone for the occurrence of rockburst of this type. Point A represents the initial stress state before excavation; and σ_c and σ_r are the uniaxial compressive strength (UCS) and the long-term peak strength, respectively. The instantaneous burst occurs with the release of σ_3 if the maximum principal stress σ_{1c} is greater than σ_c. The stress path indicates that the instantaneous burst will happen only when the strain energy accumulated in the rocks exceeds the energy that is necessary for rock failure, and there is enough excess energy (ΔE) that can be released kinetically (He *et al.* 2012).

The delayed burst criterion shown in Figure 2-7b has the area Z_2 as the potential burst-prone state of the rock. The main difference with this situation is that the rock won't burst upon sudden release of confinement. Rather it would take some time before built up stresses become overwhelming. Finally, the pillar burst criterion shown in Figure 2-7c is encountered when σ_1 is increased and σ_3 is decreased simultaneously, causing this type of strainburst (He *et al.* 2012).

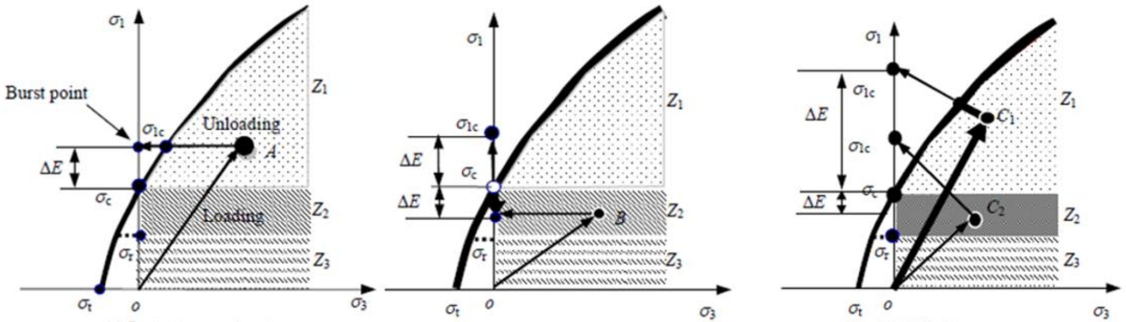

(a) Instantaneous burst. (b) Delayed burst. (c) Pillar burst.

Figure 2-7: Schematic diagram of strainburst loading paths (He *et al.* 2012)

More recently, statistically formed empirical relationships for rockburst have become popular as a means to try and predict future occurrences (Adoko *et al.* 2013; He *et al.* 2015a). One such example by Adoko *et al.* (2013) applied fuzzy modelling techniques to try and construct a predictive model for rockburst. Fuzzy modelling defines relationships between input and output variables of a system by using a series of IF-THEN statements. These IF-THEN rules assume the form, 'if x is A then y is B'. In this study 176 cases were used from recent sources (1994-2011) to construct both knowledge-based and data-driven fuzzy models for rockburst prediction. The conclusion of the study reveals that although the method shows some promise for a broad predictive technique, it is very limited by the data sets and knowledge inputs. Also, as the mechanisms and mechanics of rockburst are not fully understood the models could only predict 66.52% of the validation data sets. Therefore, due to the empirical information used in the knowledge-based modelling and the limited confident data sets the fuzzy modelling technique cannot be properly employed to predict rockburst (Adoko *et al.* 2013).

He *et al.* (2015a) also published a statistically themed paper presenting the use of data mining techniques in rockburst prediction. Using the data gathered from 139 rockburst experiments, data mining techniques were applied using multiple regression (MR), artificial neural networks (ANN) and support vector machines (SVM) algorithms. These were implemented to obtain predictive models for the rupture stress due to rockburst, σ_{RB} and the description of a rockburst index, I_{RB}. The rockburst index is given as a function of the rockburst maximum stress in earlier studies and is typified by Equation 2-5 where H is the depth of the excavation.

$$I_{RB} = 0.054\frac{H}{\sigma_{RB}} \tag{2-5}$$

By applying the methods using the R program environment, a multiple regression model was found to be the best fit for the rupture energy given the input variables. The variables found to be most relevant were the unconfined compression strength, UCS, the horizontal stresses σ_{h1} and σ_{h2}, the depth, H, the deformability modulus, E, and the vertical stress, σ_v. The final relationship for rockburst stress was reported as (He *et al.* 2015a):

$$\begin{gathered}\sigma_{RB} = 9.132 - 0.013H + 0.381UCS + \\ 0.364E + 1.211\sigma_{h1} - 0.069\sigma_{h2} + 0.365\sigma_v\end{gathered} \tag{2-6}$$

The models were then manipulated to find the rockburst index and it was found that multiple regression provided inaccurate results. In this case, ANN proved to be the most effective method of determining the equation. This was due to the relationship being very non-linear. The most important variables, in order, in Equation 2-7 are depth, maximum rupture stress, deformability modulus, bulk modulus, and unconfined compressive strength (He *et al.* 2015a).

$$I_{RB} = 1.432 + (8.035 \times 10^{-4})H - (8.429 \times 10^{-4})UCS - 0.009E - 0.007\sigma_{RB} - 0.074K \quad (2\text{-}7)$$

It is apparent from the review conducted above, that researchers believe the dominant factor in strainburst is the ability for the material to store elastic strain energy. However, to simply impose some empirically derived law based on limited test data can cause inaccurate prediction. It is also pointed out that the energy storage of the rock is calculated using the full stress-strain curve of material tests. It is therefore, vital to ensure the tests are accurate and provide a precise description of the material behaviour under load. Another finding was that strainburst is greatly affected by the level of cracking accumulated in the rock face before brittle failure. This directly relates to the amount of strain energy a rock can store or dissipate before failure and in turn could be the difference between a burst prone or spalling rock failure. To try and address these crucial factors, research has been conducted both on the numerical modelling of strainburst as well as the enhanced testing of materials in the laboratory. The following sections review the current literature in these two areas of research.

2.1.2 Numerical rockburst models

As was pointed out in the previous section, strainburst is widely believed to be dependent on the characteristic stress-strain response of a material (Wang and Park 2001; Tarasov 2010; He *et al.* 2012) and the accumulated damage of the rock face (Jiang *et al.* 2010; Zang and Wang 2012). Therefore, to try and provide some measure of numerical prediction, researchers have implemented various methods to model the phenomenon.

One of the first attempts to numerically simulate rockburst came from Bardet (1989) who investigated the applicability of the finite element method (FEM) in the modelling of rockburst and surface instability. Although, preliminary results showed the method was able to predict surface instability it was limited in terms of rockburst prediction due to the simplicity of the constitutive models used for the study (Bardet 1989).

From this initial attempt there were very few studies of note on the numerical modelling of rockburst, until Jiang *et al.* (2010) studied the rockburst events in the Jinping II hydro-power station in China. The researchers applied a new energy index called the Local Energy Release Rate (LERR) to simulate the conditions that cause rockburst. The model was applied to the pilot tunnels of the project at 2,500m depth as well as some rockburst events in the Mine-by rock tunnel in Canada. The researchers put forward a strainburst model which is based, once again, on the intrinsic condition that brittle failure is due to energy release. They calculated the index using the sudden release of energy stored in a rock mass when the strain energy became too large for the material to remain intact (Jiang *et al.* 2010).

The proposed model for the study was an elastic-brittle-plastic model. This was adopted as rockburst displays a brittle failure mechanism. Unloading caused by the excavation of a tunnel or mine opening changes the stress distribution pattern in the rock mass and causes a concentration of stress. This in turn causes microcracks and damage accumulation in the rock. The deterioration caused by this effect also alters the mechanical properties of the rock, namely the elastic modulus, the cohesive strength and the friction angle. These factors were accounted for as a function of plastic strain and the model was built using plastic mechanics. Using numerical analysis the index can be calculated in the post-processing stage as (Jiang *et al.* 2010):

$$LERR_i = U_{i\,max} - U_{i\,min} \tag{2-8}$$

Where $LERR_i$ is the local energy release rate of the *ith* element and $U_{i\,max}$ and $U_{i\,min}$ are peak and trough values of elastic strain energy intensity before and after brittle failure given by (also see Figure 2-8):

$$U_{i\,max} = [\sigma_1^2\sigma_2^2\sigma_3^2 - 2v(\sigma_1\sigma_2+\sigma_2\sigma_3+\sigma_1\sigma_3)]/2E \qquad (2\text{-}9)$$

$$U_{i\,min} = [\sigma_1'^2\sigma_2'^2\sigma_3'^2 - 2v(\sigma_1'\sigma_2' + \sigma_2'\sigma_3' + \sigma_1'\sigma_3')]/2E \qquad (2\text{-}10)$$

Where σ_1, σ_2 and σ_3 are the three principal stresses corresponding to peak strain energy, σ_1', σ_2', and σ_3' are the three principal stresses corresponding to the trough strain energy of the element, v is the Poisson's ratio and E is the Young's modulus (Jiang *et al.* 2010).

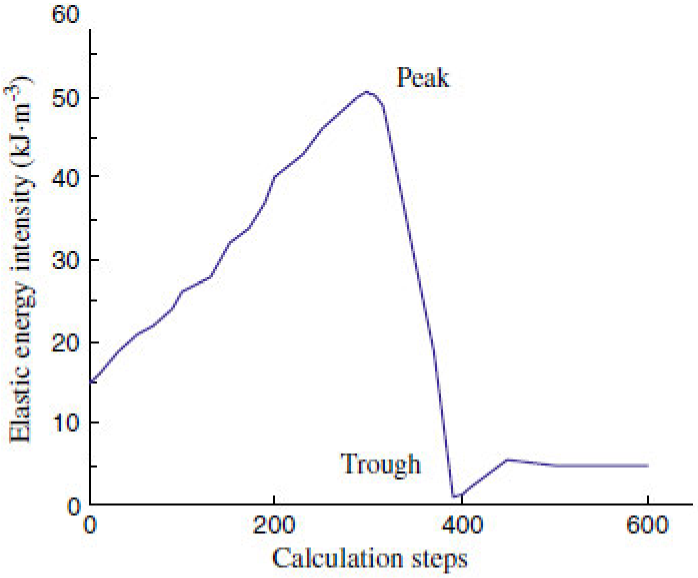

Figure 2-8: Evolution of elastic strain energy in finite element (Jiang *et al.* 2010)

The study concluded by conducting numerical analysis and found that although the relationship could reliably predict the intensity of a known rockburst event (see Figure 2-9), it could not formulate a threshold value for prediction (Jiang *et al.* 2010).

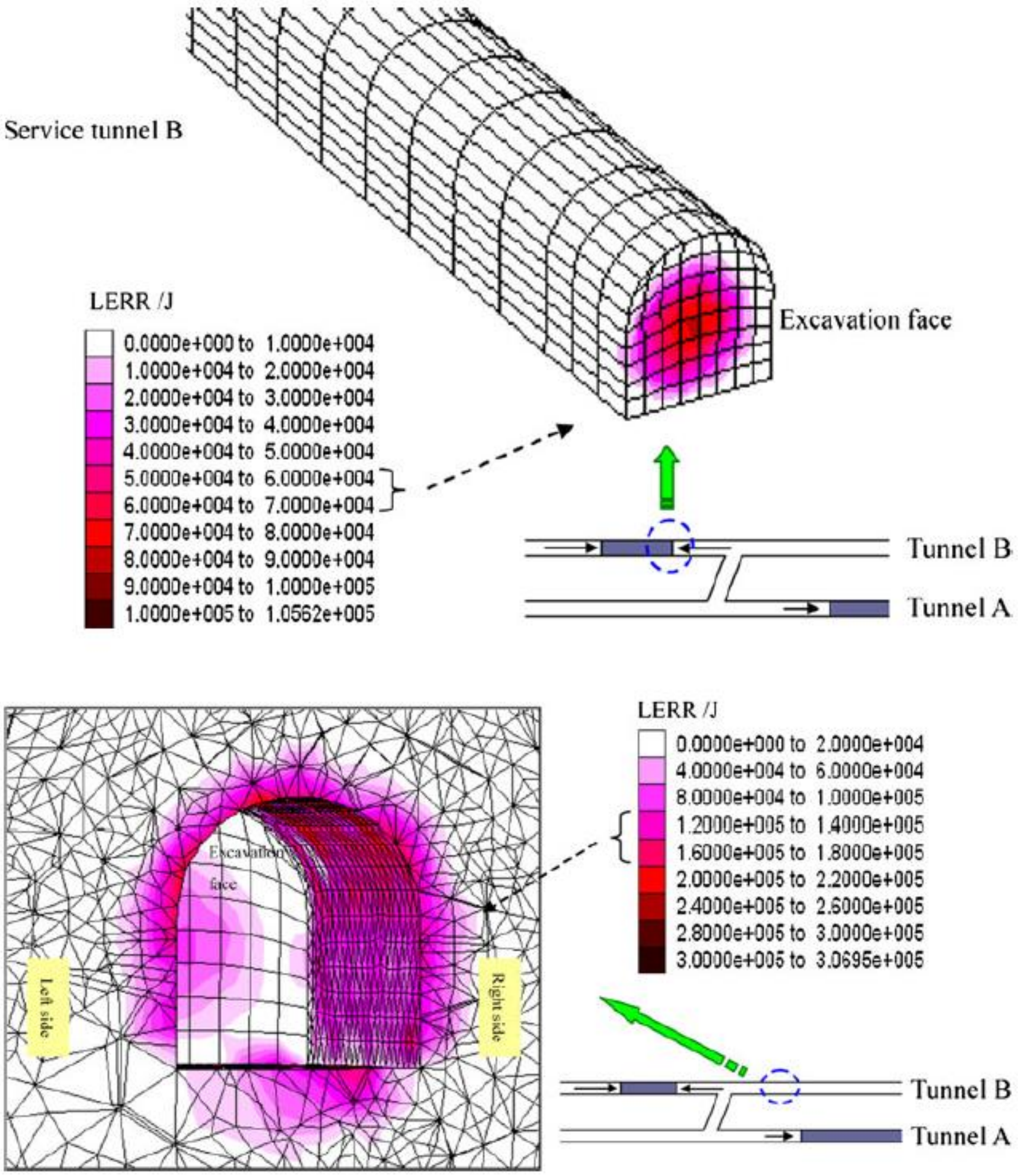

Figure 2-9: Numerical results of LERR method (Jiang *et al.* 2010)

A similar study by Weng *et al.* (2017) also used a strain energy release rate criterion. It can be seen in Figure 2-10, that the method for predicting rockburst is essentially the same as Jiang *et al.* (2010) however, it was expanded to include the effect of dynamic disturbance in the simulations.

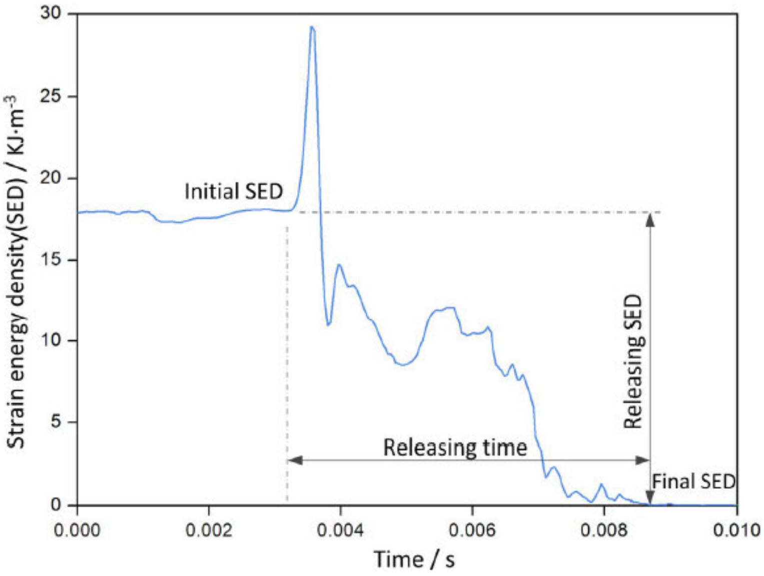

Figure 2-10: Strain energy density release rate (Weng *et al.* 2017)

The key findings of the study were that rockburst is most likely in the floor a sidewall of an excavation and most extreme 10 to 15m back from the excavation face. These are illustrated by high release rate illustrated in Figure 2-11.

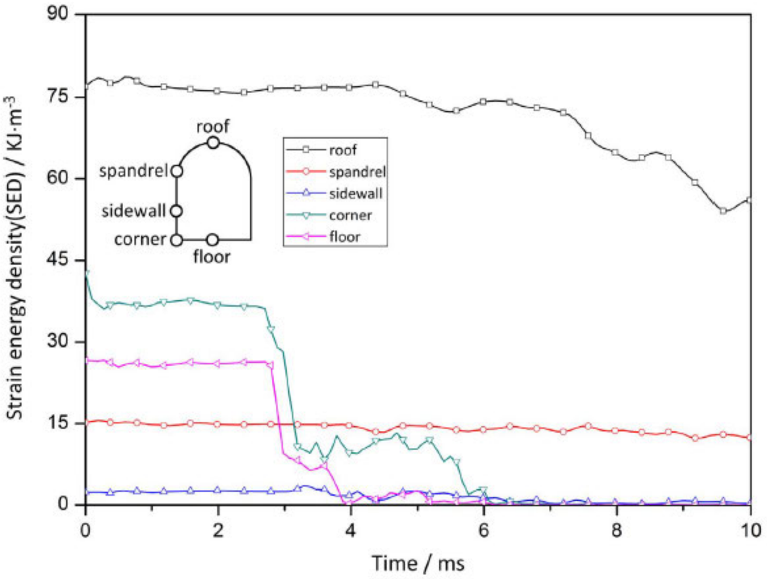

Figure 2-11: Strain energy release rates (12m from excavation face) (Weng *et al.* 2017)

Once again, although the simulations successfully predicted the existing rockburst cases, no attempt to derive a rockburst threshold or criterion was made. This was due to the model not including the full stress-strain or damage of the material. Therefore, when only calibrating to specific structural values such as already occurred events, numerical models cannot predict a future occurrence of rockburst given only fundamental strength parameters of a material.

The research by Zang and Wang (2012) sought to solve this limitation by introducing damage into the constitutive modelling of the material. By the introduction of a scalar damage parameter (discussed in Section 2.2.1) the numerical model was able to predict the stored energy more accurately than for the purely plastic modelling approach. This coupled with the criterion by Jiang *et al.* (2010) allowed the prediction of rockburst events and severity. It was also noted that with increasing damage to the rock, the likelihood and energy of a rockburst even was reduced. This provided numerical proof that to model the rockburst phenomenon correctly, damage must be incorporated. Although, the study was able to predict the events at the case site, no information was given on the calibration of the numerical model and therefore, it is impossible to use such a model to apply in different situations.

An alternative method to using FEM to model the behaviour of a rock mass is the discrete element method (DEM) used by Fakhimi *et al.* (2016). The study used fundamental contact models to describe the constitutive behaviour of the specimen that was tested and was able to replicate the experimental results. The study also showed numerically (and physically through testing) that pre-conditioning of a mine pillar by boring holes into it can reduce the severity of sudden, violent failure. This further confirms the important role of damage (or reduced strength) in the understanding of rockburst. Although the results were promising, the test set-up was specialised and no link was made between it and real life excavations. This highlights the importance of small scale laboratory testing of rockburst. Along with the fundamental testing methods for material classification, specific rockburst tests should also be conducted to calibrate numerical models. If the link between experiment and full scale excavation can be sufficiently argued, this provides a solid validation tool to ensure the correct behaviour can be captured by a proposed model. However, due to the limited numerical and analytical studies on rockburst, few have consistently made this a priority. The following section reviews the current methods to monitor real excavations as well as the small scale tests conducted to replicate rockburst.

2.1.3 Rockburst monitoring and testing

Rockburst has become more prevalent as mining excavations delve deeper into the crust. As such, it has become increasingly important to monitor the rock mass for rockburst precursors to enable safe mining operations. Therefore, researchers have tried to gain more insight from seismic and micro-seismic monitoring of rockburst prone areas. Although numerous studies have been conducted on micro-seismic methods in mines, few studies focus on the prediction of strain type rockbursts. Instead they tend to focus on the earthquake analogous, fault-slip types. Therefore, although there are many studies focussing on the seismic monitoring of mines, not all are relevant to the aims of this thesis. Thus, this section will only provide a brief summary of the application of seismic techniques for rockburst prediction.

The first to realise the potential for this method with respect to rockburst was Cook (1964). The study installed a micro-seismic monitoring system at the East Rand Proprietary Mines in the Witwatersrand region, South Africa. From this system the research was able to locate and predict the energy of seismic events in the mine at depths of around 2500-2800m, thus demonstrating the effectiveness of such a monitoring system for fault slip type bursts (Cook 1964).

Cook expanded his research in 1976 in a new paper which focused on characterising seismicity associated with mining. The study concluded that seismic events, including rockburst, are similar in most respects to earthquakes that occur naturally. In addition it remarks that most events occur in short time periods after excavation and are located within 10m of the advancing face. Finally the research describes that the rate of energy release of the events increases with depth, therefore they become more violent and dangerous to equipment and life the deeper a mine or civil project ventures (Cook 1976).

Another rockburst seismic study in the North Ural Bauxite mines, focused on the physical basis that rockbursts are similar to earthquakes in that both occur in the Earth’s crust due to stress impaction. Therefore, by definition, rockbursts must also display seismic acoustic emissions similar to earthquakes in behaviour but not magnitude. The technique used in the study consists of the kinetic theory of solid strength and the ‘rigid inclusion’ model. There were three main stages observed by the researchers of the evolutions of a ‘rigid inclusion’ they were (Mansurov 2001):

1. The forming or consolidation of the discontinuity ($t_1 – t_2$)
2. The destruction of the discontinuity ($t_2 – t_4$),
(also includes the main fault occurrence ($t_3 – t_4$))
3. The post-failure stage ($t_4 – t_5$)

The time intervals for each stage can be seen in Figure 2-12.

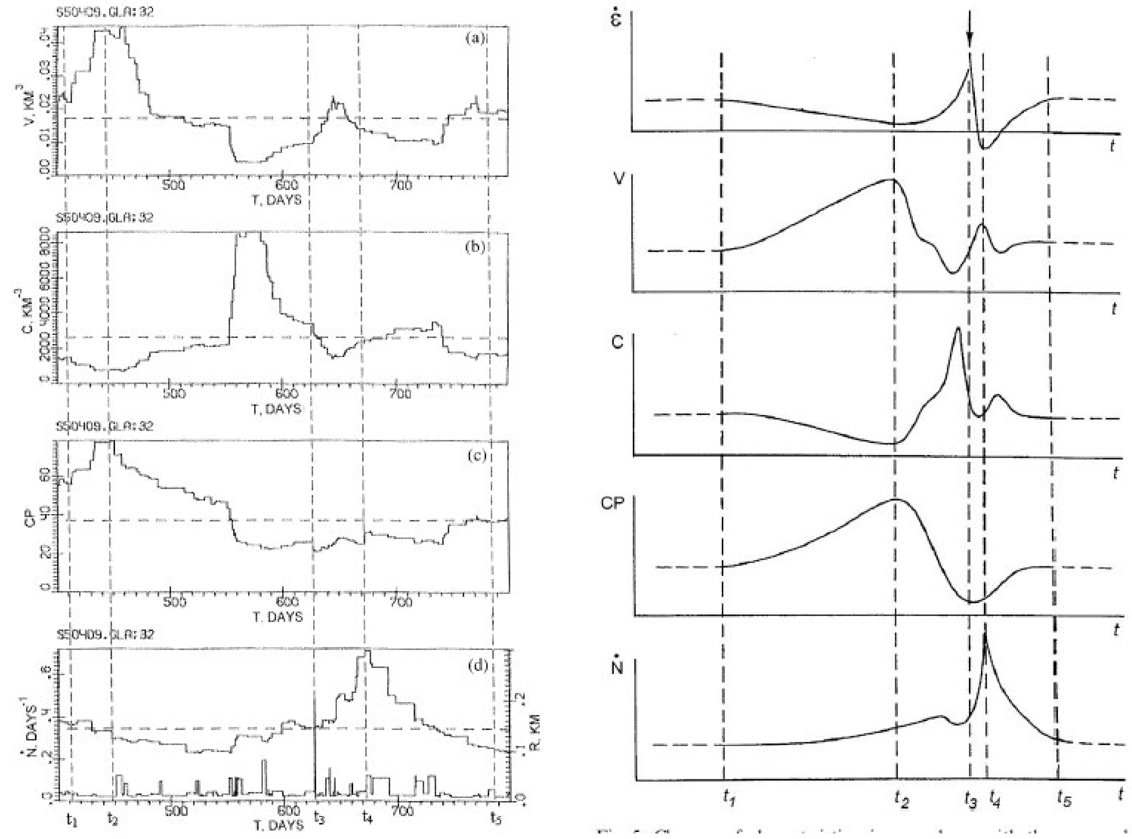

Figure 2-12: Rockburst time intervals (Mansurov 2001)

Seismic event concentration characteristics were also proposed in the study and used in the Bayes approach to model the rockburst regions. It was found that it could be applied to probabilistically predict rockburst events with limited success (Mansurov 2001).

More recently Tang *et al.* (2010) performed numerical acoustic modelling of rocks using various heterogeneity factors to better determine the seismic properties of rock to allow better prediction. The modelling found that the more heterogeneous a rock mass was, the more microcracks occur before the rockburst event (see Figure 2-13). This finding was important as it highlighted the link between rockburst severity and accumulated damage in a rock before failure.

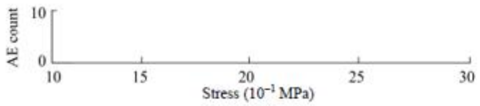

(a) Colophongy.

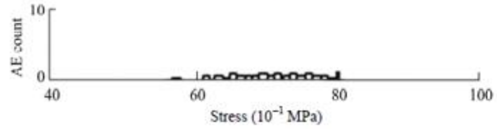

(b) Trachyte.

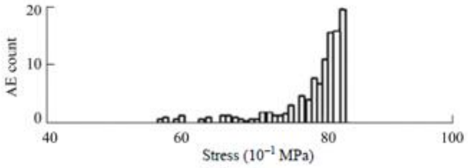

(c) Granite.

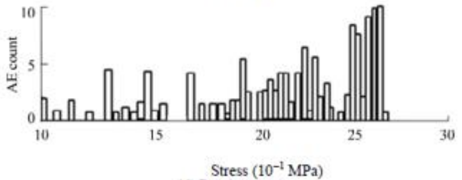

(d) Pumice stone.

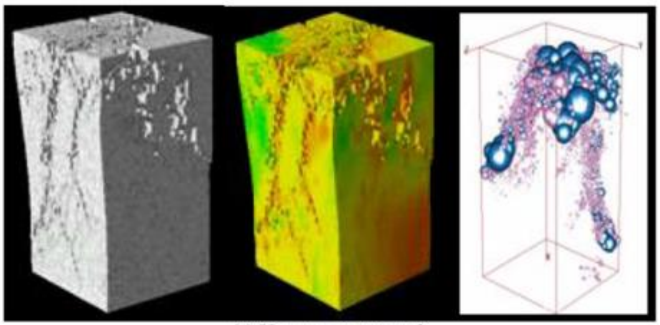

(a) Heterogeneous rock.

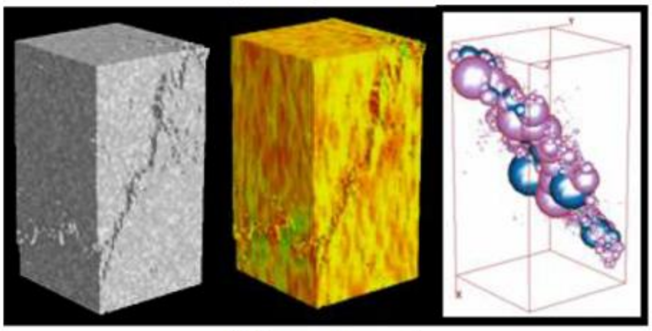

(b) Homogeneous rock.

Figure 2-13: AE count and failure process due to different homogeneity factors (Tang *et al.* 2010)

This modelling coupled with on-site seismic monitoring of the Jinping II project in China revealed that there are three main factors in the prediction of rockburst. First, the heterogeneity of rock is the controlling factor in being able to predict rockburst in real life excavations. This was coupled with the facts that deformation localisation is the intrinsic cause of rockburst and the interaction between the material and surrounding rocks of excavations is the external cause of the phenomenon. The researchers went on to describe some of the key advantages of using micro-seismic monitoring in deep mines such as the very wide range at which the system works. Therefore, the system does not have to be set up multiple times for long term operation (Tang *et al.* 2010).

Subsequently, Feng *et al.* (2012) conducted a series of tests on in-situ boreholes. Results were obtained by the use of borehole cameras and acoustic monitoring equipment. There were several direct findings from the experiments. Firstly, the cameras recorded very little deformation prior to a rockburst event, which indicated that damage prior to the event was at a microscopic level (microcracking). Then from the review of the data from the micro-seismic monitoring several other key understandings were put forward. The data showed that micro-seismicity is very active immediately leading up to and during a rockburst event, however, if the event is delayed by several days or longer the monitoring system records a quiet period in seismicity. Therefore, using self-similarity of seismic patterns, rockburst could be predicted to some degree. The quiet period over several days however, constrains these methods somewhat as the prediction can only be made a very short time before events occur which is useful in saving life but not equipment or to employ support strategies (Feng *et al.* 2012).

As can be seen from the brief review of microseismicity of rockbursts above, there is a limit to the information that can be gained from this technique. The monitoring systems implemented at mines are very useful in monitoring the excavation for impending events however, prediction cannot be made well in advance. Also the micro-seismics only indicated that there was microcracking occurring within strong competent rock and does not shed any light on the mechanisms at play and the build-up of strain energy needed to facilitate a violent strainburst event. Therefore, researchers have shifted focus to small scale laboratory testing to simulate the conditions of strainburst. This information about the mechanisms should give a constitutive or numerical model the ability to predict the phenomenon.

To date, rockburst testing is predominantly undertaken in Chinese laboratories as the problem is significant in the country’s civil and mining projects. The first type of rockburst test that was attempted utilised an unconfined loading regime such as that employed by Chen *et al.* (1997). In this experiment a double rock sample (one rock on another) was tested in an unconfined compression test to display the characteristics of a simulated rock mass event. The test results were then compared to the measured acoustic emissions to formulate a numerical code for rock failure. The study shows that there were micro-seismic events prior to the main shock of rockburst failure (Chen *et al.* 1997).

As uniaxial loading does not exactly replicate the conditions found in underground excavations, other researchers set out to describe the effects of triaxial and true-triaxial loading on rockburst behaviour. An important application of conventional triaxial testing for rockburst research was conducted by Huang *et al.* (2000). In the study it was identified that research done before only tested rocks under loading conditions and did not take into account the unloading of rocks such as the conditions found when excavating tunnels. Therefore, the methodology set out to test the unloading of rocks in two controlled situations. The first was under displacement (LVDT) control seen in Figure 2-14, where *S* represents hydrostatic stress, *SU* is the loading path and *UF* is unloading to the failure point. The second was under force (FORCE) control where *S'* is the hydrostatic stress level and *F'* is the failure point of the rock at bursting shown in Figure 2-15 (Huang *et al.* 2000).

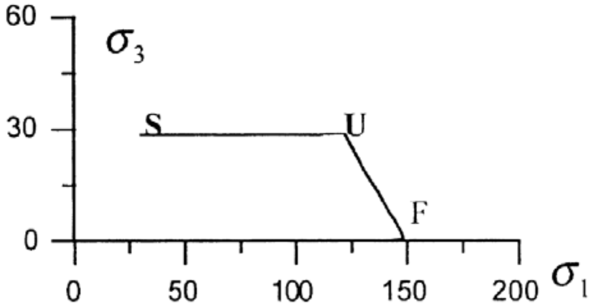

Figure 2-14: LVDT unloading regime (Huang *et al.* 2000)

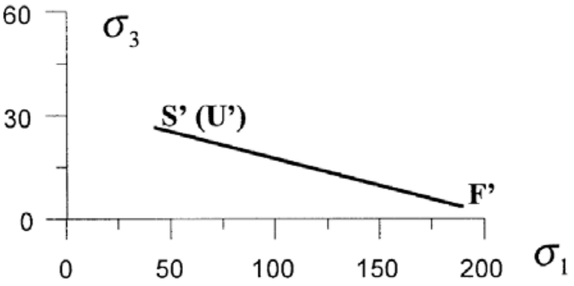

Figure 2-15: FORCE unloading regime (Huang *et al.* 2000)

These unloading tests were then compared to the loading type tests performed on the same rocks and the results are shown in Figure 2-16 (Huang *et al.* 2000).

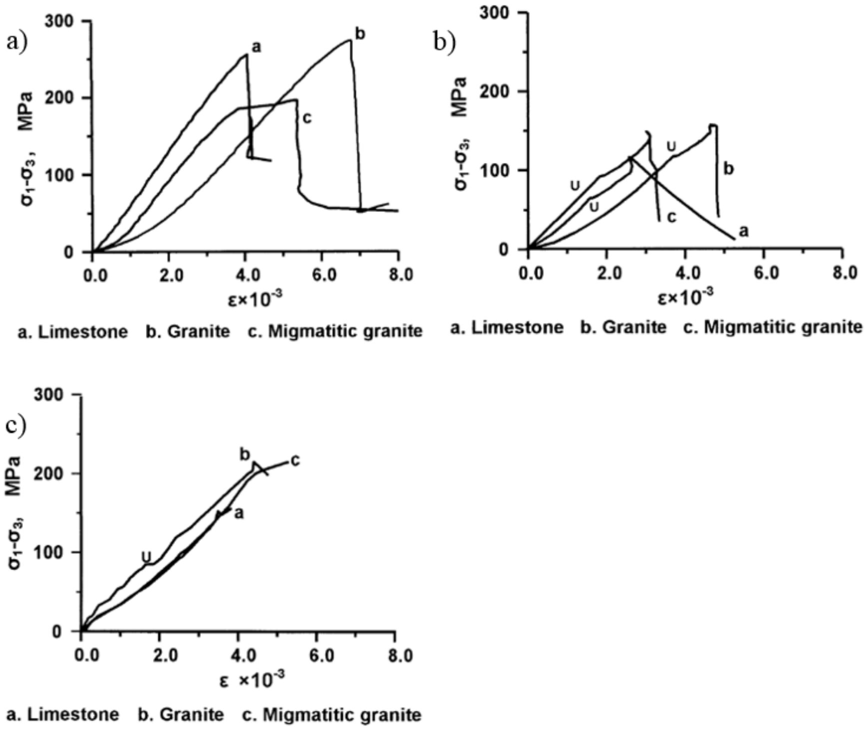

Figure 2-16: Rockburst triaxial test results a) Loading tests, b) Unloading LVDT tests and c) Unloading FORCE tests (Huang *et al.* 2000)

It was found from testing that the elastic moduli for the rocks are lower for the unloading case than for the loading case. Additionally the peak strengths of the rocks are much smaller under unloading conditions. The rate of unloading was also considered and it was discovered that the faster the unloading rate the weaker the rock specimens became. Therefore, it was deduced that in areas where the rock mass is being excavated and the in-situ rocks are highly stressed, the weaker rocks would display a ‘slaty’ type failure mechanism which would lead to rockburst (Huang *et al.* 2000).

In underground excavations, a free surface is created due to blasting or tunnelling processes. Therefore, by far the most popular testing methodology amongst current researchers today is the ‘true-triaxial unloading’ technique first described by He *et al.* (2010a). The true-triaxial rock test apparatus was developed in China and could provide dynamic loading/unloading independently in the three principal stress directions. This accounted for the complicated stress states which are be present in underground excavations. Additionally, the minor principal stress σ_3 could be released rapidly on one face to simulate the stress conditions immediately after excavation. The experimental apparatus is shown in Figure 2-17 (He *et al.* 2010a).

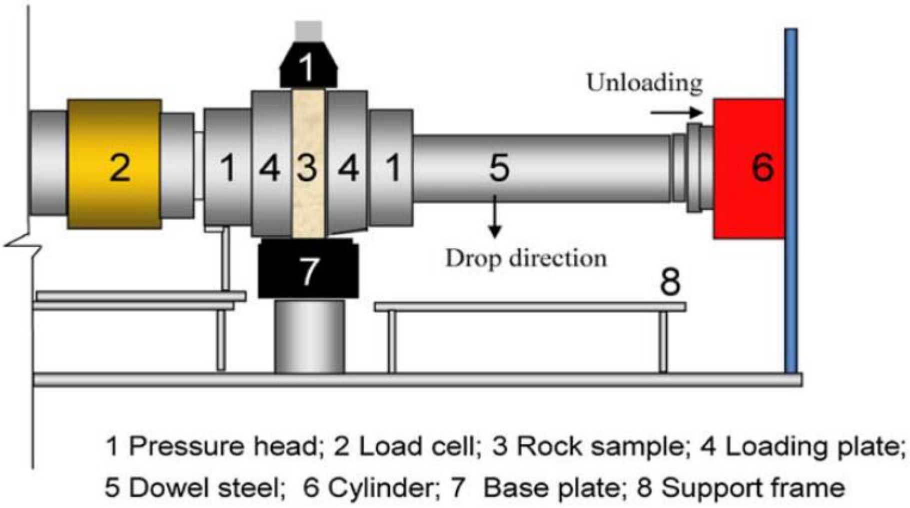

Figure 2-17: True-triaxial rockburst test apparatus (He *et al.* 2010a)

Results obtained from this apparatus were then used to study the acoustic emissions and the ejection velocity of rock fragments from the free face. A typical loading profile can be seen in Figure 2-18, from which it is evident that the acoustic emission energy rapidly increases just prior to failure.

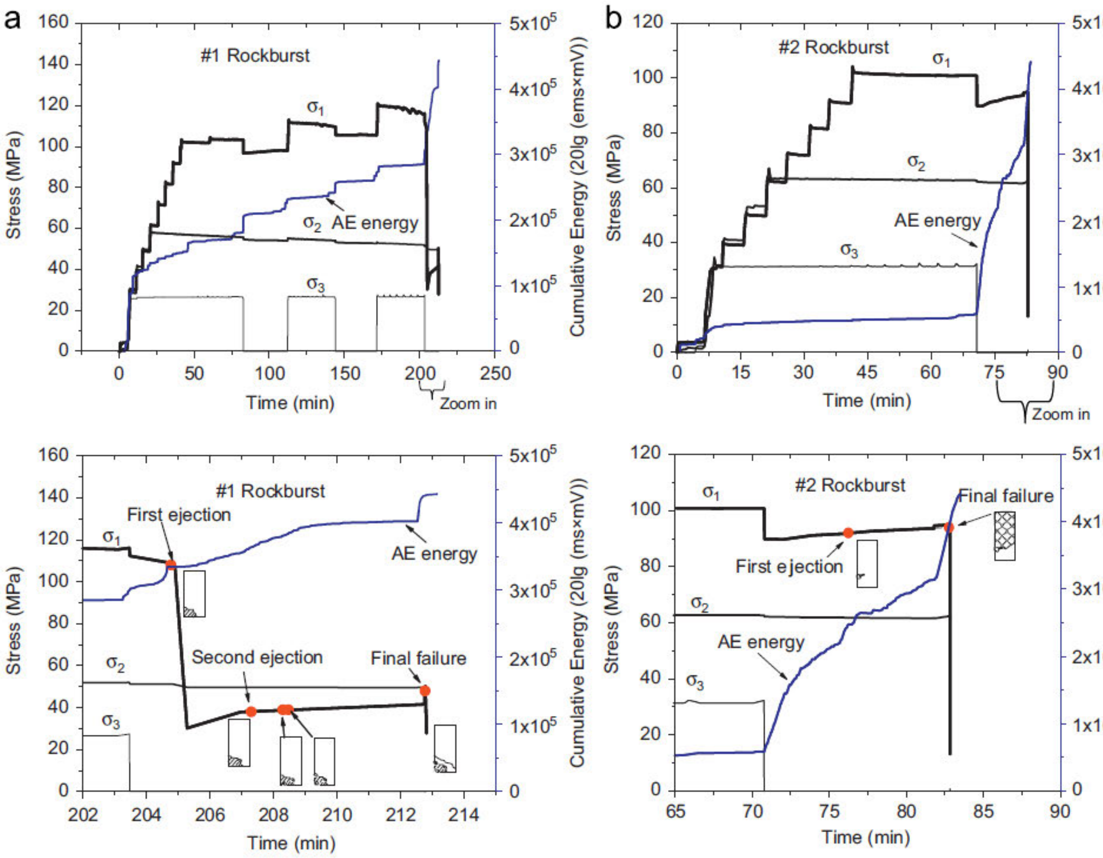

Figure 2-18: Stress path and accumulated AE for two limestone specimens (He *et al.* 2010a)

Additionally, the observed ejection of rock fragments was consistent with the strainburst type mechanism. One of the key findings was that rockburst events take place sometime after unloading and not immediately. This means that they are hard to predict based on time after excavation. The ejection velocity of the rock fragments was calculated using the relationship (He *et al.* 2010a)

$$v_e = d\sqrt{\frac{g}{2hcos^2\theta + dsin^2\theta}} \qquad (2\text{-}11)$$

Where d is the ejection distance, h the height of the ejection point, θ the ejection angle and g is the acceleration due to gravity. The parameters were shown diagrammatically in Figure 2-19. Therefore, the energy of the rockburst events could be calculated (He *et al.* 2010a).

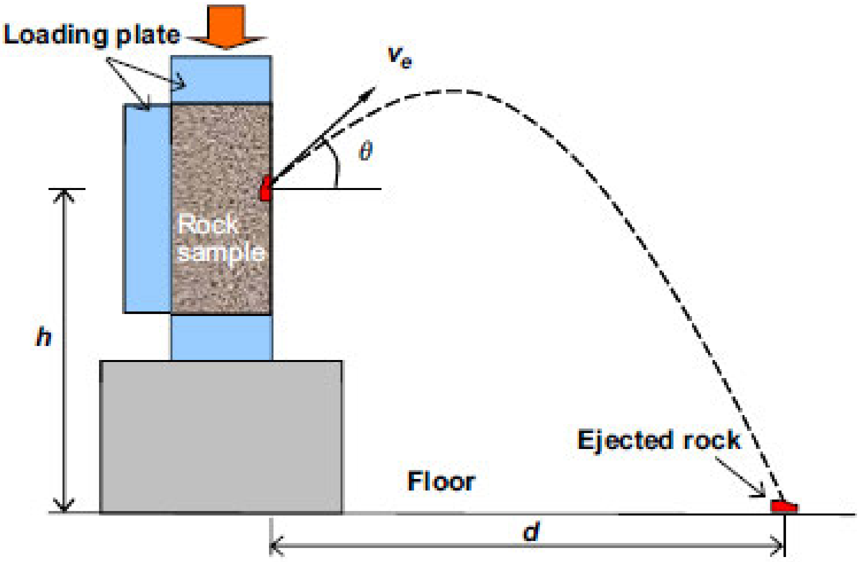

Figure 2-19: Rock ejected from surface of sample during rockburst test (He *et al.* 2010a)

Numerous other researchers have adopted the testing apparatus detailed above (Gong *et al.* 2012; He *et al.* 2012; Su *et al.* 2017; Akdag *et al.* 2018). However, the only researcher to date to apply the results to a constitutive modelling technique was Gong *et al.* (2014). The research focussed on the determination of fracture angles and faulting planes caused by rockburst processes. These were then analysed by comparing the physical model for a strainburst event and the construction of such an event using Mohr-circles. This is best described by Figure 2-20 below (Gong *et al.* 2014).

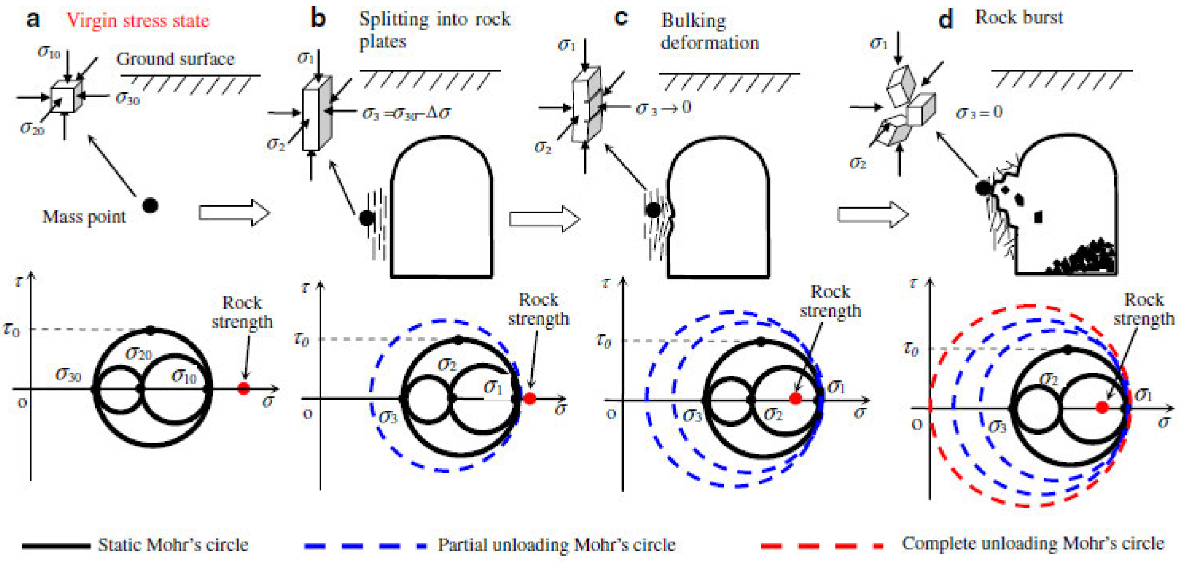

Figure 2-20: Mohr circle model for rockburst process (Gong *et al.* 2014)

Using the same experimental set-up as described above, the tests were conducted on the rock to determine the fracture behaviour of granites. An example of the time captured photography of the events is shown in Figure 2-21. After completion of the test, the loading was implemented and interpreted using Mohr-circles as shown in Figure 2-22. Using the experimental results, the research team was able to compare with numerically obtained results and field measurements and it was found to determine fracture planes of a specimen (Gong *et al.* 2014).

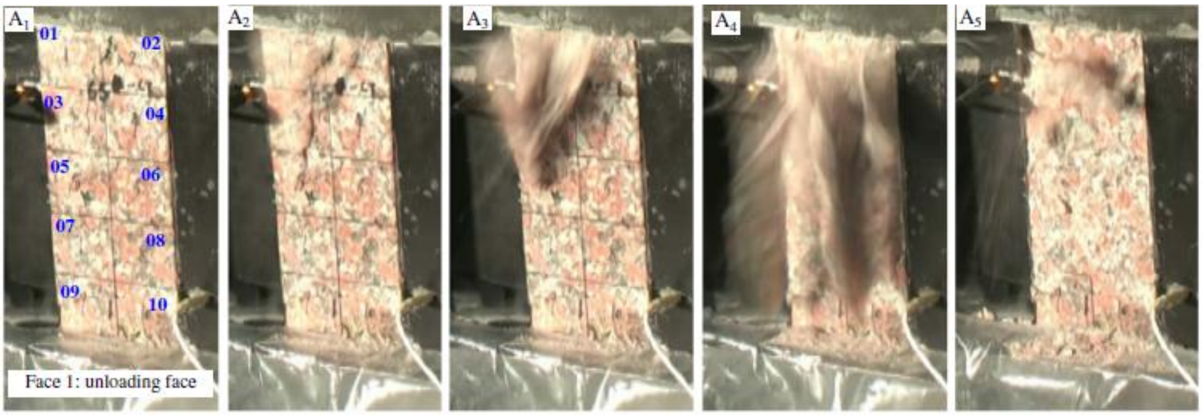

Figure 2-21: Time step photographs of rockburst in laboratory (Gong *et al.* 2014)

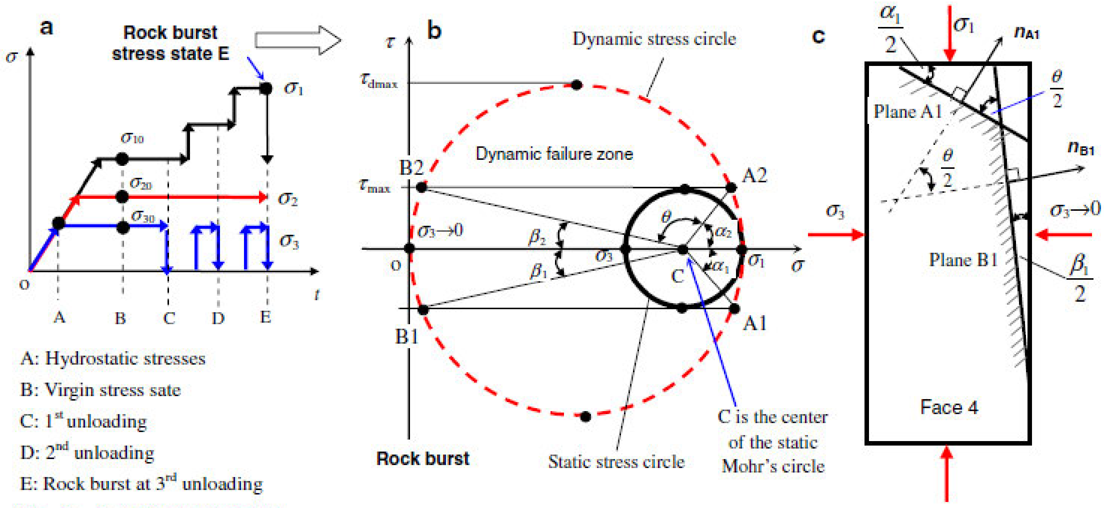

A: Hydrostatic stresses
B: Virgin stress sate
C: 1st unloading
D: 2nd unloading
E: Rock burst at 3rd unloading
(σ_{10}, σ_{20}, σ_{30}): Virgin stress state

B1 and B2: the two most possible conjugate faulting planes;
β_1 and β_2: fracture angles for the planes B1 and B2 respectively;
A1 and A2: the cut planes whose inclination angles are α_1 and α_2 respectively;
θ: the potential fracture angle range;
τ_{max}: the maximum shear stress at static stress state;
τ_{dmax}: the maximum shear stress induced by the unloading.
n_{A1}: the outward normal vector for the plane A1;
n_{B1}: the outward normal vector for the plane B1

Figure 2-22: Rockburst test interpretation a) test loading regime, b) Mohr-circle interpretation of rockburst and c) potential fracture planes on specimen (Gong *et al.* 2014)

Su *et al.* (2017) experimented with the stress loading regimes for the true triaxial rockburst test. It was shown that when tunnel axis orientation is taken into account with the in-situ stress state, the rockburst behaviour of a hard rock is changed dramatically. However, the study failed to provide any consistent link between stress state and induced damage. As can be seen in two representative tests in Figure 2-23, the rockburst events all took place near the ends of the specimen (Su *et al.* 2017). This behaviour was consistent for all of the tests conducted in the true triaxial test apparatus by all researchers (Gong *et al.* 2012; He *et al.* 2012; Gong *et al.* 2014; Su *et al.* 2017; Akdag *et al.* 2018).

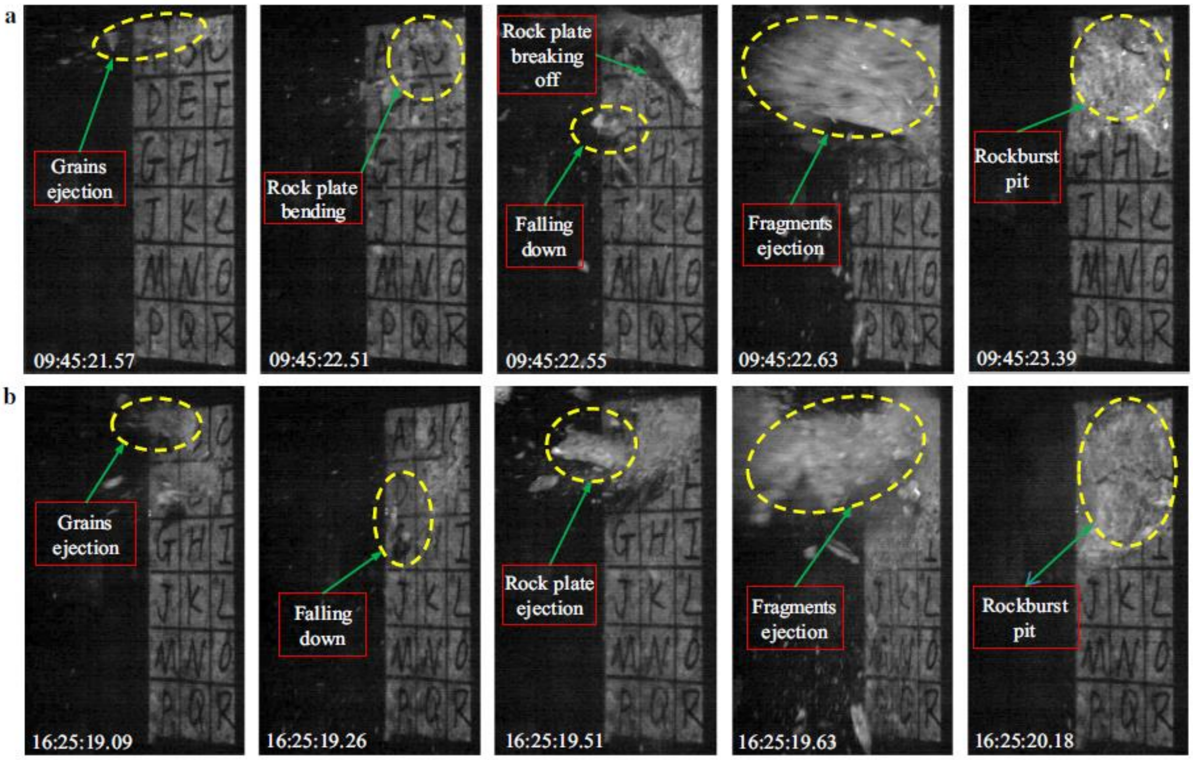

Figure 2-23: Rockburst test failure evolution (Su *et al.* 2017)

Apart from mechanical testing alone, temperature could also play a crucial role in the nature and characterisation of rockbursts. Very few researchers have studied the effects of temperature on hard, brittle rocks such as those found in deep mine conditions. The tests have to be done using recently developed triaxial compression systems for high-temperature and high-pressure testing. In a paper by Zhao *et al.* (2012), a testing apparatus was developed to allow for servo-controlled loading of high temperature specimens. The testing device enabled the testing of large size specimens up to 200mm diameter and 400mm height. Also the institution of a central borehole in the specimen could be used to test the creep behaviour of the rock or in the context of this review, the rockburst characteristics of the specimen (Zhao *et al.* 2012).

More recently Chen *et al.* (2014a) studied the temperature effect of rockburst for hard rock types under high stress. In the research, rocks were tested under uniaxial compression at temperatures of 20,40,60,90 and 130 degrees Celsius. Once the desired temperature was reached it was kept at the temperature for two hours to ensure thorough heating of the rock sample. Initial axial displacement control was used in testing followed by transverse deformation control at the yielding stages (Chen *et al.* 2014a).

From the test results it was evident that during initial heating of the granitic rock from 20-60 degrees Celsius the violent nature of rockburst increased due to the thermal stress within the rock mass. This temperature range does not change the mechanical properties of the rock just adds stress due to the expansion of grains etc. However, when the temperature exceeded this threshold range, the mechanical properties of the rock turned from brittle to ductile behaviour (Chen *et al.* 2014a).

In the most comprehensive study to date on the temperature effect on rockburst, Akdag *et al.* (2018) implemented the true triaxial testing apparatus to provide realistic stress state to heated specimens. The study found that heating granite specimens between 25 to 100 degrees Celsius would decrease the stress required to initiate a rockburst event. Also past the 100 degree point the rock began to require more stress to cause rockburst. These findings are consistent with those above, however, the addition of acoustic emission analysis revealed much about the micro-fracturing leading to failure. The main conclusion drawn from this research was that thermally induced damage greatly affected the severity of a rockburst event. In other words, the more initial damage within a rock, the less energy it is capable of storing. Hence, rockburst becomes less violent (Akdag *et al.* 2018).

Although the most relevant test for the investigation of rockburst is considered to be the true triaxial experiment proposed by He *et al.* (2010a) there are often limitations on what some laboratories are able to implement in the way of testing equipment. As the testing apparatus for true-triaxial unloading tests are very specialised and unique, some researchers have been forced to come up with different ways to impose a free surface in the testing of rocks. One study that was conducted by Liu *et al.* (2014) introduced an alternate way of testing rocks, all be it indirectly. Although the research utilised the true-triaxial machine outlined above they machined the specimen to have a central borehole, which acts as the free surface. This means that it would simulate the excavation as a whole not just a portion of exposed rock mass. The experimental layout can be seen in Figure 2-24.

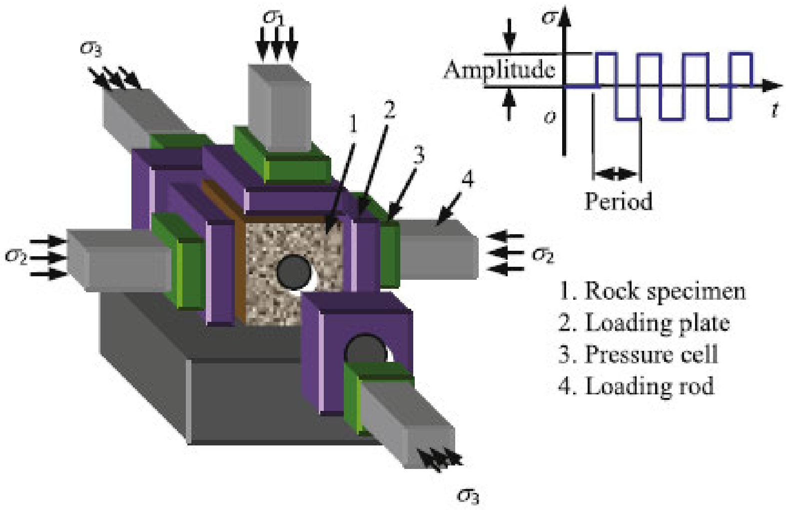

Figure 2-24: Test apparatus and cored specimen (Liu *et al.* 2014)

This provided the rockburst event to occur along the face and not be controlled by potential end effects such as those shown in the outcomes above. This study however more focussed on the dynamic loading of a specimen and its effect on rockburst. The waveforms used in the study were varied and the typical loading pattern was shown in Figure 2-25 for the case of a square wave. It was found that impact induced rockbursts typically form blockier fragments than strainburst events and that energy consumption is greater (Liu *et al.* 2014).

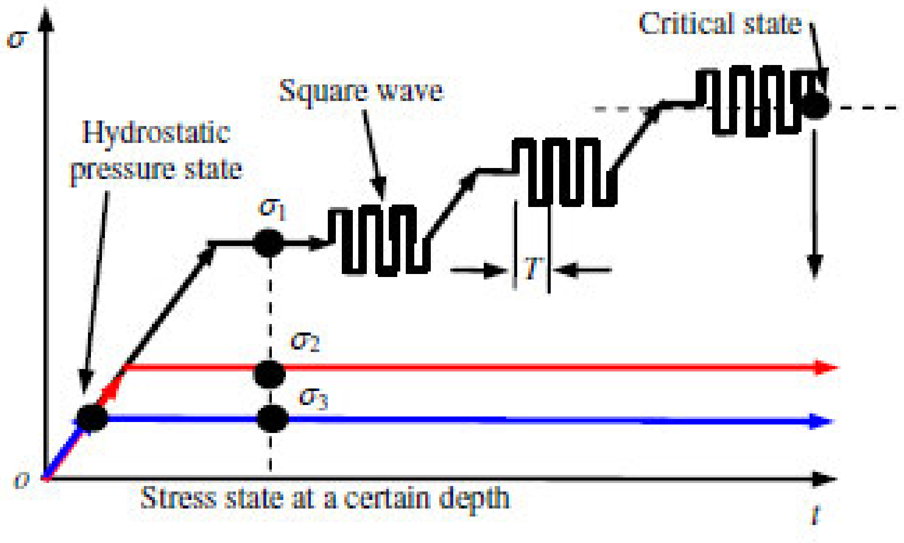

Figure 2-25: Impact rockburst test loading path (Liu *et al.* 2014)

Although dynamic loading proved to significantly influence the rockburst behaviour, perhaps the more important take away should have been the free face generation through the central borehole in the specimen. Given that this could counteract any end effects, this method of instituting an excavation face should be used in testing the rockburst phenomenon. However, as the face is always open to zero stress, the non-uniform loading during the initial phase of the test could damage the rock being used. Therefore, the energy storage ability of the rock would be compromised.

Most (if not all) works listed above rely on simple and even empirical constitutive models. These models lack strong fundamental support and correlations with experimental data on rock behaviour under a wide range of confining pressures and loading conditions. This is essential as rock is usually under different loading conditions especially during excavation, blasting and changing geological conditions. Therefore, without a detailed correlation between experimental material response and theory, it is hard to assess the validity of numerical (finite element) results. It is also clear that to date, no researchers have tried to provide a strong calibration and validation data set for the purpose of constitutive/numerical modelling as well as investigating the development of a suitable constitutive model for rockburst. Furthermore, to develop such modelling or testing techniques it has been proved from the review above that the damage accumulation in a rock mass must be understood and represented appropriately. Therefore, the next two sections of this review focus on the theory of damage mechanics and its application to constitutive modelling and experiment.

2.2 The concept of damage in rocks

Recent research in the mechanical behaviour of hard rocks has become progressively more important due to the increasing number of underground excavations under high mountains and/or increased depths where the rock mass is subjected to high stresses. As such an intimate understanding of the failure mechanisms of rock is required to allow for accurate modelling and prediction of excavation stability.

Various studies such as those conducted by Wong (1982), Fredrich and Wong (1986), Martin and Chandler (1994) and Oda *et al.* (2002), have concluded that the main failure mechanisms of hard rock are the propagation and coalescence of induced microcracks (damage) and frictional sliding of fracture planes (plasticity). Figure 2-26 illustrates the evolution of microcracks in rock. It can be seen that initially the existing cracks are closed and further loading can cause cracks to propagate and new cracks to form. In the final stages of rock failure the microcracks join to form macro-cracks and shear planes, whereupon frictional sliding becomes the dominant structural control of deformation.

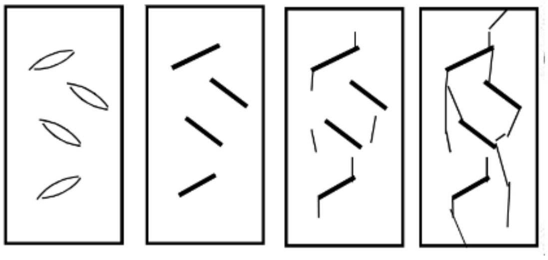

Figure 2-26: Microcrack evolution in hard rock during compression tests (increasing axial load from left to right)

Furthermore, rock behaviour can be very different under tension or low and high confining pressures. In particular, hard rock typically behaves in a brittle fashion in tension and under low confining pressure, while exhibiting much more ductile responses under high confining pressure. This is observed in experimental works as the increasing hardening behaviour of rocks as confinement increases (Chang *et al.* 2007; Arzúa and Alejano 2013; Zhao *et al.* 2013; Chen *et al.* 2015). Figure 2-27 shows a representative case for granite where hardening increases as confinement increases.

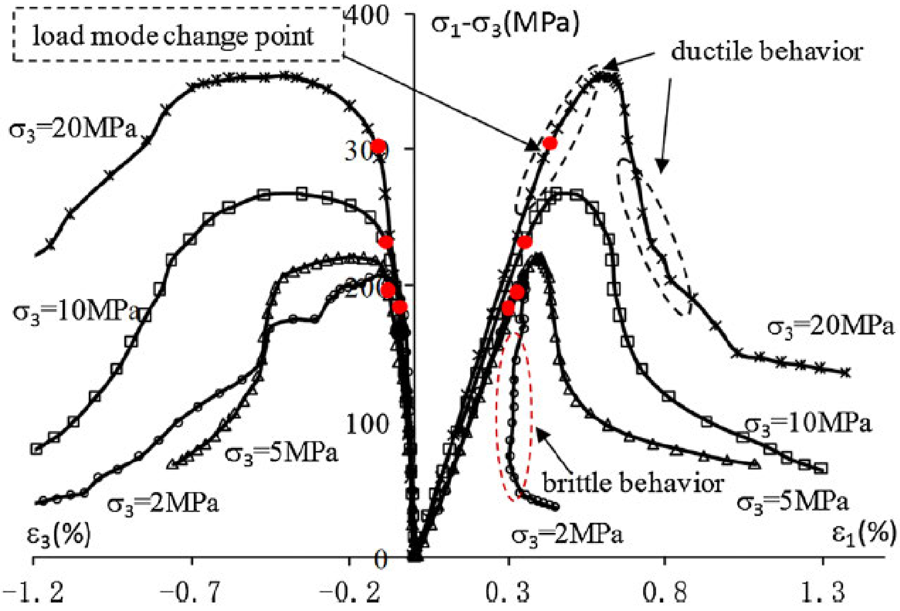

Figure 2-27: Conventional triaxial tests of Beishan granite where red dots indicate the start of hardening behaviour (Chen *et al.* 2015)

As the failure process of rock is controlled by plastic and damage processes, it is necessary to describe the mechanical behaviour of hard rocks with an appropriate constitutive model which incorporates both mechanisms. In the following sub-sections a review of existing attempts at creating a damage-plasticity model for rock will be presented. First an overview of damage mechanics and brittle material modelling will be given followed by a more in depth review of coupled damage-plasticity models for rock.

2.2.1 Damage mechanics

The concept of using continuum mechanics to describe the damage in materials was first postulated by Kachanov in 1958 and further improved by the concept of effective stress first described by Rabotnov in 1968. Since then, what is referred to now as ‘Continuum damage mechanics’, has been developed to enable the constitutive modelling of damage effected materials such as concrete and rock (Lemaitre 1992).

Continuum damage mechanics utilises the concept of a representative volume element (RVE) to describe the damage state of a material. A RVE provides a scale for the continuum mechanics framework where all material properties are represented by homogenised variables. This allows the description of damage to be averaged over a volume which is sufficiently small compared to the structure of the material and large compared to the micro processes such as cracking (Lemaitre and Desmorat 2005).

The simplest definition of damage is by the introduction of an isotropic damage variable. If we consider a RVE shown in Figure 2-28, the total cross section of the RVE, δS, is intersected by cracks or discontinuities due to damage signified by δS_D. Assuming that damage is distributed equally in all orientations, the scalar, isotropic damage variable is not effected by the normal of the RVE and takes the form of Equation 2-12.

$$D = \frac{\delta S_D}{\delta S} \tag{2-12}$$

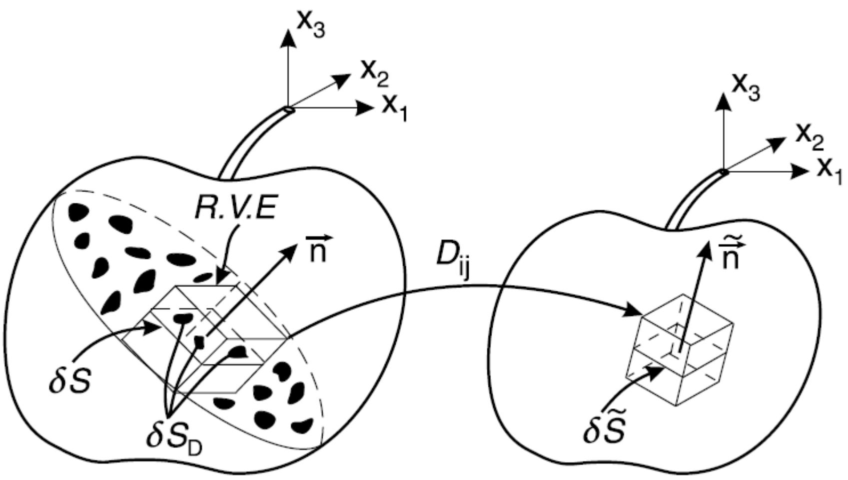

Figure 2-28: Physical and mathematical damage representation for a given RVE (Lemaitre and Desmorat 2005)

It can be observed from Equation 2-12 that values of damage can be from zero (undamaged) to one (fully damaged), therefore, this can provide a useful description of the extent of microcracking within a structure or material.

Following on from the mechanical description of damage, it is useful now to present the concept of 'effective stress.' This is defined separately to the description in the field of geotechnical engineering where the effect of porosity is ignored and substituted for the damage variable defined above. If we take the simple example of a one dimensional bar in tension, the stress is defined as the force applied, F, over the cross-sectional area, δS. However, if damage exists as open cracks, the area of the cross-section changes and is represented by $\delta S - \delta S_D$. Therefore when the effective stress, $\overline{\sigma}$, is calculated and combined with the damage variable defined in Equation 2-12, it produces the relationship (Lemaitre 1992):

$$\overline{\sigma} = \frac{\sigma}{(1-D)} \tag{2-13}$$

It can be seen in Equation 2-12 that for the case of compression, the cracks would be closed and could result in an increase in cross-sectional area, δS, from the tension case and ultimately make $\overline{\sigma}$ equal σ. It is however, assumed in this research that the damage variable is defined by the initiation, propagation and coalescence of microcracks due to compressional shear loading which is reflected as a degradation in the material stiffness (Lemaitre 1992).

To enable the use of this effective stress concept, the principle of strain equivalence is utilised to avoid the need for micromechanical analysis of discontinuity types and properties. Lemaitre (1992) describes the principle as "*Any strain constitutive equation for a damaged material may be derived in the same way as for a virgin material except that the usual stress is replaced by the effective stress".* This principle can be applied to the laws of elasticity and plasticity where it accounts for stiffness degradation of a material due to increased levels of accumulated damage (Lemaitre 1992). This is represented in this study by the linear degradation of elastic stiffness tensor with damage, $D_{ijkl} = (1 - D)C_{ijkl}$ where D_{ijkl} is the secant stiffness tensor and C_{ijkl} is the elastic stiffness tensor.

Models formed using continuum damage mechanics are normally formulated using the thermodynamic framework, however, in principle this damage theory can be applied directly to a constitutive model by incorporating the damage variable into the stress-strain and yield equations (Lee and Fenves 1998). Therefore, the direct application of damage theory will be used throughout this dissertation to provide a simple, highly flexible damage-plasticity model for hard rocks.

2.2.2 Damage-plasticity models for geomaterials

Application of damage theory for brittle geomaterials was first developed for concrete rather than rock by researchers such as Lubliner *et al.* (1989) and later by Burlion *et al.* (2000)

Jirasek *et al.* (2004), Grassl and Jirasek (2006) and Jason *et al.* (2006) among others. These models have also been applied to rocks by Chiarelli *et al.* (2003), Salari *et al.* (2004), Zhou and Zhu (2010), Chen *et al.* (2010), Unteregger *et al.* (2015), Lyakhovsky *et al.* (2015), Chen *et al.* (2015), Zhang *et al.* (2016) and Mukherjee *et al.* (2017). Due to models such as these a clear framework for the phenomenological modelling of brittle materials has been developed.

Constitutive modelling of brittle materials such as concrete first starts with a stress-strain law based on the concepts of effective stress and equivalent strain (Lubliner *et al.* 1989). As such it quite often takes the form:

$$\sigma_{ij} = (1 - D)C_{ijkl}\left(\varepsilon_{kl} - \varepsilon_{kl}^{p}\right) = D_{ijkl}\left(\varepsilon_{kl} - \varepsilon_{kl}^{p}\right) \tag{2-14}$$

where σ_{ij} is the stress tensor, ε_{kl} is the total strain tensor and ε_{kl}^{p} is the plastic strain tensor. It is useful to note that although damage has been proven to be anisotropic and better described by a tensorial variable, it is still preferred by many researchers to use an isotropic, scalar variable due to simplicity and numerical implementation (Burlion *et al.* 2000).

The simplest method to describe the evolution of the scalar damage variable is by the introduction of an empirical law. For example take the exponential and bilinear forms of damage evolution below from (Jirasek *et al.* 2004):

$$\omega = \begin{cases} 0 & if\ \kappa \le \varepsilon_0 \\ 1 - \frac{\varepsilon_0}{\kappa}\exp\left(-\frac{\kappa - \varepsilon_0}{\varepsilon_f - \varepsilon_0}\right) & if\ \varepsilon_0 \le \kappa \end{cases} \tag{2-15}$$

$$\omega = \begin{cases} 0 & if\ \kappa \le \varepsilon_0 \\ \frac{\varepsilon_1 - \sigma_1/E}{\varepsilon_1 - \varepsilon_0}\left(1 - \frac{\varepsilon_0}{\kappa}\right) & if\ \varepsilon_0 \le\ \kappa \le \varepsilon_1 \\ 1 - \frac{\sigma_1/E}{\varepsilon_2 - \varepsilon_1}\left(\frac{\varepsilon_2}{\kappa} - 1\right) & if\ \varepsilon_1 \le\ \kappa \le \varepsilon_2 \\ 1 & if\ \varepsilon_2 \le \kappa \end{cases} \tag{2-16}$$

where κ is the damage history variable, ε_f controls the slope of the damage evolution curve and E is Young's modulus (Figure 2-29a). For the stress-strain variables in the bilinear form refer to Figure 2-29b. By including a damage evolution (or softening) curve such as the types above, the model is able to be calibrated to stress-strain data to enable reproduction of tests for validation. It can be seen in Figure 2-29 that test results quite often dictate what form the damage evolution must take to ensure good calibration of stress-strain results. Damage functions such as these are used only as a hardening/softening variable for yield/failure evolution. Therefore, physical meaning is lost between the damage and stress states of a material (Jirasek *et al.* 2004).

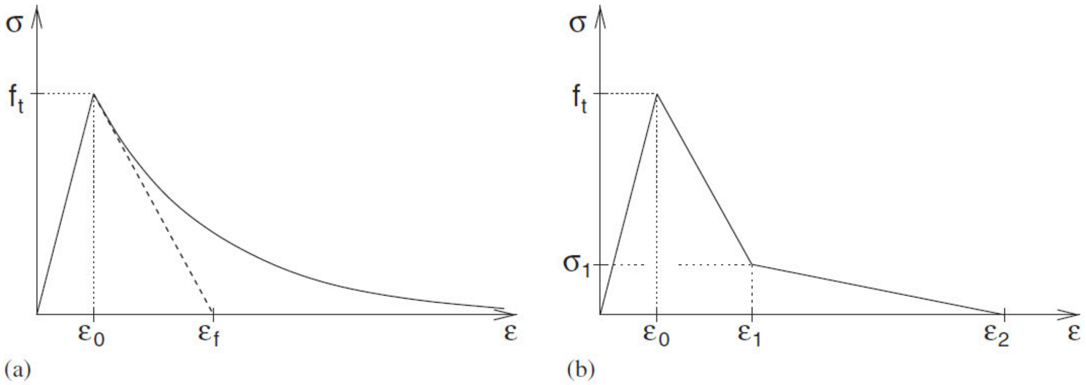

Figure 2-29: Stress-strain curve with a) exponential softening or b) bilinear softening (Jirasek *et al.* 2004)

One alternative to an empirical law is to implicitly define damage evolution by coupling yield (plastic) and damage surfaces. In this case the laws are described by the consistency conditions of the yield and damage loading functions. Often to allow better calibration and model response the loading surfaces are split into tensile and compressive damage-plasticity as shown in Equations 2-17 and 2-18 (Comi 2001; Comi and Perego 2001; Luccioni and Rougier 2005).

$$y_d^t(D_t, D_c, \sigma) = J_2 - a_t {I_1}^2 + b_t h_t I_1 - (1 - \alpha D_c) k_t {h_t}^2 = 0 \tag{2-17}$$

$$y_c^t(D_t, \sigma) = J_2 - a_c {I_1}^2 + b_c h_c I_1 - k_c {h_c}^2 = 0 \tag{2-18}$$

where a_t, b_t, k_t, α are the tension case material parameters, a_c, b_c, k_c are the compression case material parameters, D_c is the compressive damage variable and $h_t(D_t)$ and$h_c(D_c)$ are the hardening/softening functions for each surface (Comi and Perego 2001).

However, as most phenomenological yield surfaces do not account for damage of a material it is often necessary to define separate damage surfaces usually formulated from the damage conjugate force. Once each state has been evaluated they are then coupled to describe the overall material response (Chiarelli *et al.* 2003; Salari *et al.* 2004). Due to the use of separate damage and plasticity criteria, hardening and softening rules are still needed for these models to describe the behaviour of the material. In addition, as there are two separate criteria for damage and plasticity, in principle coupled behaviour with damage and plasticity both activated does not always happen (Nguyen and Houlsby 2008).

To avoid the necessity of multiple loading surfaces, the model in Grassl and Jirasek (2006) and later adapted for rocks by Unteregger *et al.* (2015) utilised a damage variable and damage induced softening behaviour driven by plastic strain. Focussing on the model by Unteregger *et al.* (2015) the yield and hardening of the material was evaluated in terms of a plastic yield function and damage was incorporated in the softening regime of the model. This separation of plasticity (pre-peak) and damage (post-peak) provided good fit for test results, however, were only calibrated using stress-strain data and a generic damage evolution law (similar to Equation 2-15). Additionally, the model required many equations to provide enough flexibility to replicate experiment. Therefore, it can be concluded that the model would only work for the specifically calibrated test results. Although both of these models were very successful in capturing the behaviour of rock and similar geological materials under a wide range of confining pressure, complex hardening functions still had to be used to allow accurate replication of material behaviour. This complexity can make the formulation difficult to implement.

A simplified attempt at this combined style of modelling has been conducted by Chen *et al.* (2015) where the yield function evolution was controlled by a damage criterion calibrated to experimental unloading curves to provide some level of physicality. This eliminated the need of a coupling strategy between two loading surfaces. Equation 2-19 shows that with this formulation the material is hardened with increasing generalised plastic strain, γ_p and softened with increasing damage, ω.

$$f_p = q - g(\theta)\eta\left(\gamma_p\right)P_a\left(C_s + \frac{p}{P_a}\right)^m = 0 \tag{2-19}$$

where p, q and $g(\theta)$ are the mean stress, deviatoric stress and function controlling the dependency of the yield surface (f_p) on lode angle, θ respectively. The material parameters P_a, C_s and m control the shape of the yield surface in the deviatoric plane and the coefficient, $\eta(\gamma_p)$, controls the hardening/softening of the material given by (Chen *et al.* 2015):

$$\eta(\gamma_p) = (1 - \omega)\left[\eta_0 + (\eta_m - \eta_0)\frac{\gamma_p}{b_1 + \gamma_p}\right] \tag{2-20}$$

where b_1 controls plastic hardening and η_0 and η_m are the initial and final locations of the plastic yield surface respectively. Although this provides more of an experimentally observed link between damage and stress state, the model still required complex formulation for the calibration of the damage variable (Chen *et al.* 2015).

A more recent model by Mir *et al.* (2016) and expanded by Mukherjee *et al.* (2017) introduced a new form of yield function where a scalar damage parameter is incorporated into the formulation allowing for direct evolution of the failure of the material. This model did not require any complex damage surfaces or hardening laws. However, there were no experimentally validated links between damage and yield-failure surface. Therefore, the calibration of the damage evolution law was entirely reliant on the macroscopic stress-strain response of triaxial tests and no relationship exists between the damage parameter and the stress state during calibration and modelling.

Therefore, an important finding when reviewing available damage-plasticity models for geomaterials is the reliance on stress-strain test results for calibration. This is evident in the fact that most, if not all models, were theoretically developed entirely independent from a well thought out experimental plan. Therefore, it is often only possible to calibrate constitutive models using macro material responses published in literature. As a consequence, the calibration is usually an issue as literature sourced experimental data usually just provides stress-strain curves and limited details on the yield-failure and damage processes of a material.

There is also a lack of experimentally obtained, damage evolution being used in modelling which forces arbitrary damage evolution laws to be postulated. Therefore, intermediate yield and damage levels throughout a material’s loading path are arbitrary and meaningless. This causes inaccuracy when using these models to simulate changing stress or deformation conditions such as the case with rockburst.

From these critiques it is clear that the development of a constitutive model for rockburst should be conducted in parallel to systematic experimental study to provide the data necessary for more robust calibration. This in turn should provide a good balance between experimental and theoretical development, which appears missing in most works to date. To properly investigate the applicability of current testing methodologies for this purpose, the next section discusses the availability and usefulness of rock compressive test data with particular focus on the control methodologies and damage evolution of the failure process.

2.3 Compressive testing and damage quantification of rocks

To enable the numerical modelling of rock failure in civil and mining engineering, small laboratory scale experiments must be conducted to provide data to calibrate the constitutive relationships. In the early days of rock mechanics this was as easy as conducting conventional uniaxial and triaxial compressive tests to determine the failure envelope of a material (Hoek *et al.* 2002). However, with the increasing need for the simulation of complex failure mechanisms encountered with modern day excavation, both models and rock testing have to evolve to allow more information to be taken into account. This section looks at the compressive testing of rock to obtain the full stress-strain and damage behaviours of the material. First the stress-strain testing of rock will be examined in terms of confinement and loading methodology, then the quantification of damage due to cracks will be addressed.

2.3.1 The full load-displacement response of rock

The compressive testing of rock for use in constitutive modelling is detailed in the International Society for Rock Mechanics and Rock Engineering (ISRM) suggested methods for testing (ISRM 2007). These guidelines contain a collection of papers explaining the consistent procedure for determining the strength of rock which should be followed in the laboratory. Upon review there are three main control methods for the axial or multiaxial compression testing for rock; axial load or displacement/strain control and lateral (circumferential) displacement/strain control (ISRM 2007).

The earliest compressive experiments had to utilise industrial hydraulic presses for applying load to a specimen. As these machines were only able to be controlled via load or machine displacement, therefore tests were run at a constant loading or axial strain rate, usually in the range of 0.5-1 MPa/s or 10^{-2}-10^{-5} strain/s (ISRM 2007). This is often sufficient to capture the full stress-strain response of soft rocks; however, it has been pointed out by Fairhurst and Hudson (1999) to be insufficient for hard or brittle rock, as it is usually impossible to obtain the full stress-strain response of a specimen under varying confinement due to self-sustaining failure.

It was first demonstrated by Wawersik (1968), that brittle rock tends to exhibit ‘snap-back’ behaviour during compressional loading at low confinements. This led to the classification of post-peak behaviour of rocks into Class I and Class II (refer to Figure 2-30). Class I behaviour is when a rock is soft and to induce further strength reduction, increased deformation must be applied to the specimen. Class II on the other hand is very brittle behaviour where the strength reduction is self-sustaining due to the built up elastic strain energy in a specimen. Class II behaviour is seen commonly in brittle rocks (Wawersik 1968; Labuz and Biolzi 1991).

As can be seen in Figure 2-30, the surplus stored elastic strain energy in a Class II rock allows for self-sustaining failure. Therefore, it stands to reason that if energy is constantly applied during a test, the failure of a rock cannot be controlled past the very early stages of failure. This could correspond to incorrect stress-strain data and hence inaccurate calibration of material models.

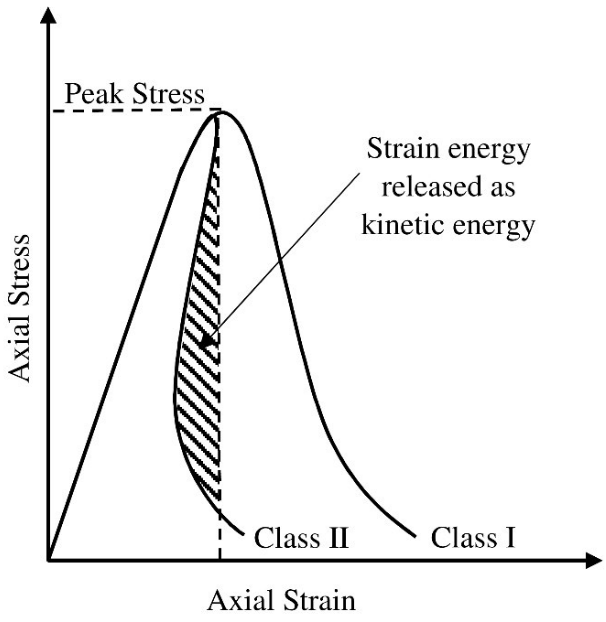

Figure 2-30: The energy difference between Class I and II rocks

Initial attempts to obtain the full stress-strain behaviour of a rock during compression concentrated on the stiffness of the loading system (Wawersik 1968; Hudson *et al.* 1970; Wawersik and Fairhurst 1970; Wawersik and Brace 1971; Hudson *et al.* 1972) however, more recently it is thought that by controlling the application of load through a feedback loop of circumferential strain, the correct behaviour of each test can be obtained (Fairhurst and Hudson 1999). Therefore, it stands to reason that if the failure of a rock can be tested and captured correctly using circumferential strain, the damage measurements can also be reliably obtained.

2.3.2 The measurement of damage in rocks

As stated at the beginning of the chapter, numerous studies have concluded that the predominant failure mechanisms for rock are the initiation, propagation and coalescence of micro and macro cracks formed by the redistribution of stresses during or after an excavation (Wong 1982; Fredrich and Wong 1986; Martin and Chandler 1994; Oda *et al.* 2002).

Therefore, when creating any constitutive model for rocks, appropriate damage evolution should be calibrated against experimentally obtained data.

Initial attempts to understand the damage process in rocks, was the identification of stress related damage thresholds. This method, shown in Figure 2-31, characterises the evolution of cracking or damage into several thresholds, typically, crack closure (σ_{cc}), crack initiation (σ_{ci}) and crack damage (σ_{cd}). The crack closure threshold, σ_{cc}, refers to the point in the test where all pre-existing microcracks in the material have been closed due to compression of the specimen. This threshold is identified when the stress-strain curve becomes linear or when the inelastic volumetric strain plateaus indicating no further, permanent compaction. After crack closure, a material will behave elastically until the onset of dilation caused by the initiation of microcracks. The crack initiation threshold, σ_{ci}, is therefore calculated as the onset of inelastic deformation (dilation) after the linear elastic loading phase. The cracking which initiates at this stage of loading is considered to be stable as it requires an increase in load to induce further dilation and cracking in the specimen. Finally, the point at which a reversal of total volumetric strain occurs is referred to as the crack damage threshold, σ_{cd}. This assumes that the switch from compaction to dilation behaviour is the result of microcracks in the specimen starting to open and coalesce and damage evolution becomes unstable (Bieniawski 1967a; Bieniawski 1967b; Wawersik and Fairhurst 1970; Martin 1993; Martin and Chandler 1994; Eberhardt *et al.* 1998; Eberhardt *et al.* 1999).

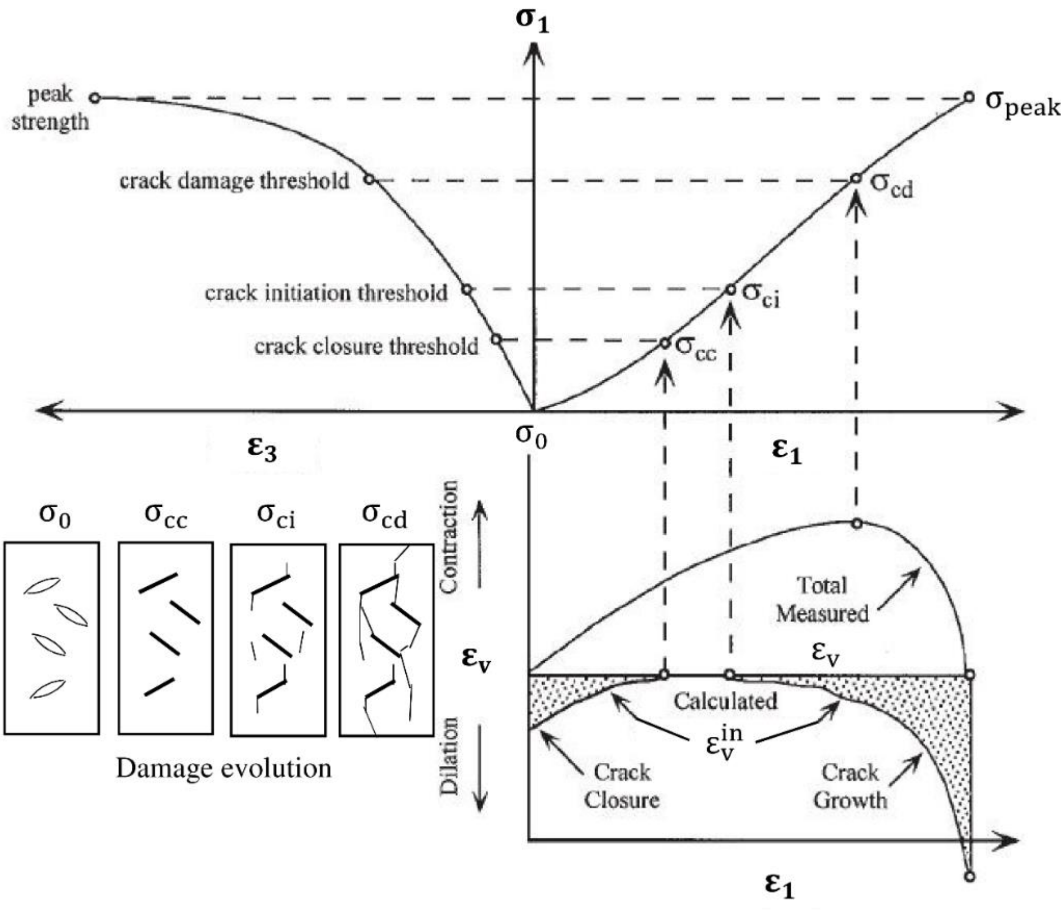

Figure 2-31: Stages of crack development in rock during uniaxial compressive test (modified from Eberhardt *et al.* (1998))

The calculation of these thresholds, first proposed by Martin (1993), were then expanded by Eberhardt *et al.* (1998) to include the change in axial stiffness as another measure of the crack closure and initiation thresholds. It can be seen from Figure 2-32 that as the average axial stiffness plateaus, signifying the beginning of linear elasticity, crack closure is assumed to be complete. Following this, the departure of the average axial stiffness from this plateau indicates the onset of microcrack growth and hence crack initiation.

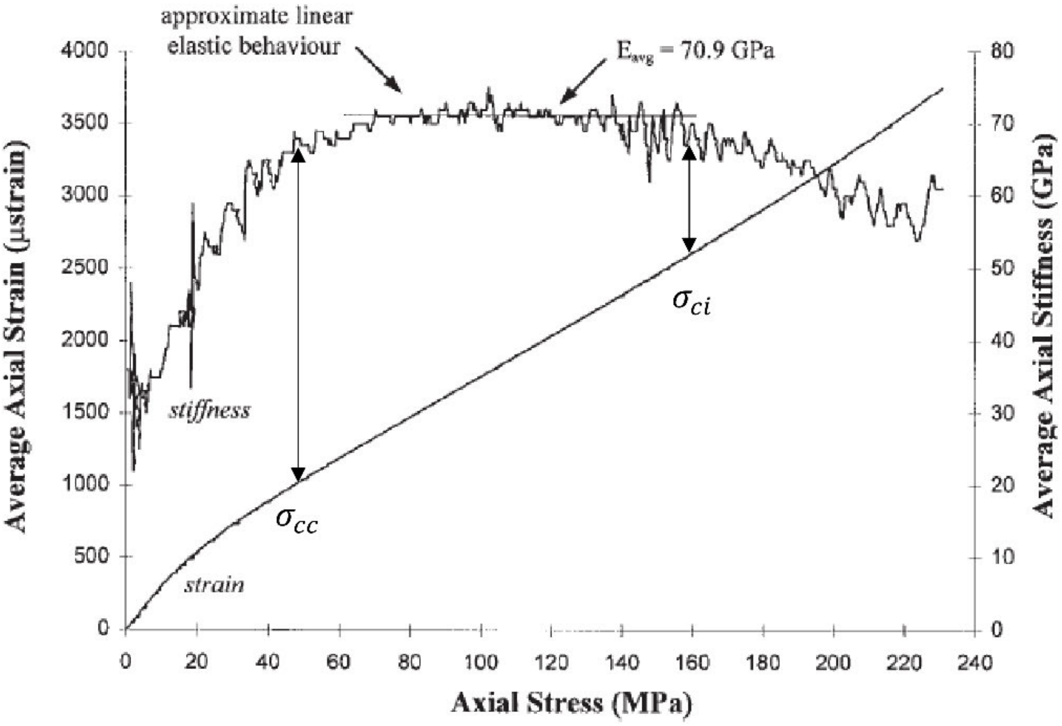

Figure 2-32: Example of crack closure and initiation thresholds derived from average axial stiffness (Eberhardt *et al.* 1998)

Further developments in the field lead to the formation of objective methods to determine the damage thresholds of a rock. Focussing on the lateral strain measure, Nicksiar and Martin (2012) developed the Lateral Strain Response (LSR) method shown in Figure 2-33. This method uses the point of maximum volumetric strain as a reference and determines the point of maximum lateral strain difference which signifies the start of crack initiation (Nicksiar and Martin 2012). Another similar objective method was proposed by Zhao *et al.* (2015) which used a cumulative AE hit method to predicted the crack initiation threshold.

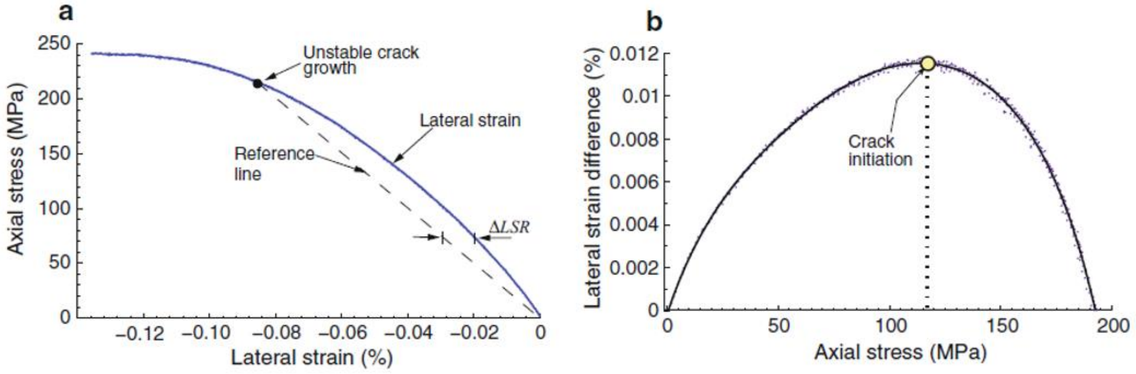

Figure 2-33: Lateral strain response method proposed by Nicksiar and Martin (2012)

The strain and stiffness methods have been widely used and as such, extensive data has been accumulated for many rock types. Table 2-2 is a compilation of a variety of hard rock studies and subsequent values for damage thresholds where the confinement level of each study is shown as σ_3. It is clear from Table 2-2, that although there has been numerous tests conducted on hard rocks that show the thresholds as being consistent, they all share the same loading methodology or similar. Studies that do include the effects of circumferential control are few and only uniaxial in nature (Nicksiar and Martin 2012; Zhao *et al.* 2015). There are no current studies that report the calculation of damage thresholds specifically for circumferentially controlled, triaxial tests and overall, there is limited information on the effects of confinement on damage threshold values for hard igneous rock (see Figure 2-34).

Table 2-2: Experimental damage threshold values

Rock	σ_3 (MPa)	$\frac{\sigma_{cc}}{\sigma_p}$	$\frac{\sigma_{ci}}{\sigma_p}$	$\frac{\sigma_{cd}}{\sigma_p}$	Test Control	Reference
Diorite	0	-	0.51	0.90	Axial Load	Hidalgo and Nordlund (2013)
Diorite	0	-	0.49	-	Circumferential	Nicksiar and Martin (2012)
Dolomite	0-25	-	0.71	0.90	Axial Disp.	Hatzor and Palchik (1997)
Gabbro	0	-	0.58	0.80	Axial Load	Hidalgo and Nordlund (2013)
Granite	0	0.23	0.39	0.76	Axial Disp.	Eberhardt *et al.* (1998)
Granite	0-60	-	0.48	0.61	Axial Disp.	Hoek and Martin (2014)
Granite	0	-	0.48	0.60	Axial Disp.	Ghazvinian *et al.* (2015)
Granite	0-20	0.10	0.40	0.84	Axial Disp.	Chang and Lee (2004)
Granite	0	-	0.39	0.75	Axial Disp.	Eberhardt *et al.* (1999)
Granite	41	-	0.40	0.84	Axial Disp.	Katz and Reches (2004)
Granite	0	-	0.36	0.80	Axial Disp.	Martin (1993)
Granite	4.9	-	0.40	0.71	Axial Disp.	Heo *et al.* (2001)
Granite	0	0.39	0.51	0.71	Axial Disp.	Kim *et al.* (2015)
Granite	0	-	0.52	0.81	Axial Load	Hidalgo and Nordlund (2013)
Granite	0	-	0.43	0.76	Axial Load	Hidalgo and Nordlund (2013)
Granite	0-40	-	0.48	0.80	Unknown	Zhao *et al.* (2013)
Mixed	0	-	0.48	-	Circumferential	Zhao *et al.* (2015)

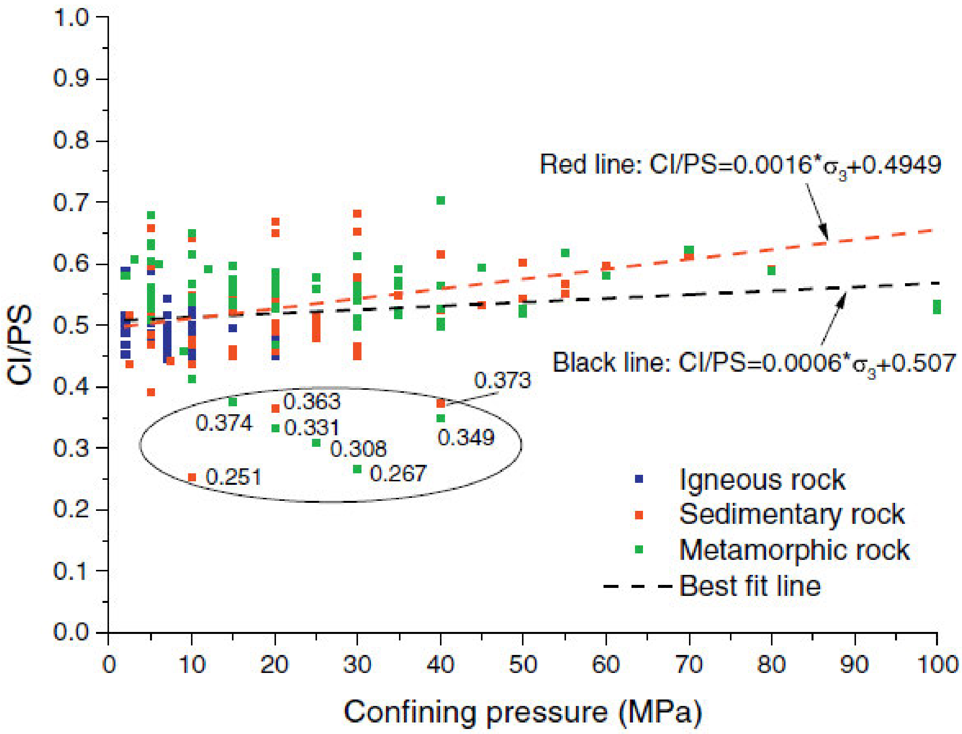

Figure 2-34: Compilation of calculated crack initiation thresholds for rock (where CI/PS is the ratio of crack initiation and peak stresses) (Wen *et al.* 2018)

Therefore, if the full failure process of a brittle rock cannot be captured by a constant axial loading methodology, then the damage thresholds could also prove to be reliant on the loading method. This could correspond to under-estimation of the crack initiation and damage thresholds, making it difficult to determine the onset of damage-plasticity behaviour for brittle rock. In the context of constitutive modelling the correct prediction of damage thresholds supplies the model with an accurate prediction of initial yield due to damage processes, σ_{ci} and the point where damage switches from hardening to softening the material, σ_{cd}. After these two points, the post-peak portion of the stress-strain curve usually starts evolving. To capture the post-peak damage accumulation in the sample, several methods have been proposed.

The first method used to provide some measure of damage during tests was the unloading-reloading of compressive tests at different stages during failure. Figure 2-35 shows the stress-strain response from a triaxial compression test.

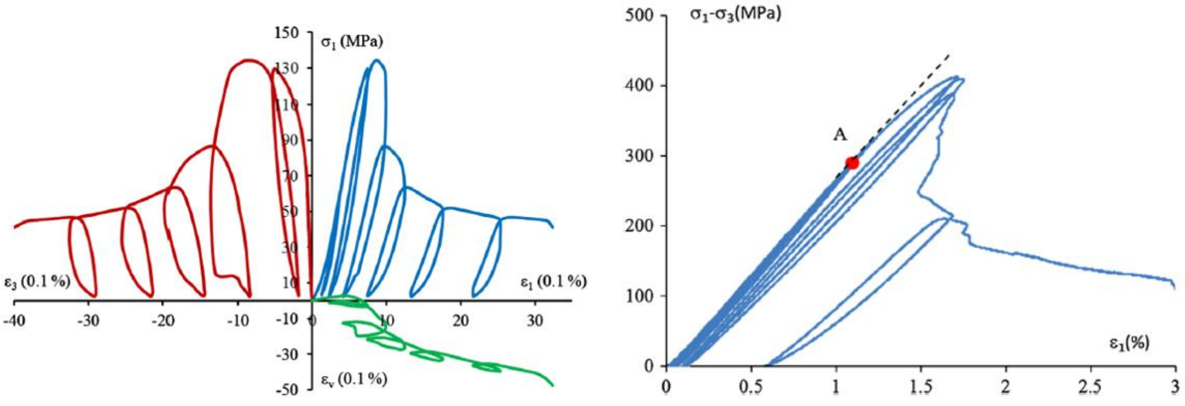

Figure 2-35: Triaxial unloading-loading tests for granite under different confinement (left) 4MPa (Arzúa and Alejano 2013) (right) 30MPa (Chen *et al.* 2015)

It can be seen that using the unloading-reloading curves from these types of test, the stiffness is commonly only degraded by 10-20% (Arzúa and Alejano 2013; Chen *et al.* 2015). Considering the localised failure of a specimen it stands to reason that the stiffness degrades by this small percentage until the correctly orientated cracks coalesce and cause shear failure. However, when attempting to model the material behaviour using a damage-plasticity model with a scalar damage variable it is necessary to obtain the damage relative to the overall failure of the rock.

Aside from the direct imaging of microcracks using X-Ray or CT tomography (Tapponnier and Brace 1976; Wong 1982; Fonseka *et al.* 1985), the most appropriate method for damage assessment is the use of elastic waves emitted during micro-crack generation and propagation. The acoustic emission (AE) phenomenon is created by local deformation at the micro scale. At this scale, rock experiences small fracturing events which correspond to the instantaneous release of elastic strain energy in the form of elastic waves. The monitoring of these waves throughout a rock test can give a direct measure of the damage state of the material relative to its original structure (Cox and Meredith 1993; Lockner 1993; Zhang *et al.* 2015b; Zong *et al.* 2016). This method has also been used for rockburst risk assessment (Tang *et al.* 2010; Ma *et al.* 2015) and roof fall prediction (Butt *et al.* 2000). To quantify the damage from acoustic emissions the following relationship can be implemented:

$$D = \frac{\Omega}{\Omega_{total}} \tag{2-21}$$

where Ω is the accumulated acoustic emission energy at a certain time of the test, Ω_{total} is the total acoustic energy over the whole duration and D is the damage variable. It is also important to note that, $0 \leq \Omega \leq \Omega_{total}$ and $0 \leq D \leq 1$, where 0 represents the initial undamaged state of the material and 1 is the point of final frictional failure. The definition of damage using AE energy has been discussed in the literature by previous researchers (Grosse and Ohtsu 2008; Ji *et al.* 2014; Kim *et al.* 2015; Akdag *et al.* 2018) and therefore, can facilitate the formation of a robust law to quantify the relative damage levels of an experiment. Although experimental damage evolution has been used in calibration (Chen *et al.* 2015), usually it is not coupled to stress states or the overall yield of the material. Also there exists no systematic approach to combine the full stress-strain curve with the damage evolution.

2.4 Research motivation

This chapter has provided a comprehensive review on the rockburst phenomenon and the concept of damage in rocks. It is clear from this review that several gaps in current knowledge exist. To address the rockburst problem, it is evident from numerous studies that the controlling mechanism for the strainburst type is the storage of elastic strain energy in the material prior to failure. This directly controls the propensity and severity of a strainburst event. Given that this is the dominant factor, few studies have attempted to address the short comings with all areas of rock mechanics regarding damage processes.

The overall goal of this research is to provide a firm experimental and theoretical platform to enable the future numerical modelling of rockburst in a mine. For complicated phenomenon such as rockburst, it is essential to study the intrinsic rock properties as well as the specific properties relating to the mechanism of failure. In this sense, a constitutive model must be provided with calibration data consisting of material properties formed from conventional stress-strain and damage behaviour along with validation data which is indicative of the bursting event. It is clear from current research, that there exists no systematic approach for obtaining calibration and validation data sets to base the formulation of a constitutive model for rockburst. However, it is important to provide both of these sets to ensure larger scale analysis is valid. Furthermore, existing literature does not derive consistent calibration processes for damage-plasticity models. Instead they rely on the formation of generic, theoretical laws which tend to lose physicality once applied to more complex geometries. Therefore, the main objective is broken down into three areas of focus.

The first motivation for this dissertation is to conduct comprehensive conventional testing on hard granitic rock, with particular focus on obtaining the full load-displacement (and hence stress-strain) and damage evolution behaviours of the material. As pointed out in this review chapter, hard, brittle rocks commonly display snap-back or self-sustaining failure, where the stored energy in the rock is enough to continue failure without added external work. The capturing of this behaviour is vital to properly describe the damage accumulation in a specimen for the purpose of modelling rockburst. Therefore, this research will adopt the full circumferential strain control method for testing. Using this testing method along with the acoustic emission measure of microcracking, it will be shown that more coherent and relatable data can be produced and used for calibration of constitutive models.

Furthermore, as was evident in the synopsis of current plastic-damage models, it is necessary to define a new unified yield-failure surface which can allow the enhanced calibration necessary for numerical modelling of rockburst behaviour. The unified criterion developed in this study will eliminate the need for multiple surfaces and complex hardening and softening laws often found in such models. Therefore, more focus will be levelled on the calibration of yield and damage evolution. In this thesis, a new approach for calibration of a plastic-damage model will be proposed. It will highlight the ability to calibrate the yield surface so that damage and stress are explicitly linked allowing changing loading paths to be correctly represented with one evolution function. This also allows the use of a purely experimental damage evolution law which includes the effects of confinement. Therefore, by intimately connecting coupled experimental results to the calibration of theoretical relationships, the model can be relied upon to maintain physically more so than traditionally calibrated models.

Finally, current research shows few attempts to numerically model the rockburst phenomenon. This is due to the fact that existing models are not supplied with a validation data set which includes the effects of rockburst mechanisms. To supply this validation set, it is necessary to conduct small scale laboratory tests to replicate the conditions leading to the mechanism of rockburst. Given the material response it is then possible to compare numerical analysis to these tests to ensure the model can capture the desired behaviour. Therefore, the final component to this research is to develop an innovative, new testing apparatus for small scale rockburst testing. The design of the test platens will allow the use of a conventional Hoek triaxial cell and hydraulic press for multi-axial stress testing of hard rock. The borehole type free face will also allow rockburst to occur without the end effects that plague the existing true-triaxial rockburst testing apparatus. This coupled with the inventive internal pressure system, will enable the rock to be loaded hydrostatically and for excavation to be performed mid-test. The data obtained from these tests can then be used to show the relationship between depth (and hence in-situ pressure) and the rockburst propensity to identify at risk areas. This coupled with the full material response during testing should provide a numerical model with a comprehensive data set for validation. As such, the future focus of this research is to apply this strategy to the finite element platform and produce a model capable of predicting burst prone regions of a mine.

Chapter 3 – EXPERIMENTAL INVESTIGATION OF DAMAGE EVOLUTION IN HARD ROCKS

The calibration of constitutive models is reliant on the experimentally derived data obtained in small scale laboratory testing. As such, it is important to ensure that the response of a material, such as the granite dealt with in this study, is obtained systematically and fully. Therefore, this section presents an experimental methodology for the conventional compression testing of hard rock, focussed around the acquisition of full material response and damage evolution. Using circumferential control in a Hoek triaxial cell, the full stress-strain response of the specimens was recorded showing the ‘snap back’ behaviour at low confinements.

Furthermore, this section investigates the damage thresholds and overall evolution of fully circumferentially controlled (FCC) triaxial compression tests of granite. As such, multiple confinements were tested to uncover any relationships it may have to damage evolution. Although it is widely accepted that the damage thresholds of a rock are material parameters, this study aimed to provide evidence that there is some pre-peak reliance on the control method used to conduct a test. Hence, it was attempted to provide a basis for understanding the damage evolution in close comparison to full compressive stress-strain responses. This should enable more accurate analysis using damage-plasticity models such as the one proposed in Chapter 4 of this dissertation. This, in turn, would lead to reliable numerical modelling of rock behaviour under high confining pressures.

3.1 Experimental Procedure

3.1.1 Sample preparation and loading method

The rock used in this experimental investigation was a granite sourced from a borehole located in South Australia at a depth of 1020-1035m. It is generally observed as coarse grained, massive granite with weak to moderate alteration, occasionally with weak gneissic foliation. This is a brittle rock with grain size ranging from 0.5 mm to 3 mm and a density of 2730 kg/m^3. The mineral composition of the granite almost exclusively consists of potassium feldspar, quartz and chlorite. The alteration materials found in the samples are predominantly red earthy hematite and minor chlorite and occasionally displays veins and stringers of dark-grey hematite, red earthy hematite, chlorite, quartz and carbonate. Figure 3-1 displays the typical appearance of the rock used in tests.

Figure 3-1: South Australian granite

Samples were prepared in accordance with the ISRM suggested method for triaxial compression tests (ISRM 2007). As uniaxial compressive strength (UCS) test results of the rock type showed an average strength of $\sigma_{UCS} = 158$ MPa, the 63 mm diameter drill core was sub-cored to 42 mm diameter and cut to 100 mm in length to allow for higher confining pressures during triaxial testing. The ends were ground and polished to allow for uniform contact with the test platens.

The loading method used in this study was based on the technique outlined in the ISRM method for obtaining the complete stress-strain curve in a compressive test (Fairhurst and Hudson 1999). As stated in the standard, the specimen was loaded axially such that the growth of circumferential strain ($\Delta\varepsilon_3$) was constant at $1\text{x}10^{-5}$ mm/mm/sec. To begin each test the rock specimen was loaded into the triaxial cell and confining pressure was applied by the cell and loading frame up to the desired isotropic loading condition. Then as lateral pressure remained constant, axial loading was applied using the circumferential control method. This method differed from the standard in that there was no initial axial displacement or load control of the specimen.

To ensure there were no strength losses due to the proposed loading, UCS tests were conducted using this slightly adjusted method and the exact method outlined in the ISRM standard (Table 3-1). It was found that both methods returned approximately the same average and range of peak stresses. Therefore, the method was deemed suitable for application to triaxial testing in this study. The overall goal of this adjusted method was to investigate the effect that circumferential strain control has on a test during the pre-peak response. FCC also largely avoided the situation of complete brittle failure of the material observed in axial control tests due to the constant application of pressure in the initial stages of loading which causes faster damage accumulation. Thus, FCC in turn allowed the capturing of full Class II stress-strain behaviour. The FCC loading scenario was able to provide the maximum level of control of the failure process of hard rock and to enable accurate and precise measurement of the characteristic damage evolution of the material without the effect of the loading rate. The FCC method has also been adopted in industry but at much faster lateral strain rates which are normally calibrated to reflect an equivalent axial load control (Eloranta 2004; Jacobsson 2004b; Jacobsson 2004a).

Table 3-1: UCS results for conventional (ISRM) and full circumferential strain control (FCC) loading methods

Sample ID	Loading Method	UCS (MPa)	Average UCS (MPa)
UCS-1	ISRM	188	159
UCS-2	ISRM	171	
UCS-3	ISRM	127	
UCS-4	FCC	168	156
UCS-5	FCC	124	
UCS-6	FCC	175	

In this study compressive stresses and strains are defined as positive. The principal stresses are in the axial (σ_1) and lateral ($\sigma_2 = \sigma_3$) directions in triaxial space. As explained above the axial (ε_1) and lateral ($\varepsilon_2 = \varepsilon_3$) strains are directly measured from the tests and used to define volumetric and shear strains given by, $\varepsilon_v = \varepsilon_1 + 2\varepsilon_3$ and $\varepsilon_s = \frac{2(\varepsilon_1 - \varepsilon_3)}{3}$ respectively (Puzrin 2012).

3.1.2 Triaxial compression tests

The testing frame used to carry out triaxial compression tests was an INSTRON 1282 with an axial load capacity of 1000 kN. Specimen confinement was achieved using a Hoek cell with capacity up to 65 MPa. Linear variable differential transformers (LVDTs) were used to measure the axial strain and all data acquisition was done using a National Instruments cDAQ module. To measure the circumferential strain for each test, a Hoek cell membrane was fitted with four strain gauges internally within the cell. This was achieved by fitting a high pressure wire feed through connector to the cell. Each gauge was attached immediately alongside one another around the centre of the liner and connected to a Wheatstone bridge to provide the input for the control circuit. This then averaged the signal received by each gauge and thus provided accurate measurements of the circumferential strain of each specimen. This signal was then input into the Instron Labtronic 8800 control unit which controlled the test based on circumferential strain rate. The wiring and setup for this method is shown in Figure 3-2.

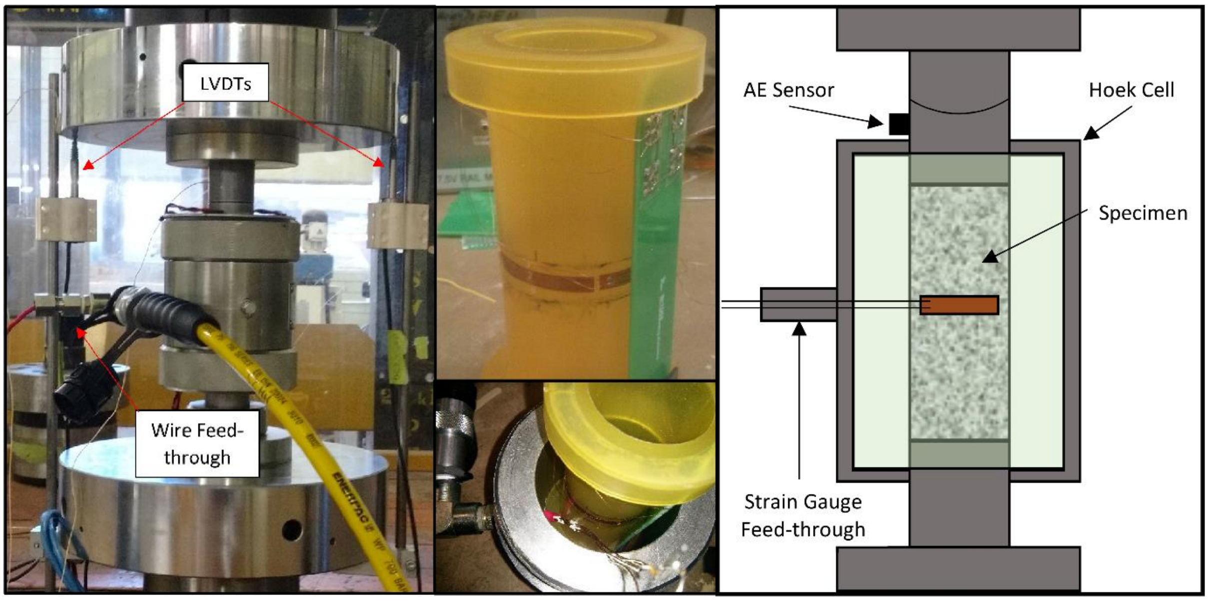

Figure 3-2: Strain gauged membrane and test set-up

To ensure this method was accurate, strain gauges were also attached directly to the specimen for low confinement tests (10 and 20 MPa) and the strain response were compared. Figure 3-3 shows the comparison between the two lateral strain measurement methods for tests where the specimen gauges remained intact until post-peak loading. It is clear that no significant resolution or behaviour was lost using the gauged membrane method. The small offset in lateral strain magnitudes was a consequence of averaging four strain gauges around the entire outside diameter of the membrane as opposed to the averaging of two attached to the specimen. Additionally, strain gauges attached to the specimen were commonly broken at early stages in the test (elastic material loading). This can occur even at low confining pressures and resulted in the loss of the ability to average gauges around the specimen and therefore, lateral strain output would become location dependent. It can also be seen that when larger radial strains were reached during post-peak loading, gauges attached directly to the specimen were lost due to excessive pressure and deformation. Therefore, as the membrane gauges remained intact during the entire experiment and could reduce local variance due to the averaging of four gauges, which were used for all tests for accurate measurement of lateral strains and for circumferential control.

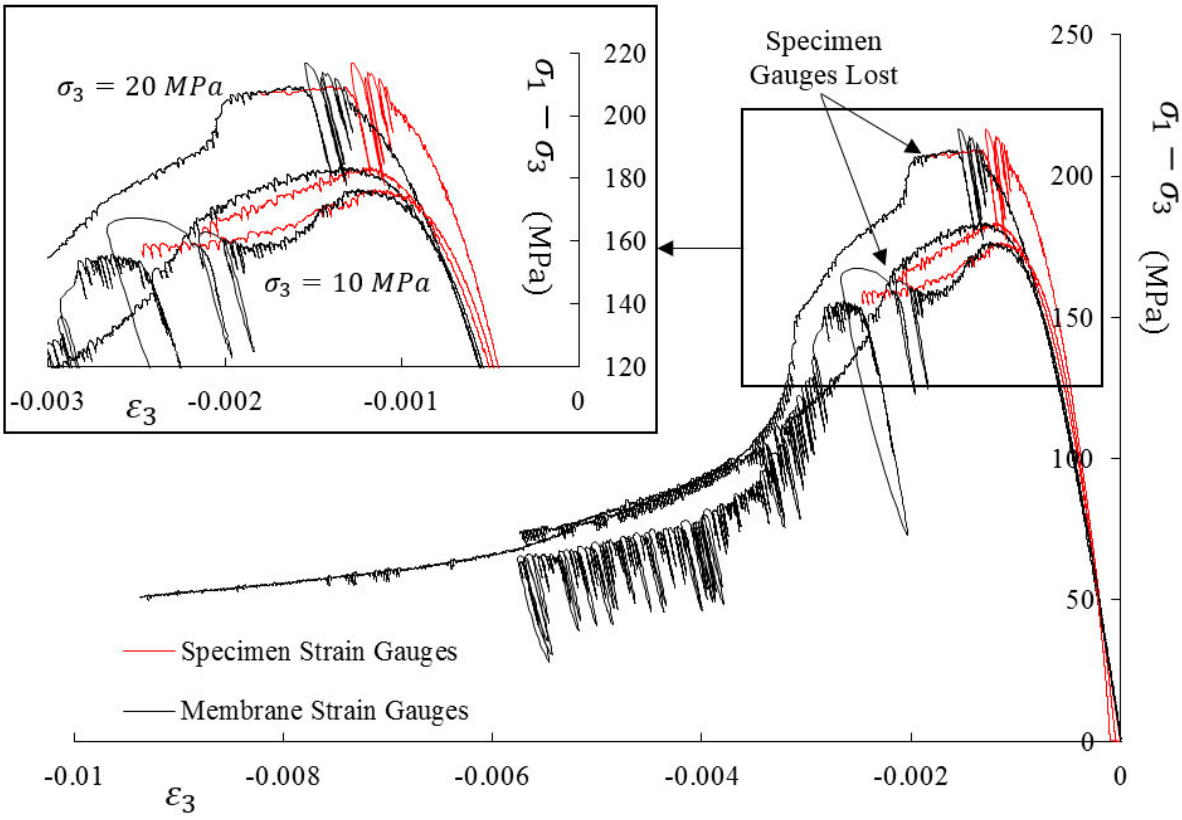

Figure 3-3: Comparison of lateral strain gauge responses

3.1.3 Acoustic Emission Monitoring

Throughout testing the acoustic emissions of each specimen were recorded by placing sensors on the loading piston and spherical seat directly above the specimen. The sensor on the loading piston was to enable the identification and filtering of any mechanical noise. The acoustic signals were captured using miniature PICO sensors and were amplified using a pre-amplifier set to 60 dB of gain (Type 2/4/6). Express-8 data acquisition card was used and sampling rate was set to a 2 MSPS (mega samples per second). The signal then was processed using the MISTRAS AEwin software. The lower threshold value for mechanical and ambient noise was set 45 dB. This was established by setting a low threshold (20dB) then increasing until the loading frame noise was no longer registering during acquisition. To ensure the acoustic emissions could be compared to certain loading scenarios, the recording for stress-strain and acoustic emissions signals were simultaneously started for each test. To quantify the damage from acoustic emissions the following relationship was implemented:

$$D = \frac{\Omega}{\Omega_{total}} \tag{3-1}$$

where Ω is the accumulated acoustic emission energy at a certain time of the test, Ω_{total} is the total acoustic energy over the whole duration and D is the damage variable. It is also important to note that, $0 \leq \Omega \leq \Omega_{total}$ and $0 \leq D \leq 1$, where 0 represents the initial undamaged state of the material and 1 is the point of final frictional failure. The definition of damage using AE energy has been discussed in the literature by previous researchers (Grosse and Ohtsu 2008; Ji *et al.* 2014; Kim *et al.* 2015; Akdag *et al.* 2018). It is concluded by these studies that the energy associated with AE response is more representative of the extent of microcracking in rock than the recorded hits. Therefore, the cumulative energy approach given in Equation 3-1 was used to quantify the relative damage levels in this study.

3.2 Experimental Results

Triaxial compression tests were conducted on the prepared specimens over the confining pressure range of 10 to 60 MPa. Results for all successful tests are presented in Table 3-2 where σ_3 is the confining pressure, σ_y, σ_p and σ_r are the initial yield, peak and residual strengths respectively and E is Young's Modulus and ν is Poisson's ratio of each specimen. In this sense, initial yield is determined as the point where the stress-strain curve departs elastic linearity and the residual strength is the plateau of the post-peak response. Despite the careful control strategy in place, some samples were still lost to brittle failure due to existing discontinuities in granite. This mobilised the failure too fast for some specimens

(TX10-1, TX20-4 and TX30-3) during triaxial testing. These results were excluded from the study to avoid inconsistency.

Table 3-2: Triaxial test results

Sample ID	σ_3 (MPa)	σ_y (MPa)	σ_p (MPa)	σ_{res} (MPa)	E (GPa)	ν
TX10-2	10	188.41	192.20	56.46	32.10	0.14
TX10-3	10	184.09	186.33	71.53	33.70	0.14
TX10-4	10	190.01	210.96	86.70	31.40	0.13
TX10-5	10	155.33	167.98	65.02	35.10	0.14
TX20-1	20	225.58	227.76	93.14	36.20	0.12
TX20-2	20	248.57	269.24	162.27	36.70	0.14
TX20-3	20	231.95	234.14	86.07	34.50	0.14
TX20-5	20	292.18	306.79	-	33.50	0.13
TX30-1	30	277.90	286.61	136.41	31.50	0.14
TX30-2	30	225.36	232.63	126.49	31.60	0.14
TX30-4	30	289.89	307.37	190.10	36.20	0.13
TX40-1	40	364.18	391.86	201.76	37.40	0.12
TX40-2	40	261.61	274.73	153.03	35.10	0.13
TX40-3	40	364.18	375.84	218.51	36.50	0.11
TX40-4	40	337.64	359.47	192.83	36.20	0.14
TX50-1	50	326.00	343.46	216.12	35.80	0.14
TX50-2	50	304.75	328.08	240.59	37.10	0.14
TX50-3	50	372.61	393.59	257.57	36.70	0.15
TX60-1	60	479.80	521.97	252.26	38.50	0.14
TX60-2	60	350.12	388.05	231.95	34.40	0.14
TX60-3	60	357.07	388.40	266.71	36.10	0.12

The full stress-strain response for each test is given in Figure 3-4.

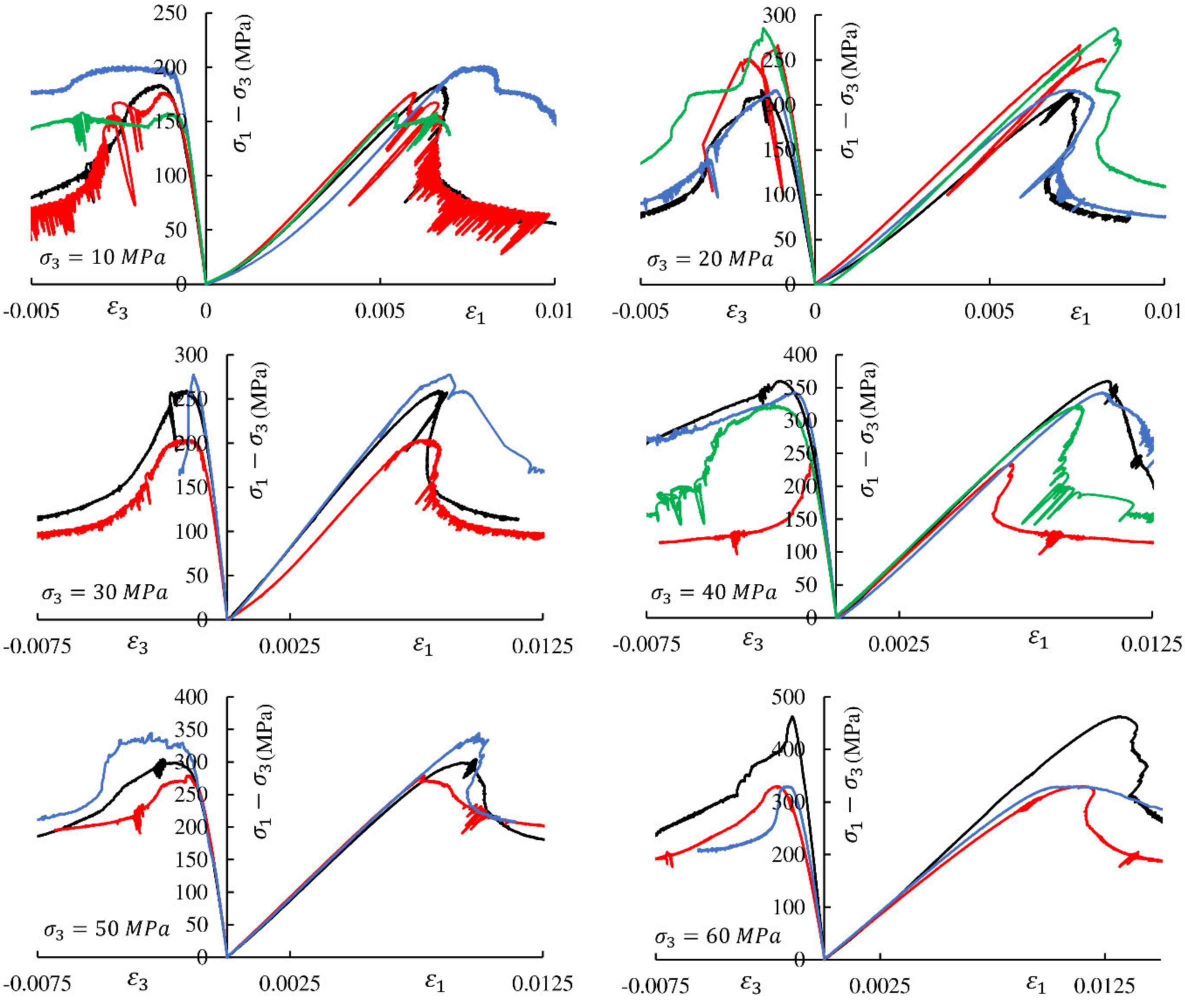

Figure 3-4: Test data for each confinement level (10-60 MPa)

It can be seen from Figure 3-4 that at confinements below 40 MPa the predominant failure mode is Class II, i.e. snap-back behaviour. However, beyond this confinement level it is observed that the Class II transitions to Class I behaviour. It is the author’s belief that as confinement level increases, there is more opposition to self-sustaining failure. This means that for the rock to continue to yield, more energy must be added to the system via the continued application of axial load. Conversely, at low confinements, the rock stores adequate energy during the pre-peak phase of loading to continue to fail under little to no added external work. It is interesting to note that at 40 MPa confinement for this rock, both

Class I and II behaviours were recorded. This provides some estimation of the transition point for this rock. A zoomed in picture of the 40 MPa tests are given in Figure 3-5.

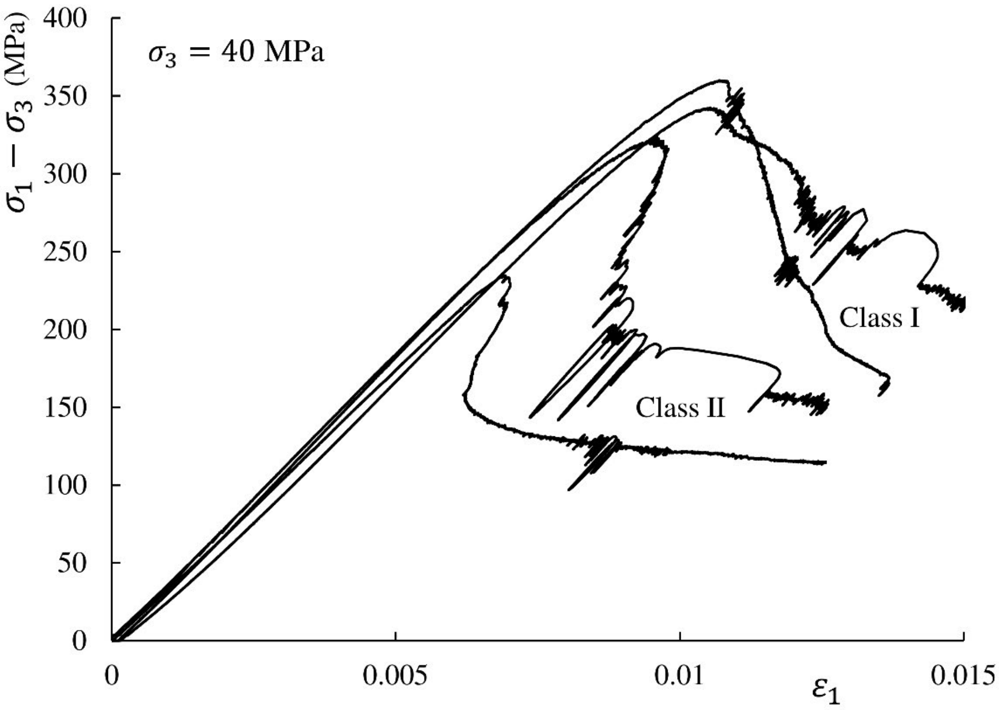

Figure 3-5: Class I and II behaviours of granite at constant confinement

To provide a full characteristic data set for the rock, the axial stiffness and Poisson's ratio was plotted for each confining pressure (Figure 3-6). It was found that stiffness increased with confining pressure and Poisson's ratio is constant throughout the confining pressure range.

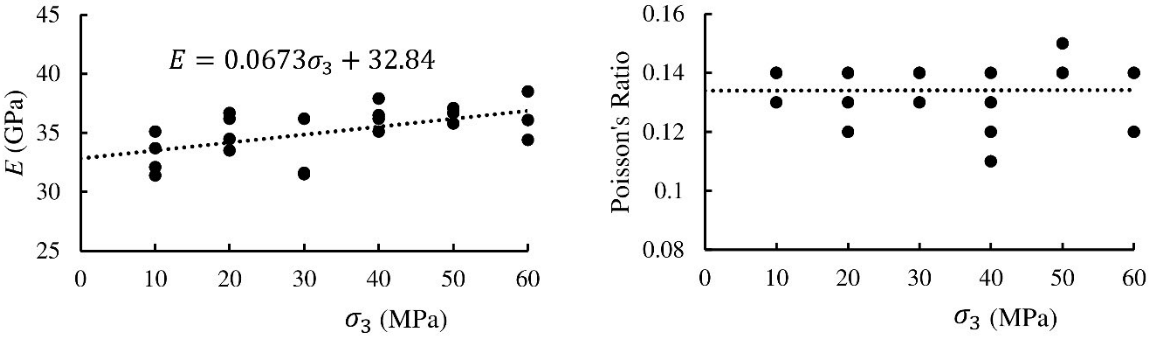

Figure 3-6: Elastic constants of each triaxial test (due to data overlap please refer to Table 2 for individual results)

3.2.1 Damage evolution

This study has already postulated that the cumulative acoustic emission energy relates to damage using Equation 3-1 and therefore, it was possible to gather information about the damage evolution of the material under different levels of confinement. As such, the damage variable from acoustic emission response captured in each test was compared with axial strain. It is important to note that all analysis in this section was undertaken on individual tests and no averaging of data over similar confinement pressures was undertaken. This ensured that the AE response was coupled with the stress-strain results correctly for each test. Examples of an individual acoustic response for each confinement is presented in Figure 3-7 and it can be seen that as lateral pressure increases the emissions occur more gradually with increasing axial strain. This corresponds to the damage evolution process becoming slower due to the increasing degree of opposing stress imparted by confinement. In other words, the hardening and more gradual softening behaviour of a rock under high confinement corresponds to the rate of microcrack initiation, propagation and coalescence competing against the consolidation effect of lateral pressure.

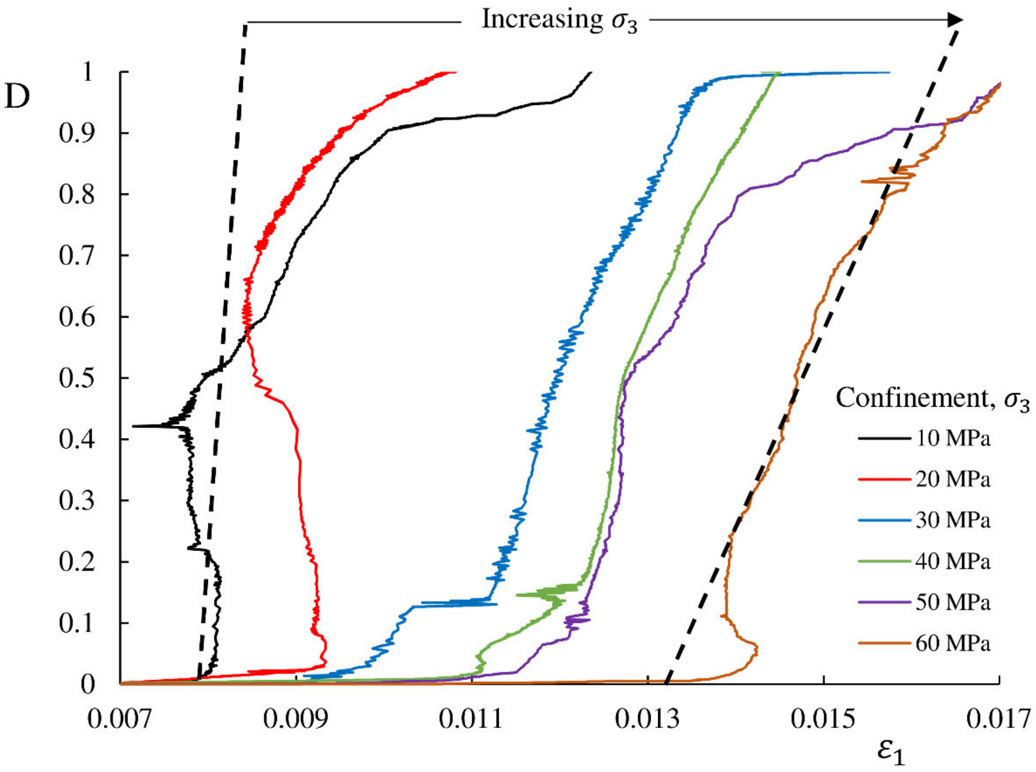

Figure 3-7: Effect of confinement pressure on damage evolution based on AE response

Furthermore, as rock undergoes compressive deformation, microcrack development increases, which is evident by the increased rate of acoustic emission signals. It has also been observed in experiments that as the number of microcracks (damage) increases in a material during testing, the stiffness of the rock decreases (Eberhardt *et al.* 1999; Chen *et al.* 2014b; Chen *et al.* 2015). Therefore to describe this overall behaviour, the scalar damage parameter outlined by Equation 3-1 was used in the damage mechanics framework described in the works by Krajcinovic (1996), Lemaitre and Desmorat (2005) and Murakami (2012):

$$p = (1 - D)K(\varepsilon_v - \varepsilon_v^{in}) \quad (3\text{-}2)$$

$$q = (1 - D)3G(\varepsilon_s - \varepsilon_s^{in}) \quad (3\text{-}3)$$

where K and G are the elastic bulk and shear moduli, respectively. Therefore, the triaxial volumetric and shear inelastic strains throughout testing are implicitly assumed to take the form:

$$\varepsilon_v^{in} = \varepsilon_v - \frac{p}{(1-D)K} = \varepsilon_v - \left[\left(\frac{1-2\nu}{(1-D)E}\right)(\sigma_1 + 2\sigma_3)\right] \qquad (3\text{-}4)$$

$$\varepsilon_s^{in} = \varepsilon_s - \frac{q}{(1-D)3G} = \varepsilon_s - \left[\frac{\sigma_1-\sigma_3}{(1-D)3G}\right] \qquad (3\text{-}5)$$

It is acknowledged that the damage state defined in the above relationships is assumed to correlate to the acoustic emission definition (Equation 3-1) provided in this research. Given the fact that microcrack formation and propagation in rock specimen affects the elastic stiffness, this assumption is reasonable in our opinion and can be used for quantifying the experimental results.

Once the inelastic strains were calculated, they were compared to the damage variable shown in Figure 3-8. This revealed for a representative test, that as confinement increases, the damage evolution of the material is more gradual over increasing permanent deformation of the material. Data such as this could be used to calibrate or form damage evolution laws for constitutive modelling.

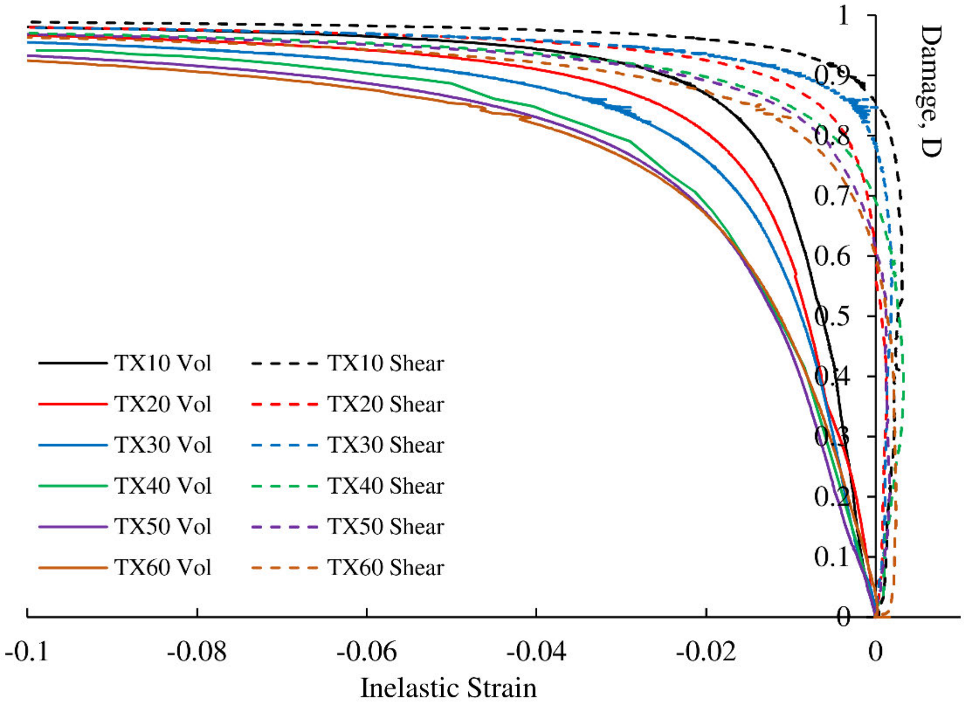

Figure 3-8: Damage evolution with inelastic strains (shear and volumetric) at various triaxial (TX) stresses

3.3 Damage Threshold Estimation

This section focuses on the determination of the damage thresholds for the triaxial compression of rock using methods from previous publications as well as the proposed inelastic strain and acoustic emission techniques. To date, limited research has been done to apply these methods to fully circumferential strain controlled, triaxial tests. Therefore, as the true pre- and post-peak behaviour of Class II rocks is not accounted for, differences in the calculated values for thresholds could exist for hard rocks. Additionally, very few studies have dealt with the calculation of these thresholds for confined igneous specimens (Wen *et al.* 2018). As such it is important to provide a comprehensive study on the calculation of crack damage thresholds for the tests conducted in this research. For the granite specimens tested, the full Class I and II stress-strain responses were successfully recorded. Therefore, the calculation of these thresholds in this section can be compared to the literature results and discussed. The first method utilised was after Martin (1993). Shown in detail in Figure 2-31 the total volumetric strain from each test was plotted and compared to find the crack damage threshold (σ_{cd}). The initial estimates of crack initiation were done using the axial strain method (ASM) proposed by (Eberhardt *et al.* 1998), the lateral strain response (LSR) method Nicksiar and Martin (2012) and the accumulated AE hit method (CAEM) outlined in Zhao *et al.* (2013). These methods were then used as a baseline for validating the proposed methods in this study. The damage inelastic strain method (DISM) used in this study was modified from those used widely in the literature (Martin 1993). This was done by comparing the damage state at a certain axial strain increment using Equation 3-1 and inputting into the triaxial stress-strain relationships to calculate inelastic volumetric (ε_v^{in}, Equation 3-4) and shear (ε_s^{in}, Equation 3-5) strains. The values for inelastic volumetric and shear strains were then graphed against axial strain and cross-referenced with the stress and damage curves to determine the location of crack closure (σ_{cc}) and crack initiation (σ_{ci}). The results are similar in nature to those shown in Figure 2-31, however, by including the damage variable in the calculation of the inelastic strains, the dependence of crack thresholds on constant elastic parameters highlighted by Eberhardt *et al.* (1998) could be avoided. The other proposed technique to determine damage thresholds was the acoustic emission damage method (AEDM). The calculation of a damage variable using acoustic emission energy (Equation 3-1) has not been used by many studies (Grosse and Ohtsu 2008; Ji *et al.* 2014; Kim *et al.* 2015; Akdag *et al.* 2018) and only the cumulative hits method has been applied to crack damage thresholds. Therefore, as energy reveals much more about the magnitude of microcracks (and hence provides a more quantifiable measure), it is crucial to calculate the crack damage thresholds using this measurement. It was found that the crack initiation threshold could be estimated by the point where acoustic emission activity begins after the linear elastic phase of loading. Then the crack damage threshold can be calculated as the increase in damage evolution, indicated by a change in slope of the damage vs. axial strain curve due to the acceleration of microcracking and unstable fracture propagation. The calculation of these thresholds using acoustic energy is shown in Figure 3-9 for a triaxial test with a confining pressure of 30 MPa conducted in this research.

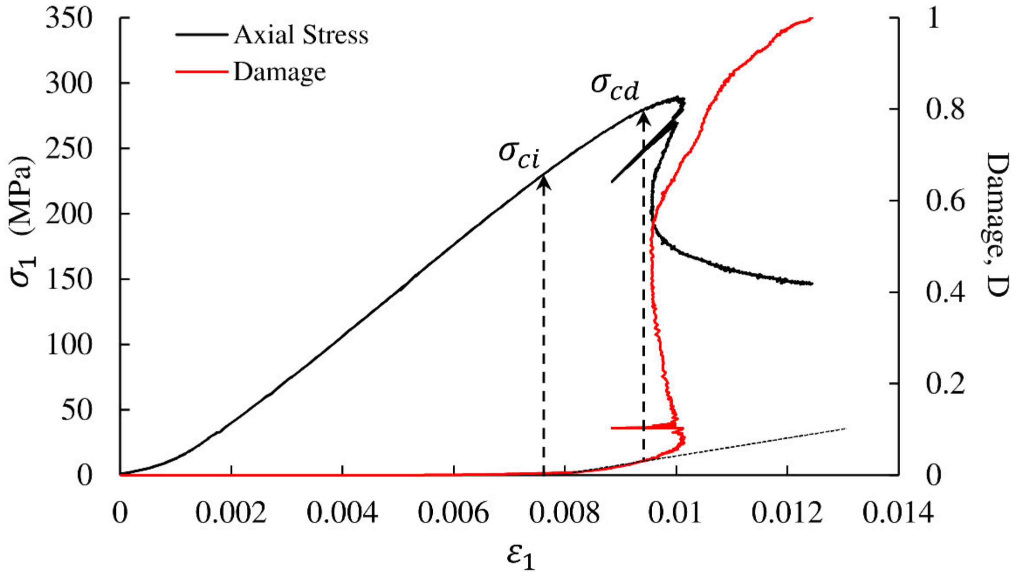

Figure 3-9: Determination of damage thresholds from damage parameter/AE energy

Once each test was conducted, all of the methods described above were implemented to calculate the crack damage thresholds. Figures 3-10 to 3-15 present a typical full data set for a test at each confinement. As LSR is not plotted against axial strain these graphs were omitted from the figure. By applying each of the methods and displaying them all together it was possible to compare the result of each method and hence determine the effectiveness of each to determine the crack thresholds. Although only a single test is given in full for each confinement, the calculations were done for every sample listed in Table 3-2. Therefore, further discussion on the crack damage thresholds is based on at least three tests at each confining pressure. Table 3-3 displays the results of every crack initiation method along with overall statistics for each test where SD is standard deviation and CoV is the coefficient of variance.

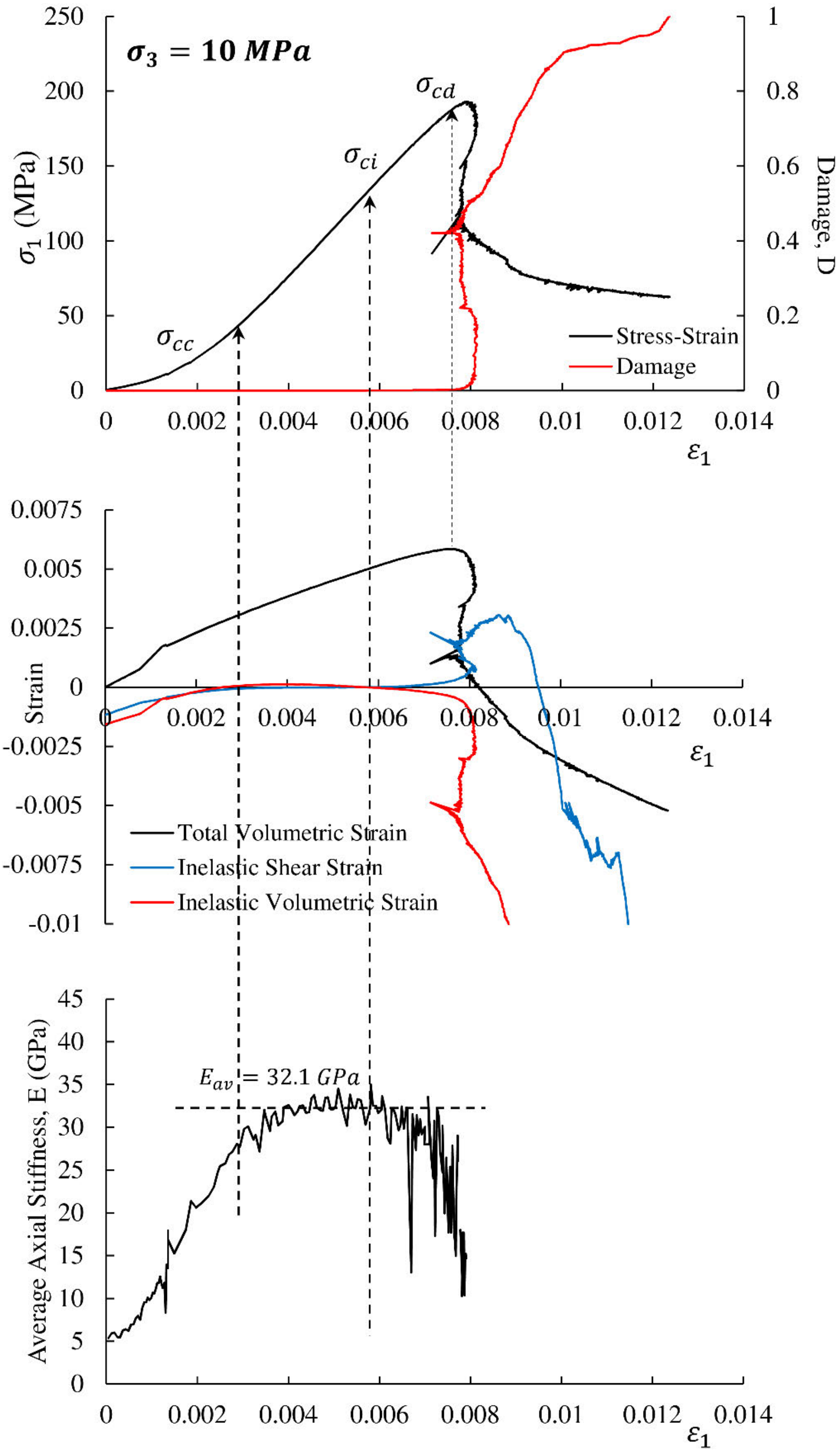

Figure 3-10: Typical full test results for 10MPa confinement

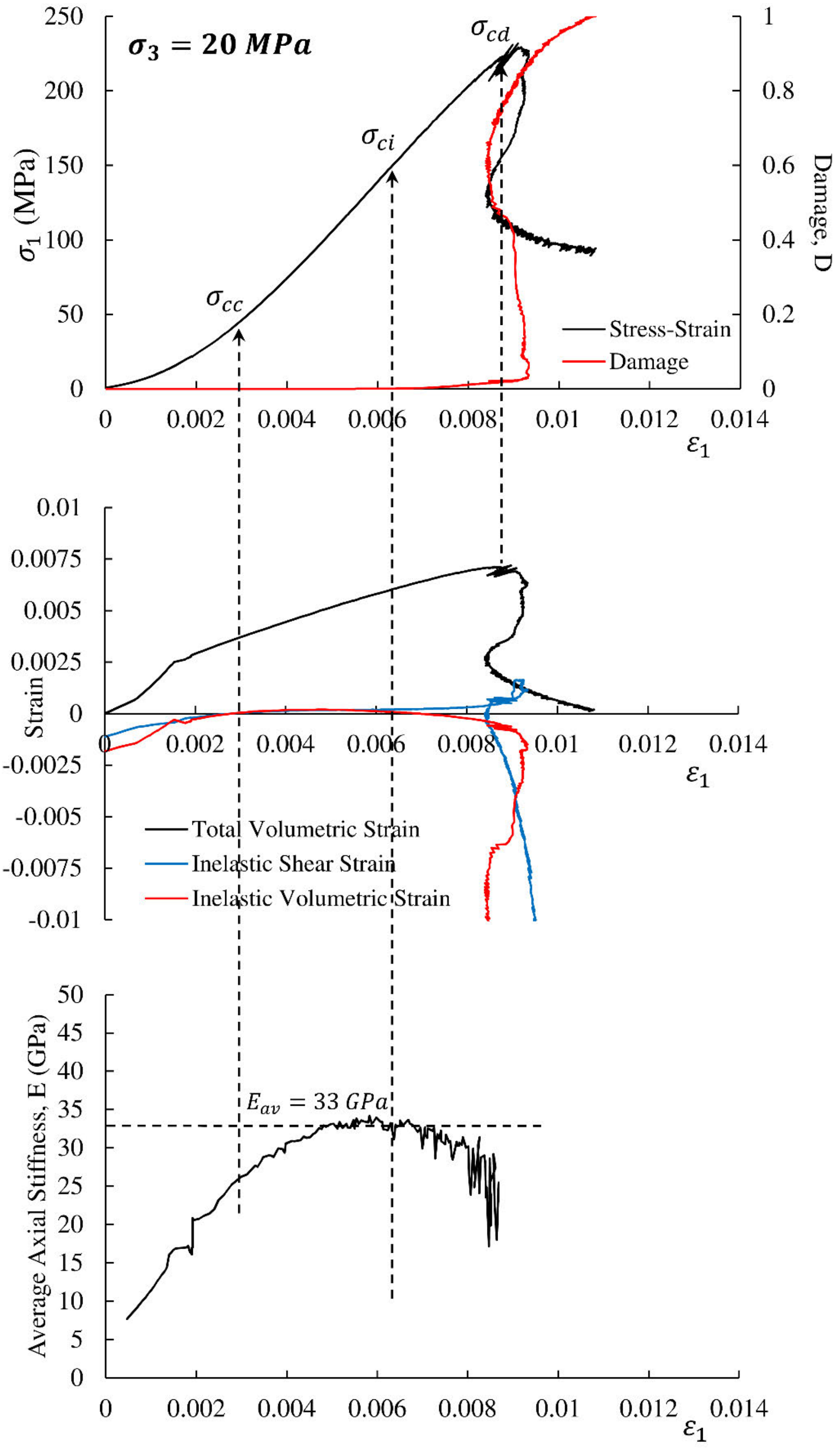

Figure 3-11: Typical full test results for 20MPa confinement

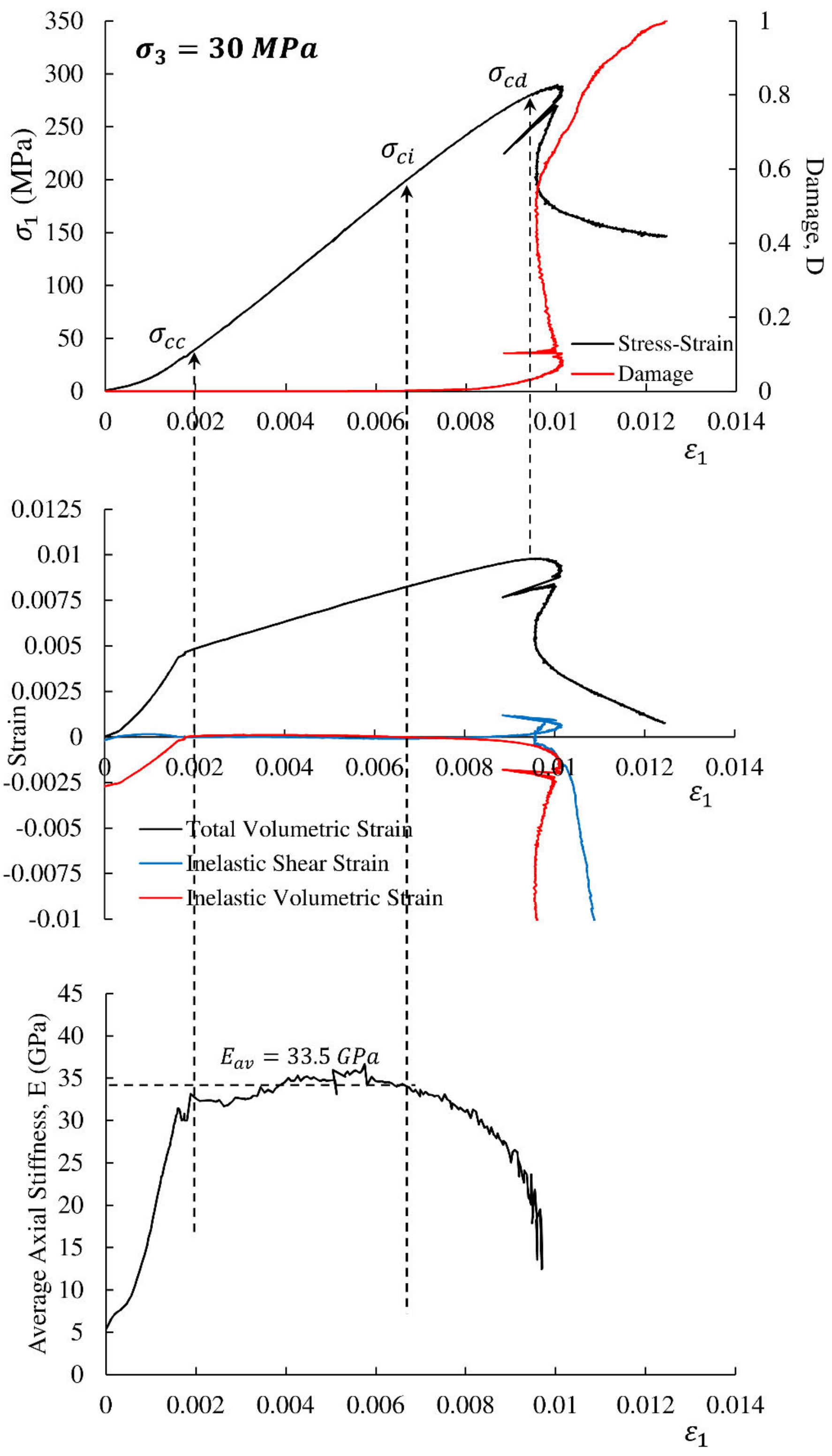

Figure 3-12: Typical full test results for 30MPa confinement

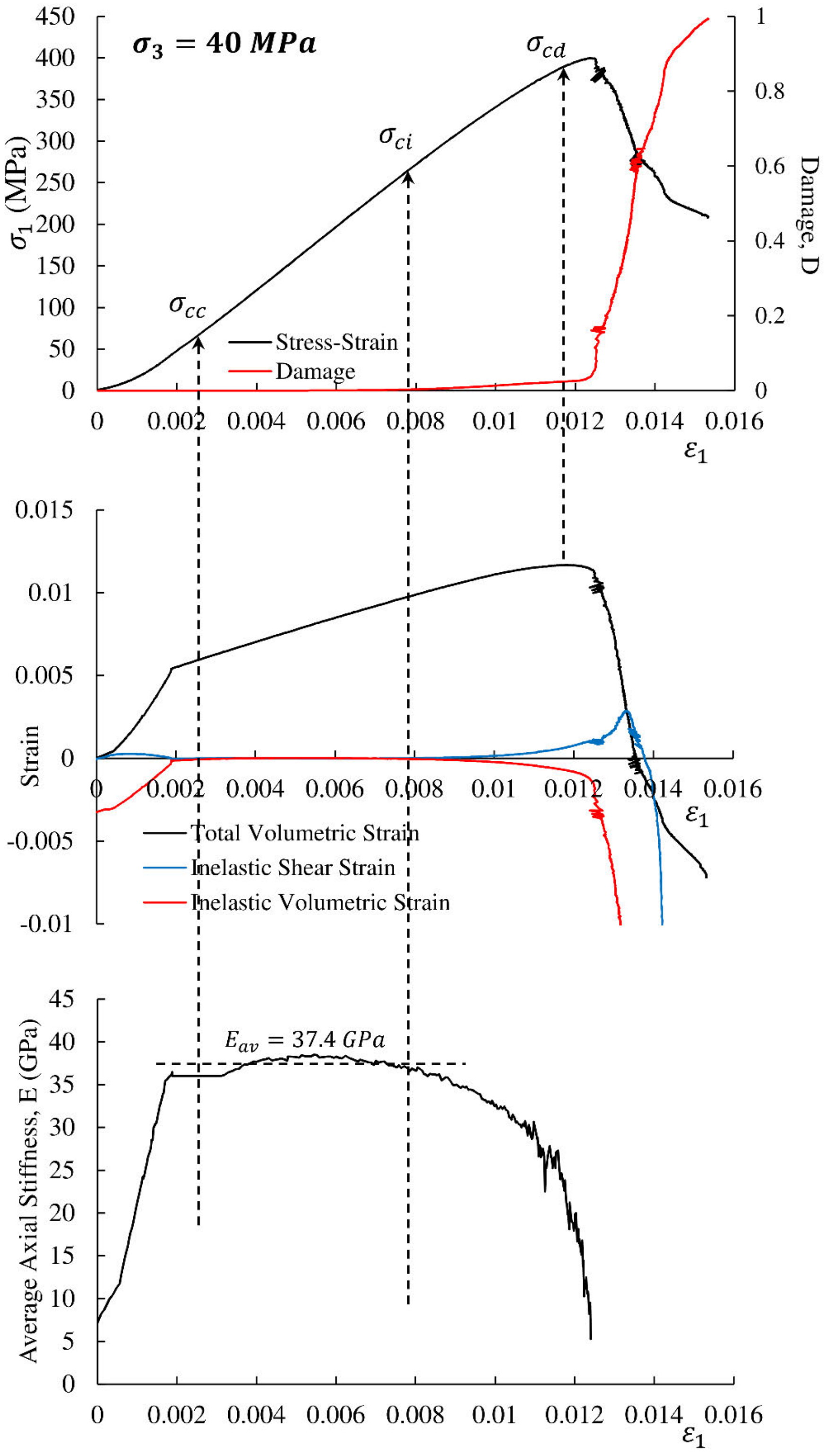

Figure 3-13: Typical full test results for 40MPa confinement

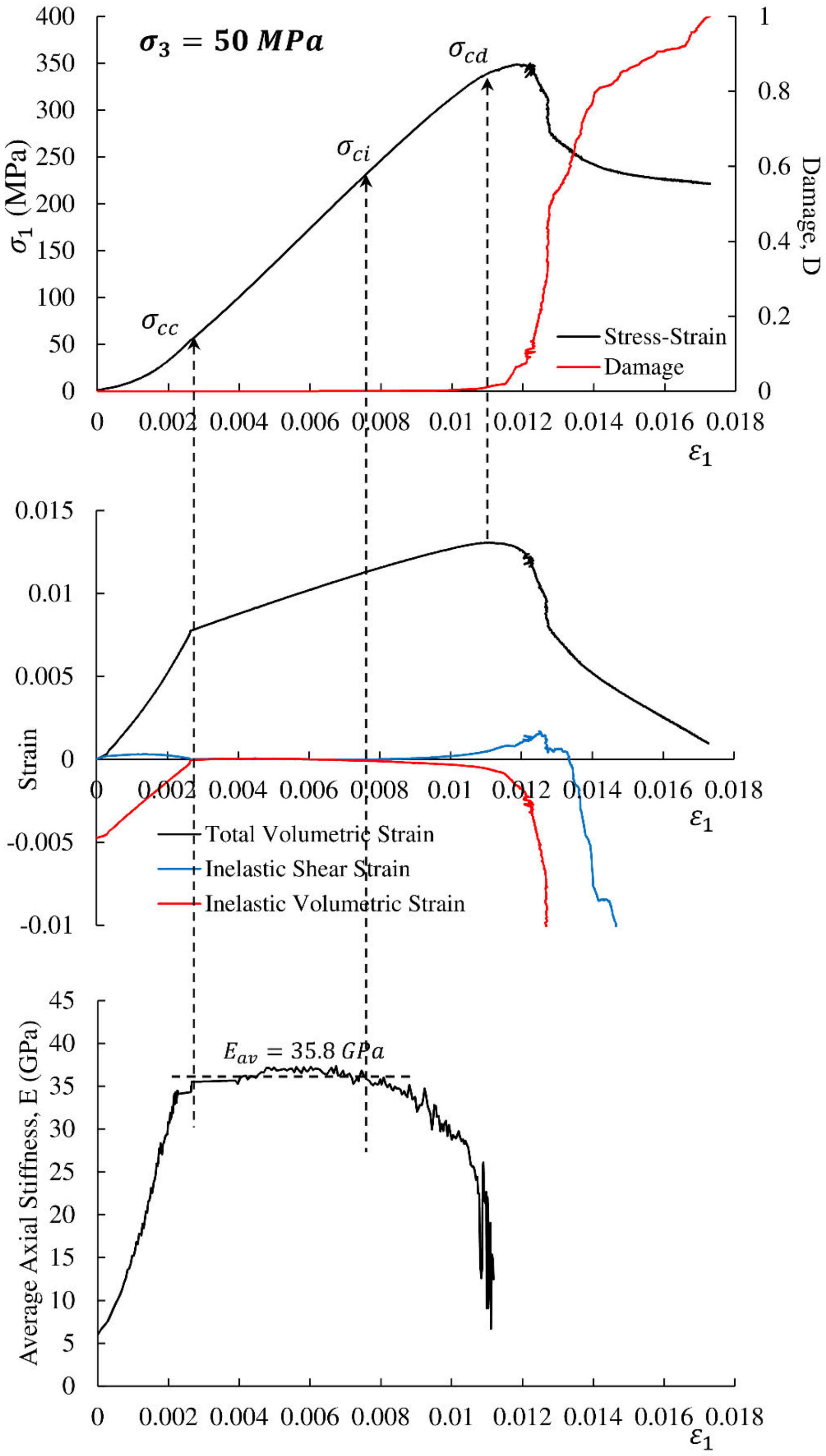

Figure 3-14: Typical full test results for 50MPa confinement

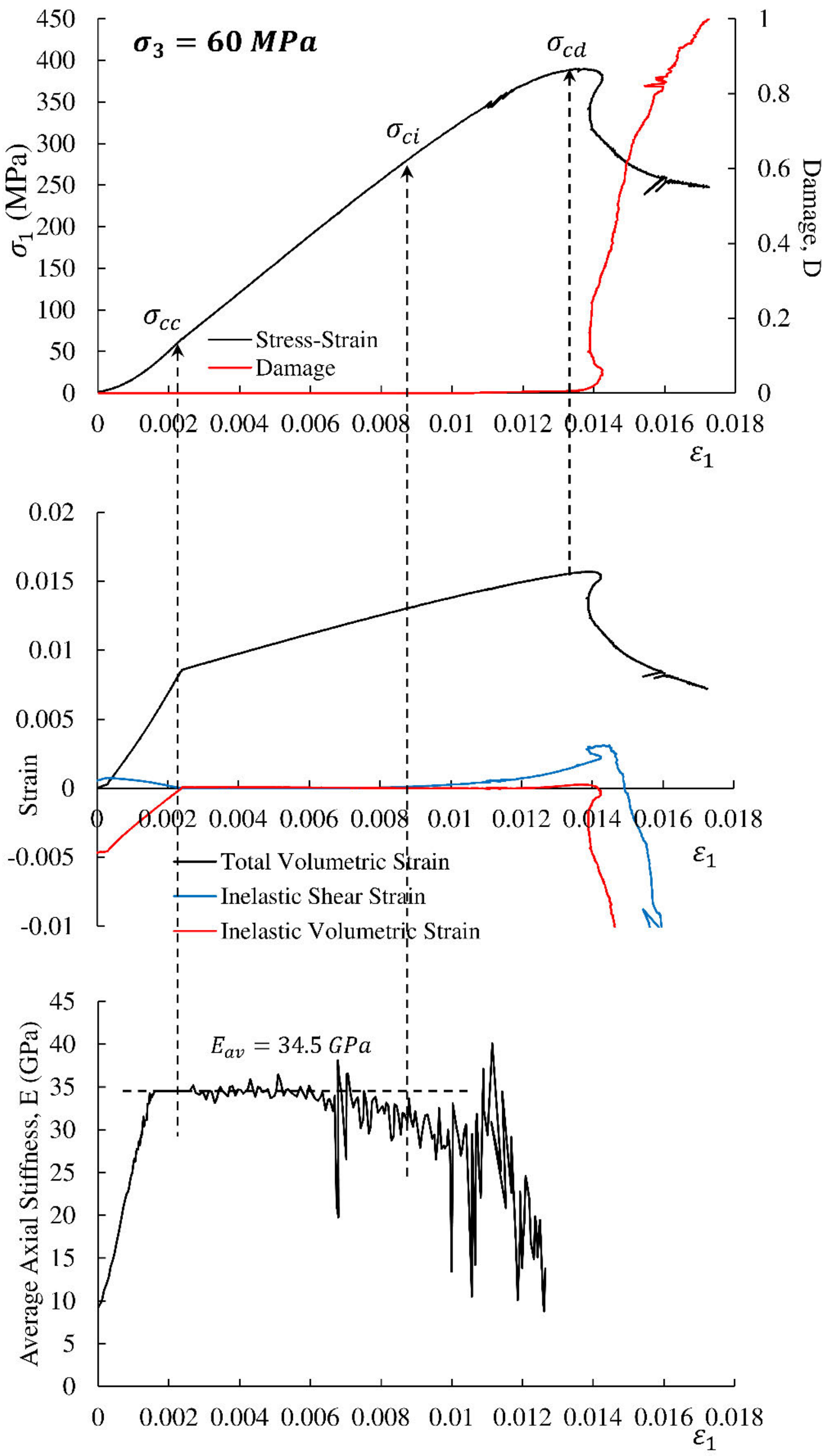

Figure 3-15: Typical full test results for 60MPa confinement

Table 3-3: Crack damage thresholds for each specimen

Sample ID	Crack Initiation Stress σ_{ci} (MPa)						SD (MPa)	CoV	σ_{ci}/σ_p	Average σ_{ci}/σ_p	SD	CoV
	ASM	LSR	CAEM	AEDM	DISM	Average						
TX10-2	143	142	135	129	143	137	6.6	4.8%	0.71	0.62	0.06	10.2%
TX10-3	110	105	96	100	117	105	9.1	8.7%	0.56			
TX10-4	130	129	121	131	120	125	5.6	4.4%	0.59			
TX10-5	101	96	110	95	107	102	7.6	7 5%	0.61			
TX20-1	168	151	136	152	146	146	7.3	5.0%	0.62	0.68	0.06	9.0%
TX20-3	170	172	150	158	170	163	10.4	6.4%	0.69			
TX20-5	228	239	220	220	226	226	9.0	4.0%	0.74			
TX30-1	201	199	200	185	190	194	7.2	3.7%	0.67	0.68	0.01	1.5%
TX30-2	178	133	163	178	163	159	18.9	11.9%	0.68			
TX30-4	215	220	210	208	208	212	5.7	2.7%	0.69			
TX40-1	260	295	250	280	293	280	20.8	7.4%	0.70	0.71	0.02	2.6%
TX40-2	195	186	180	200	195	190	9.0	4.7%	0.69			
TX40-3	290	265	270	258	290	271	13.7	5 1%	0.71			
TX40-4	255	270	250	283	268	268	13.6	5 1%	0.74			
TX50-1	230	242	240	227	241	238	7.0	3.0%	0.67	0.69	0.02	2.4%
TX50-2	220	210	233	243	235	230	14.2	6 2%	0.70			
TX50-3	280	277	277	261	282	274	9.1	3 3%	0.70			
TX60-1	387	391	388	403	380	391	9.5	2.4%	0.75	0.72	0.07	9.3%
TX60-2	270	293	317	305	281	299	15.5	5 2%	0.77			
TX60-3	235	251	250	241	260	251	7.8	3 1%	0.64			

It can be seen that crack closure is consistently calculated by the inelastic volumetric strain and average axial stiffness methods. However, the step size for the moving point regression technique can affect the location of the plateau for lower confinement tests. Therefore, the more accurate method for determining the crack closure threshold was found to be the modified inelastic volumetric strain curve.

Figures 3-10 to 3-15 and Table 3-3 also show that the crack initiation thresholds show good agreeance for all of the prediction methods. Therefore, the onset of damage and hence initial yield of the material can be calculated with confidence from these circumferentially controlled tests. Therefore, due to the correlation between the methods of this initial yield estimation, damage-plasticity numerical models can be calibrated to this stress level and damage evolution studied from the initiation point.

Furthermore, the crack damage threshold was found using total volumetric strain at the onset of dilation and the proposed AE method. These two methods predicted the same value for this threshold and therefore, it was concluded that sufficient accuracy of the AE emission energy method was achieved. It was also found that the rate of inelastic shear and volumetric strain increased at the calculated point of crack damage. Figure 3-16 shows the increase in inelastic strains corresponding to the point of maximum total volumetric strain. Therefore, it is concluded that this measure can also be used to predict the crack damage threshold of a circumferentially controlled test.

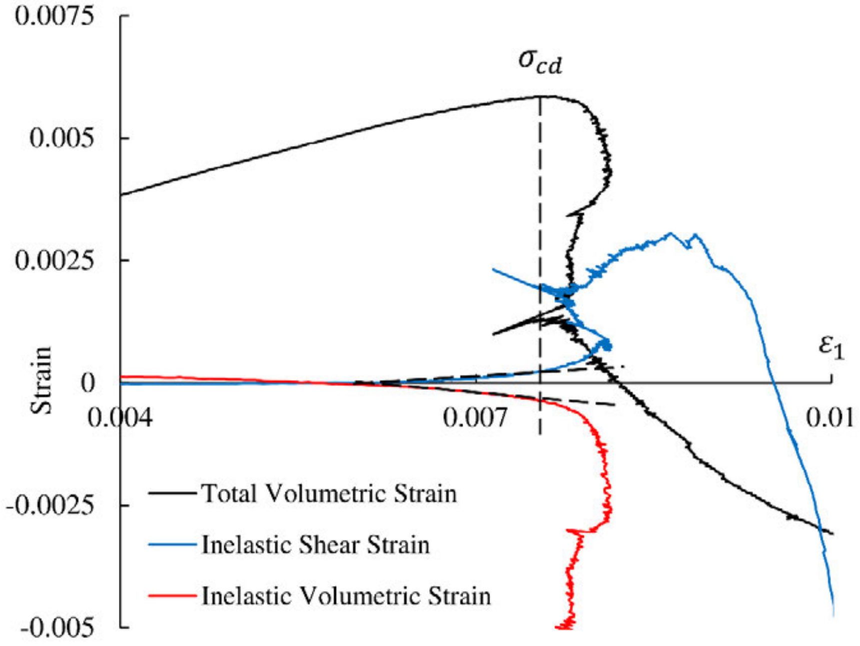

Figure 3-16: Prediction of crack damage threshold with damage-inelastic strain measures

Once the process of estimation was conducted for each test, the results were compiled and plotted to show the relationship between the thresholds and confinement. Figure 3-17 shows the proportion of peak stress for each damage threshold and also shows the standard deviation of the results for each confinement.

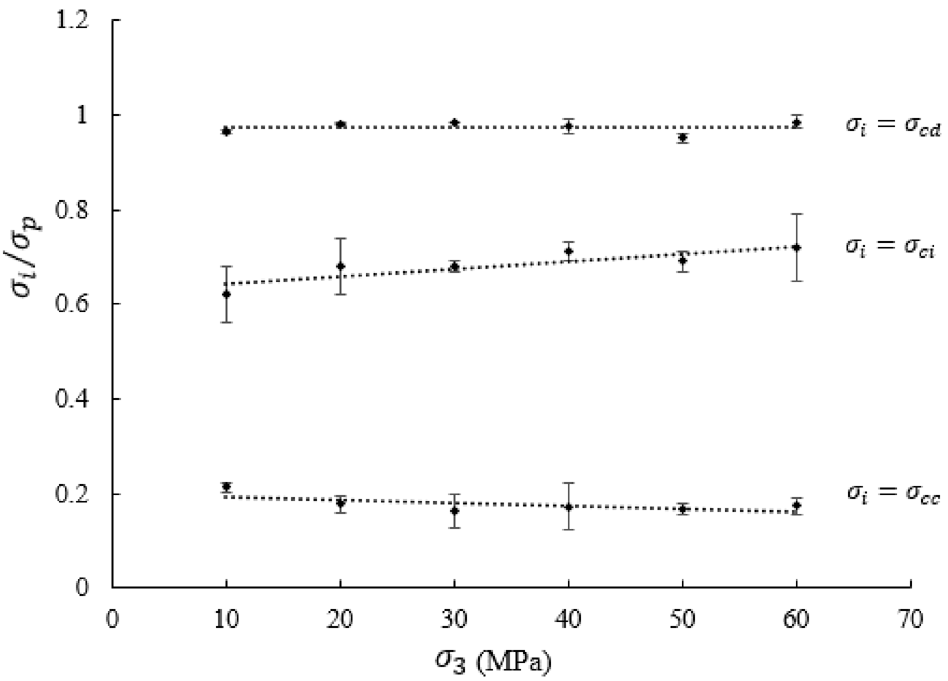

Figure 3-17: Proportion of peak stress for each threshold over increasing confinement

3.4 Discussion

Estimations of damage thresholds in the literature have usually revealed that crack closure occurs at around 20% of peak stress (Eberhardt *et al.* 1998; Eberhardt *et al.* 1999). The test results in this study also display that this threshold holds true under the FCC method, however, some variation of test results was also realised. It is postulated to be the result of the different extent and properties of microcracking present in each sample before testing. Therefore, the samples can take variable proportions of peak stress to consolidate and for microcracks to close. The most effective method for measuring the crack closure threshold was found to be the modified inelastic volumetric strain method (Eq. 4) as this coincided much more closely to the stress-strain linearisation than the stiffness method for all confinement levels. This is due to the effect of the range of values employed for the moving point regression technique on the stiffness method.

The crack initiation thresholds calculated in this research were found to be higher than for most other tests found in previous studies. Contrary to the 50-60% of peak stress found for granitic rocks in existing publications, the crack initiation threshold was found to be in the range of 60-70% of peak stress. The contrast is displayed graphically in Figure 3-18. Although the thresholds are relatively high, the levels have been recorded in the past by Hatzor and Palchik (1997).

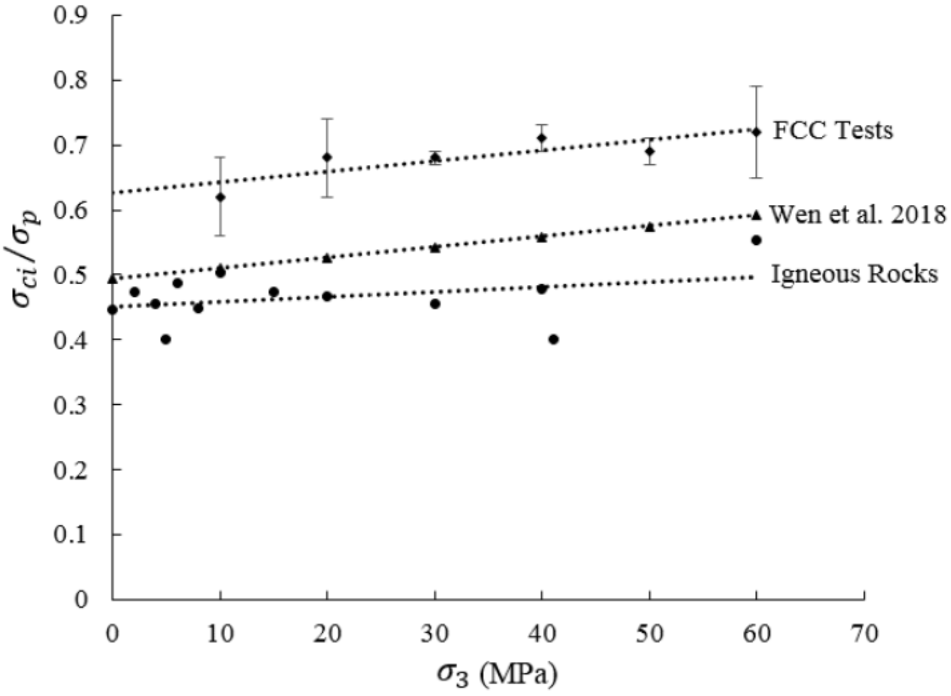

Figure 3-18: Proportional crack initiation thresholds for FCC tests versus literature data

It is also apparent from the FCC tests that as confinement increases, the proportional crack initiation stress increases. Therefore, although the loading control does seem to effect the magnitude of the crack initiation threshold, the overall increasing trend is not affected. This can also be seen in Figure 3-18 as the current research displays the same slope as the compiled results for all rocks in Wen *et al.* (2018). Furthermore, the crack initiation threshold from circumferential control tests could be used as the initial yield point of a material in a plasticity or damage-plasticity constitutive model. This is a more accurate estimate than relying on the deviation of axial stiffness alone as there is obscurity with the estimation of the point at which the Young's modulus decreases enough to identify overall structural weakening of the material. Additionally, as the test is controlled by dilation, it is less likely that there is a sudden failure of the specimen. Therefore, the initial yield of the material can be captured somewhat independent of loading rate.

Another important finding of these tests is the predictor for the crack damage threshold for each test. The results do not match typical results nor behaviours reported in numerous studies on granite or similar rocks under axial pre-peak control (Table 2-2). When the volumetric strain reaches its peak value for each test the damage threshold is found to be 95-98% of the peak stress. This is also consistent when using the acoustic emission method. This highlights the importance of the loading method in determining the point at which damage is uncontrollable. Therefore, if the pre-peak loading method is axial control, the crack damage threshold would be a lower percentage of the peak stress of a rock due to the constant application of displacement or load throughout the test. On the other hand, if the test is controlled by constant dilation of the specimen with time, which was implemented in the current research, the loading can be relaxed and even reversed slightly to allow the rock to undergo self-sustaining failure where the post-peak response is not dependent on the stiffness of the loading frame. This has also been documented in other FCC studies (Eloranta 2004; Jacobsson 2004b; Jacobsson 2004a). Therefore, the damage is controllable up to much higher proportions of the peak stress. This is very important in the context of constitutive modelling as the damage evolution is not loading rate or method dependent, allowing for accurate representation of material behaviour. Also, as the damage can be controlled longer throughout the test, it provides much more accurate estimations of pre-peak damage levels in a material, which can then be used to effectively calibrate hardening and softening phases in constitutive modelling. Other applications for this finding can be multiple-step triaxial loading or cyclic loading where the peak stress or damage level of the specimen must be controlled and monitored throughout the duration of the test.

This study also shows that the circumferential strain method of control during a triaxial compression test can capture the range of Class I and Class II behaviours of a rock under the confining stress. It was found throughout most confinements that although the occurrence and degree of Class II behaviour was reduced with increased lateral pressure, it was still present and may not be lost until very high pressures are tested. This reveals that for engineering situations, such as the confinement levels addressed here, it is very important to obtain the ‘true’ stress-strain response of a material along with the associated damage evolution under these conditions. The experimental results also showed the transition phase of a material (in this case 40 MPa confinement), where the predominant response switches from Class II to Class I.

Finally, the relationship between damage evolution and confinement showed that as lateral stress increases, the rate of damage accumulation decreases. Due to the careful control method employed in this study, this response can be used in determining the effect of confinement on damage evolution and is again important to allow for correct modelling in damage-plasticity frameworks.

3.5 Conclusion

In this study a series of triaxial compression tests were conducted using full circumferential strain control (FCC) on granite exhibiting Class II behaviour. The results were then used to identify damage thresholds using a variety of existing and proposed methods. It was found that although the crack closure threshold was similar to literature, the crack initiation and damage thresholds were noticeably higher using this control method. The derived crack initiation thresholds identified that they are highly dependent on confining pressure, where the proportion of stress increases with increasing confinement. This indicates that contrary to some opinions, the damage thresholds are dependent on the method of test control and loading, more specifically on the stress-strain behaviour of Class I or II rocks. As the rock specimens in this paper were controlled by allowing self-sustaining dilation or failure, a more reliable estimation of crack initiation could be obtained. Therefore, values for the crack initiation thresholds found in this research can be directly applied as the ‘initial yield’ point in plasticity or damage-plasticity models as they provide more insight into material behaviour.

Another result of dilation control is that the crack damage threshold can be delayed until essentially the peak stress is obtained. Therefore, triaxial tests can be controlled for a lot longer with the circumferential method than for the axial control methods. The main advantage of this testing methodology is that the true pre- and post-peak behaviour of a highly brittle rock can be captured alongside the true damage evolution under self-sustaining failure. This, in turn, is essential to correct modelling of engineering excavations using plasticity or damage-plasticity frameworks as it provides a more complete and justifiable data set for the rock tested.

It is clear from the research that the capturing of the ‘true’ damage evolution and stress-strain response enables the correct calibration of damage-plasticity models. However, there are few simple models available that enable the coupling of damage with yield. Most of the existing models require complex formulations as pointed out in Chapter 2 of this dissertation. Therefore, the following chapter focusses on the formulation of a new unified yield-failure surface and calibration procedure for constitutive modelling of hard rock.

Chapter 4 – A NEW CONSTITUTIVE MODEL FOR HARD ROCKS

This chapter focuses on the development of a unified yield-failure function which was then implemented into a damage-plasticity framework. The proposed approach made better use of the concepts of initial inelastic behaviour (yielding) and the remaining residual strength mostly due to friction (failure). Hardening or softening was then related to how the yield surface evolves to the ultimate failure surface. This approach eliminated the need for separate loading surfaces and individually defined hardening and softening laws. Therefore, this resulted in a much simpler model, facilitating the numerical implementation and practical engineering applications. Furthermore, the definition of 'unified yield-failure' in this study is a single criterion that continually evolves an initial yield surface for the material to a final frictional failure surface via an appropriate damage evolution law. Therefore, this criterion allows description of both brittle, ductile and transitional behaviour of hard brittle rocks under compressive loading at different confining pressures. In this sense, the experimental calibration of the initial and final states of the unified yield-failure surface automatically induced brittle behaviour under low confinement and ductile under high confinement, together with the transition between the rock responses. The damage evolution rule is combined with plastic strain to take into account the combined effects of microcrack closure, initiation and coalescence and frictional sliding of the rock during failure. It is shown that the proposed model is able to replicate a wide range of hard rock behaviour. In addition, enhancement of the model is also proposed to account for some minor hardening under low confinement, as a consequence of competition between microcrack closure and initiation prior to peak strength. The proposed model was validated using triaxial test data for granite (Arzúa and Alejano 2013; Chen *et al.* 2015) and marble (Zhang *et al.* 2011; Unteregger *et al.* 2015) sourced from experimental works in literature.

The evolving yield surface also enabled the adjustment of the formulation to facilitate calibration between the measured damage states of the rock to the true stress-strain responses from testing. This combined with an experimentally derived damage evolution law simulated the behaviour of the tests conducted in Chapter 3 in this dissertation.

4.1 The constitutive model framework

This study assumed for illustrative purposes that compressive stresses are positive and tensile are negative. This is common amongst most rock mechanics models (Jaeger *et al.* 2007). The isotropic, unified yield-failure model was restricted to the meridian plane to simplify formulation, where the effects of Lode angle were omitted. The deviatoric section of the function can be adopted in future works without modification of the proposed meridional function. Furthermore, it was assumed that the principal stresses are ordered as $\sigma_1 \geq \sigma_2 \geq \sigma_3$ and the first invariant of the stress tensor took the form $I_1 = tr(\sigma_{ij})$ and the second invariant of the deviatoric stress tensor was described as $J_2 = \frac{s_{ij}s_{ij}}{2}$ where $s_{ij} = \sigma_{ij} - I_1\delta_{ij}/3$. The hydrostatic and deviatoric stress components used in the formulation of yield and failure were given by the invariants $p = -I_1/3$ and $q = \sqrt{3J_2}$.

The framework selected for modelling in this research was based on the theories of continuum damage mechanics and plasticity. The complete discussion of these theories can be found in Chapter 2 and in detail in works such as Chen and Han (1988), Lemaitre (1992) and Murakami (2012). Therefore, an in depth discussion on the theory is not included in this chapter. It was assumed that the stress-strain relationship for rock takes the following form:

$$\sigma_{ij} = (1 - D)C_{ijkl}(\varepsilon_{kl} - \varepsilon_{kl}^{p}) \tag{4-1}$$

where ε_{kl}^{p} is the plastic strain tensor and D is the damage variable where $0 \leq D < 1$. This followed the definition given by Lemaitre and Desmorat (2005) that 0 corresponds to an undamaged/intact material and 1 refers to a fully damaged representative volume element. To maintain simplicity, the damage variable used in this study was isotropic and hence scalar. Therefore, the formulation is applicable to proportional loading of a material. It is important to note that the function is bounded by initial yield and final critical state, therefore when $D = 1$ stress is always non-zero (refer to Figure 4-1). The evolution of damage was characterised by an exponential evolution law so the problem of the zero stress state in Equation 4-1 can never be realised even for large strains.

In addition, this study was mainly concerned with the behaviour of rocks under compression, as this is the case in many underground and/or mining applications. Therefore, the unilateral behaviour due to crack closure effects when going from tension to compression is ignored in the formulation. This helped significantly simplify the formulation for a clear presentation and allowed the focus to be on the compressive behaviour of a material under a wide range of confining pressures.

The integral parts of any continuum damage-plasticity model are the definition of yield and failure of a material, together with the evolution of internal variables, which were damage, D and plastic strain, ε_{kl}^{p} in this case. Traditionally the initial yield that signifies the onset of inelastic behaviour can be obtained from experimental data, while the failure state is related to the stage at which the material loses all tensile strength and its residual frictional shear strength is fully mobilised. The complete description of material behaviour therefore should include these initial and final stages of deformation together with an evolution rule to describe the transition from yield to failure. In this sense, the initial focus was on the formulation of a generic yield and failure that incorporates stresses and the damage variable, D. This was then supplied with evolution rules for both plastic strain and damage variable to complete the model definition.

4.2 The unified yield-failure criterion

The yield function in a damage-plasticity model determines whether or not the material is undergoing elastic or plastic/damage deformation. This allows one to calculate the inelastic and elastic strains and to correctly determine the stresses. The mechanical behaviour of a rock mass can exhibit plastic deformations caused by mechanisms such as frictional sliding of cracks/discontinuities or grain crushing as well as stiffness reductions due to the accumulated damage as a result of microcracks (Unteregger *et al.* 2015).

Most studies to date focus on the development of plastic and damage surfaces then via a coupling procedure, the contribution of each process can be determined (Lubliner *et al.* 1989; Yazdani and Schreyer 1990; Salari *et al.* 2004; Luccioni and Rougier 2005; Grassl and Jirasek 2006; Jason *et al.* 2006; Chen *et al.* 2010; Chen *et al.* 2015; Zhang *et al.* 2016). By forming a unified yield-failure function which takes into account both plastic and damage processes during the evolution from yield to failure, combined effects of microcracking and frictional sliding on the macro behaviour of rocks can be accounted for without separate surfaces or individual definitions of hardening and softening. This helps avoid the situations involving only one mechanism (either damage or plasticity) in models using two separate criteria for damage and plasticity.

To begin this research a generic initial yield surface from the literature was chosen to allow calibration of initial yield to rock data. The function suggested by Bigoni and Piccolroaz (2004) (the BP model) was selected. This initial yield function provided good calibration parameters that could fit a wide range of engineering materials. Figure 4-1, shows the shape of the initial yield surface adopted for this study. Equations.4-2 and 4-3 describe the yield surface, outlined by Bigoni and Piccolroaz (2004), in terms of stress components p, q and Lode angle, θ. The non-negative material parameters describe the shape of the initial yield surface, where M controls the pressure sensitivity, p_c and c are the yield strengths under isotropic compression and tension respectively and parameters α, m define the shape of the meridian section (Bigoni and Piccolroaz 2004).

$$y_{BP} = f(p) + \frac{q}{g(\theta)} \tag{4-2}$$

where:

$$f(p) = \begin{cases} -Mp_c\sqrt{(\Phi - \Phi^m)[2(1-\alpha)\Phi + \alpha]} & \text{if } \Phi \in [0,1] \\ \infty & \text{if } \Phi \notin [0,1] \end{cases} \tag{4-3}$$

$$g(\theta) = 1 \text{ (deviatoric section omitted in this formulation)}$$

with:

$$\Phi = \frac{p + c}{p_c + c}$$

The non-negative material parameters were restricted to the following ranges (Bigoni and Piccolroaz 2004):

$$M > 0, \qquad p_c > 0, \qquad c \geq 0, \qquad 0 < \alpha < 2, \qquad m > 1$$

Using this function as an initial yield, the unified yield-failure criterion was developed to include the effects of stiffness reduction (damage) along with irreversible, plastic deformations. The resulting derivation comprises of a single surface with a single, simple damage evolution law which can describe the yield and failure behaviours of hard rock (Wong 1982; Fredrich and Wong 1986; Martin and Chandler 1994; Oda *et al.* 2002).

The ultimate goal of this function was to model plasticity and damage by evolving an initial yield function to the ultimate residual failure surface observed during rock testing, such as that shown in Figure 4-1. The justification for the implementation of such a yield-failure surface was as the material becomes increasingly damaged, tending to its ultimate limit (D=1) the failure behaviour becomes close to purely frictional and can be described by a linear failure criterion. This is observed in triaxial testing, that throughout the failure process of an intact rock, damage due to microcracking accumulates until only the load to maintain frictional sliding remains (Chen *et al.* 2015). It is also important to note that when modelling a material, cohesion is present even for large values of strain. Therefore, by gradually evolving the yield surface closer to the final failure line with increasing damage, the model can phenomenologically represent the effects of crack propagation and coalescence on the macroscopic behaviour. To acquire the desired yield to failure evolution behaviour, a scalar damage variable was introduced to transform the initial yield function ($D = 0$) outlined in Equations 4-2 and 4-3 to a purely frictional failure slope ($D = 1$) given by:

$$y(p, q, D = 1) = q - Mp \tag{4-4}$$

It can be seen that the function for the frictional failure surface will yield a straight line with slope M in triaxial stress space when $D = 1$. This form of failure is in fact the Drucker-Prager failure criterion with zero tensile strength and is a widely used function due to its simplicity. A non-linear failure criterion such as Hoek-Brown (Hoek *et al.* 2002) could also be used if experimental residuals do not follow a linear trend over large confining pressure ranges. The failure slope in this case can be calibrated to the residual stress data obtained from triaxial tests presented in detail in Section 4.2.2. The transformation of the unified yield-failure surface over the domain, $0 \leq D \leq 1$, requires identification of the correct involvement of damage into the initial yield formulation. As such, the meridional component of the yield-failure function must reduce the initial yield to the final surface when $D = 1$.

Another fundamental consideration for the failure process of a rock is when damage increases, the ability for the material to hold tensile stress will decrease. Therefore, there must be zero tensile strength when $D = 1$. This is due to the fact that when the failure plane completely bisects the material the resistance to tensile load is completely lost. Therefore, Equation 4-5 is necessary in the formulation of the yield-failure criterion and replaces Φ from the BP model.

$$\omega = \frac{p+(1-D)c}{p_c+(1-D)c} \tag{4-5}$$

Furthermore, with correct substitution of the damage variable in the meridional component, the formulation of the unified yield-failure function for this study takes the form of Equation 4-6.

$$y(p,q,D) = q - Mp_c\sqrt{[\omega - (1-\mathrm{D})\omega^m]\left[\left(1-\frac{D}{2}\right)2(1-(1-D)\alpha)\omega + (1-D)\alpha\right]} \tag{4-6}$$

The proposed unified yield-failure function provides a range of shapes of the loading surface utilising the parameters built into the initial yield function. It also describes the full evolution of the surface, which in principle can fit a wide range of rock failure data for various levels of damage and loading/unloading cases. In particular, the entire behaviour of the material, including hardening/softening under low and high confining pressures and the transition zone, is bounded by the initial yield and the final failure surfaces. The evolution of initial yield to final failure is also encapsulated in this evolving function without having to define hardening and softening rules separately. This enables one to directly relate the function to experimentally observed behaviour (see Section 4.4).

Furthermore, Figure 4-1 (with generic values for calibration parameters) shows the evolution zones of the yield function. Zone A describes the brittle failure mechanism at low confinement. As can be seen, once the stress state hits the initial yield, the evolution from yield to failure implicitly induces a reduction of shear stress, which mimics the material softening under low confinement. The evolution from yield to failure in Zone C gives a purely hardening material behaviour at high confinements, as in this zone the yield surface is expanding towards the hydrostatic compression axis. The transition Zone, B, displays the brittle-ductile transitional behaviour where slight hardening precedes softening. Examples of this brittle-ductile transition observed in rocks is given in works by Unteregger *et al.* (2015), Zhang *et al.* (2011), Paterson and Wong (2005) and Cristescu and Gioda (1994). A full parametric study of the unified yield-failure surface is given in the following section. Unlike several existing coupled damage-plasticity models in the literature, this evolution of the shape of the yield surface automatically contains the overall softening/hardening behaviour of the material under a wide range of confining pressures. In addition, the function is flexible enough to allow small modifications to better describe any experimentally observed small scale behaviours (discussed in Section 4.4).

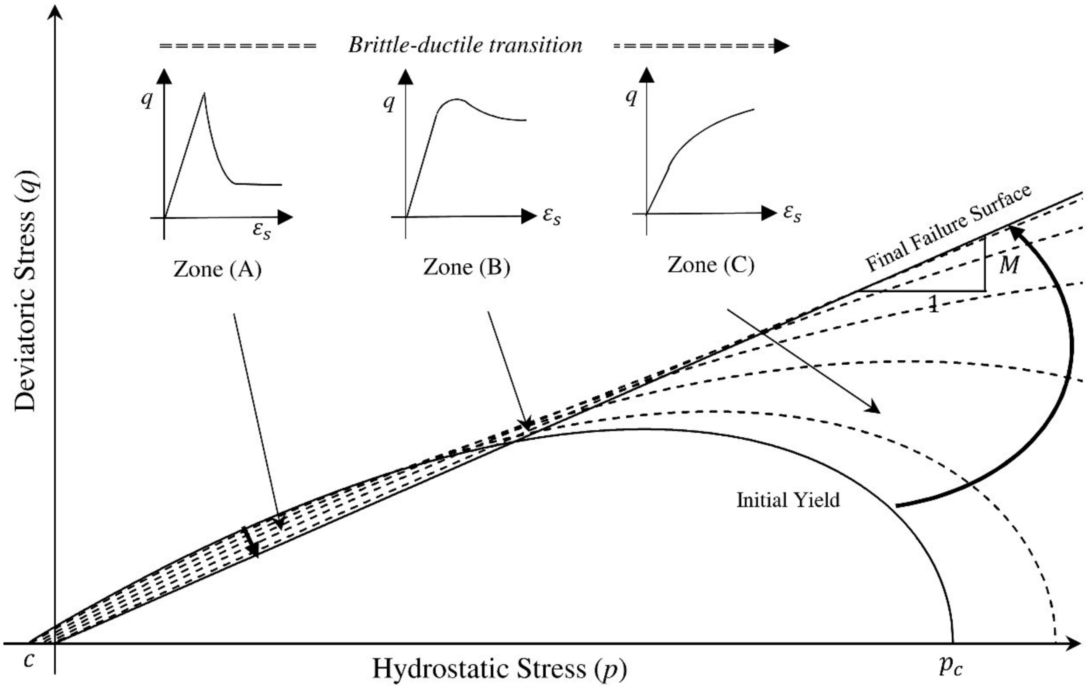

Figure 4-1: Evolving yield-failure surface concept sketch of the meridian section (bold arrows show the evolution direction for hardening and softening)

4.2.1 Parametric study

This section presents the parametric study of the unified yield-failure function. This was conducted to investigate the behaviour of surface evolution with damage for each model parameter. The initial yield variation with each of the curve fitting parameters was carried out by Bigoni and Piccolroaz (2004) and therefore is not included in this paper. It can be seen from their study that the initial yield function is very versatile and can be fit to any suite of hard rock compressive tests in p-q space (Bigoni and Piccolroaz 2004). To identify the capabilities of the derived unified yield-failure function, a parametric study on the effects of parameters on the unified yield-failure surface was also carried out (Figure 4-2).

As can be seen in Figure 4-2, the proposed unified yield-failure function provides a range of shapes of the loading surface. It also describes the full evolution of the surface, which in principle can fit a wide range of rock failure data. This then provides a firm basis for further development of damage evolution and constitutive modelling techniques for hard rock in the following sections.

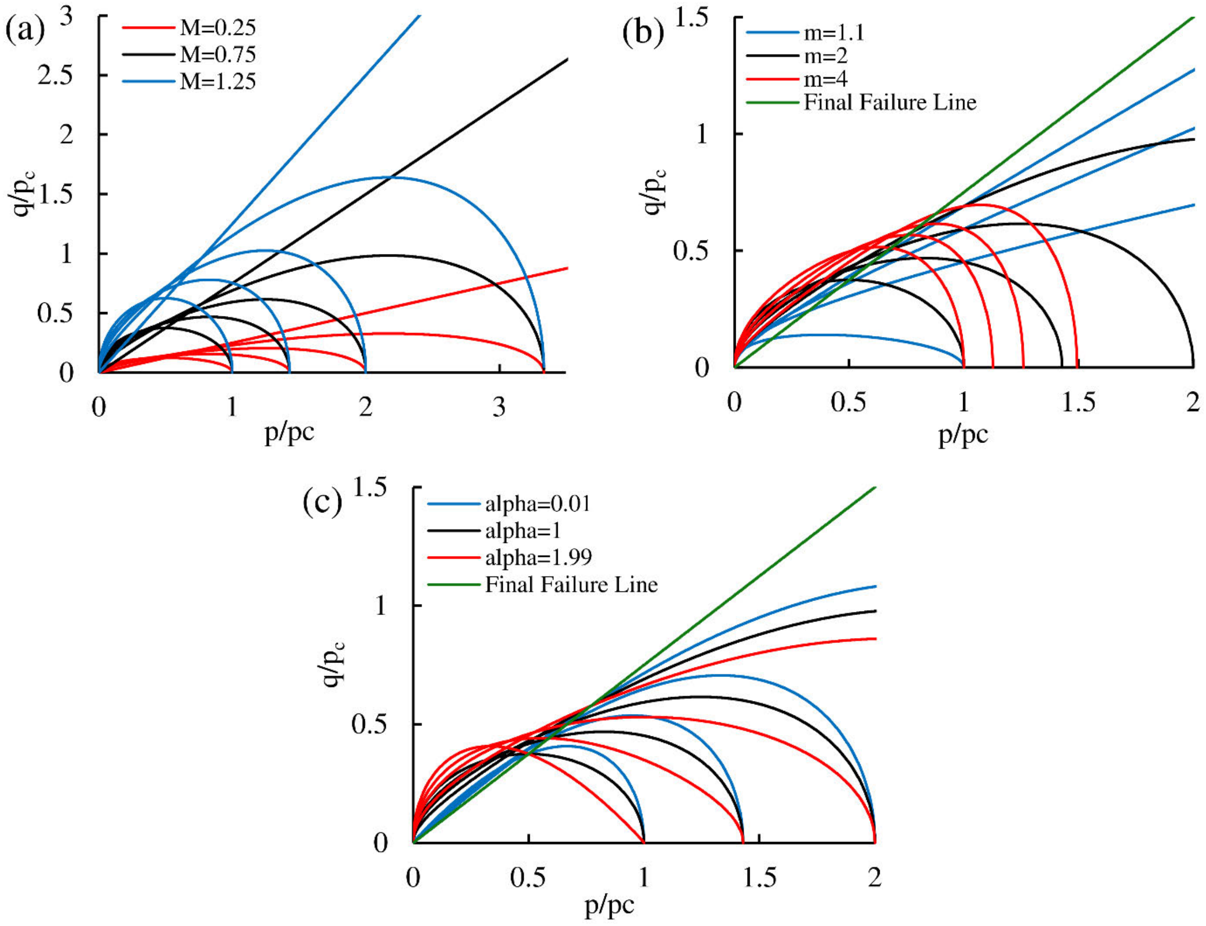

Figure 4-2: Variation of yield surface with increasing damage evolution with respect to (a) M, (b) m and (c) α (Bruning *et al.* 2016)

4.2.2 Unified yield-failure surface calibration

The formulation of the unified yield-failure surface in the previous sections allows modelling of rock behaviour over a wide range of confining pressures. The function also has simple scalar parameters to allow for flexible calibration of initial yield and final failure to experimental data. The first step in calibrating the yield-failure function is to determine the strengths of the rock type under isotropic compression, p_c and tension, c. For hard rock, tensile strengths are relatively low therefore, it is possible to indirectly determine the value for c from the interception of the calibrated initial yield with the hydrostatic axis and a uniaxial tension test. Alternatively the interception of the yield with the vertical axis can also be determined from experiment and used for the calibration. The method used to evaluate c from a uniaxial tension test was the generalised reduced gradient (GRG) non-linear algorithm to minimise the error between calibrated values and the experimental data (Lasdon *et al.* 1974).

The next step in the calibration of the yield-failure surface is to determine the final frictional failure slope defined by M. To do this, the residual stress data from conventional triaxial tests can be plotted in p-q space and a slope can be selected to fit again utilising the GRG nonlinear method. Figure 4-3 shows the calibration of the frictional failure surface to residual stress data from Arzúa and Alejano (2013). If residual data is not known or accessible for the rock type, the final frictional failure slope can be modelled with a frictional failure model such as Mohr-Coulomb or linear Drucker-Prager using the friction angle of the material.

Once the frictional failure slope is determined the other parameters p_c, α and m are adjusted using the GRG method to reduce the cumulative error of the yield surface to each data point. Initially, a value of p_c is selected to provide the appropriate level of slope to the yield surface and initial guesses for α and m are calculated. This initial calibration is shown in Figure 4-3.

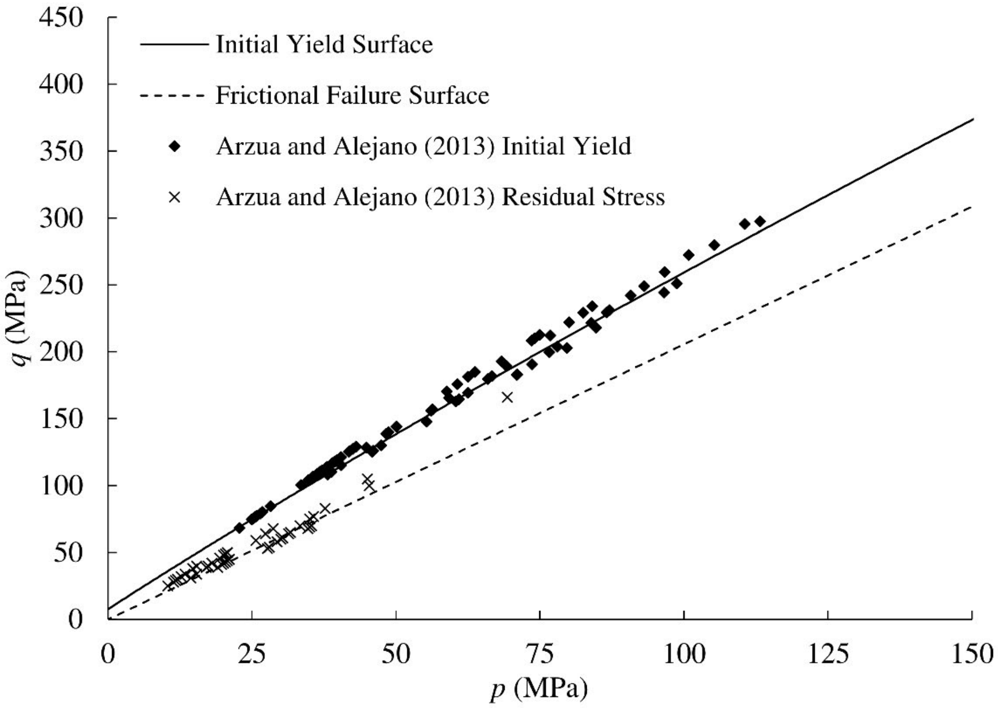

Figure 4-3: Initial yield and final frictional failure surface for three granites from (Arzúa and Alejano 2013)

The precise calculation of p_c can prove to be difficult due to the large pressures required for isotropic compression of hard rock. These pressures cannot be tested in a laboratory and as such an alternative strategy is proposed. If no high pressure triaxial data are available for the subject rock, data for similar mineralogy or rock type must be used to provide an estimate of p_c. For example, the data obtained from Arzúa and Alejano (2013) for three different types of granitic rock. However, to the best of our knowledge, there exist no high confinement data for those specific rocks in the literature. Therefore, by incorporating the high confinement triaxial data for Westerly granite (Summers and Byerlee 1977) which is another granite, a range of p_c can be estimated when the yield surface is fit to all the experimental data using the initial estimates of all other parameters. This is shown in Figure 4-4 and this range can be input as a constant into the GRG algorithm to allow calibration of other parameters in the model. It is also useful to highlight in Figure 4-4, that the precise value of this parameter does not significantly affect the shape of the yield surface over the confining pressures relevant to engineering applications. Therefore, it is evident from this procedure that the estimation of p_c is only useful in defining an initial value for the parameter and should be refined to provide the best description of the rock data being focussed on. In other words, the shape of the yield surface over the tested and focus confinement range as well as the identified brittle-ductile transition should be optimised.

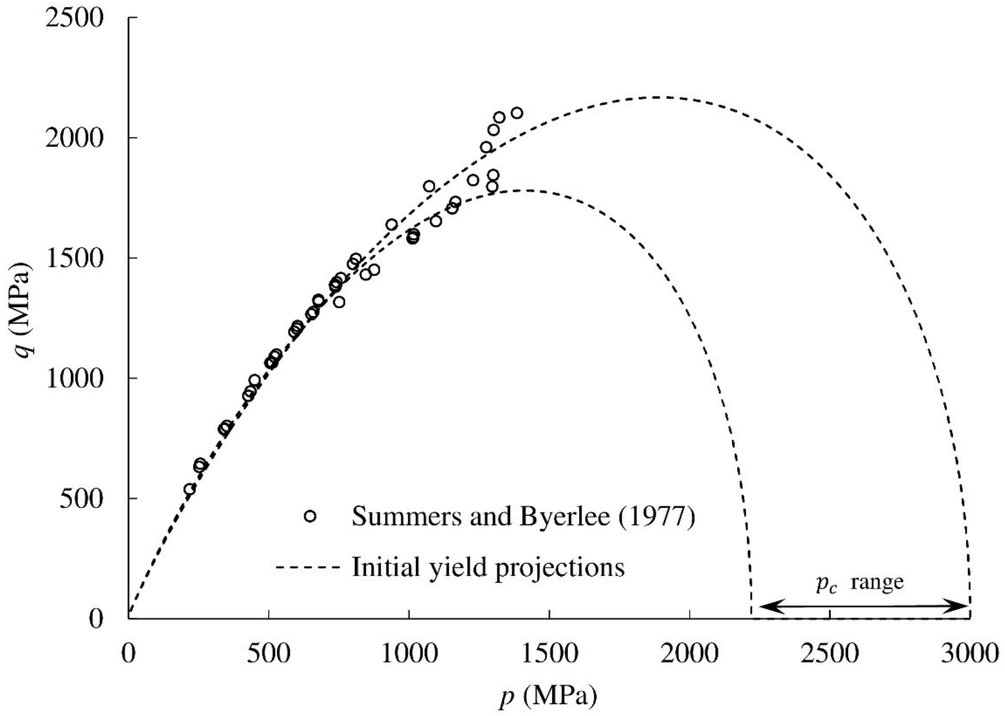

Figure 4-4: Isotropic compressive strength range for Westerly granite sourced from Summers and Byerlee (1977)

Finally, once appropriate iteration of the parameters is completed, the final calibrated function is derived, shown in Figure 4-5 for the granite data mentioned above.

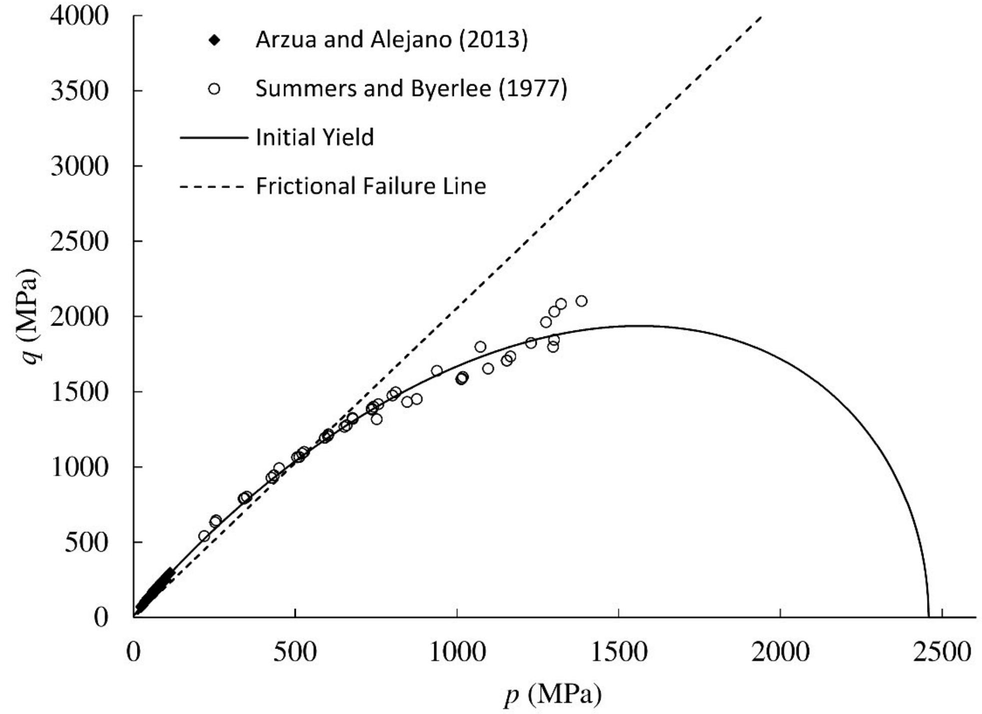

Figure 4-5: Final yield-failure calibration for granite data

This process highlights the flexibility of the proposed criterion to fit hard rock experimental data and hence describe brittle and ductile behaviour. Full calibration applied to the data (Arzúa and Alejano 2013) revealed the following parameters for the unified yield-failure surface: $M = 2.05$, $m = 1.44$, $\alpha = 0.00095$, $p_c = 2458$ MPa and $c = 2.08$ MPa.

4.2.3 Plastic-damage potential

It has been observed in many studies that the dilation of a rock specimen cannot be accurately predicted by an associated flow rule in a plasticity or damage-plasticity framework (Alejano and Alonso 2005; Paterson and Wong 2005; Walton and Diederichs 2015b; Walton and Diederichs 2015a). Therefore, an appropriate plastic-damage potential function must be selected to allow for accurate modelling of the material. The two main considerations in determining the plastic-damage potential is to capture the effects of dilation angle as well as the critical state. Dilation of a rock or rock mass has been described in many models by the use of a dilation angle or parameter to control the level of dilation throughout the mechanical behaviour of the material (Walton and Diederichs 2015b; Walton and Diederichs 2015a). It has also been determined from adaptions of critical state soil mechanics that when a granular material has completely failed, in this case reached the critical state or residual stress, it displays no increased inelastic volumetric strain (Schofield and Wroth 1968; Shah 1997; Nguyen and Einav 2009). Therefore, to account for these constraints phenomenologically, γ is used to control the dilations of the material and the damage parameter, D is used to degrade the effect of inelastic volumetric behaviour towards the critical state/frictional failure curve. The plastic potential, using the considerations above, takes the form similar to the yield-failure function (Equation 4-6) and is given in Equation 4-7 below.

$$g(p,q,D) = \gamma q - (1-D)Mp_c\sqrt{[\omega - (1-\mathrm{D})\omega^m]\left[\left(1-\frac{D}{2}\right)2\big(1-(1-D)\alpha\big)\omega + (1-D)\alpha\right]} \quad (4\text{-}7)$$

Therefore, when $\gamma < 1$ the volumetric strain component is increased and when $\gamma > 1$ it is decreased. As such, the non-associated flow rules for shear and volumetric inelastic strains become:

$$\Delta\varepsilon_s^p = \Delta\lambda\frac{\partial g}{\partial q} = \gamma\Delta\lambda\frac{\partial y}{\partial q} \quad \text{and} \quad \Delta\varepsilon_v^p = \Delta\lambda\frac{\partial g}{\partial p} = (1-D)\Delta\lambda\frac{\partial y}{\partial p} \qquad (4\text{-}8)$$

4.2.4 Generic damage evolution law

Hardening and softening of hard rock are mainly consequences of the closure and reopening of microcracks, and frictional sliding respectively at the micro scale. Other mechanisms do exist but are omitted from this study as the above were considered more dominant in hard rock behaviour. Given the existence of flaws in ‘intact’ rock, frictional sliding and microcracking can take place at the same time during compressive loading. At the macro scale, this leads to the combined effects of strength and stiffness reduction. As these effects are represented by plastic strain and damage in the coupled approach, a dependence of one on another is needed in the model to characterise the coupling effects. This is a common and widely accepted assumption in the modelling of geomaterials (Salari *et al.* 2004; Grassl and Jirasek 2006; Jason *et al.* 2006; Chen *et al.* 2010; Unteregger *et al.* 2015). It will later be shown that this assumption can work well and lead to predictions that compare favourably with experimental data. The function selected to capture this behaviour utilises a diminishing exponential relationship dependent on increasing accumulated plastic strain given by:

$$\Delta\epsilon_p = \sqrt{\frac{2}{9}\left(A\Delta\varepsilon_v^p\right)^2 + \left(B\Delta\varepsilon_s^p\right)^2} \tag{4-9}$$

where A and B are material constants. Therefore, the damage variable evolution for a material was represented by:

$$D = 1 - e^{-\epsilon_p} \tag{4-10}$$

This relationship can be calibrated using low confinement triaxial data as there is often no significant pre-peak hardening of hard rock observed during such tests. As such to calibrate the numerical model, deriving a values of A and B, the stress-strain response in both the axial and lateral directions must be matched to experimental data.

Complete calibration of the yield-failure evolution is accomplished through iteration of values for the damage evolution constants and dilation parameter γ simultaneously. Values are trialled until the dilation and stress-strain behaviours of the hard rock are matched for zero or low confining experimental rock data.

4.3 Numerical implementation

The model implemented in this study only requires five equations to describe hard rock behaviour:

Stress-strain-damage relationship:

$$\sigma_{ij} = (1 - D)C_{ijkl}(\varepsilon_{kl} - \varepsilon_{kl}^{p}) \qquad (4\text{-}1)$$

Yield-failure criterion:

$$y(p, q, D) = q - Mp_{c}\sqrt{[\omega - (1 - \mathrm{D})\omega^{m}]\left[\left(1 - \frac{D}{2}\right)2(1 - (1 - D)\alpha)\omega + (1 - D)\alpha\right]} \qquad (4\text{-}6)$$

Plastic potential and flow rules:

$$g(p, q, D) = \gamma q - (1 - D)Mp_{c}\sqrt{[\omega - (1 - \mathrm{D})\omega^{m}]\left[\left(1 - \frac{D}{2}\right)2(1 - (1 - D)\alpha)\omega + (1 - D)\alpha\right]} \qquad (4\text{-}7)$$

$$\Delta\varepsilon_{s}^{p} = \Delta\lambda\frac{\partial g}{\partial q} = \gamma\Delta\lambda\frac{\partial y}{\partial q} \quad \text{and} \quad \Delta\varepsilon_{v}^{p} = \Delta\lambda\frac{\partial g}{\partial p} = (1 - D)\Delta\lambda\frac{\partial y}{\partial p} \qquad (4\text{-}8)$$

Damage evolution law:

$$D = 1 - e^{-\epsilon_{p}} \qquad (4\text{-}10)$$

As such, a manageable ten (twelve including pre-peak hardening explained in Section 1.3.2.2) parameters including Young’s modulus and Poisson’s ratio are required to calibrate the model. In addition the calibration of the material parameters is straightforward and only requires conventional triaxial test data. As can be seen, the model description is much simpler than many existing ones in the literature, thanks to the implicit hardening/softening rules already embedded in the evolution of the unified yield-failure criterion. The implementation of the model in this case just follows standard algorithms in plasticity theory (e.g. Crisfield (2000), Chapter 6) with an extra evolution rule for damage. The governing equations for the constitutive driver are given in the following sections along with the pseudo-code for a material point behaviour.

4.3.1 Stress return algorithm

To determine the stress at each strain increment in the model, the stress is expressed in terms of the relationship:

$$\sigma_{ij}{}^{k+1} = \sigma_{ij}{}^{k} + \Delta\sigma_{ij}{}^{k+1} \tag{4-11}$$

where σ_{ij}^{k+1} is the stress state in the current strain increment or step, σ_{ij}^{k} is the previous stress state and $\Delta\sigma_{ij}^{k+1}$ is the incremental stress change from the previous to the current step given by:

$$\Delta\sigma_{ij}{}^{k+1} = \Delta\sigma_{ij}{}^{trial} - (1 - D^k)C_{ijkl}\varepsilon_{kl}^{p} - \frac{\sigma_{ij}{}^{trial}}{(1-D^k)}\Delta D \tag{4-12}$$

where D^k is the damage state from the previous strain increment, ε_{kl}^{k} is the previous strain state, and the trial stress change is evaluated elastically using the equations:

$$\Delta\sigma_{ij}{}^{trial} = (1 - D^k)C_{ijkl}\Delta\varepsilon_{kl}{}^{k} \tag{4-13}$$

The trial stress state is therefore:

$$\sigma_{ij}{}^{trial} = \sigma_{ij}{}^{k} + \Delta\sigma_{ij}{}^{trial} \tag{4-14}$$

Using this trial stress, the yield function, y can be evaluated to determine if the material is behaving elastically or is yielding. Therefore, if $y \leq 0$ the elastic solution is accepted, however if $y > 0$ the function undergoes a semi-implicit stress return algorithm to adjust for damage-plasticity.

This semi-implicit stress return algorithm provides a stable and simple method to evaluate the stress increment when a model is being controlled by strain. The complete theory and implementation of the algorithm is given in the publication by Crisfield (2000) and is taken as a simplified form of the backward Euler stress return. Once it has been deemed that the yield is greater than zero, the model employs a first order Taylor series expansion of the yield function:

$$y^{\text{new}} = y^{\text{trial}} + \Delta\sigma_{ij}{}^{corrector} \left.\frac{\partial y}{\partial \sigma_{ij}}\right|^{\text{trial}} + \Delta D \left.\frac{\partial y}{\partial D}\right|^{\text{trial}} \tag{4-15}$$

where y^{new} is the updated value of yield, $\left.\frac{\partial y}{\partial \sigma_{ij}}\right|^{\text{trial}}$ and $\left.\frac{\partial y}{\partial D}\right|^{\text{trial}}$ are the derivatives of the yield function at the trial stress state. Given the explicit form of the unified yield-failure criterion (Equation 4-6), the derivatives of the function with respect to stress and damage are derived.

For the derivative with respect to damage it is useful to convert Equation 4-6 into the form:

$$y(p, q, D) = q - H \tag{4-16}$$

where:

$$H = Mp_c\sqrt{[\omega - (1 - \mathrm{D})\omega^m]\left[\left(1 - \frac{D}{2}\right)2(1 - (1 - D)\alpha)\omega + (1 - D)\alpha\right]} \tag{4-17}$$

Therefore,

$$\frac{\partial y}{\partial \sigma_{ij}} = \frac{\partial y}{\partial \omega}\frac{\partial \omega}{\partial p}\frac{\partial p}{\partial \sigma_{ij}} + \frac{\partial y}{\partial q}\frac{\partial q}{\partial J_2}\frac{\partial J_2}{\partial \sigma_{ij}} \tag{4-18}$$

$$\frac{\partial y}{\partial D} = \frac{\partial y}{\partial H}\left(\frac{\partial H}{\partial D} + \frac{\partial H}{\partial \omega}\frac{\partial \omega}{\partial D} + \frac{\partial H}{\partial M}\frac{\partial M}{\partial D}\right) \tag{4-19}$$

Where:

$$\frac{\partial y}{\partial \omega}=\frac{\partial y}{\partial H}\frac{\partial H}{\partial \omega}=-Mp_c\frac{(1-(1-D)m\omega^{m-1})\left(\left(1-\frac{D}{2}\right)2(1-(1-D)\alpha)\omega+(1-D)\alpha\right)+(\omega-(1-\mathrm{D})\omega^{m})\left(2\left(1-\frac{D}{2}\right)(1-\alpha(1-D))\right)}{2\left(\sqrt{[\omega-(1-\mathrm{D})\omega^{m}]\left[\left(1-\frac{D}{2}\right)2(1-(1-D)\alpha)\omega+(1-D)\alpha\right]}\right)}$$

(4-20)

$$\frac{\partial \omega}{\partial p}=\frac{1}{c(1-D)+p_c} \tag{4-21}$$

$$\frac{\partial y}{\partial q}=1 \tag{4-22}$$

$$\frac{\partial y}{\partial H}\frac{\partial H}{\partial D}=-Mp_c\frac{\omega^{m}\left(\left(1-\frac{D}{2}\right)2(1-(1-D)\alpha)\omega+(1-D)\alpha\right)+(\omega-(1-\mathrm{D})\omega^{m})\left(2\alpha\left(1-\frac{D}{2}\right)\omega-\omega(1-\alpha(1-D))-\alpha\right)}{2\left(\sqrt{[\omega-(1-\mathrm{D})\omega^{m}]\left[\left(1-\frac{D}{2}\right)2(1-(1-D)\alpha)\omega+(1-D)\alpha\right]}\right)}$$

(4-23)

$$\frac{\partial \omega}{\partial D}=\frac{c(p^{trial}-p_c)}{(c(D-1)-p_c)^2} \tag{4-24}$$

Given in detail in the following section, the derivatives for the pre-peak hardening function with respect to damage are given by:

$$\frac{\partial y}{\partial H}\frac{\partial H}{\partial M}=-p_c\sqrt{[\omega-(1-\mathrm{D})\omega^{m}]\left[\left(1-\frac{D}{2}\right)2(1-(1-D)\alpha)\omega+(1-D)\alpha\right]}$$

(4-25)

$$\frac{\partial M}{\partial D}=-a(1-D)^{b-1}(bD+D-1) \tag{4-26}$$

Plastic-damage potential:

$$\frac{\partial g}{\partial \sigma_{ij}}=\frac{\partial g}{\partial \omega}\frac{\partial \omega}{\partial p}\frac{\partial p}{\partial \sigma_{ij}}+\frac{\partial g}{\partial q}\frac{\partial q}{\partial J_2}\frac{\partial J_2}{\partial \sigma_{ij}} \tag{4-27}$$

Therefore, from the trial (predictor) state, the corrector stress is

$$\Delta{\sigma_{ij}}^{corrector}=-(1-D^k)C_{ijkl}\Delta\varepsilon_{kl}^{p}-\frac{{\sigma_{ij}}^{trial}}{(1-D^k)}\Delta D \tag{4-28}$$

where the flow rule is defined as:

$$\Delta\varepsilon_{ij}^{p} = \Delta\lambda \frac{\partial g}{\partial\sigma_{ij}} \tag{4-29}$$

The expression for the full derivative of the damage variable, ΔD is given by:

$$\Delta D = \left(-e^{-\epsilon_p{}^{k}}\right) \Delta\epsilon_p \tag{4-30}$$

where $\epsilon_p{}^{k}$ is the accumulated plastic strain from the previous step. Using Equation 4-9 and substitution of the flow rule yields:

$$\Delta D = \Delta\lambda \left(-e^{-\epsilon_p^k}\right) \sqrt{\frac{2}{9}\left(A\frac{\partial g}{\partial p}\right)^2 + \left(B\frac{\partial g}{\partial q}\right)^2} \tag{4-31}$$

Through substitution into Equation 4-15 and setting $y^{new} = 0$, the function for the plastic-damage multiplier can be expressed as:

$$\Delta\lambda = \frac{y^{\mathrm{trial}}}{\left(\frac{\partial y}{\partial\sigma_{ij}}(1-D^k)C_{ijkl}\frac{\partial g}{\partial\sigma_{kl}}\right)+\left(\frac{\partial y}{\partial\sigma_{ij}}\frac{\sigma_{ij}{}^{trial}}{(1-D^k)}\left(-e^{-\epsilon_p{}^{k}}\right)\sqrt{\frac{2}{9}\left(A\frac{\partial g}{\partial p}\right)^2+\left(B\frac{\partial g}{\partial q}\right)^2}\right)-\left(\frac{\partial y}{\partial D}\left(-e^{-\epsilon_p{}^{k}}\right)\sqrt{\frac{2}{9}\left(A\frac{\partial g}{\partial p}\right)^2+\left(B\frac{\partial g}{\partial q}\right)^2}\right)} \tag{4-32}$$

Once a value for the scalar damage-plastic multiplier, $\Delta\lambda$ has been obtained for the increment, the flow rule is evaluated and the new stress increment is derived using an expanded form of Equation 4-12:

$$\Delta\sigma_{ij}{}^{k+1} = \Delta\sigma_{ij}{}^{trial} - \frac{\partial g}{\partial\sigma_{ij}}(1-D^k)C_{ijkl}\Delta\lambda - \frac{\sigma_{ij}{}^{trial}}{(1-D^k)}\Delta D \tag{4-33}$$

Finally the stress state can be updated for the strain increment using Equation 4-11. Due to the first order nature of the Taylor series expansion and the finite strain increment $\Delta\varepsilon_{kl}{}^{k}$, the new stress state is usually not on the updated yield surface and this error can be minimised to some tolerance by the implementation of sub-incrementation in the numerical scheme (Crisfield 2000).

To enable the numerical modelling of strain control triaxial compressive tests of hard rocks, a constitutive driver code was constructed using the FORTRAN95 programming language and given on the next page.

Start of Constitutive Driver

```
1. Input elasticity constants and unified yield-failure function parameters.
2. Set initial strain, stress, damage and accumulated plastic strain to zero.
3. Evaluate initial 'intact' rock stiffness tensor, $C_{ijkl}$ and set desired displacement control, $\Delta\varepsilon_{kl}$.
DO WHILE sets up the simulation duration.
    4. Save the previous stress ${\sigma_{ij}}^k$, damage, $D^k$ and accumulated plastic strain, ${\epsilon_p}^k$.
    5. Calculate the secant stiffness, $(1-D)C_{ijkl}$.
    6. Determine trial stress state (Equation 4-13).
    7. Evaluate yield condition (Equation 4-6).
    IF $(y \leq 0)$ THEN
        8. Adopt elastic solution and GOTO step 13.
    ELSE
        9. Derive the derivatives of yield and plastic-damage functions.
        10. Find plastic-damage multiplier (Equation 4-32).
        11. Update stress, damage and plastic strain.
    ENDIF
    12. Re-calculate yield and p and q values and adopt solution if it satisfies required tolerance $\left(\frac{|y^{\mathrm{new}}|}{q} < 10^{-3}\right)$, if not met, repeat steps 5 to 12 with updated stress state.
    13. WRITE stresses, strains and damage data to file.
ENDDO
```

4.3.2 Model validation

In this section, the model proposed in this study was validated using data for the mechanical behaviour of granite under compression by Arzúa and Alejano (2013), Chen *et al.* (2015) and marble under compression by Zhang *et al.* (2011) and Unteregger *et al.* (2015). To enable the model to simulate the experimental data, a full yield-failure calibration and damage variable identification were undertaken for each set of results. The first validation carried out was for the Amarelo País granite reported in the work by Arzúa and Alejano (2013). Full calibration of the unified yield-failure surface for this rock type was outlined in Section 4.2.2 and therefore will be omitted from the following validation discussion.

It is noted here that the demonstration in this section is for a material point behaviour and hence issues related to localised failure and size effects are not addressed. In addition, the experimental stress-strain data are associated with the corresponding specimen sizes, especially in the case of softening under low confining pressures. They are used here just for the purpose of demonstrating the capability of the proposed model at the constitutive level, as in principle the analysis of boundary value problems of the experiments must be carried out.

4.3.2.1 Amarelo País Granite (Arzúa and Alejano 2013)

The first data set selected for validation was sourced from a study by Arzúa and Alejano (2013). This particular information was considered due to the completeness of the stress-strain curves and extent of testing conducted by the researchers. It can be seen in the data from the study (Figure 4-7) that the rock behaviour displayed very little hardening under low confinement pressures, therefore, the initial yield surface can be calibrated using peak strength data. This ultimately derived the values for yield surface parameters given in Section 4.2.2. The Young’s modulus and Poisson’s ratio of the rock was also derived from these data. In the case of Young’s modulus however, it was also observed, that the stiffness of the rock was variable over different confinement levels reported in the study. These can be modelled separately, but for the purpose of calibration of this model, an average Young's modulus was assumed, shown as the elastic portion of the curves in Figure 4-7. The values calculated for Young's modulus and Poisson's ratio were 18.42 GPa and 0.27 respectively.

To calibrate the yield-failure and damage evolution of the material for modelling the 4 MPa confinement was selected for comparison purposes. The main reason for choosing the data set is that volumetric strain for 4 MPa confinement was reported (Arzúa and Alejano 2013) at much greater accuracy than for the other values reported in the study. A trial and error procedure was undertaken to calibrate the volumetric strain of the material as seen in Figure 4-6(a) and also the axial stress-strain response, Figure 4-6(b). The calibration yielded the values for the dilation and damage evolution parameters as, $\gamma = 0.95$, $A = 20$ and $B = 50$.

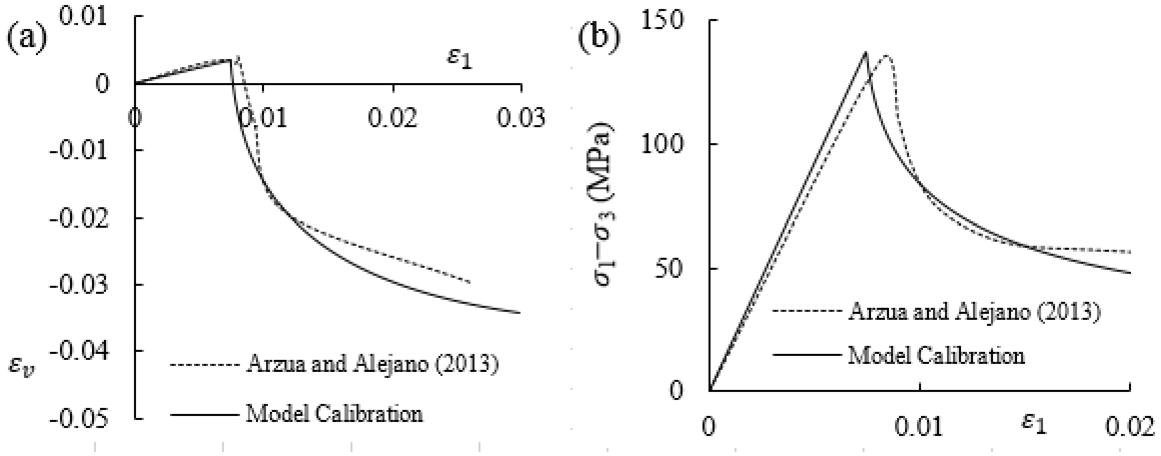

Figure 4-6: Calibration of Amarelo País granite using (a) volumetric strain and (b) axial stress-strain

The parameters calibrated for Amarelo País granite were then used to model all available confining pressures. This was to demonstrate the capability of the proposed model in predicting behaviour under different loading conditions, once calibrated against experimental data for a given loading path. In Figure 4-7 it can be seen that with increasing confinement, the model automatically adjusts the yield-failure evolution to incorporate the effects of decreasing brittleness of the material. It can also be seen that the model behaviour of the 10 MPa confinement test is different from the literature data. This is partly due to the sample showing significantly different trends in elasticity and therefore, being offset from the other tests. This can be expected in the study of hard rocks as each specimen used for testing can contain flaws or mineralogical differences that contributes to anomalous behaviour from the average expected outcome. This can only be dealt with in a model if the entire structure is known and, this is nearly impossible to obtain. Therefore, it can be concluded that the model is able to sufficiently replicate experimental results for hard, brittle rock such as granite.

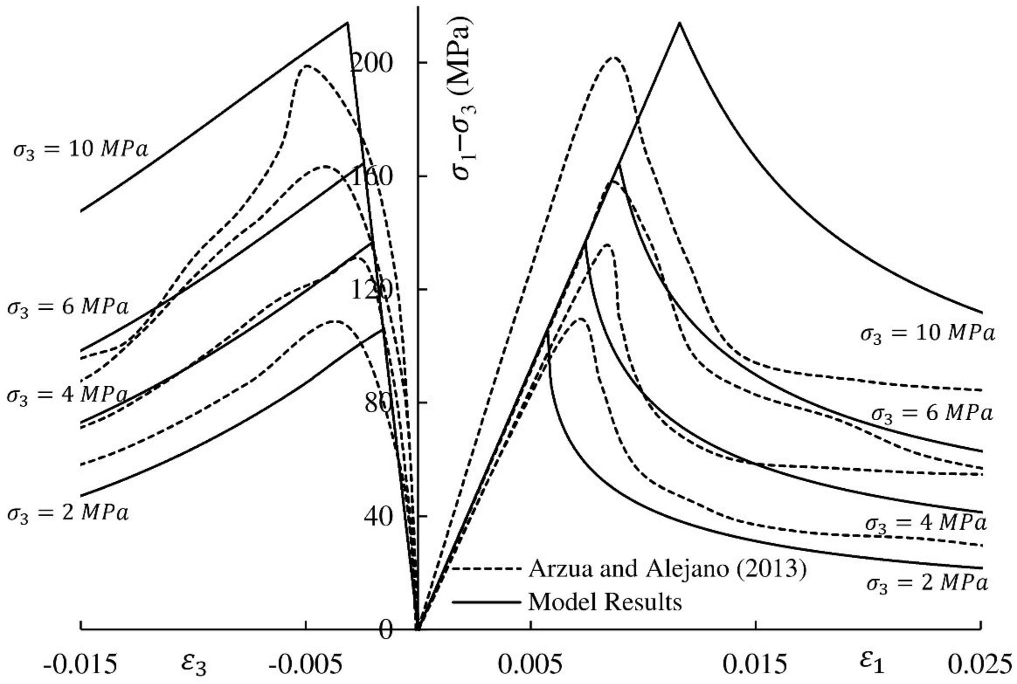

Figure 4-7: Constitutive driver model response for Amarelo País granite

4.3.2.2 Pre-peak hardening of Beishan granite (Chen et al. 2015)

To ensure the new model is capable of replicating a variety of hard rock data, another data set was utilised to validate the results. The second literature sourced rock type was Beishan granite tested by Chen *et al.* (2015). It could be seen from the study (Figure 4-10), that the rock exhibits significant hardening before peak stress for low confining pressures. Therefore, to properly calibrate the model the initial yield surface must be compared to the onset of plastic-damage behaviour, highlighted by the beginning of the pre-peak hardening phase.

Another consideration is the level of damage accumulated in the rock due to hardening until peak stress. It has been proposed by numerous researchers, that even during hardening of rock such as granite, microcracks are formed causing an increase in the damage state (Wong 1982; Fredrich and Wong 1986; Martin and Chandler 1994; Oda *et al.* 2002). Therefore, it is crucial to pair the peak stress of the rock with the accumulated damage value for the rock. This can be done by comparing secant Young's modulus of cyclically loaded specimens, with one cycle being at initial yield and the second being at or near the peak stress. This was calculated using the unloading/reloading curves sourced from the publication and damage at peak stress was found to be approximately 5% ($D = 0.05$), shown in Fig. 8.

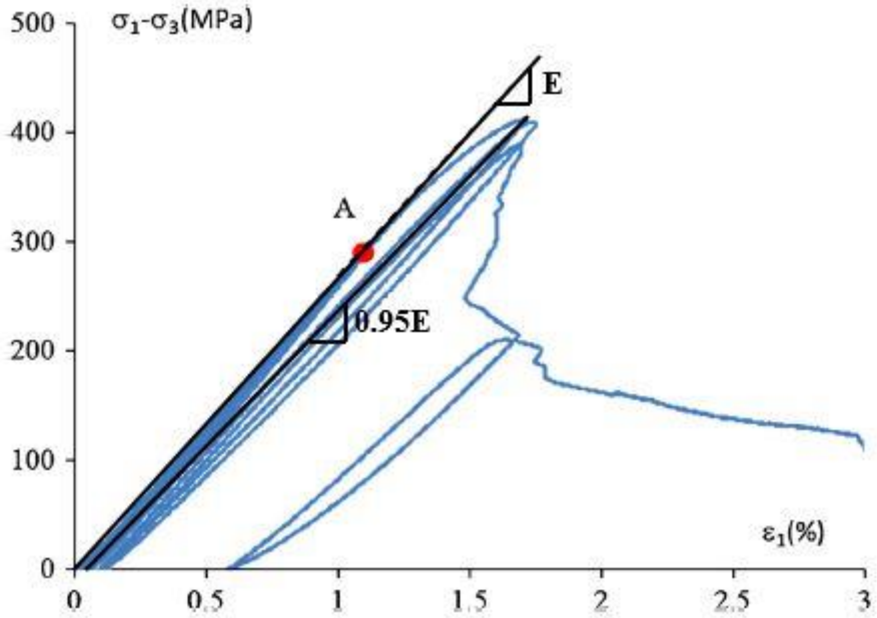

Figure 4-8: Damage determination from unloading/reloading curves (modified from Chen *et al.* (2015))

Considering Figure 4-1 in Section 4.2, the size and positioning of Zone B can be both very small, in terms of confinement range and at high confining pressures, which limits the model's effectiveness for low confinement hardening. It is also very difficult, given the proposed formulation, to position this zone at low confinements while maintaining logical meaning at higher confinements. This leads to the initial function being incapable of capturing small scale hardening at low confinement levels.

Additionally it is pointed out in some studies that hard, brittle rocks show a decrease in cohesion and an increase friction angle during failure with both phenomena acting at different stages in deformation. Therefore a model must have the ability to allow for mobilisation of cohesion and friction angle independently and hence also enable the calibration of each component to experimental data (Martin 1997; Hajiabdolmajid *et al.* 2002). As the data sets used for validation in this research did not reveal anything about the cohesion of the rocks tested, it was initially assumed during modelling that there was a linear decrease with damage during failure, characterised by the decay of the isotropic tensile stress, $(1-D)c$ in Equation 4-5. However, as initial hardening of the materials could be seen, the constant parameter, M in the formulation was replaced with a simple hardening function to allow for increase in the friction angle of the material during deformation. Another consideration in formulating the frictional behaviour was the assumption that hardening of the material at low confining pressures was predominantly due to microcrack closure within the specimen. However, other mechanisms working at the same time, such as crack initiation, are in direct competition with closure causing a gradual ramping down of the hardening effect until only softening mechanisms are present as all cracks aligned correctly have been closed (Batzle *et al.* 1980; Hoek and Martin 2014). Therefore, it is assumed that after stress-strain hardening, the friction angle returns to its initial value and the entire process is accounted for, phenomenologically, by Equation 4-34.

$$M = M_0 + aD(1-D)^b \tag{4-34}$$

The postulated function isotropically hardens the initial slope of the frictional failure surface, M_0 to allow for initial small scale isotropic hardening without changing the characteristics of the yield evolution via kinematic hardening or variations of shape. The parameters a and b control the level of frictional failure slope change and the extent of hardening with damage (skew) respectively, shown in Figure 4-9.

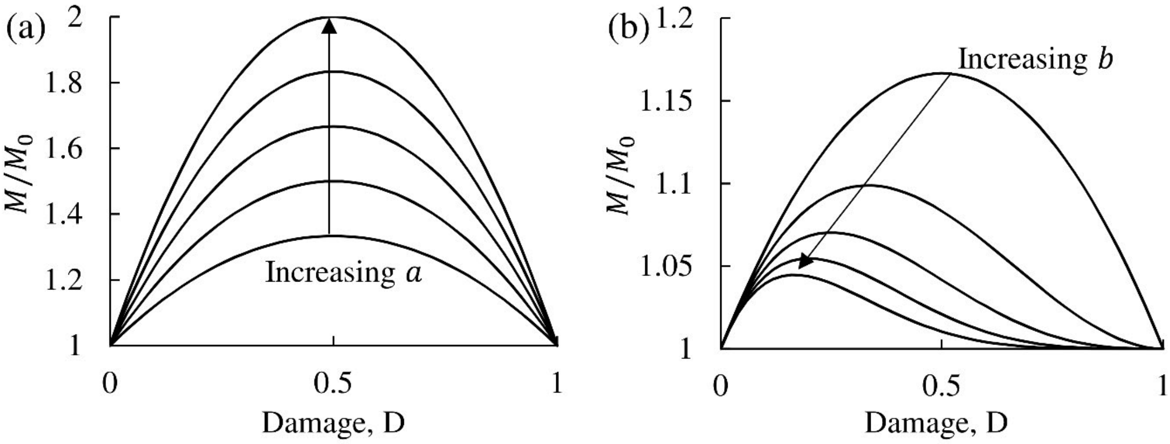

Figure 4-9: Effect of isotropic hardening function by varying (a) parameter a ($b = 1$) and (b) parameter b ($a = 1$)

Therefore, given the new formulation including this hardening function, the unified yield failure surface was calibrated to match the experimental data by Chen *et al.* (2015). The final calibration of the yield-failure function with respect to reported testing on Beishan granite yielded the following values for all parameters; $E = 63.97$ GPa, $\nu = 0.15$, $M_0 = 1.68$, $m = 1.7$, $\alpha = 0.0263$, $p_c = 2400$ MPa, $c = 3.47$ MPa, $\gamma = 0.85$, $A = 90$, $B = 80$, $a = 1.84$, and $b = 5.98$. Figure 4-10 shows the validation procedure including hardening effects and this provided a much better correlation with experimental results. Therefore, it could be concluded that the isotropic hardening function based on phenomenological microcrack interactions was sufficient in describing the hardening of rocks at relatively low confinement levels.

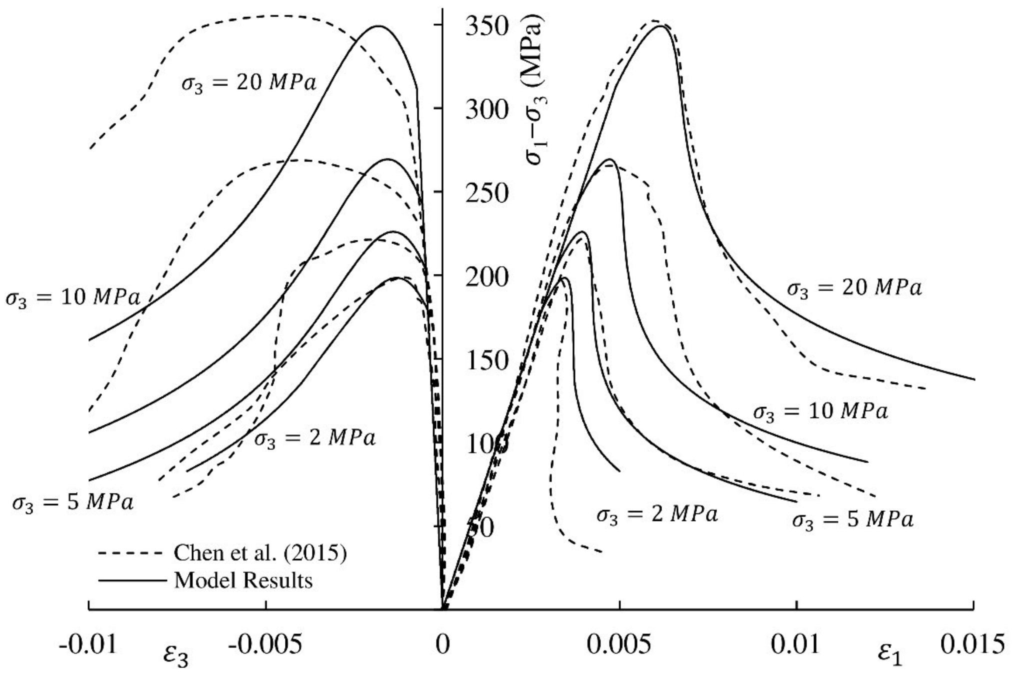

Figure 4-10: Model response with pre-peak hardening

4.3.2.3 Brittle-ductile transition (Zhang et al. 2011)

In the previous sections, the model has been validated for the case of hard brittle rock, specifically granite. However, the formulation proposed in this study is also able to model the transition of a hard, crystalline rock from the brittle regime where confining pressures are low, to the more ductile behaviour of a rock under high confinement. The advantage of this model is that the use of a single unified yield-failure function allows complete modelling of this transition in a continuous and robust manner without the need for separate loading surfaces held together by mathematical coupling procedures. The data set selected for the validation of the brittle-ductile transition capability of the model was from Zhang *et al.* (2011). The rock tested in the study was a marble sourced from the Jinping II hydropower project. Once the calibration procedure was carried out, the values for the variables were derived to be,$E = 43$ GPa, $\nu = 0.19$, $M_0 = 1.726$, $m = 1.57$, $\alpha = 0.255$, $p_c = 427$ MPa, $c = 3$ MPa,$\gamma = 1$, $A = 100$, $B = 300$, $a = 0.5$, and $b = 10$.

The constitutive driver was run for each confining pressure given in the literature and the results are shown in Figure 4-11.

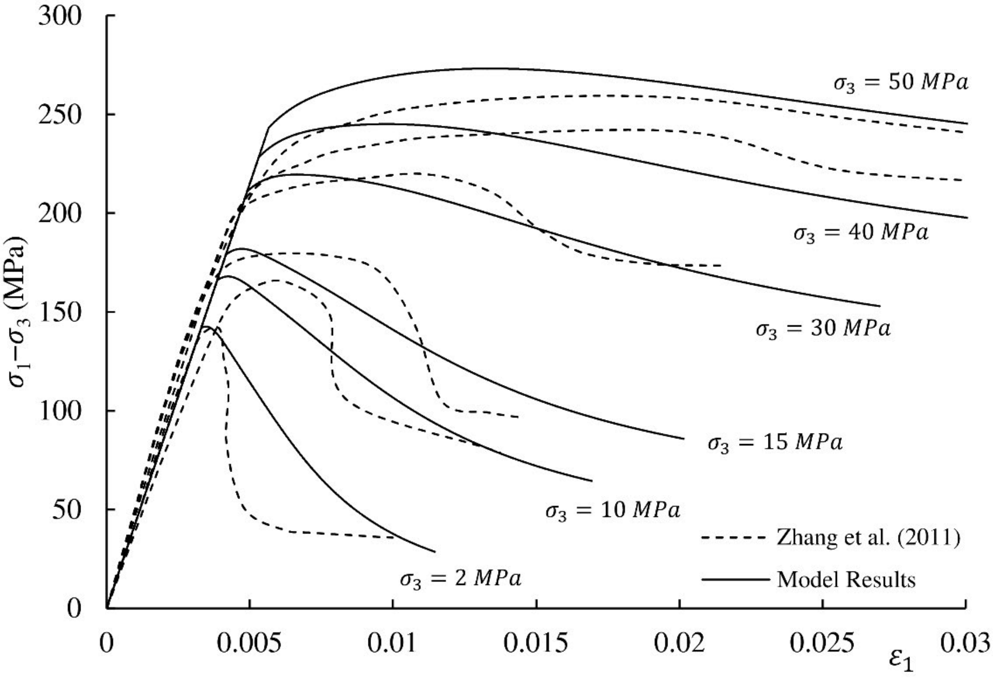

Figure 4-11: Model response for Jinping II marble

As can be seen in Figure 4-11, the model can automatically capture the transition from brittle to ductile behaviour with increasing confinement of the material.

4.3.3 Discussion

The implementation of the proposed model in the preceding sections revealed several limitations to the unified yield-failure function as well as the procedure used to calibrate to experimental data. The first drawback of the model was the mathematical definition of the initial yield surface selected. As discussed in Stupkiewicz *et al.* (2014) and Penasa *et al.* (2014), the radical term in Equation 4-3 can cause convergence problems when return mapping schemes are employed. This was also found to be the case in this study as the derivatives were very complicated and numerical implementation was difficult. Therefore, it is concluded that a simplified form of the yield surface should be employed to allow for easier and more accurate implementation. The following section makes suitable adjustments to the proposed unified yield-failure function along with analysis on the parameters.

Furthermore, it was also found that calibration of the initial yield and final failure can be limited due to a lack of flexibility in the function to include the effects of confinement and non-linear evolution of the hydrostatic parameters c and p_c. Although the overall effect of increasing confinement is captured in the model, it is difficult or often impossible to match experimental data for hard rock, especially in the cases of very brittle failure and rapidly/slowly evolving brittle to ductile transitions. The following section will address this phenomenologically by providing the model with a simply adjusted hardening and damage definitions.

Speaking more generally, the major drawback of the validation of most constitutive damage-plasticity models in existing research, is the lack of a fully coupled data set such as the one obtained in Chapter 3 of this research. Given only stress-strain responses, it is impossible to describe an explicitly linked damage evolution of the material. Instead it is common practice to impose a generic function which can be calibrated to match the macro response of the model to the test data. This displays the obvious problem that, if the loading path of a material changes, which is common for engineering situations, there is no relationship between the stress-state and the damage state of the material. Therefore, physicality of the model is lost immediately and no reliable estimates of strength can be made henceforth. This shortcoming is addressed in the next section, where, via the use of simple enhancements to the proposed model, the link between damage and stress states is maintained in the calibration of damage surfaces.

Finally, the experimentally derived damage evolution of the granite in Chapter 3 is used to calibrate an improved damage evolution law. This is shown to result in a comprehensively validated damage-plasticity model for later use in the modelling of engineering problems such as rockburst.

4.4 Enhanced damage-plasticity model

It is evident from past studies that the calibration of constitutive models is heavily dependent on the quality and nature of the data used for validation. It is commonly observed (Salari *et al.* 2004; Unteregger *et al.* 2015; Mukherjee *et al.* 2017) that damage-plasticity models are almost exclusively calibrated using just stress-strain responses from conventional testing. Although, this gives some physicality to the models, the relationship between loading and damage is only given a generic form, such as that displayed in Equation 4-10. This generic definition does not allow the calibration of the damage state of the material throughout the loading path, it only provides curve fitting of the overall macro stress-strain response. As it is pointed out by Lemaitre (1992) it is important to have some physical measurement of damage to calibrate the model. Some studies do attempt this, but do not directly relate the shape and evolution of the yield function to the level of damage throughout conventional testing. Therefore, this section addresses the limitations of the original formulation as well as the derivation of a comprehensive, new calibration procedure for a damage-plasticity models. The new approach maintains the link between damage and loading path of a material and hence should be useful in future engineering applications.

4.4.1 Simple unified yield-failure function

The proposed unified yield-failure function in Section 4.2 was able to model a variety of hard rock responses without the need for complex hardening/softening laws and independent or coupled damage surfaces. However, this function also revealed some limitations in terms of numerical implementation. Therefore, a comprehensive review of the formulation was conducted and a new simpler, function was derived. First, to simplify the derivatives of the function and to avoid the restriction on the ω parameter, the whole function was squared and rearranged to remove the radical and to normalise the calculation of yield. This was similar to the procedure done by Penasa *et al.* (2014). To further simplify the implementation, the parameter, m in Equation 4-6 was replaced by a constant power of two. This again prevented radicals being present in the derivatives of the function.

Equation 4-35 shows the new form of the unified yield-failure function.

$$y(p,q,D) = \left(\frac{q}{Mp_c}\right)^2 - \left[(\omega - (1-D)\omega^2)\big((1-(1-D)\alpha)\omega + (1-D)\alpha\big)\right] \tag{4-35}$$

To maintain the flexibility of calibration, the function for M in Equation 4-34 was modified to allow the friction angle of the material to change from initial yield to final failure. This has experimental justification in works such as Ma *et al.* (2017) and Zhang *et al.* (2015a) where the internal friction angle which determines the slope of M changes from initial yielding to final residual failure throughout a conventional triaxial test. Therefore, the final form of pre-peak hardening function is given in Equation 4-36.

$$M = DM_u + (1-D)M_0 + aD(1-D)^b \tag{4-36}$$

where M_0 is the initial friction slope and M_u is the final/ultimate slope of the final frictional failure line. The parameters, a and b still control the evolution of pre-peak hardening similar to Figure 4-9.

It can be seen that given the same number of parameters as before, the function has been significantly simplified for numerical implementation. As such referring to Equations 4-18 and 4-19, the effected derivatives now take the form:

$$\frac{\partial y}{\partial \omega} = \frac{\partial y}{\partial H}\frac{\partial H}{\partial \omega} = -(1-(1-D)2\omega)\big((1-(1-D)\alpha)\omega + (1-D)\alpha\big) - (\omega - (1-D)\omega^2)\big(1-\alpha(1-D)\big) \tag{4-38}$$

$$\frac{\partial y}{\partial q} = \frac{2q}{M^2 {p_c}^2} \tag{4-39}$$

For the derivative with respect to damage, Equation 4-19 now takes the form:

$$\frac{\partial y}{\partial D} = \frac{\partial y}{\partial H}\left(\frac{\partial H}{\partial D} + \frac{\partial H}{\partial \omega}\frac{\partial \omega}{\partial D}\right) + \frac{\partial y}{\partial M}\frac{\partial M}{\partial D} \tag{4-40}$$

$$\frac{\partial y}{\partial H}\frac{\partial H}{\partial D} = -\,\omega^2\big((1-(1-D)\alpha)\omega + (1-D)\alpha\big) -$$

$$(\omega - (1-\mathrm{D})\omega^2)(\alpha\omega - \alpha) \tag{4-41}$$

$$\frac{\partial y}{\partial M} = -\frac{2q^2}{M^3 {p_c}^2} \tag{4-42}$$

$$\frac{\partial M}{\partial D} = M_u - M_0 - a(1-D)^{b-1}(bD + D - 1) \tag{4-43}$$

Finally for the plastic potential function:

$$g(p,q,D) = \left(\frac{\gamma q}{M p_c}\right)^2 - \big[(1-D)(\omega - (1-D)\omega^2)\big((1-(1-D)\alpha)\omega + (1-D)\alpha\big)\big] \tag{4-44}$$

where

$$\frac{\partial g}{\partial \sigma_{ij}} = \frac{\partial g}{\partial \omega}\frac{\partial \omega}{\partial p}\frac{\partial p}{\partial \sigma_{ij}} + \frac{\partial g}{\partial q}\frac{\partial q}{\partial J_2}\frac{\partial J_2}{\partial \sigma_{ij}} \tag{4-45}$$

$$\frac{\partial g}{\partial \omega} = (1-D)\frac{\partial y}{\partial \omega} \tag{4-46}$$

$$\frac{\partial g}{\partial q} = \gamma^2\frac{\partial y}{\partial q} \tag{4-47}$$

Given this much simpler form of the yield-failure function it was made possible to supply the model with straightforward, phenomenological enhancements to facilitate the innovative calibration procedure outlined in the next few sections. As such, the calibration to literature and the data obtained in Chapter 3 of this study will be presented to highlight the flexibility of the simple unified yield-failure function.

4.4.2 Confinement dependent damage evolution

As stated in the introduction to this chapter, although the damage-plasticity model in this dissertation is highly flexible, it can be caught out by certain rock tests where it is difficult to capture the brittle-ductile transition with the yield surface calibration alone. This indirectly exhibits the loss of physicality between damage and load, as the damage evolution is assumed constant for all confinement pressures in the model. To show this discrepancy the data for Ural marble from Unteregger *et al.* (2015) was modelled. The calibration and modelling process was carried out for this data and it was observed that a compromise had to be made to provide the best fit for the large confinement range. It can be seen in Figure 4-12 that the low and high confinement tests had diverged from the experimental results due to the constant damage evolution.

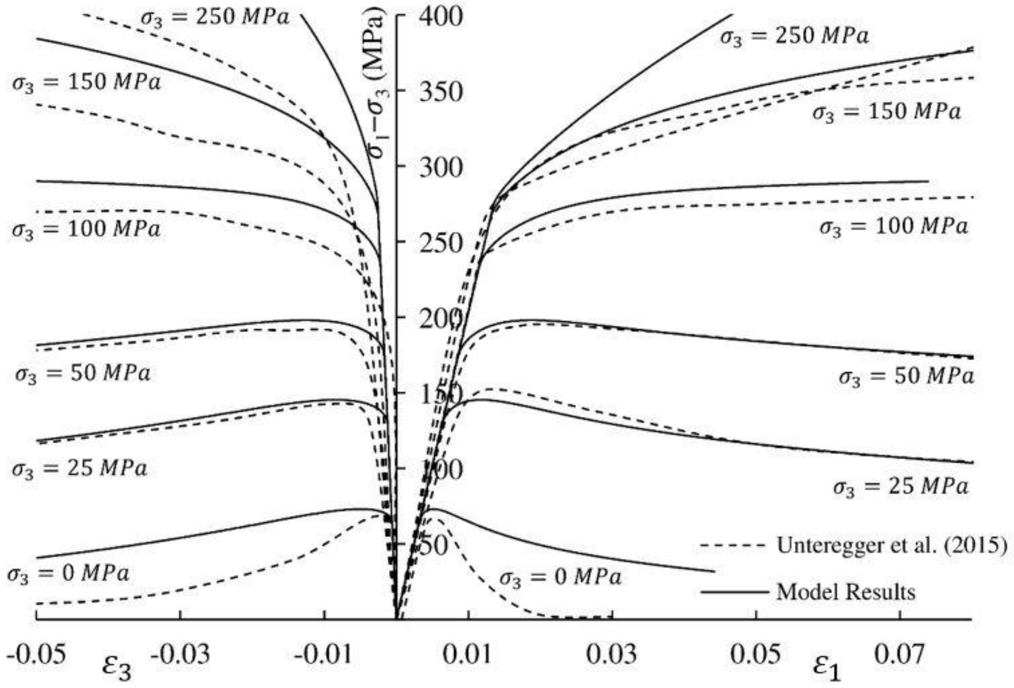

Figure 4-12: Model response for Ural marble (original formulation)

To counteract this divergence and to show the flexibility of the formulation, a simple pressure dependent damage evolution law was derived to enable the better modelling of this marble:

$$D = 1 - e^{-Z\epsilon_p} \tag{4-48}$$

where

$$\Delta\epsilon_p = \sqrt{\frac{2}{3}\Delta\varepsilon_{ij}^{p}\Delta\varepsilon_{ij}^{p}} \tag{4-49}$$

$$Z = c_1\, e^{-c_2\,\sigma_3} \tag{4-50}$$

where σ_3 is the confining pressure and c_1 and c_2 are curve fitting constants obtained by comparing the values of best fit for Equation 4-48 for multiple confinements. In the case of Ural marble the constants c_1 and c_2 were calculated to be 40 and 0.0108 respectively. Final calibrated parameters for this case were, $E = 20.3$ GPa, $\nu = 0.19$, $M_0 = M_u = 1.4$, $\alpha =$

0.138, $p_c = 488$ MPa, $c = 3.5$ MPa, $\gamma = 0.8$, $a = 2$, and $b = 7.5$. Figure 4-13 shows the results of this modelling and it is clear that the formulation can capture the transition of material behaviour from brittle to ductile regimes over a large range of confinements.

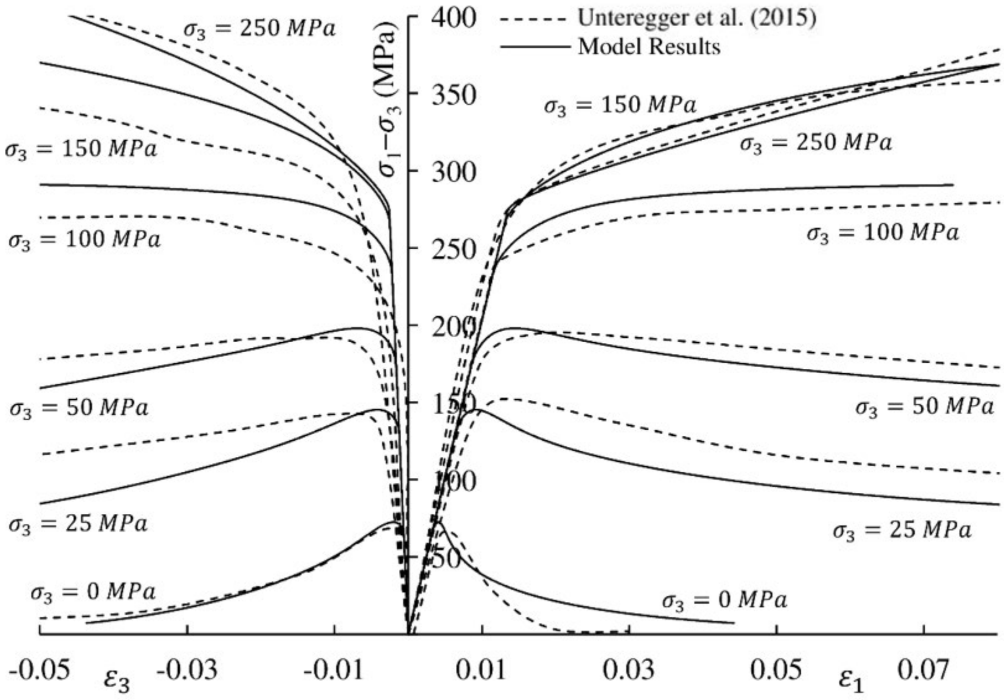

Figure 4-13: Model response for Ural marble (with pressure dependent damage evolution)

Although simple and specialised, the adjusted damage evolution law was able to capture the material response more accurately. Therefore, the conclusion can be drawn that a damage evolution law must be selected based on experimental results, in the very least, taking into account confinement pressure. As it will be shown in Section 4.4.4, the more representative of the data this law is, the more coupled the damage state to the loading state of a material. Therefore, greater confidence can be drawn from the validation of constitutive models for application to engineering problems. Although laws such as Equation 4-48 and 4-50 work at the constitutive level for simple loading scenarios, more care must be taken when applying the model to numerical codes. Therefore, the next section presents a new, comprehensive calibration procedure to intimately couple the damage and stress states, such that generic laws can still be used to describe damage evolution.

4.4.3 Fully coupled stress-strain-damage calibration

The most important factor in determining the effectiveness of a constitutive model is the data with which the functions are calibrated. To this end, it is important that the calibration data set contains all of the information which is relevant to the engineering problems which will be modelled using the proposed constitutive relationships. It is evident in the discussions of this dissertation, that most researchers validate constitutive models using only the mechanical response of conventional tests, such as uniaxial and triaxial compression. This is also true for many damage-plasticity models, where the damage evolution is governed by generic equations and parameters to provide a good fit to stress-strain response. The obvious shortcoming of this method is that for loading situations outside calibrated cases, the material could behave contrarily to the prediction. Some researchers do try to provide the model with experimental damage evolution (Chiarelli *et al.* 2003; Salari *et al.* 2004), however, the nature of the proposed constitutive models means that the link between mechanical response and damage is lost in the complex formulation and coupling procedures.

Therefore, this section proposes a new, simple method of calibrating a damage-plasticity model. The results obtained in Chapter 3 provide a full data set for confinements ranging from 10-60 MPa. The full stress-strain response along with the acoustic emission (AE) measurement of damage was recorded and cross-referenced against time. Therefore, by investigating certain damage levels, it was possible to determine the corresponding triaxial response of the material for each confinement. Therefore, for each test, the stress state was recorded for each damage level between 0 and 1 in intervals of 0.1. These stresses were then averaged to provide a single data point for each confinement level. Figure 4-14 shows the average stress values for each damage interval and the linear trend describing the evolution over increasing confinement.

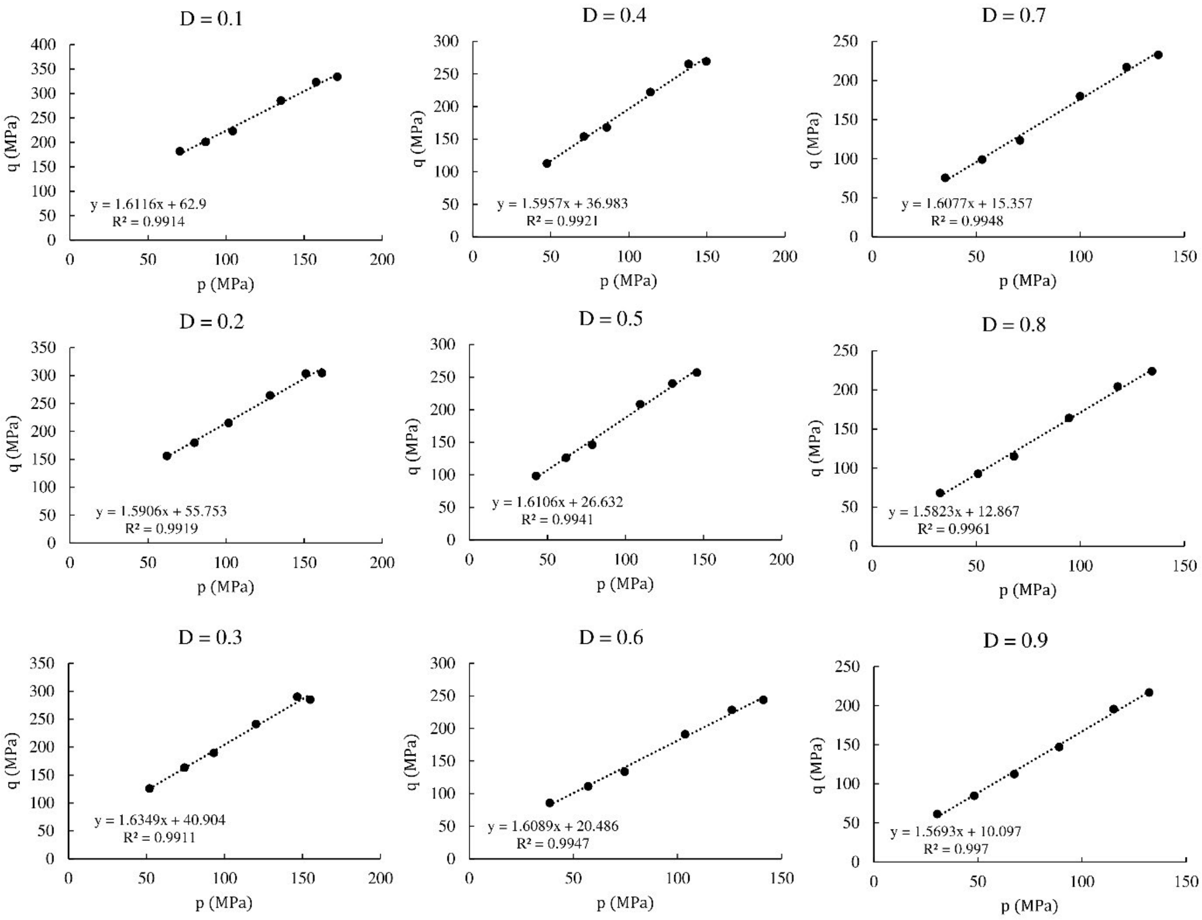

Figure 4-14: Experimental damage surface trend lines

Although the intervals calculated above describe the general trend of damage evolution, higher resolution of the damage increment was also analysed to depict the pre-peak hardening evolution with increasing confinement. It can be seen from Figure 4-15 that at low damage levels, the damage surfaces intersect the initial yield surface. This intersection point indicates where pre-peak hardening is first experienced for the material.

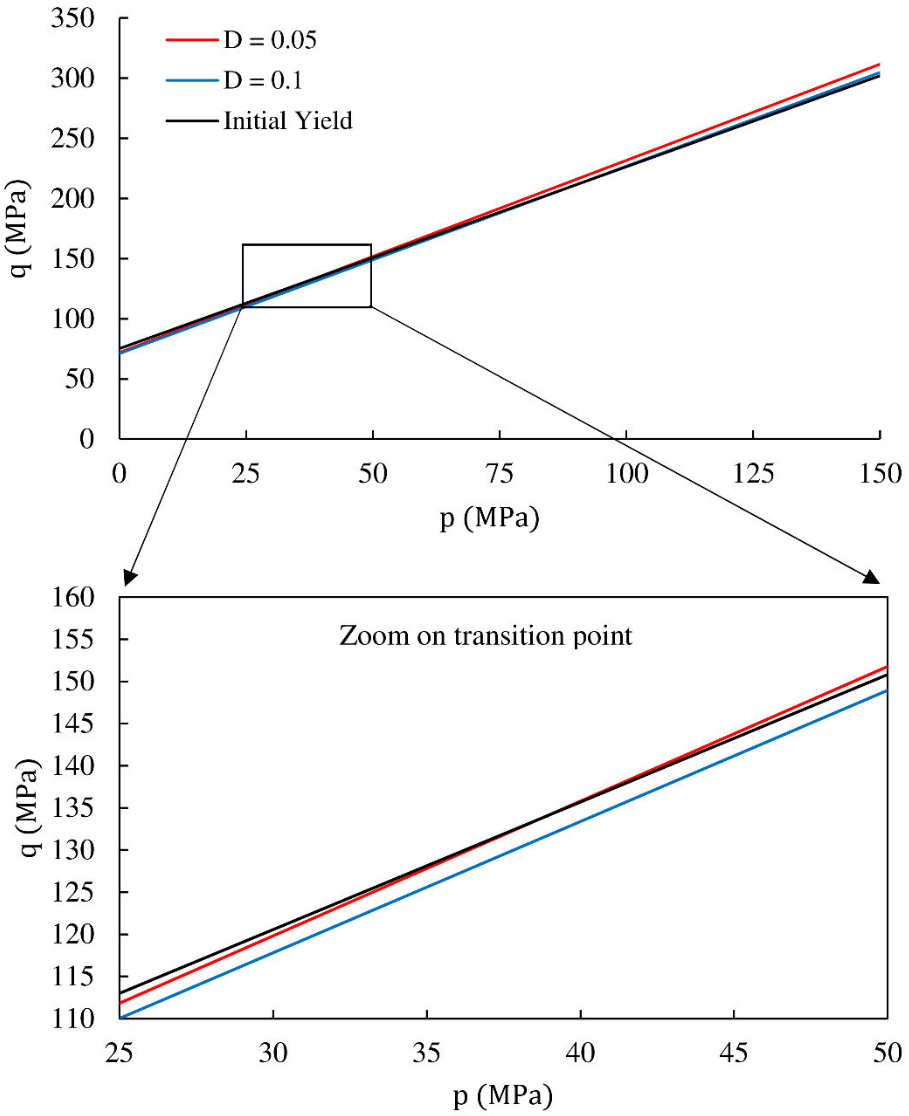

Figure 4-15: Pre-peak hardening transition

All of these surfaces, combined with the initial yield and final residual failure surfaces provide a complete picture of the damage evolution under triaxial loading. As can be seen in Figure 4-16, calculating the damage surfaces in this way reveals the nature of damage evolution in p-q stress space. Therefore, if a constitutive model is then calibrated to match this data, the relationship between damage state and loading path can be maintained for engineering applications. This should ensure the accuracy of the function when loading path is changed.

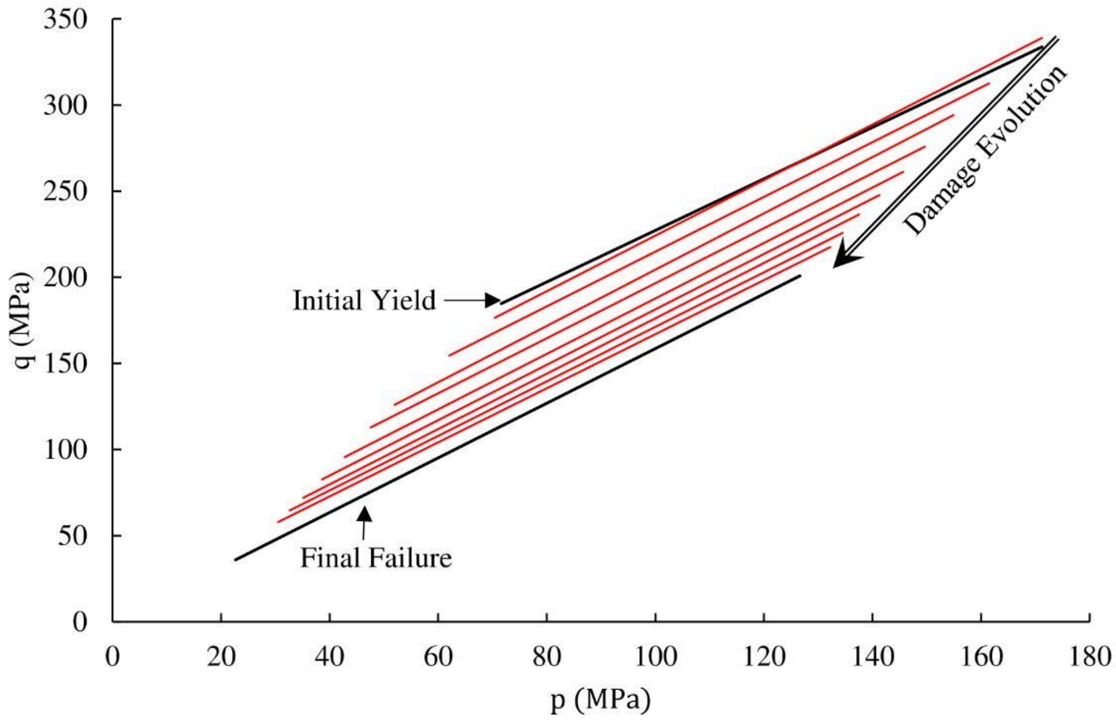

Figure 4-16: Experimental damage surfaces for triaxial compression

To begin the process of calibration of the unified yield-failure surface to the damage surface chart shown above the slopes of initial and final yield were determined. This was done using a linear relationship, however, the function could be slightly modified to include non-linear residual failure if needed for a certain material. The initial and final slopes were found to be $M_0 = 1.53$ and $M_u = 1.59$ respectively. Next the initial yield shape was determined using the methodology described in Section 4.2.2. Next, it was observed in Figure 4-16 that damage evolution was fast at low values of damage and slower at higher damage levels. Therefore, to enable the calibration of the intermediate damage surfaces the unified yield-failure function had to be improved to allow this flexibility. To accomplish this, the tensile strength parameter, c, was investigated. As damage increases in a material, the tensile strength capacity, by definition, is decreased (Lemaitre 1992). Therefore, by creating a function for c which allows damage dependent calibration, this effect can be calibrated given a complete data set.

Therefore, the new expression for ω was given the following form:

$$\omega = \frac{p+(1-D)ce^{-\beta D}}{p_c+(1-D)ce^{-\beta D}} \tag{4-51}$$

The optimisation algorithm discussed in Section 4.2.2 was then run given the new form and the final calibrated yield-failure parameters for the granite tested in this research were, $M_0 = 1.53$, $M_u = 1.59$, $\alpha = 0.035$, $p_c = 3000$ MPa, $c = 10$ MPa, $a = 2.5$, $b = 10$ and $\beta = 5.9$. Figure 4-17 shows the calibration for the test results reported in Chapter 3. It can be seen that with this simple modification it was possible to maintain the link found in experiments between the damage and stress states. This however, was not enough to ensure damage was accounted for correctly. It was also important to make sure that the damage evolution against displacement or strain was also coupled. This provided a complete material response for triaxial compression. The next section investigates the damage evolution of the material and proposes a suitable law to characterise the material response.

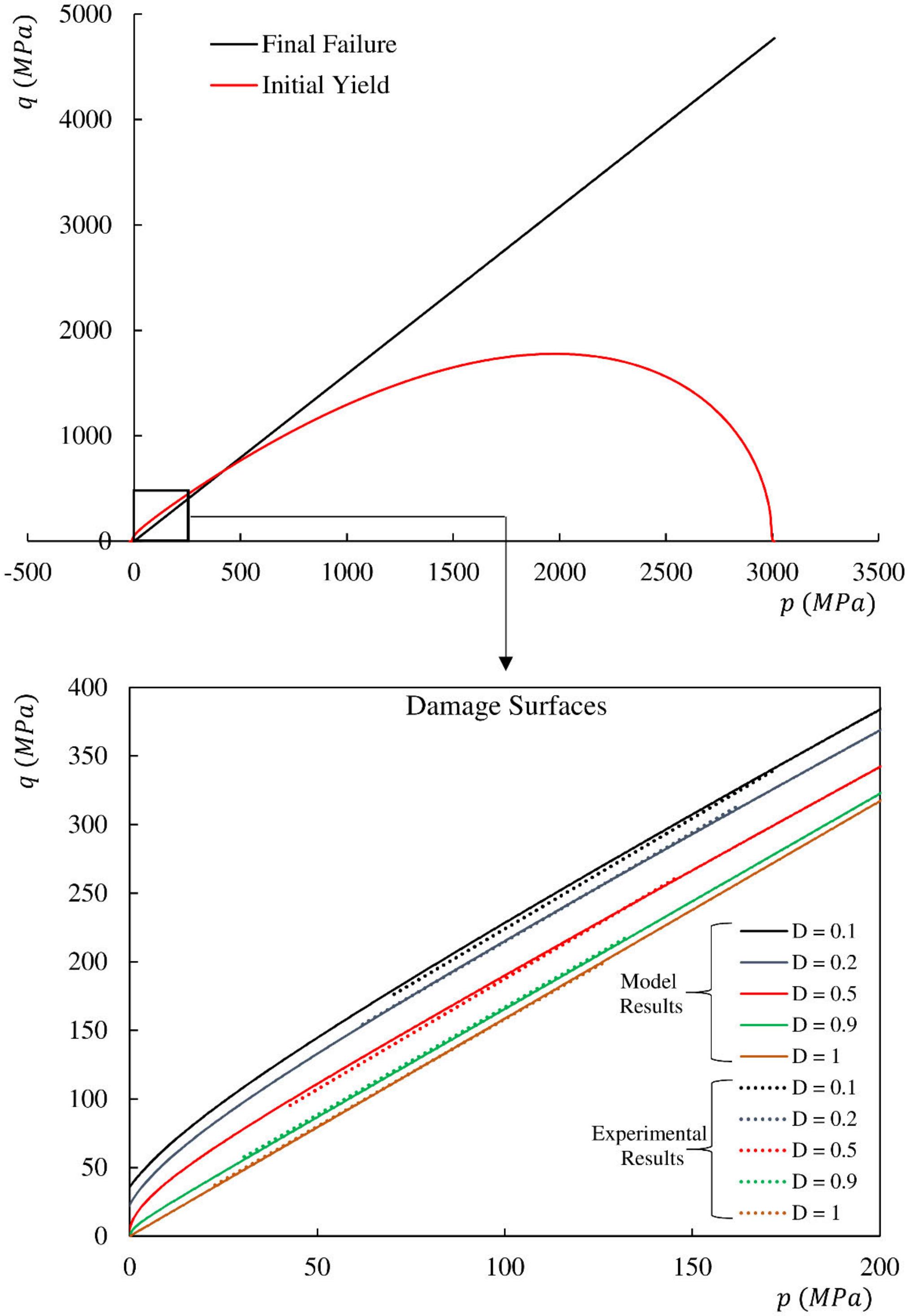

Figure 4-17: Damage surface calibration

4.4.4 Experimental damage evolution

The damage evolution of a material is normally given a generic form such as those discussed in Section 2.2 then calibrated so the stress-strain response of the material is consistent with experimental results. The drawback of this method is that the concept of damage conveys no physical meaning. Essentially it becomes analogous to the hardening/softening variables used in general plasticity formulations. As mentioned previously, some studies do attempt to provide a model with experimentally derived damage evolution (Chiarelli *et al.* 2003; Salari *et al.* 2004). However, most of the time the direct link between experiments and modelling is lost due to complex functions and coupling procedures. Also it is rare that the effects of confinement are studied and damage is normally based on uniaxial test results. To address this shortcoming in existing research, this section proposes a simple method to incorporate experimentally sourced damage evolution into a constitutive model.

To begin we recall Figure 3-8 in Section 3.3. This shows the characteristic damage evolution over increasing confinement for the granite tested. It is clear from this figure that as confinement increased the damage evolution is slowed. Also, perhaps more importantly, the general trend for each confinement displays a bimodal relationship to increasing inelastic strains. Therefore a function must be selected which is flexible enough to capture the true behaviour of damage evolution for the material. As such, a modified form of Equation 4-9 was selected to represent the measure of the combined volumetric and shear inelastic strains:

$$\epsilon_p = \sqrt{\frac{2}{9}\left(\varepsilon_v^p\right)^2 + \left(\varepsilon_s^p\right)^2} \tag{4-52}$$

where ϵ_p is the accumulated plastic strain and ε_v^p and ε_s^p are the volumetric and shear inelastic strains respectively. It can be seen in Figure 4-18 that the strain measure used still displays the same behaviour as the experimental results in Chapter 3.

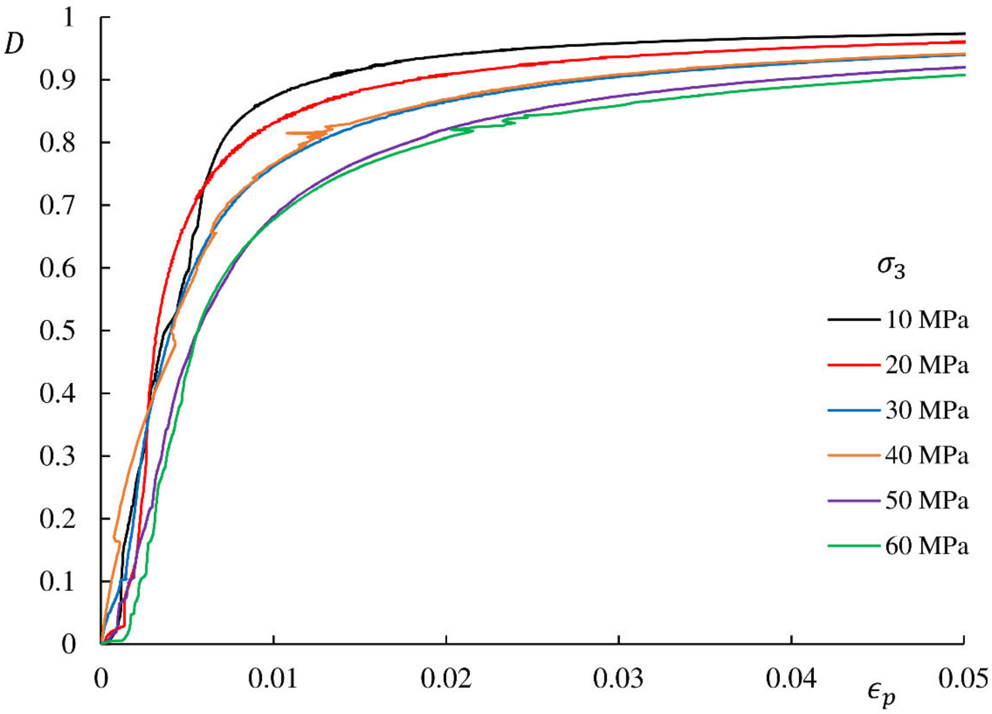

Figure 4-18: Experimental damage evolution with respect to accumulated plastic strain measure

Using the accumulated plastic strain, a new damage evolution function was developed to focus on the bimodal behaviour. The function took the form of Equation 4-53, where D_i is the bimodal damage pivot and Γ and Υ are curve fitting parameters for calibration to experiment.

$$D = 1 - \left[D_i e^{-\Gamma \epsilon_p} + (1 - D_i) e^{-\Upsilon \epsilon_p}\right] \tag{4-53}$$

Using this new form of damage evolution it was possible to recreate the damage evolution from tests in the constitutive model. The calibrated material parameters and functions for each confinement are given in Table 4-1 and Figure 4-19 respectively.

Table 4-1: Damage evolution parameters

σ_3 (MPa)	D_i	Γ	Υ
10	0.96	215	3.5
20	0.92	205	7
30	0.88	195	10.5
40	0.84	185	14
50	0.80	175	17.5
60	0.76	165	21

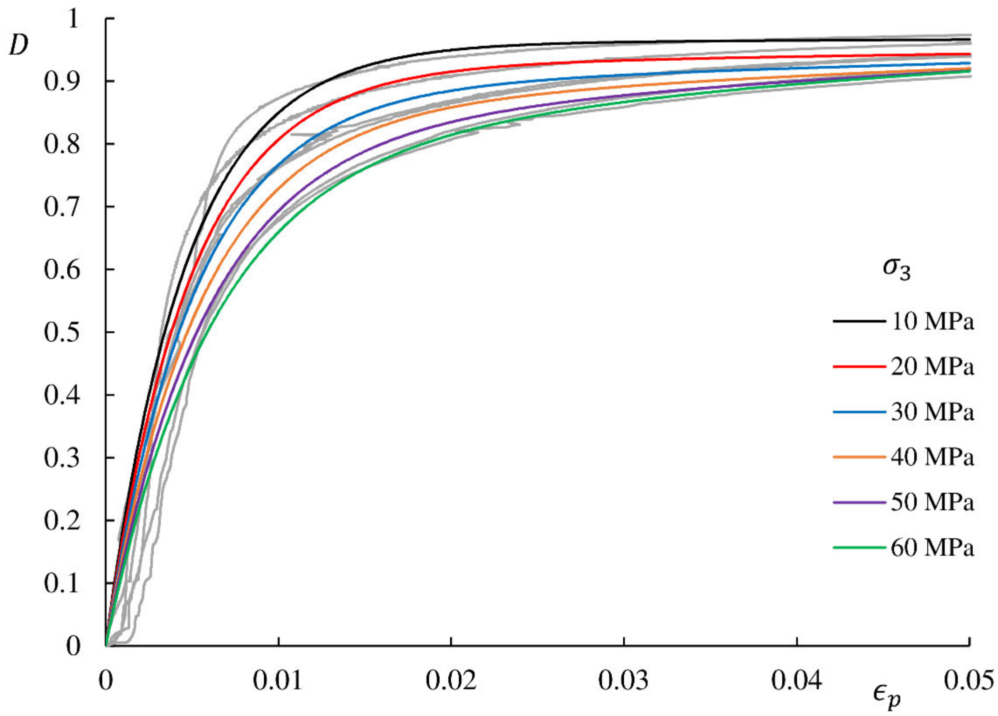

Figure 4-19: Calibrated damage evolution (experimental curves for comparison given in grey)

From this calibration procedure, it was clear that there existed simple laws to describe the relationship between the function parameters and confinement. Figure 4-20 shows the dependence of each parameter on the triaxial confinement of each test. This information can be used at the constitutive level, however, more investigation would be needed to include this effect into a consistent numerical model.

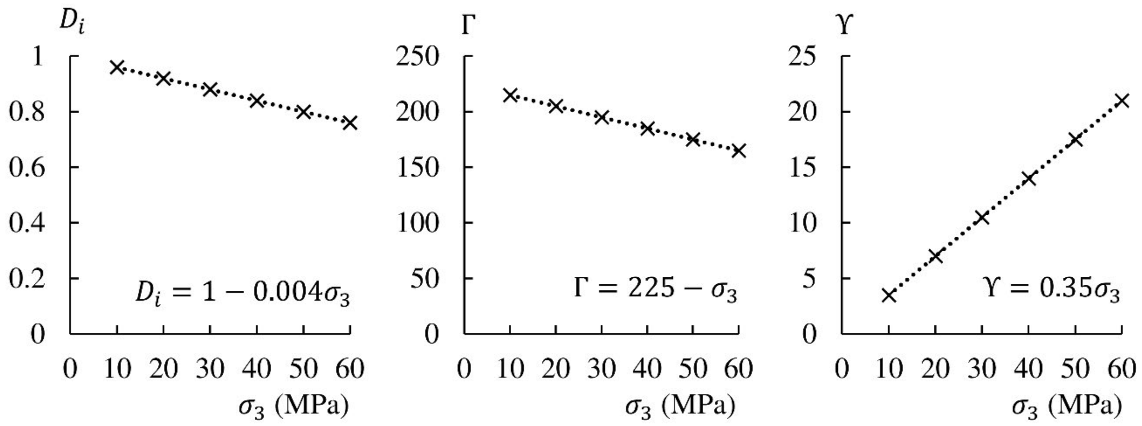

Figure 4-20: Damage evolution parameters against confinement level

4.4.5 Model Validation

This section provides the constitutive model results for the fully calibrated enhanced unified-yield failure model. Given the modified functions proposed in Equations 4-35 to 4-53 and the updated derivatives below, the constitutive model was run for each confinement.

$$\frac{\partial \omega}{\partial p} = \frac{1}{p_c + (1-D)ce^{-\beta D}} \tag{4-54}$$

$$\frac{\partial \omega}{\partial D} = \left[\frac{-\beta(1-D)ce^{-\beta D} - ce^{-\beta D}}{p_c + (1-D)ce^{-\beta D}}\right] - \left[\frac{\left(-\beta(1-D)ce^{-\beta D} - ce^{-\beta D}\right)\left(p + (1-D)ce^{-\beta D}\right)}{\left(p_c + (1-D)ce^{-\beta D}\right)^2}\right] \tag{4-55}$$

$$\Delta D = \left(\Gamma D_i e^{-\Gamma \epsilon_p} + (1 - D_i)\Upsilon e^{-\Upsilon \epsilon_p}\right)\Delta\epsilon_p \tag{4-56}$$

$$\Delta\epsilon_p = \Delta\lambda\sqrt{\frac{2}{9}\left(\frac{\partial g}{\partial p}\right)^2 + \left(\frac{\partial g}{\partial q}\right)^2} \tag{4-57}$$

Although the damage evolution changes over confinement, a single set of variables was used for the validation procedure. As previously mentioned, this was to keep the process consistent and to avoid the use of stress states as constants for each test. The variables obtained in the calibration process were $E = 33.5$ GPa, $\nu = 0.14$, $M_0 = 1.53$, $M_u = 1.59$, $\alpha = 0.035$, $p_c = 3000$ MPa, $c = 10$ MPa, $a = 2.5$, $b = 10$, $\gamma = 1$, $\beta = 5.9$, $D_i = 0.96$, $\Gamma = 215$ and $\Upsilon = 3.5$. The results of each modelled test were then compared to the experimental material responses given in Figure 4-21. It can be seen that although the response is reasonable given the variability of the data, there was some systematic difference for the low confinement tests. This difference stems from the snap-back behaviour of granite under low confinements. This could be accounted for by re-calibrating the damage evolution function to provide a faster damage evolution, however, this causes the uncoupling of stress state and damage. Therefore, a future work will be conducted on developing a model to capture the strain (displacement) response as well as stress and damage.

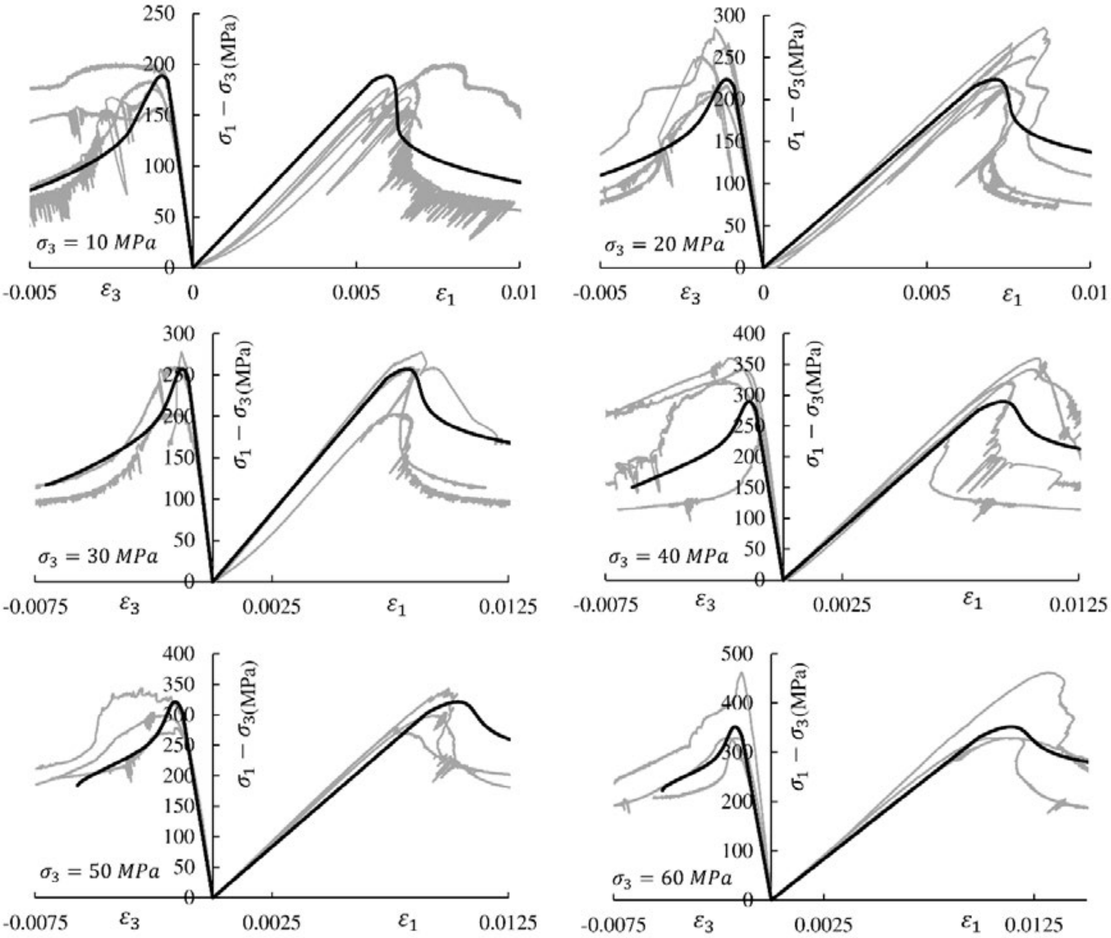

Figure 4-21: Model results (black) compared to experimental responses (grey)

4.5 Conclusion

The formulation of a unified yield-failure damage-plasticity model to represent intact hard rock behaviour was presented in this chapter. The function, outlined in Equation 4-35, evolves an initial yield surface to a final frictional failure surface by utilising a single damage evolution law to phenomenologically account for damage as well as plasticity related mechanisms. This allows for softening, hardening and the transition between the responses to be automatically captured without using separately defined softening/hardening rules. As demonstrated, this can significantly simplify the model formulation and description, as the complete model can be described by a set of five equations and the corresponding parameters. This, in turn, should aide the calibration and modification of the function for other materials.

This chapter also introduced a new, innovative procedure to calibrate a constitutive model to experimental data. By obtaining the damage-stress-strain response of a material, it is possible using this formulation to derive simple enhancements of the model to facilitate the calibration of damage states and evolution. This ensures the physicality of damage to loading responses and removes the need for complex coupling procedures. This is useful as a change in load path can be taken into account by the model and the correct damage and stress states should be maintained.

Throughout the validation process it was shown that the model can capture key hard rock responses during triaxial tests, however, the model is currently limited to material point implementation. For now the numerical implementation of this model is beyond the scope of this dissertation and therefore, further studies will be conducted on the implementation of the formulation for real engineering applications. Finally, as is evident in Section 4.4.5, although the model performed adequately, there was some difference between the experimental and model responses. This was due to the snap-back behaviour of granite under low confinement pressures causing a mismatch between the axial strain states. As accumulated plastic strain is always increasing, the damage evolves throughout constant application of axial strain. However, as is evident in the experimental results in Chapter 3, the material undergoes some measure of axial strain reversal which cannot be captured by the current model. Therefore, the snap-back behaviour should be studied in more detail to understand the modifications needed to precisely match these responses.

Although this chapter provides a simple, highly flexible model for the modelling of hard rocks under compression, the application to real engineering problems could prove difficult. This is because, although calibrated to appropriate test data, the experiments conducted to validate constitutive models are quite often a very simplified or an ideal case. Therefore, when aiming to numerically model complex phenomena such as rockburst, the model should also be validated using data from a test designed to replicate the conditions of rockburst in the laboratory. Additional to this, the model should be extended to link it more closely with tensile strength and fracture energy. However, as the focus of this research is the stress state leading up until burst, the model was developed to take into account the high confinement and compressional behaviour of deep excavations. Therefore, once the model is enhanced and validated by matching the numerical results with the laboratory burst mechanisms, it should be possible to extend the model to the prediction of future events in a mine or civil excavation setting. Along this vein, the next chapter proposes a new, innovative design for small scale rockburst testing in the laboratory, with the long term goal to provide rockburst specific validation data sets for numerical modelling.

Chapter 5 – AN INNOVATIVE METHOD FOR SMALL SCALE ROCKBURST TESTING

Numerous attempts have been made to investigate the mechanisms of strainburst in the laboratory under varying stress states and test configurations (Mogi 1971; Huang *et al.* 2000; Wang and Park 2001; He *et al.* 2010a; He *et al.* 2010b; Gong *et al.* 2014; Zhao and Cai 2014; Zhao *et al.* 2014; He *et al.* 2015a; He *et al.* 2015b; Li *et al.* 2015; Su *et al.* 2017; Akdag *et al.* 2018). Based on uniaxial compressive tests and energy calculations, He *et al.* (2012) developed conceptual stress paths which are necessary for bursting to occur (Figure 5-1). It is also evident from this figure that there was no consideration for the effect of the intermediate principal stress when determining the conceptual stress paths.

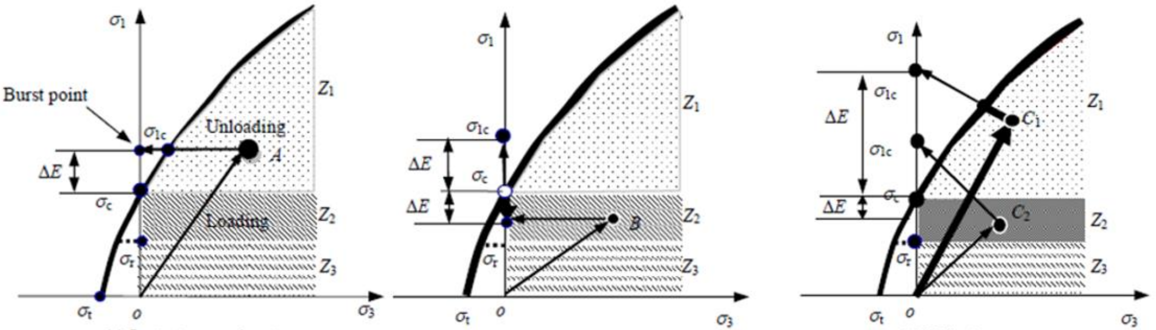

(a) Instantaneous burst. (b) Delayed burst. (c) Pillar burst.

Figure 5-1: Rockburst loading paths (He *et al.* 2012)

Therefore, by far the most popular testing methodology amongst current researchers is the ‘true-triaxial unloading’ technique first described by He *et al.* (2010a). The rockburst test apparatus was developed in China and can provide dynamic loading/unloading independently in the three principal stress directions, $\sigma_1 > \sigma_2 > \sigma_3$, where σ_1, σ_2, σ_3 are the major, intermediate, and minor principal stresses respectively. This accounted for the complicated stress states which are present in underground excavations. Additionally, the minor principal stress σ_3 could be released rapidly on one face to simulate the stress conditions immediately after excavation. Although influential in determining the mechanisms of strainburst, the true-triaxial methodology adopted by most researchers is plagued by platen effects on the rock specimens, often resulting in bursts occurring at the edges of a specimen in contact with the steel platens (Gong *et al.* 2014; Su *et al.* 2017; Akdag *et al.* 2018). This coupled with the high cost of such systems, highlights the need for a cheaper, more accessible test to model the rockburst phenomenon without the associated end effects of prismatic specimens. In order to create a new method for rockburst testing, a suitable specimen geometry must be selected to allow replication of the three dimensional stress state found in underground excavations. One study that was conducted by Liu *et al.* (2014) introduced an alternate way of testing rockburst, all be it using the same apparatus. Although the research utilised the true-triaxial loading frame, the specimen was machined to have a central borehole, which acted as the free face of an excavation. This provided the rockburst event to occur along the face and not be controlled by potential end effects. Another advantage of this method was it simulated the excavation as a whole profile not just a portion of exposed rock mass at a point in the tunnel wall. To enable the comparison of these tests to the true triaxial apparatus, the relationship proposed by Su *et al.* (2017) shown in Figure 5-2 could, in theory, be used to convert between cylindrical and principal stresses.

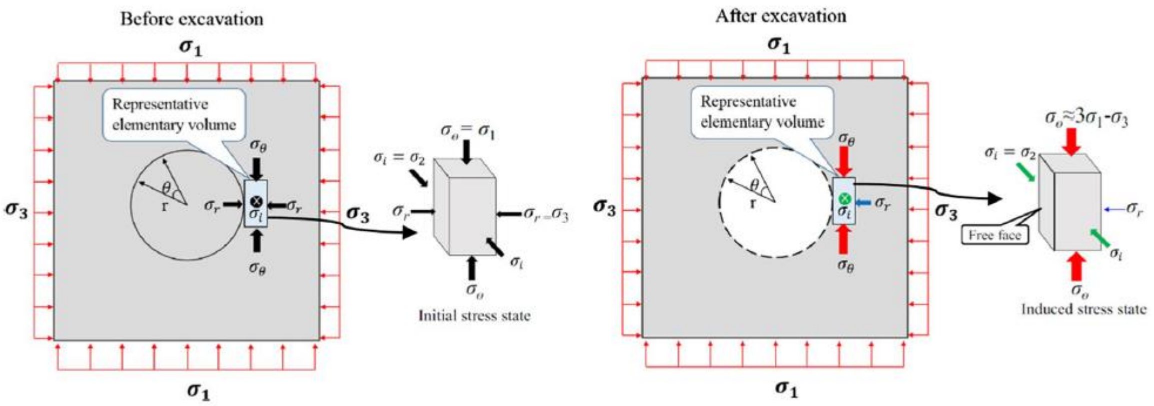

Figure 5-2: Cylindrical representative volume element before and after free face excavation proposed by Su *et al.* (2017)

5.1 A brief review of hollow cylinder testing

In order to create a new method for rockburst testing, first a suitable specimen geometry had to be selected to allow for three dimensional stress testing. As such, the research on hollow cylinders was reviewed in this section to provide a basis for specialised platen development for application to rockburst testing.

There have been numerous studies (Robertson 1955; Hoskins 1969; Ewy and Cook 1990; Lee *et al.* 1999; Alsayed 2002; Labiouse *et al.* 2014) on the testing of hollow cylinders and as such they have been categorised into two main fields; thin walled and thick walled hollow cylinders. In the case of thin walled hollow cylinders, the stress distribution inside the wall is relatively homogenous due to the relatively small thickness with respect to internal diameter. On the other hand, thick walled hollow cylinders do not display constant stresses in the walls. This is useful in the case of rockburst testing, as it leads to concentration of the stress state on the internal surface to enable burst, but also exhibits minimal stress on the external face to avoid total specimen (shear) failure. Therefore, to investigate the stress-states of thick walled hollow cylinders in this thesis, the form proposed by Alsayed (2002) was adopted. Considering the general case given in Figure 5-3 along with adopting conventional cylindrical coordinates (r, θ, z), the solution takes the form:

$$\sigma_r = \frac{P_o R_o^2 - P_i R_i^2}{R_o^2 - R_i^2} - \frac{(P_o - P_i) R_i^2 R_o^2}{r^2 (R_o^2 - R_i^2)} \tag{5-1}$$

$$\sigma_\theta = \frac{P_o R_o^2 - P_i R_i^2}{R_o^2 - R_i^2} + \frac{(P_o - P_i) R_i^2 R_o^2}{r^2 (R_o^2 - R_i^2)} \tag{5-2}$$

$$\sigma_z = \frac{F}{\pi (R_o^2 - R_i^2)} - \frac{P_i R_i^2}{R_o^2 - R_i^2} \tag{5-3}$$

where R_i and R_o are the inner and outer radius of the cylinder respectively, P_i is the internal pressure, P_o is the external pressure and F is the axial force. The three cylindrical stresses are the radial, σ_r, the tangential, σ_θ both calculated at any point of radial distance, r and the axial, σ_z, which is the difference between internal pressure and axial loading (Alsayed 2002).

As this formulation includes all of the parameters for a Hoek cell type triaxial test, it was deemed appropriate to be used in the design of the rockburst test methodology. Another advantage of using a hollow cylinder for rockburst testing is that there would be no platen effects on the mode of failure on the internal borehole as the stress concentration would be uniform over the length of the specimen. Also by adopting the readily available Hoek triaxial cell, the test could be developed using specialist platens, which are markedly cheaper to purchase than servo controlled poly-axial apparatus.

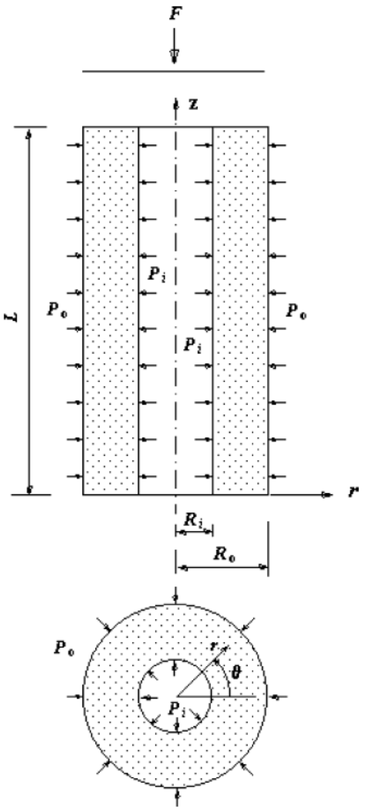

Figure 5-3: Thick walled hollow cylinder under internal, external and axial pressures (Alsayed 2002)

Another important consideration in hollow cylinder testing is the application of internal hydraulic pressure during a test. This has been studied in a limited fashion, predominantly by Alsayed (2002) and has not been applied to rockburst research. As bursting can occur when an excavation is made in a rock mass, it is important to be able to bring the specimen up to in-situ pressures hydrostatically, as is done in the true-triaxial tests (He *et al.* 2010a; He *et al.* 2010b; He *et al.* 2012; He *et al.* 2015a). Imparting internal pressure inside a hollow cylinder and then releasing to create the excavated face could be potentially used to replicate conditions similar to the platen release in the true triaxial apparatus.

Separately rockburst and hollow cylinder studies have significantly contributed to better understand the mechanical behaviour of rocks under various stress paths. However, in previous works, very few experimental studies have focused on investigating rockburst mechanisms using hollow cylinders. In this sense, an innovative hollow cylinder testing methodology, accompanied with an in-cell acoustic emission (AE) system for small-scale rockburst testing is presented in this manuscript. The following sections address the design, development and implementation of the new method along with discussion of the results and test validation. Furthermore, the characteristic AE response for rockburst occurrence is established and the stress states conducive to bursting are examined in detail. Finally, the effectiveness of the test setup is discussed and future improvements and studies are recommended.

5.2 Rockburst platen design

To replicate the conditions for rockburst in the laboratory, it is necessary to create an excavated face while the rock is under in-situ pressure. One method to create this three dimensional stress state is to test thick walled hollow cylinders with internal borehole pressure. The optimal internal and external diameters for thick walled hollow cylinders is variable across existing research. For example, Alsayed (2002) claimed that the internal diameter of the cylinder should be no larger than the thickness of the resulting wall at a ratio of $R_i/R_o = 0.33$. However, other researchers such as Hoskins (1969) and Lee *et al.* (1999) believe that this ratio can be increased, resulting in an internal to external radius ratio (R_i/R_o) of anywhere from 0.4 to 0.7. The exact ratio for testing thick walled cylinders is highly dependent on the parameters or mechanisms being tested. For this study, a ratio of approximately 0.45 was selected to provide a sufficiently thick wall to provide the stress difference between internal and external faces as well as offer the maximum excavated opening (free face) in the rock to facilitate bursting. Therefore, given the 63mm Hoek cell available $(d_o = 63mm)$, the internal diameter of each specimen was set to 28mm $(d_i = 28mm)$.

Using this specimen geometry, the new rockburst test platens were designed to provide a means to introduce internal pressure inside a rock cylinder for the hydrostatic loading phase and to also provide a release mechanism to create a free face or ‘excavation’ during the test. The first consideration for platen design was that the test could not implement an internal membrane to provide the seal for internal pressure, as demonstrated in Alsayed (2002). This was to ensure that the rockburst event during each experiment was not supported or masked by the stiffness of the internal membrane. It is important to note that the rock tested in this apparatus exhibited very low porosity and permeability (granite). Therefore, the injection fluid (water) could not infiltrate the specimen during testing. This was later proved by weighing specimens before and after testing and it was found there was no increase in mass. To provide the seal, a custom made axial O-ring was designed into the platen to seal the rock-platen interface.

The second design consideration for the rockburst platens was the application of acoustic emission (AE) sensors to the rock. This is an important component of rockburst testing, as quite often it is possible to identify bursting via characteristic AE responses (Akdag *et al.* 2018). For this new experiment, the AE measurements were even more vital, as the rock could not be observed during the test to determine if bursting had occurred. The only way to determine when the rock had undergone bursting was the careful monitoring of the AE signals during a test. Therefore, the platens were designed to enable the placing of AE sensors in direct contact with the ends of the specimen. This was done using a new, innovative platen design were the sensors were housed in the platen and the wires allowed to exit the Hoek cell via a protective ring assembly shown in Figure 5-4. Each platen, top and bottom, were designed to house four AE sensors, separated at 90 degrees. Hence, it is possible to use the platens to conduct location analysis in future studies.

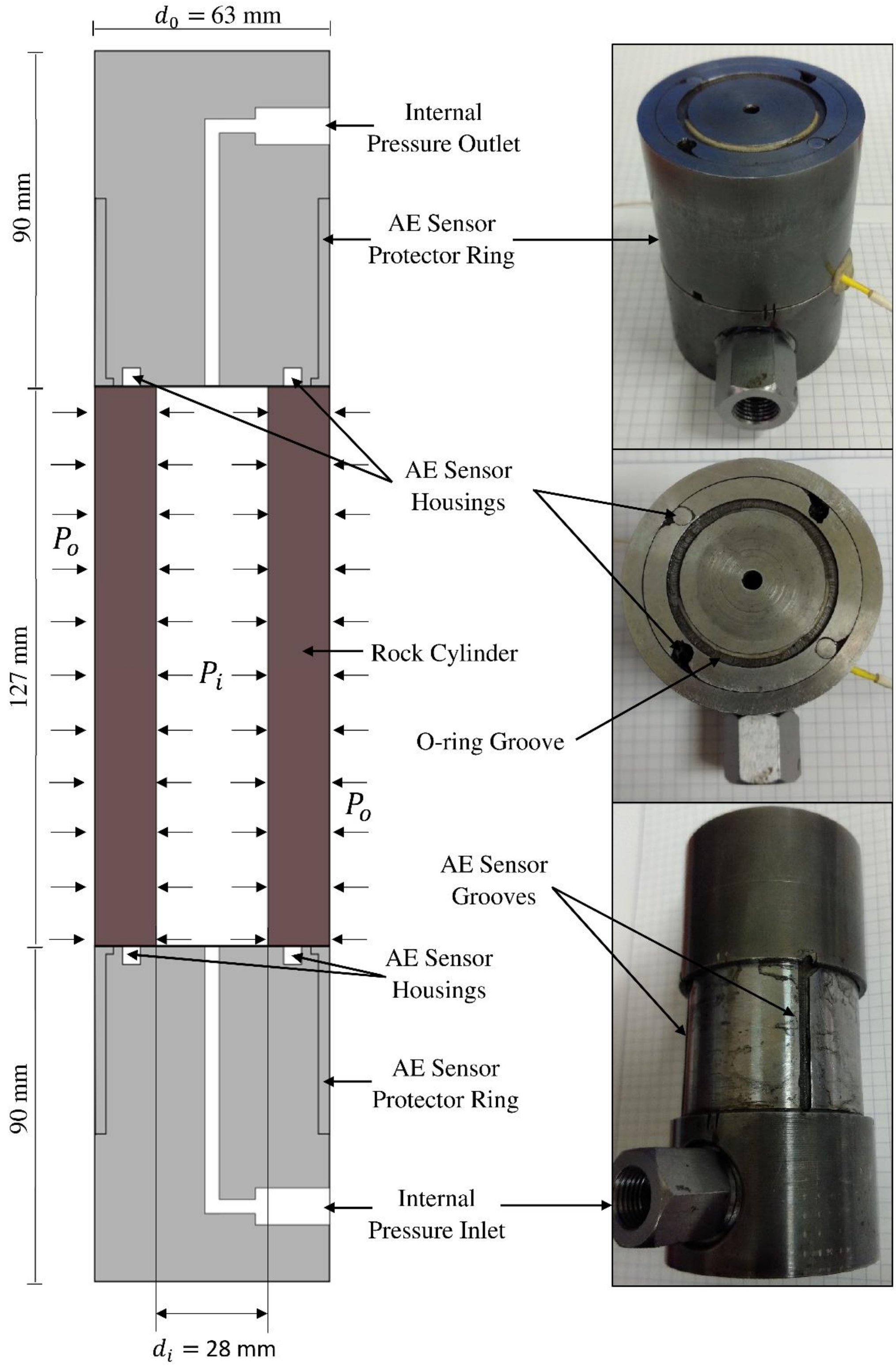

Figure 5-4: Rockburst platen schematic and photos

5.3 Rockburst test methodology

The utilisation of hollow cylinders of rock has never before been used for rockburst testing. Therefore, a comprehensive study on the development of a test procedure had to be performed. This section outlines the final testing methodology used for recreating small scale rockbursts in the laboratory.

5.3.1 Specimen preparation

The rock selected for this study was a granite from New South Wales, Australia, and named ‘Grandee’. The petrographic description revealed that it is a medium-grained (1-5mm) dark grey, equigranular rock consisting mainly of plagioclase feldspar (63%) and pyroxene (23%). Biotite and quartz were also found in significant quantities (10% and 5% respectively) with other accessory minerals such as hornblende, apatite and zircon. This was selected as it is very homogenous, hard and relatively fine grained rock (Figure 5-5) which is analogous to burst prone rock masses. The bulk density of the rock was recorded to be 2930 kg/m^3 with a uniaxial compressive strength of approximately 240 MPa. It was also readily available as it is quarried for use as dimension stone. Therefore, for future tests a slab can be easily found which closely matches the grain size a mineralogy of the tests conducted in this dissertation. Therefore, all future results can be compared and correlated to form a good understanding of the test and rockburst mechanisms.

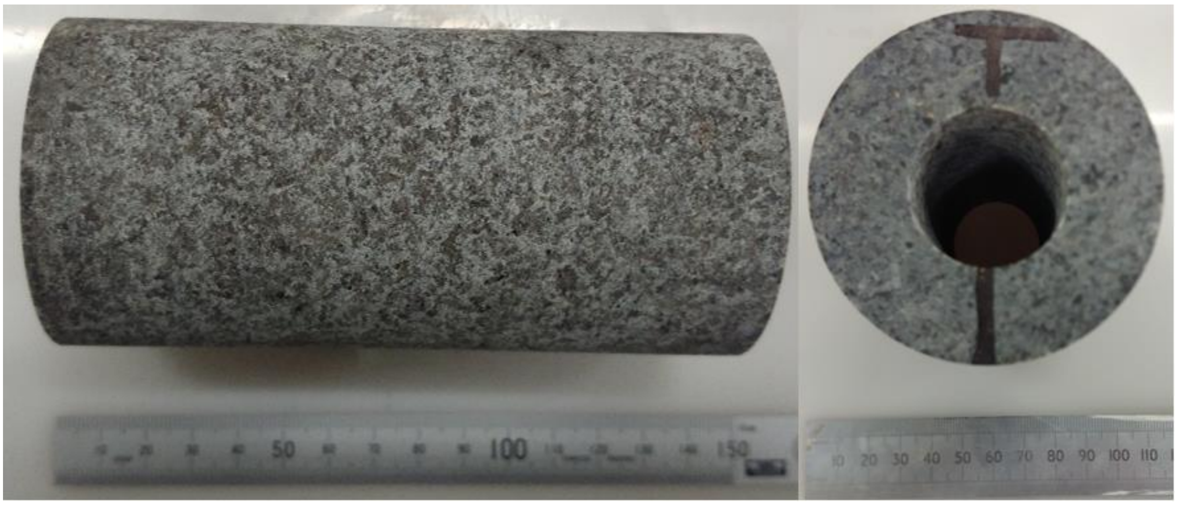

Figure 5-5: Grandee granite specimen

Each sample was prepared by first over-coring the slab to 10mm depth to a diameter of 63mm. This was done to ensure the location of the central borehole and external wall to be centralised. Next the internal core was machined using a diamond impregnated core drill. Once complete, the 63mm bit was reattached and the external core was taken. The specimens were then cut to size and surface ground flat to aid the coupling between platen and rock. The finished dimensions of each specimen, were on average, 62.7mm external diameter, 28.2mm internal diameter and 127.5mm in length.

5.3.2 Rockburst apparatus

After the manufacture of the platens, the appropriate hydraulic fittings and equipment had to be sourced to enable the application of pressure to the specimen. To apply axial load to the platens at the specimen ends, an INSTRON 1282 was selected with an axial load capacity of 1000 kN. For external confinement of the rock cylinder, the previously mentioned 63 mm Hoek cell was used in conjunction with a 65 MPa capacity pressure maintainer. Then to provide good control of internal pressure and creation of the free face, a Teledyne D-series syringe pump was used to prime, maintain and release the internal pressure. All data acquisition was done using a National Instruments cDAQ module.

Acoustic emission signals were captured using miniature PICO sensors and were passed through a pre-amplifier set to 60 dB of gain (Type 2/4/6). This study only required the recording of AE signals to provide information about event occurrence, not location analysis. Therefore, testing was conducted with 4 out of the maximum 8 sensors arranged as shown in Figure 5-4. An Express-8 data acquisition card was used and sampling rate was set to a 2 MSPS (mega samples per second). The lower threshold value for mechanical and ambient noise was set 45 dB. This was established by setting a low threshold (20dB) then increasing until the loading frame noise was no longer registering during acquisition. To ensure the acoustic emissions could be compared to certain loading scenarios, the recording for stress-strain and acoustic emissions signals were simultaneously started for each test.

The entire test apparatus is shown in Figure 5-6 in schematic form. This displays the control loops (solid lines) and data acquisition loops (dotted lines) as they were during testing. A photograph of the experimental setup is also presented in the figure for context. It is important to note that the internal pressure was released by the manual operation of a ball valve attached to the outlet of the syringe pump (shown in Figure 5-6).

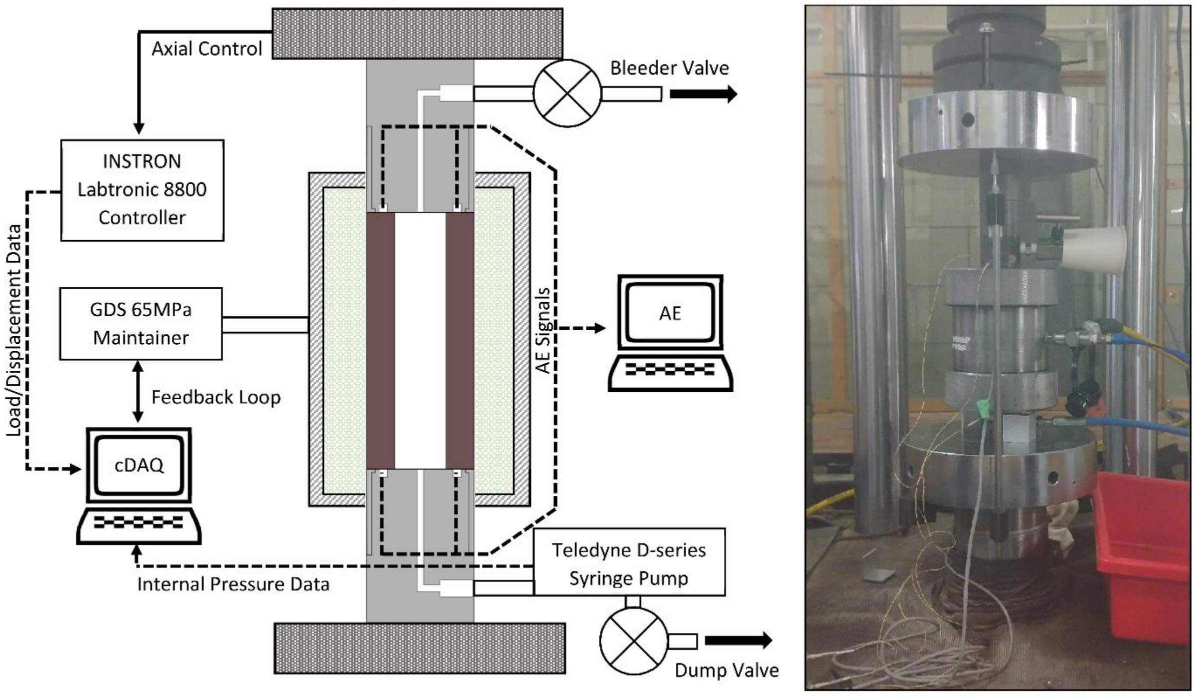

Figure 5-6: Experimental rockburst apparatus schematic (left) and photographed during a test (right)

5.3.3 Rockburst test procedure

To date, the small scale laboratory testing of rockburst has relied upon the visual observation of the free face during a test (He *et al.* 2010a; He *et al.* 2010b; Gong *et al.* 2012; He *et al.* 2012; Gong *et al.* 2014; He *et al.* 2015a; Akdag *et al.* 2018). However, in this research it was impossible to observe the free face due to the specimen being enclosed in a Hoek cell. Some research has been done on fitting a borehole camera in a Hoek cell platen (Hashemi *et al.* 2015), however, due to the internal pressure being applied and released from the cavity in this test setup, it would cause the camera to be destroyed or the field of view to be distorted. Therefore, an alternative method had to be developed to identify rockburst before final frictional (shear) failure of the specimen.

Initial tests using the rockburst apparatus were conducted using a loading methodology similar to Akdag *et al.* (2018), where the three principal stresses were brought to defined levels hydrostatically. Then by releasing the minor principal stress and increasing the major principal stress, the rock is made to undergo bursting. Figure 5-2 shows the principal stress relationships assumed for this research. However, due to the relatively low capacity of the Hoek cell used in this research (70 MPa), the major principal stress was switched to the axial loading direction and the tangential stress imparted by the cell acted as the intermediate stress. Also evident in Figure 5-2, it can be seen that, although the specimen opening is cylindrical the rockburst problem is replicated at the wall (via the representative volume element). Therefore, the three dimensional stress state described above can be adopted. Also as the grain size of the rock was much less than the diameter of the opening, bridging effects and individual grain failure were ignored.

In the study by Akdag *et al.* (2018), the typical in-situ stress state for Australian deep mines was given as $\sigma_1 = 43\,MPa$, $\sigma_2 = 23\,MPa$ and $\sigma_3 = 11\,MPa$. This corresponds to a theoretical depth of approximately 1300m below ground surface. Therefore, given the information above, the following test procedure was initially conducted to determine the characteristics of burst. First, all stresses were increased hydrostatically to the minor principal stress level (internal pressure) of $\sigma_3 = 11\,MPa$. Then axial load and Hoek cell pressure were increased hydrostatically to the intermediate principal stress (tangential stress) of $\sigma_2 = 23\,MPa$. Finally, the axial load was increased to the major principal stress of $\sigma_1 = 43\,MPa$. Once the in-situ stress state was reached, the loading was held for 5 minutes to allow the stress field to come to equilibrium. This avoids any dynamic effects of loading on further stages of testing. The next stage was to release the internal pressure of the specimen by manually operating the ball valve close to the syringe pump. It was observed that pressure was immediately drained from the borehole within one second. This pressure release simulated the creation of a free face or excavation in the rock. Another important finding was that as internal pressure was released, there was a significant spike in tangential stress

(Figure 5-7). This highlights the difference in using a full profile in testing rather than direct control using a true-triaxial frame. In the previous research this dynamic effect is ignored and could be important if the rock was to display instantaneous bursting (He *et al.* 2012). However, the granite used in this study was very strong, so the sudden release of internal pressure did not cause a significant increase in AE activity. This was interpreted as no burst and therefore, axial loading was continued to add energy to the rock. During the axial loading AE activity was observed to increase and finally the specimen failed under shear. This failure mechanism was not desirable, as once the specimen was retrieved from the cell, it was impossible to distinguish any localised bursting in the large zone effected by shear. Therefore, upon the review of the test data, it was found that there existed two main predictors of shear failure. First, the material displayed slight hardening immediately prior to sudden, total brittle failure. Therefore, this was considered as an upper bound to stop further rockburst tests to ensure the specimens did not shear and destroy any evidence of localised rockburst. Perhaps more importantly, several key behaviours were observed in the AE response of the rock during the test. During the first three loading steps, low energy AE signals were recorded which indicated the crack closure response of the rock. This response was mimicked when the internal pressure was released, where the sensors picked up the sound of the water being drained. This was followed by a period of few to no emissions. This corresponded to the elastic loading of the sample. Figure 5-7 also showed that a distinct AE pattern was realised during the later stages of the test. After the quiet, elastic loading period, low energy emissions were captured. This was thought to be due to the crack initiation of the specimen. Following this, a ramped spike in AE signals was detected in both hits and energy. The sudden increase, followed by a gradual decrease was determined to be the characteristic signal formed by a rockburst event. The idealised, conceptual form of this signal is also shown in Figure 5-7. After burst, the specimen started to display hardening and increased levels of AE activity, which was the second precursor, leading up to the violent final shear failure.

Post-test inspection of the specimen revealed two burst zones in the intact portion away from the shear zone failure. Therefore, given these burst zones and the measured data during the test, a consistent method was developed to predict rockburst in the specimens and to prevent shear failure. During the initial stages of each test the magnitude of AE hits and energy during the in-situ and elastic loading phases was recorded and marked in the AE acquisition software. Then via continual monitoring, the AE signals recorded after the elastic stage were considered stable cracking if below the elastic AE threshold and the test continued until a ramped increase in AE hits and energy higher than the threshold was realised. At this point the response was carefully monitored to determine the characteristic shape of a rockburst event. Loading for each test was then continued to observe any further events. Each test was stopped if the operator was certain of a strong characteristic rockburst signature or if specimen hardening was observed via a change in stiffness. Given the methodology above more tests were conducted to determine the effectiveness of the newly proposed rockburst apparatus. The next section presents the results of each test and discusses the unique features of each burst occurrence.

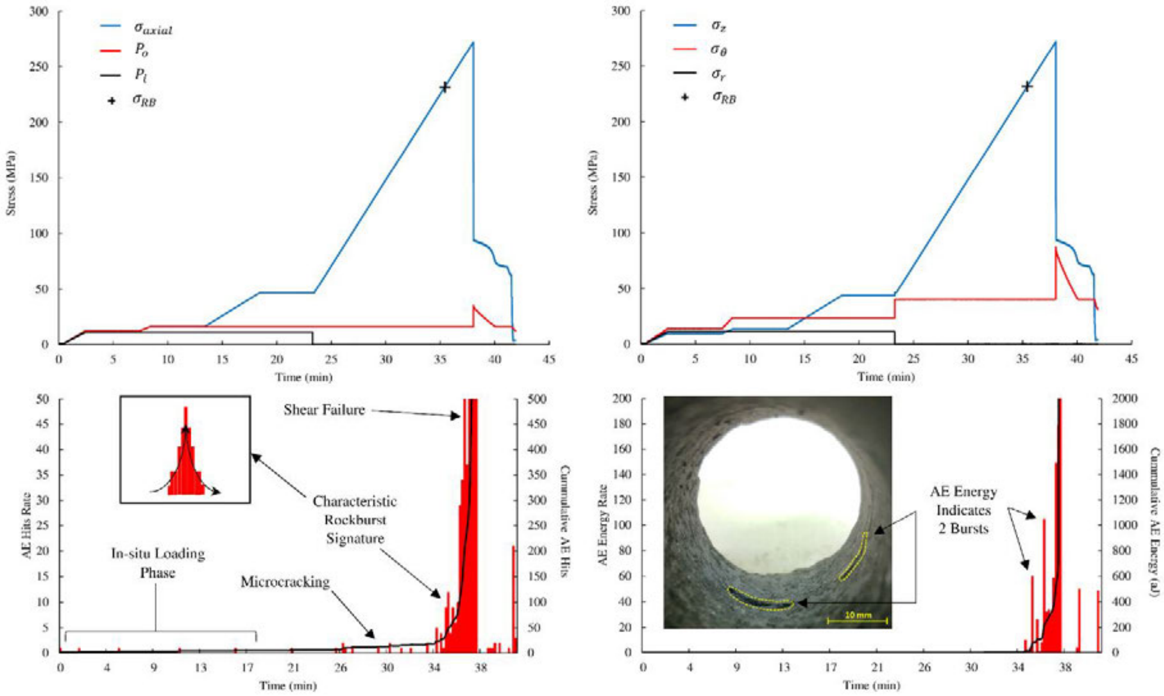

Figure 5-7: Investigative rockburst test results (RB0)

5.4 Test results

To ensure the test method was able to consistently replicate a rockburst event in the laboratory a total of nine additional tests were performed. Three were conducted at the same level of in-situ pressure as described in the previous section, then increased to 1.25 and 1.5 times in-situ pressure for the remaining six tests (three for each in-situ pressure). The full results of each test is displayed in Figures 5-8 to 5-16 following the discussion of each test below.

Figure 5-8 shows the first test conducted using the full predictive methodology. It can be seen that the loading was stopped when rockburst was believed to have occurred and it was confirmed when the crater was observed after the test. Therefore, immediately the methodology was confirmed and it was possible to create rockburst without the full shear failure of a specimen. The following test, shown in Figure 5-9, recorded three distinct rockburst peaks, which correlated exactly with the number of bursts observed in the specimen after the experiment. The last original in-situ pressure test (Figure 5-10) was stopped right when a large AE signature was recorded. Upon inspection post-test it was found that there was burst and the signal was high energy due to the closely spaced nature of the failure zones. This test also recorded a sudden spike in AE energy signature prior to rockburst. This was an isolated response and no physical justification could be found in the specimen post-test.

All three tests conducted at 1.25x the in-situ pressure (Figures 5-11 to 5-13) displayed more widespread bursting than those conducted at 1x in-situ pressure. The recorded AE responses were also much more prevalent and over a wider range of axial pressure. The physical observations of these test revealed that there were multiple bursts in each specimen, or for the case of Figure 5-13, the burst zone was elongated and could have been formed by two or more burst zones.

Once the in-situ pressure was increased to 50% higher than the original it was found to cause highly variable behaviour, ranging from similar to 1x in-situ pressure (Figure 5-16) to wide spread bursting with distinct AE signatures (Figures 5-14 and 5-15). It was also found that at these pressures, the test was more difficult to control due to the loading rates used. Therefore, for future testing it is proposed to develop a control system which institutes cylindrical coordinate pressures, not the triaxial pressures used in this study. This would require the development of computer algorithms to convert the analogue signals of the existing apparatus to digital control outputs. This development is addressed briefly in the future work section of this dissertation.

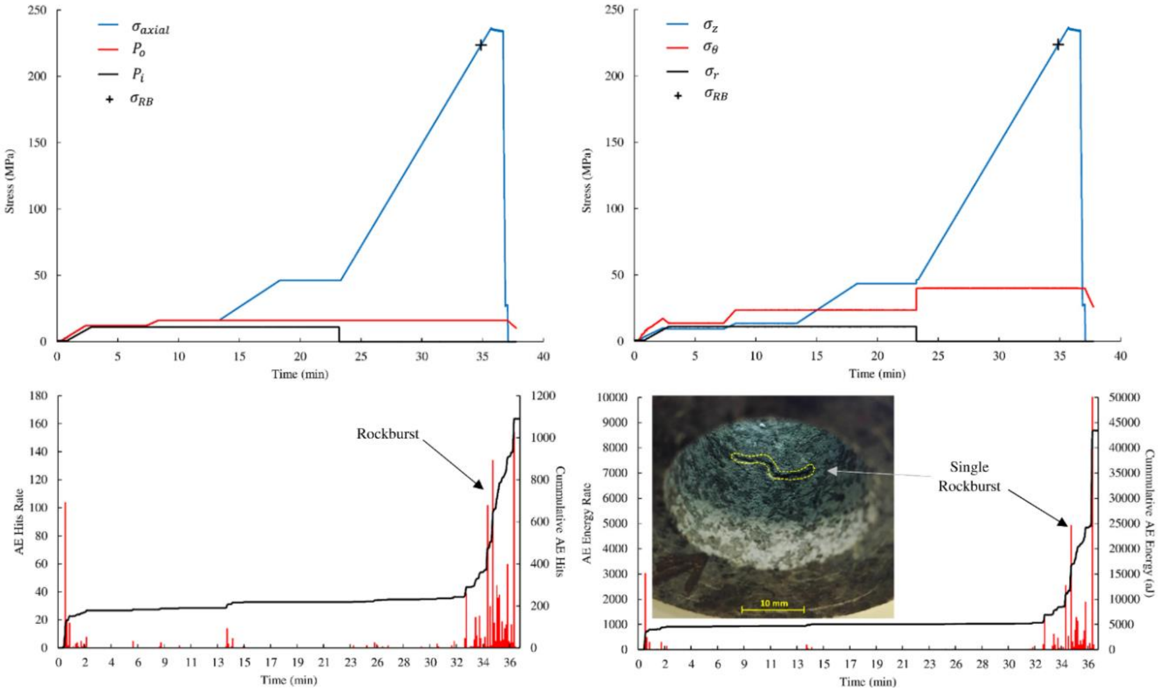

Figure 5-8: RB1 test results (1x in-situ pressure)

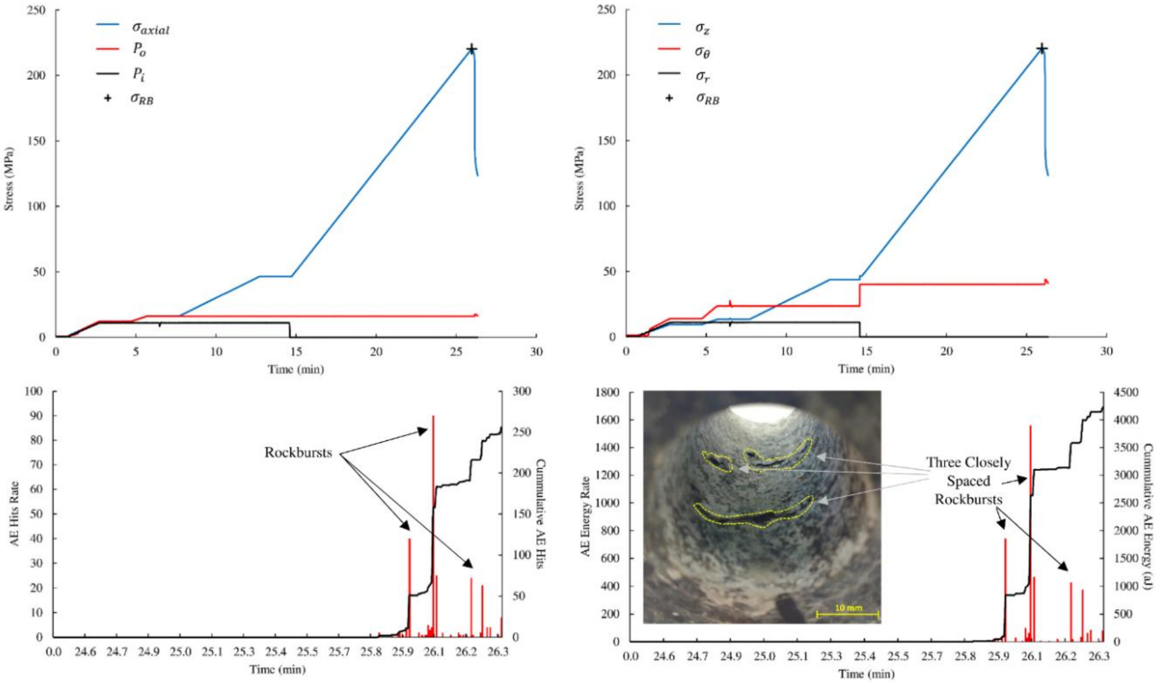

Figure 5-9: RB2 test results (1x in-situ pressure)

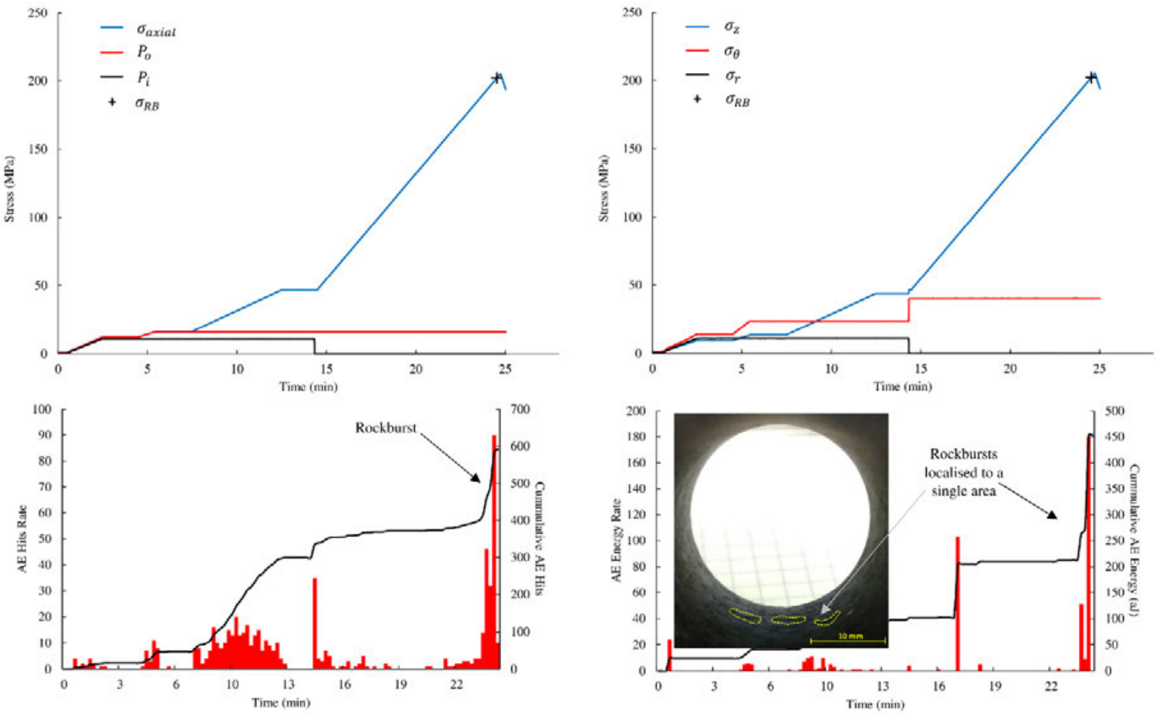

Figure 5-10: RB3 test results (1x in-situ pressure)

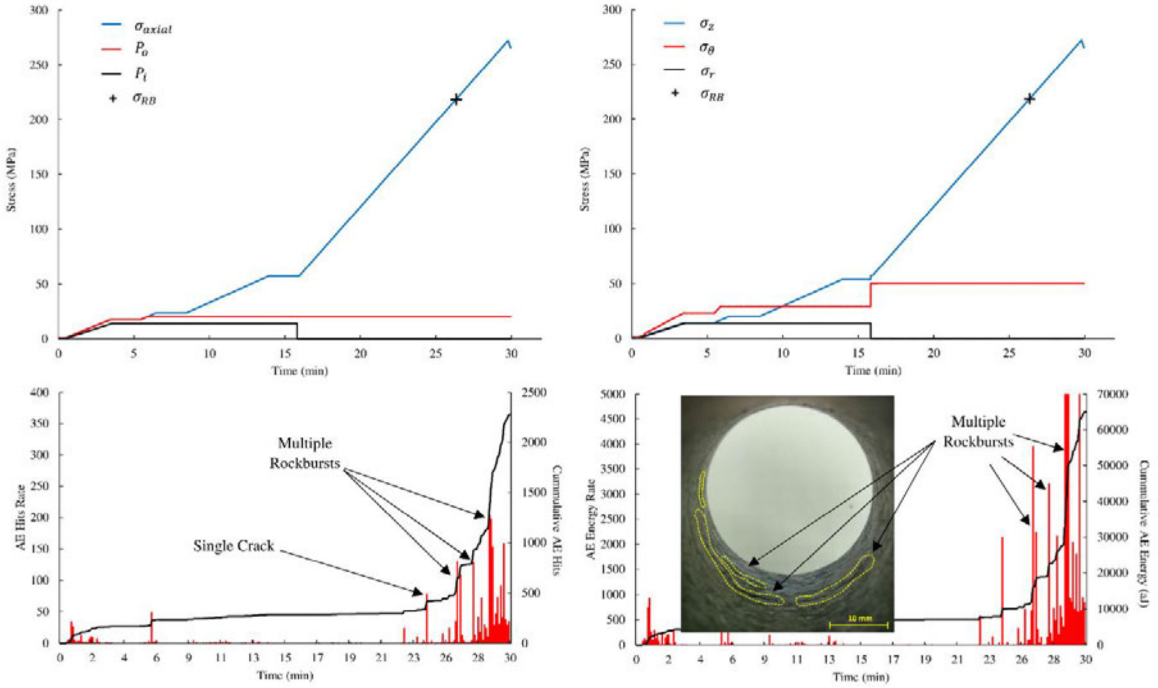

Figure 5-11: RB4 test results (1.25x in-situ pressure)

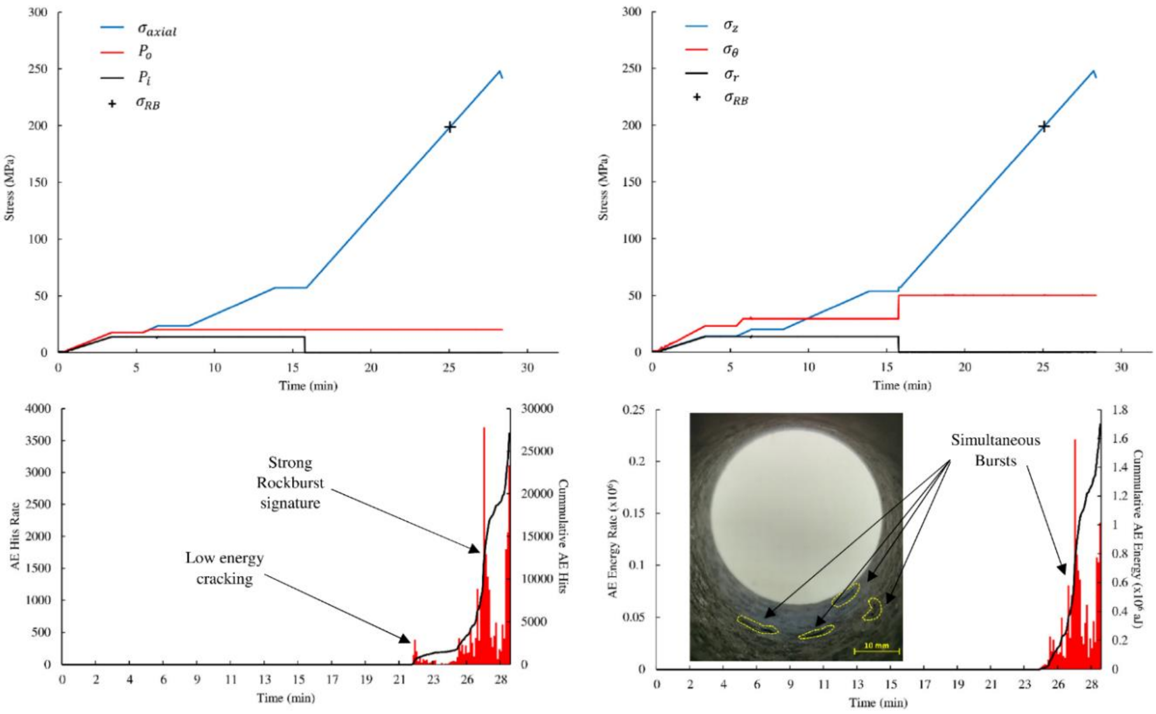

Figure 5-12: RB5 test results (1.25x in-situ pressure)

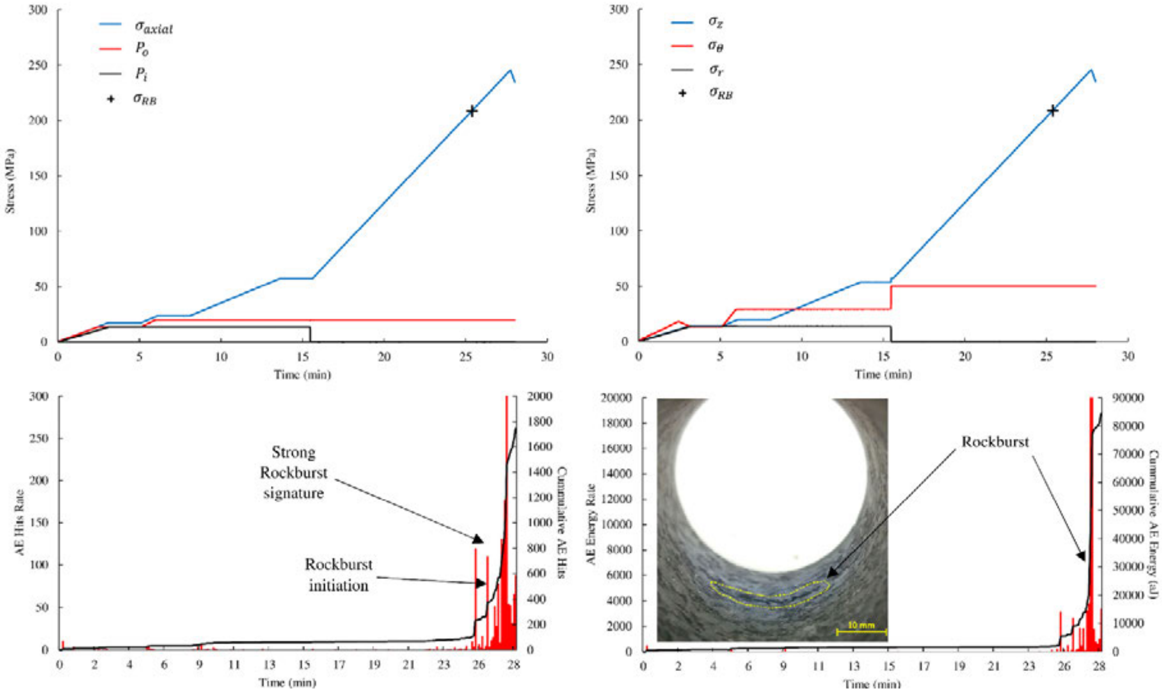

Figure 5-13: RB6 test results (1.25x in-situ pressure)

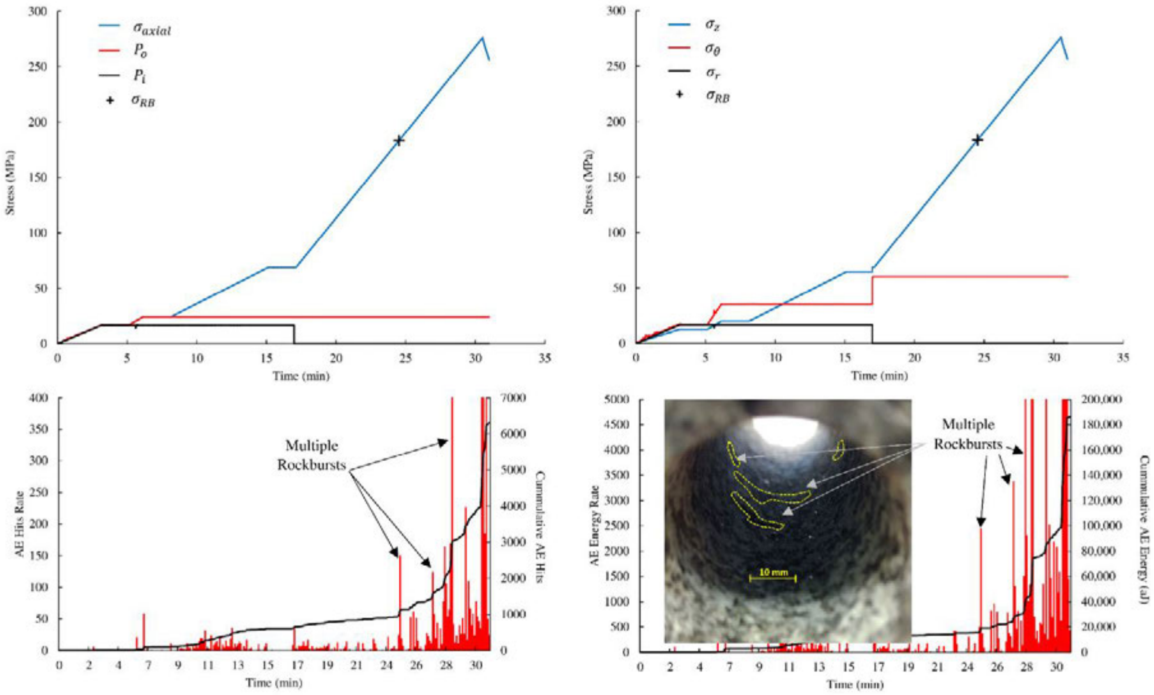

Figure 5-14: RB7 test results (1.5x in-situ pressure)

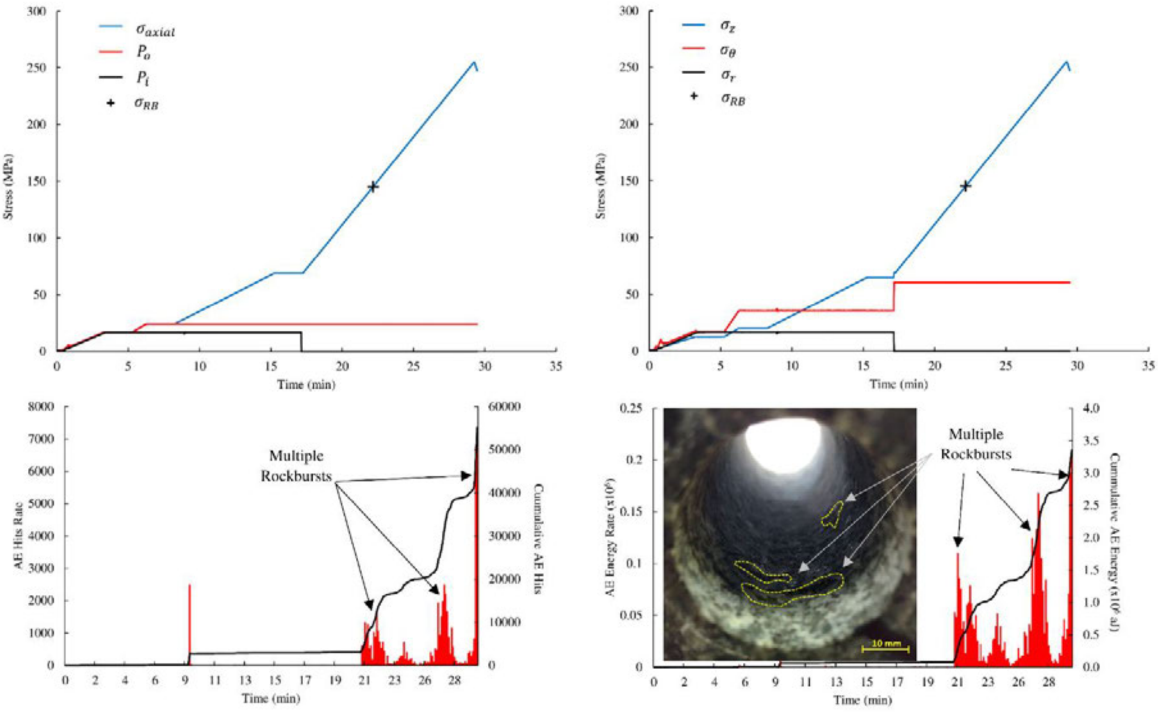

Figure 5-15: RB8 test results (1.5x in-situ pressure)

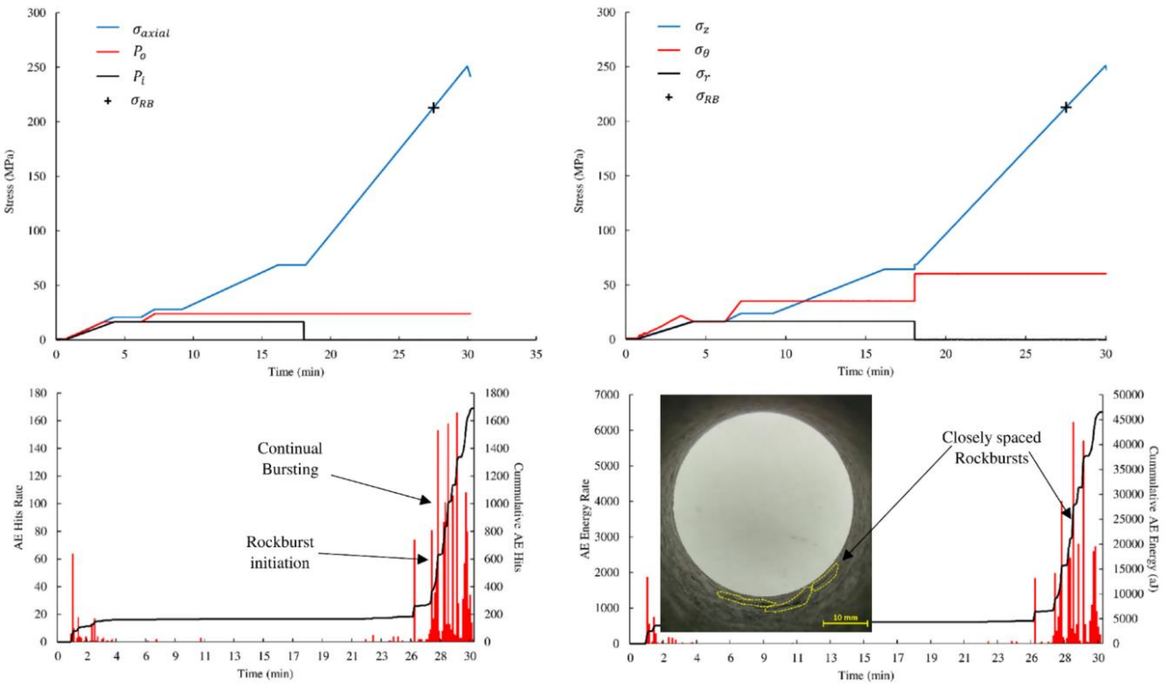

Figure 5-16: RB9 test results (1.5x in-situ pressure)

5.5 Discussion

It is clear from the results presented in the previous section that the new method of testing does replicate small scale rockburst in the borehole of each specimen. Through acoustic emissions (AE) it was possible to predict the occurrence of bursting and stop each test before complete shear failure. Therefore, the failure zones were preserved in the otherwise intact specimens (Figures 7 to 16). Although only small chips and fractures were observed, the scale of the specimens being tested produced burst sites analogous to the full excavation scale. Furthermore, as each test revealed the same characteristic rockburst AE signature, it could be concluded that the prediction method is accurate to identify bursting within the specimens. However, as this method is subjective, another technique for identifying burst would be to pair this with the increase in slope of cumulative AE energy. It was observed in all tests that the characteristic AE hits and energy would suddenly increase above the elastic loading threshold then slowly decrease. This would be apparent in the cumulative response of AE energy as an increase in slope followed by a plateau (see the sites for each rockburst response in Figures 7 to 16). Therefore, using this cumulative approach, the sudden increase in slope and levelling out of the curve could provide another robust indication of rockburst in future tests.

To further verify the testing apparatus, a detailed investigation of the stress states leading to burst was conducted. It can be seen in Figure 5-17 that the σ_1-σ_3 stress path for the tests conducted in this research was similar to the conceptual stress path for delayed bursting outlined by He *et al.* (2012). It is important to note that as there was no conventional triaxial compression data available for the rock tests and the Hoek-Brown (HB) failure envelope was created using the uniaxial compressive strength (UCS) and standard constants for granitic rock. However, the shape of the surface does not affect the intersection of the principal stress axis and as such, does not affect the conclusions drawn from Figure 5-17. From the figure it is evident that the higher the in-situ pressure of the test, the further the bursting point away from the UCS of the rock. This is due to the effect of the intermediate principal stress on the face, which is not taken into account in the conceptual model proposed by He *et al.* (2012). Therefore, this result shows that the testing conducted in this research does accurately replicate the conditions for delayed rockburst.

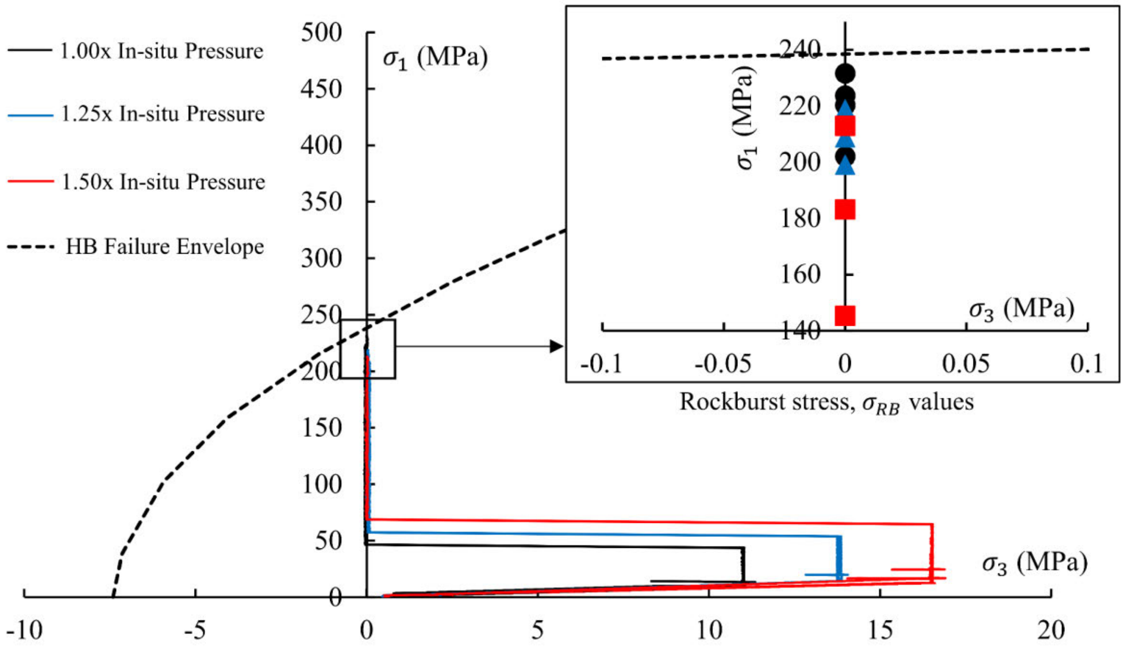

Figure 5-17: σ_1-σ_3 stress paths showing rockburst stress levels compared to failure envelope

The rock used in this study was very strong and homogenous to avoid the complications imposed by weak and jointed strata. To gain some insight into the pressure required for instantaneous burst, the hydrostatic (p) and deviatoric (q) stress paths were plotted in Figure 5-18. The stress measures used for this figure are given by:

$$p = \frac{1}{3}[\sigma_z + \sigma_\theta + \sigma_r] \tag{5-4}$$

$$q = \sqrt{3J_2} = \sqrt{\frac{1}{2}[(\sigma_z - \sigma_\theta)^2 + (\sigma_\theta - \sigma_r)^2 + (\sigma_r - \sigma_z)^2]} \tag{5-5}$$

From this chart it is observed that the rockburst stress state (apart from the identified outlier) occurs at a hydrostatic stress (p) around the level required for UCS failure, approximately 240/3 = 80 MPa. Given this relationship, the predicted pressure required for instantaneous burst would be three times the in-situ pressure in this study. This corresponds to a theoretical depth of 3900 m. Therefore, the pressure at which this rock would possibly display instantaneous burst is predicted to be much higher than possible engineering excavations.

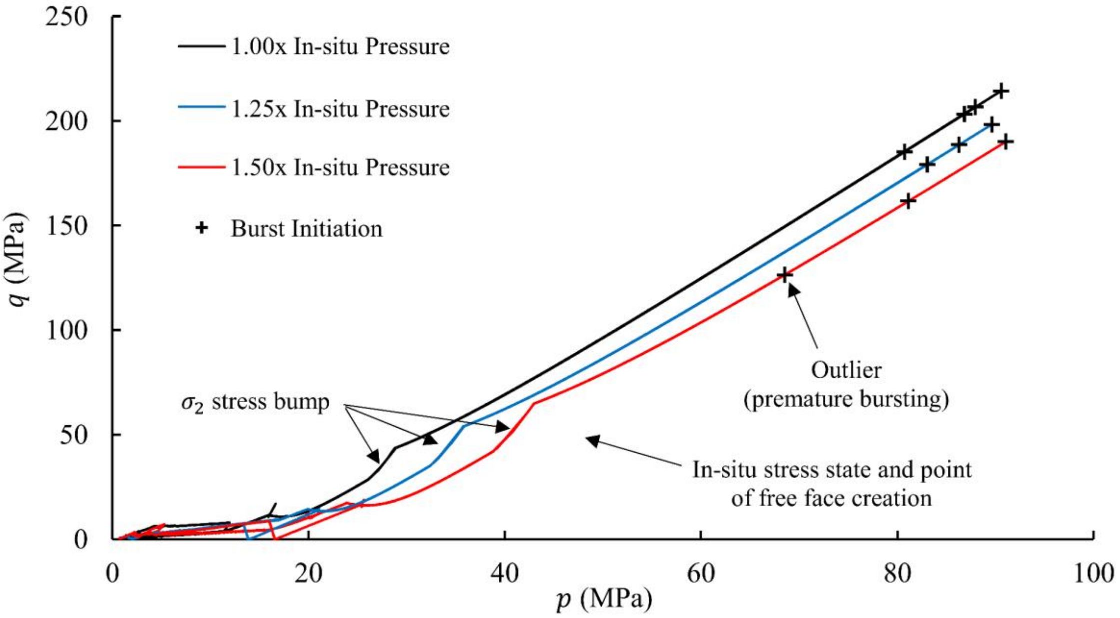

Figure 5-18: p-q stress paths for rockburst tests highlighting the critical burst pressures

Furthermore, Figure 5-18 displayed an anomaly at the time of internal pressure release. This was deemed to be a stress ‘bump’ caused by the immediate redistribution of in-situ stress at the time of free face creation.

To better understand this stress-state at the time of bursting, the three dimensional stress path was plotted, displayed in Figure 5-19, where the major, intermediate and minor principal stresses are given by the axial, tangential and radial cylindrical stresses respectively. It can be seen in this figure that when the internal pressure for each test was released, a sudden increase in the tangential stress was observed.

This effectively increased the stress state at the wall of the excavation instantaneously with respect to the release of radial stress. This reaction is not captured in the servo-controlled true-triaxial apparatus used in other studies, as the intermediate stress is kept constant throughout the test. This stress ‘bump’ can be seen clearer when graphing the projection of the stress path on the major and intermediate principal stress plane in Figure 5-20.

The influence of the intermediate principal stress (tangential stress) is also highlighted by the apparent linear relationship given in the figure. From this relationship it is also apparent that with increasing in-situ stress, the rock needs less external work once excavation is created.

Therefore, the rockburst susceptibility increases the deeper the excavation is located. This behaviour could prove to be important when rocks are at an in-situ stress level that, upon excavation, this stress bump could cause the intact material to burst due to the sudden increase in energy to the face. The granite used in this study was very high strength and therefore, this phenomenon did not cause bursting, however, weaker burst prone rocks such as limestone and marble could be effected.

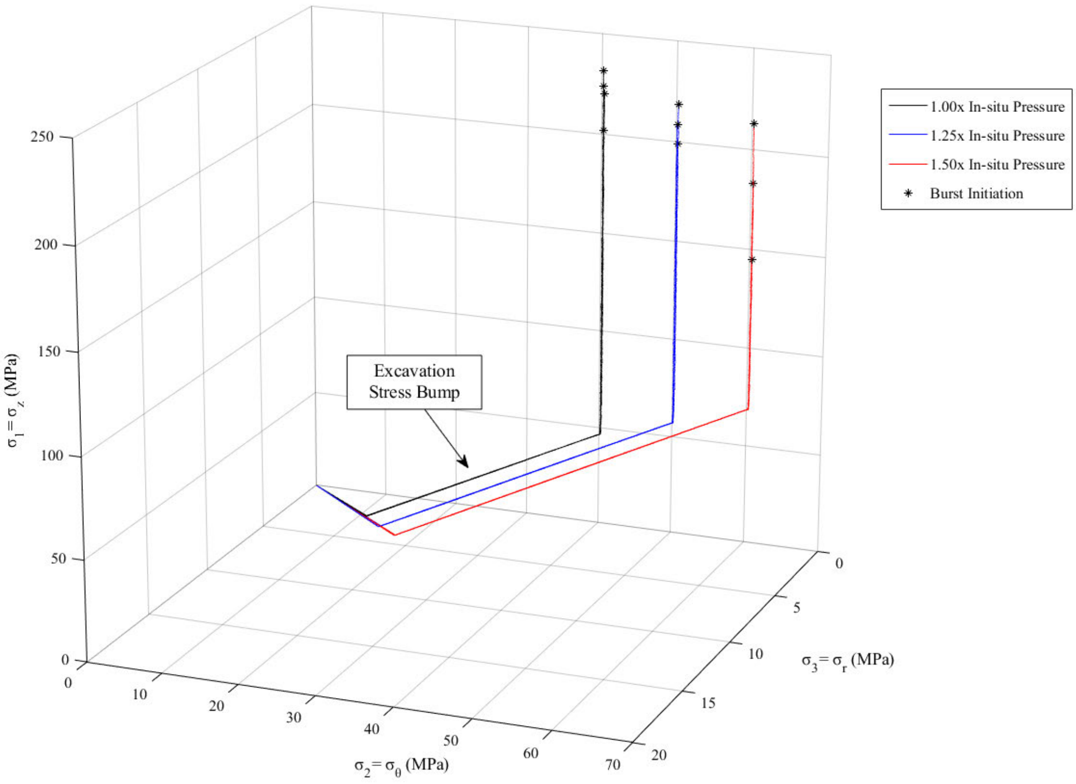

Figure 5-19: Rockburst test principal stress path

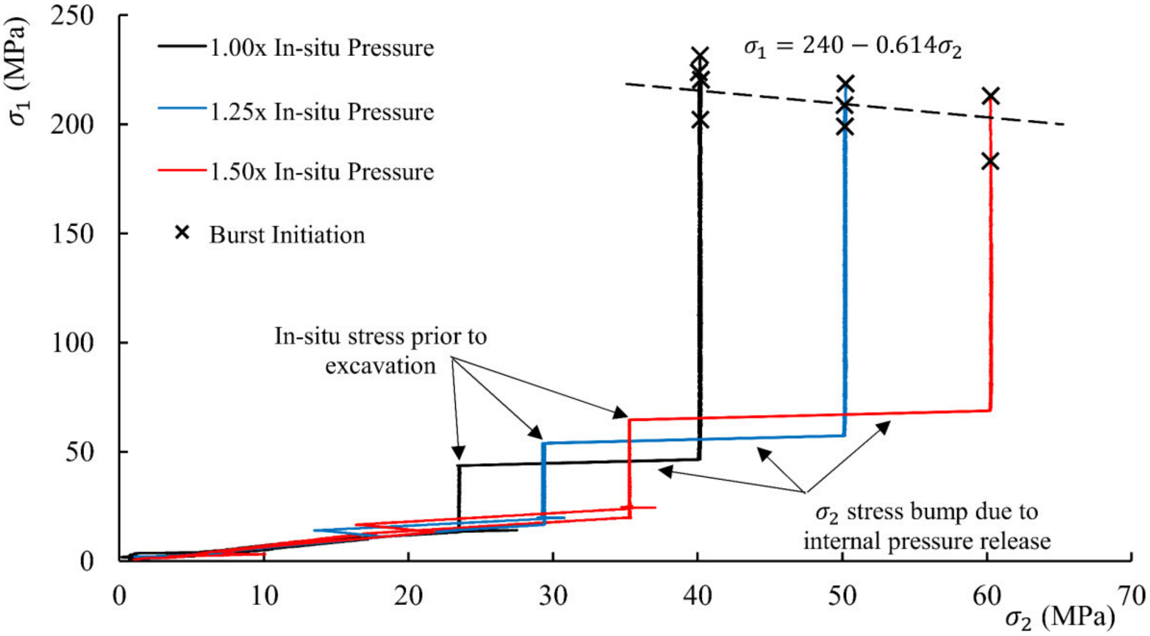

Figure 5-20: Stress path projection onto σ_1-σ_2 plane

As the rockburst stress, σ_{RB} was dependent on the specific test conducted, the deviatoric stress measure at rockburst initiation (q_{RB}) was also used to provide another general, systematic approximation of the stress state at the time of rockburst for this rock type. Once calculated for each test the results were compiled in Table 5-1. It can be seen from the table that the in-situ stress states used for testing correspond to realistic depths for current and future mining operations in hard rock. By examining Figure 5-21, it is clear that as in-situ pressure increases, the deviatoric stress magnitude necessary for bursting decreases. Therefore, as an excavation delves deeper, there is a higher chance of rockburst as the differential stress required for bursting is lower.

Table 5-1: Rockburst stress state results

Test Name	In-situ Level	Approximate Depth (m)	σ_{RB} (MPa)	σ_{θ} (MPa)	q_{RB} (MPa)	Average q_{RB} (MPa)
RB0	1.00x	1300	231.6	40	214.4	202.4
RB1			223.7		206.6	
RB2			220.3		203.2	
RB3			202.0		185.3	
RB4	1.25x	1625	218.7	50	198.4	188.8
RB5			199.0		179.2	
RB6			208.7		188.7	
RB7	1.50x	1950	183.2	60	161.7	159.4
RB8			145.0		126.5	
RB9			212.0		190.1	

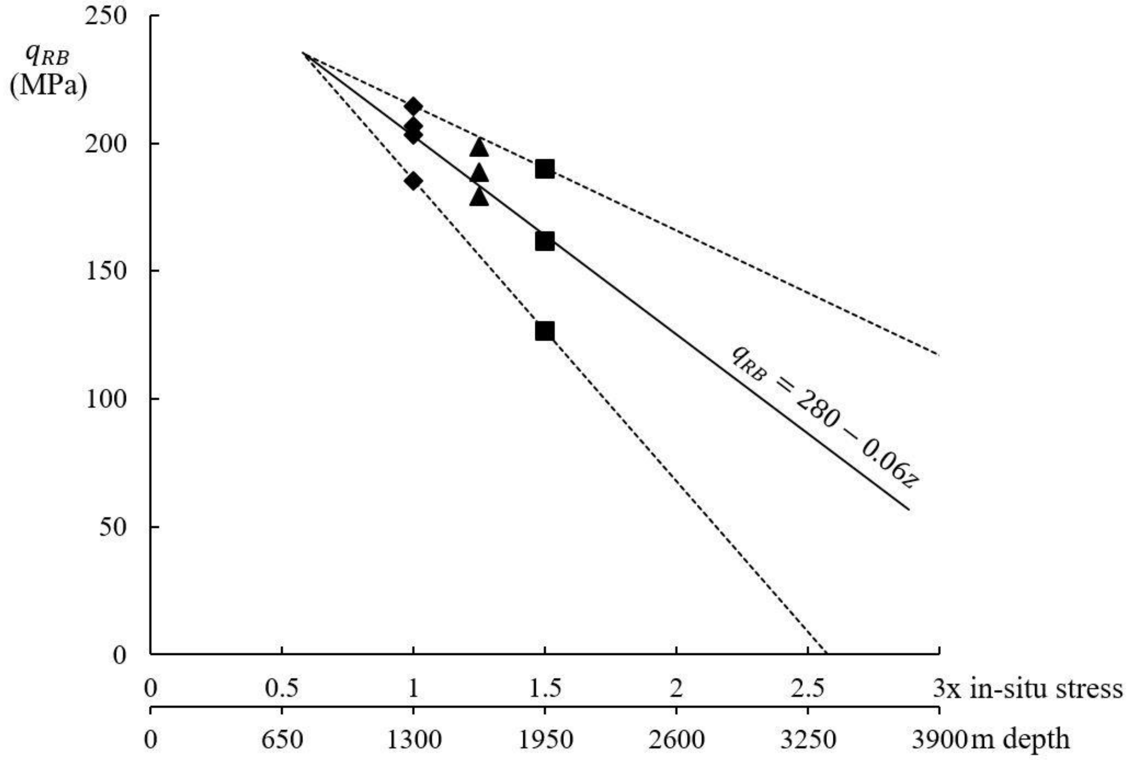

Figure 5-21: Rockburst deviatoric stress vs. in-situ stress/depth

It is also evident in Figure 5-21 that as depth increases (and hence in-situ pressure increases) the range of potential deviatoric stresses for rockburst increases. This is shown as wider ranges of deviatoric stresses, which display the rockburst mechanism. Therefore, this figure may be able to be used and in future expanded upon, to predict key depths in granitic rock where rockburst is likely to occur. On the other hand, as the range of q_{RB} is eliminated at approximately 0.6 times in-situ pressure, it is possible that this signifies the depth at which bursting will not occur and traditional rock mechanics mechanisms could be sufficient to analyse the excavation. To check, future testing should be conducted at higher and lower in-situ pressures to investigate the relationship between q_{RB} range and rockburst occurrence.

5.6 Conclusion

This study outlines the development of a new, innovative apparatus for small scale rockburst testing in the laboratory. The design of the rockburst platens enabled the application of internal pressure to a specimen and the sudden release to simulate an excavation while under in-situ stress. The special consideration of acoustic emission (AE) housings in the platens also enabled the direct contact between sensors and specimen. Therefore, the energy from rockburst could be accurately recorded and analysed. It is clear from the results, that the new apparatus which utilises hollow, cylindrical specimens was able to replicate the stress state conducive to bursting and reveal the same failure signatures as those observed in underground excavations. As such, the following specific conclusions can be drawn:

- The testing methodology was able to initiate delayed rockbursts under a variety of in-situ pressures and lead to the development of a test control strategy. Although subjective, the control method was able to predict rockburst occurrence based purely on the monitoring of AE signals. Given the characteristic rockburst signal it was also possible to determine the number or extent of burst sites.
- Using this new test geometry, the end effects of specimen to platen contact were avoided and bursting was located entirely within the excavation face. Furthermore, upon release of the internal pressure, the stress redistribution at the excavation face was replicated at the laboratory scale and could prove influential in the instantaneous bursting of different rock types under varying in-situ pressures.
- The identified stress ‘bump’ could cause rocks that are close to the threshold of instantaneous burst to undergo violent failure due to the sudden redistribution of energy to the free face of the excavation.

- For bursting to occur, the results of this study show that in general the hydrostatic stress (p) at the excavation face has to be approximately equivalent to the value of uniaxial hydrostatic strength (in the case of this study ~80 MPa).
- The deeper an excavation and hence the higher the in-situ stress, the more likely a rockburst event will occur. It is also evident that there exists a transition between delayed and instantaneous rockburst as depth/in-situ stress increases.
- It is evident from Figure 5-21 that as depth increases, the magnitude of q_{RB} decreases and the range of differential stresses that can accommodate rockburst increases. Therefore, it is suggested that the higher energies stored within the rock with higher in-situ pressures enable much earlier and more prolific bursting. In future it may be possible to use the relationship between deviatoric stress and depth (or in-situ pressure) as a guideline to estimate the propensity of bursting in granitic rock.

Most importantly, this apparatus shows potential as an alternative, more cost effective method for testing rockburst in the laboratory. This in turn, should lead to more data for the development of constitutive models to in future predict and mitigate the threat of bursting in deep underground mines. Additionally, further application of this method could also be used to study the effect of thin spray liners and orientation of excavation (with respect to in-situ stress) on the proneness of bursting.

Finally, as the full stress paths are measured for each test, it should then be possible to plot them in stress space and to validate constitutive models, such as the model described in Chapter 4 of this dissertation. This in turn, gives some indication of the accuracy of a model to replicate the conditions of rockburst and then allows full scale numerical modelling. As such, this is one of the focuses of future research explained in the following section.

Chapter 6 – CONCLUSIONS AND FUTURE WORK

6.1 Conclusions

This thesis provides a strong correlation between the mechanical responses of hard rock observed and measured during experiment and a theoretical framework to accommodate the numerical modelling of rock failure and rockburst. It also devises, for the first time, a new experimental design to both replicate and quantitatively analyse small scale rockburst in the laboratory. This can then be used to provide data to the numerical model to ensure it can capture rockburst behaviour and hence be used for mine scale prediction and simulation. Therefore, the rockburst modelling framework, which can be seen in Figure 6-1, is a direct finding of this study. It was recognised that to create a reliable model, there needs to be a calibration and validation data set to enable the constitutive model to correctly simulate rockburst. As such, several key findings were found to be essential to building this framework.

It was found that when providing a constitutive model with experimental results for calibration, it is important to ensure the data set contains all behaviours and mechanisms associated with the material. In the case of hard rock this includes, full stress-strain and damage data as well as capturing the Class II behaviour under low confinements. Therefore, it is crucial to employ a control method such as the full circumferential control (FFC) used in this study as it allows the rock to undergo self-sustaining failure and hence enables the capture of snap-back. In the context of rockburst, this behaviour is vital in determining the amount of stored and dissipated energy which governs the likelihood and severity of such events. Conversely, if the rock undergoes pre-burst damage accumulation the stored energy is dissipated and it becomes less likely for a rockburst to occur. Therefore, the use of acoustic emission (AE) monitoring gives an important measure of the accumulated damage within the rock specimen. This coupled to the stress state then provides a robust data set for constitutive model calibration.

However, as most constitutive models are calibrated using only the macroscopic stress-strain responses from triaxial tests, this study proposed a new framework to allow the link between damage and stress state to be maintained. It was demonstrated that a single yield-failure criterion can be used to capture the brittle to ductile transition, hardening and softening due to damage instead of using separate criteria for damage and plasticity along with explicitly defined softening/hardening laws. The proposed approach both simplifies the formulation and provides an easy way to correlate the model behaviour with experimental results/findings. As the proposed unified yield-failure function constantly evolves from initial to final failure, it was possible to calibrate the model to damage surfaces, preserving the physical coupling between damage and stress states. This then allows the model to remain reliable when the loading path is changed due to events such as bursting. Pairing this new calibration procedure with an experimentally derived damage evolution law eliminated the need for arbitrary functions and parameters to match limited test data.

Finally, a new small scale laboratory apparatus for rockburst testing was developed to enable cheaper and more consistent experimental data for numerical model validation. To provide a robust data set for validation of a constitutive model it’s crucial to measure the full stress-strain response as well as damage accumulation leading up to rockburst. The uniquely designed platens facilitated the use of acoustic emission sensors in a triaxial cell and therefore, it was possible to gather all relevant data for use in model validation. The successful capture of rockburst characteristic signals allowed the estimation of deviatoric stress measurements for increasing depth and hence, it is concluded that, as depth increases, the magnitude of deviatoric stress decreases. Therefore, this can be used to further enhance the numerical model to identify the stress states conducive to bursting.

Given the findings above, it is clear that this research provides a firm baseline to developing a consistent modelling strategy for rockburst simulation. However, more work needs to be conducted to complete the process outlined by Figure 6-1 and to provide industry with an effective methodology for the modelling of rockburst behaviour. As such, the final section of this dissertation addresses some of the remaining components as well as some shortcomings of the proposed research.

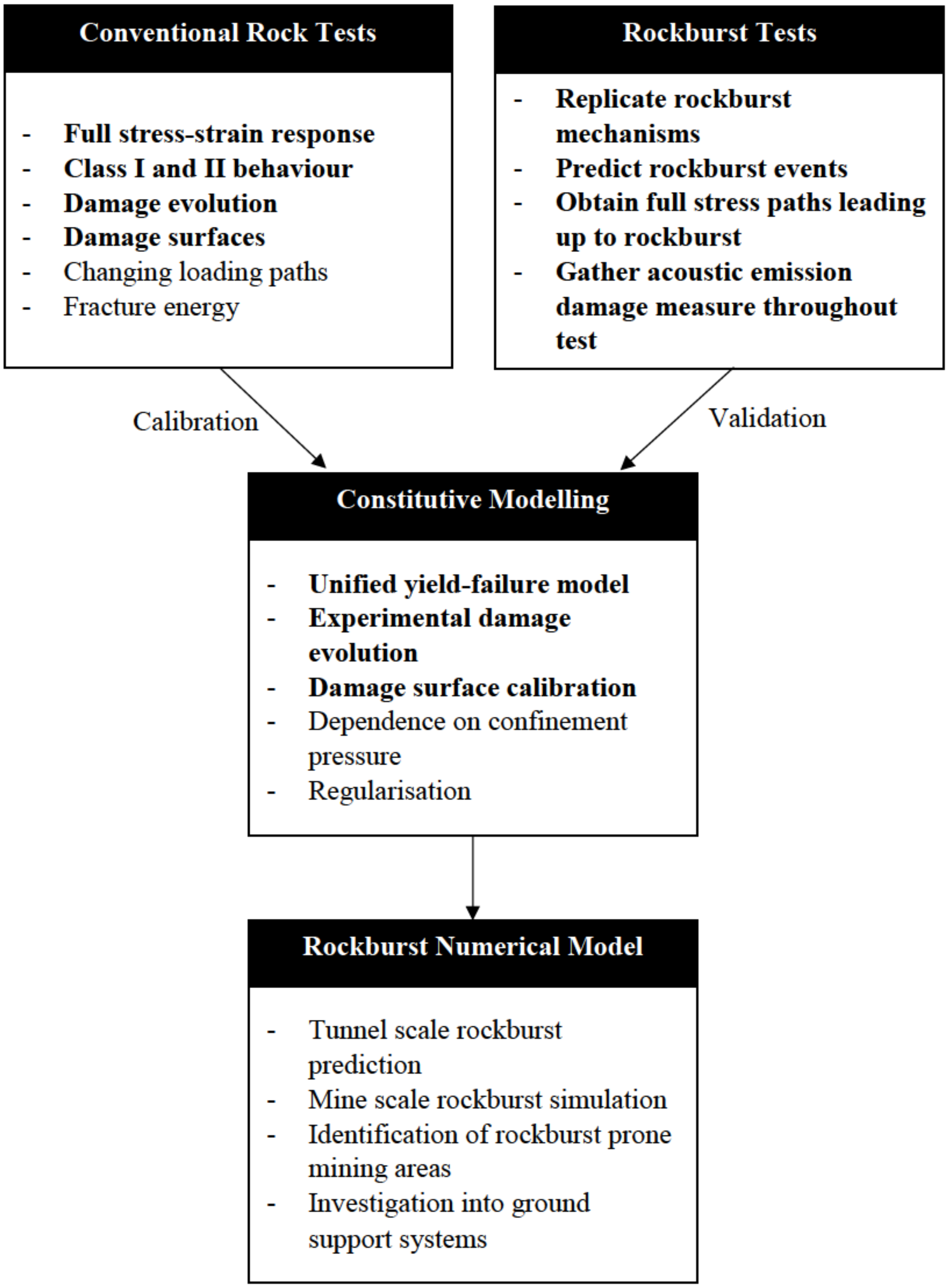

Figure 6-1: Process flowchart for creation of rockburst numerical model

6.2 Future work

As outlined by Figure 6-1, the development of a robust rockburst numerical model requires many aspects from all three fields of experimental, theoretical and numerical rock mechanics. As such, the work conducted in this dissertation was focussed on the development of testing methodologies and a constitutive model to maintain a better link between experiment and theory (shown as bold text in the figure).

Therefore, the main shortcoming of this research is the lack of implementation of the calibrated model into a numerical scheme. Although not within the scope of this study, the regularisation of the constitutive model along with calibration of the localisation behaviour should be investigated. Once calibrated, the model should then be able to be used to simulate rockburst stress paths measured from the experimental apparatus designed in this thesis. Then, once the model is able to replicate the small scale rockburst conditions, it can be used to simulate the tunnel or mine scale to determine the burst prone ground.

More generally, this framework of maintaining the close link between the experimental, theoretical and (in future) numerical aspects of a model could provide some insight into the relationship between material parameters such as elastic fracture properties and rockburst. Some further recommendations are now given for work within the scope in this thesis.

The initial focus of this dissertation was the design of an experimental control method to provide fully coupled stress-strain-damage data to enable the formulation of an appropriate constitutive model. This did provide good data for model calibration, however, more loading paths should be tested in future to ensure the model can describe more complex stress states, i.e. true-triaxial experiments. Given the more advanced data, the constitutive model could then be calibrated or even modified to provide more physicality to the damage-stress relationship. Another important test to be considered is the fracture toughness of the material.

This data could be used to draw more stable conclusions about the unilateral behaviour of the material and hence provide more of a link between tensile and compressive damage processes.

To maintain the link between experimental and theoretical approaches, the proposed damage-plasticity model should also be iteratively improved and re-calibrated to include the material responses from the newly proposed test. The unified yield-failure function proposed in this dissertation excluded the effects of Lode angle to maintain simplicity, however, given future true-triaxial and tensile data, the model should be adjusted. A further investigation should also be conducted on the form of the Lode angle function so it can be appropriately calibrated to test data.

Finally, the full procedure to produce a numerical model for rockburst requires the validation of the model using small scale rockburst tests. A new testing apparatus for rockburst was designed in this research. However, due to the limited implementation of this new test, more tests should be conducted to provide the model with a sufficient rockburst data set. Given the conclusions in Chapter 5, it is necessary to carry out more tests under varying in-situ pressures to determine the role of depth in the behaviour and likelihood of burst. Then once firm conclusions on the stress paths leading to bursting can be drawn, the data set can be compared against simulation to determine the effectiveness of the numerical model. It is also important to test the flexibility of the rockburst apparatus determine the reliability of the data obtained. To this end tests should be conducted on the effect of borehole diameter, loading configuration and the effect of potential weakening due to water infiltration.

Furthermore, to increase accuracy in future rockburst tests the following small improvements should be made to the methodology:

- Introduce more acoustic sensors to the platen set-up to enable the use of location analysis to confirm that the characteristic signals do relate to rockburst location and are not a product of another mechanism.
- Develop control software to directly control the cylindrical stress state throughout the test.

Finally, as rockburst occurs in many mines and civil excavations around the world, the entire methodology for developing a rockburst numerical model should be applied to different rock types. This would further validate the framework or provide new insight into what might be necessary in determining a more accurate alternative.

REFERENCES

Adoko A, Gokceoglu C, Wu L, Zuo Q (2013) Knowledge-based and data driven fuzzy modelling for rockburst prediction. International Journal of Rock Mechanics and Mining Sciences 61:86-95

Akdag S, Karakus M, Taheri A, Nguyen G, He M (2018) Effects of thermal damage on strain burst mechanism for brittle rocks under true-triaxial loading conditions. Rock Mechanics and Rock Engineering 51:1657-1682 doi:https://doi.org/10.1007/s00603-018-1415-3

Alejano L, Alonso E (2005) Considerations of the dilatancy angle in rocks and rock masses. International Journal of Rock Mechanics and Mining Sciences 42:481-507

Alsayed M (2002) Utilising the Hoek triaxial cell for multiaxial testing of hollow rock cylinders. International Journal of Rock Mechanics and Mining Sciences 39:355-366

Arzúa J, Alejano L (2013) Dilation in granite during servo-controlled triaxial strength tests. International Journal of Rock Mechanics and Mining Sciences 61:43-56

Bardet J (1989) Finite element analysis of rockburst as surface instability. Computers and Geotechnics 8:177-193

Batzle M, Simmons G, Siegfried R (1980) Microcrack closure in rocks under stress: direct observation. Journal of Geophysical Research 85:7072-7090

Bieniawski Z (1967a) Mechanism of brittle fracture of rock: Part I - Theory of the fracture process. International Journal of Rock Mechanics and Mining Sciences 4:395-406

Bieniawski Z (1967b) Mechanism of brittle fracture of rock: Part II - Experimental studies. International Journal of Rock Mechanics and Mining Sciences 4:407-423

Bigoni D, Piccolroaz A (2004) Yield criteria for quasibrittle and frictional materials. International Journal of Solids and Structures 41:2855-2878

Bruning T, Karakus M, Nguyen G, Goodchild D Development of a unified yield-failure criterion for the modelling of hard rocks. In: International Conference on Geomechanics, Geo-energy and Geo-resources (IC3G), Melbourne, Australia, 2016.

Bruning T, Karakus M, Nguyen G, Goodchild D (2018) Damage-plasticity model calibration for hard rock with a unified yield-failure function. International Journal of Rock Mechanics and Mining Sciences (Prepared to Submit)

Burlion N, Gatuingt F, Pijaudier-Cabot G, Daudeville L (2000) Compaction and tensile damage in concrete: constitutive modelling and application to dynamics. Computer Methods in Applied Mechanics and Engineering 183:291-308

Butt S, Mukherjee C, Lebans G (2000) Evaluation of acoustic attenuation as an indicator of roof stability in advancing headings. International Journal of Rock Mechanics and Mining Sciences 37:1123-1131

Chang S, Lee C (2004) Estimation of cracking and damage mechanisms in rock under triaxial compression by moment tensor analysis of acoustic emission. International Journal of Rock Mechanics and Mining Sciences 41:1069-1086

Chang S, Lee C, Lee Y (2007) An experimental damage model and its application to the evaluation of the excavation damage zone. Rock Mechanics and Rock Engineering 40:245-285

Chen G, Li T, Zhang G, Yin H, Zhang H (2014a) Temperature effect of rock burst for hard rock in deep-buried tunnel. Natural Hazards 72:915-926

Chen L, Liu J, Wang C, Liu J, Su R, Wang J (2014b) Characterisation of damage evolution in granite under compressive stress condition and its effect on permeability. International Journal of Rock Mechanics and Mining Sciences 71:340-349

Chen L, Shao J, Huang H (2010) Coupled elastoplastic damage modeling of anisotropic rocks. Computers and Geotechnics 37:187-194

Chen L, Wang C, Liu J, Liu J, Wang J, Jia Y, Shao J (2015) Damage and plastic deformation modeling of beishan granite under compressive stress conditions. Rock Mechanics and Rock Engineering 48:1623-1633

Chen W, Han D (1988) Plasticity for structural engineers. Springer-Verlag,

Chen Z, Tang C, Huang R (1997) A double rock sample model for rockbursts. International Journal of Rock Mechanics & Mining Sciences 34:991-1000

Chiarelli A, Shao J, Hoteit N (2003) Modeling of elastoplastic damage behaviour of a claystone. International Journal of Plasticity 19:23-45

Comi C (2001) A non-local model with tension and compression damage mechanisms. European Journal of Mechanics - A/Solids 20:1-22

Comi C, Perego U (2001) Fracture energy based bi-dissipative damage model for concrete. International Journal of Solids and Structures 38:6427-6454

Cook N (1964) The application of seismic techniques to problems in rock mechanics. International Journal of Rock Mechanics & Mining Sciences 1

Cook N (1976) Seismicity associated with mining. Engineering Geology 10:99-122

Cox S, Meredith P (1993) Microcrack formation and material softening in rock measured by monitoring acoustic emissions. International Journal of Rock Mechanics and Mining Sciences 30:11-24

Crisfield M (2000) Non-linear finite element analysis of solids and structures. vol Volume 1: Essentials. John Wiley & Sons, West Sussex, England

Cristescu N, Gioda G (1994) Visco-plastic behaviour of geomaterials. Springer-Verlag, New York

Daniell J, Love D The socio-economic impact of historic australian earthquakes. In: Australian Earthquake Engineering Society, Perth, Australia, 2010.

Eberhardt E, Stead D, Stimpson B (1999) Quantifying progressive pre-peak brittle fracture damage in rock during uniaxial compression. International Journal of Rock Mechanics and Mining Sciences 36:361-380

Eberhardt E, Stead D, Stimpson B, Read R (1998) Identifying crack initiation and propagation thresholds in brittle rock. Canadian Geotechnical Journal 35:222-233

Eloranta P (2004) Forsmark site investigation, Drill hole KFM01A, Triaxial compression test (HUT), P-04-177. Helsinki University of Technology, Rock Engineering, Stockholm, Sweden

Ewy R, Cook N (1990) Deformation and fracture around cylindrical openings in rock - I oberservations and analysis of deformations. International Journal of Rock Mechanics and Mining Sciences and Geomechanical Abstracts 27:387-407

Fairhurst C, Hudson J (1999) Draft ISRM suggested method for the complete stress-strain curve for intact rock in uniaxial compression. International Journal of Rock Mechanics and Mining Sciences 36:279-289

Fakhimi A, Hosseini O, Theodore R (2016) Physical and numerical study of strain burst of mine pillars. Computers and Geotechnics 74:36-44

Feng X *et al.* (2012) Studies on the evolution process of rockbursts in deep tunnels. Journal of Rock Mechanics and Geotechnical Engineering 4:289-295

Fonseka G, Murrell S, Barnes P (1985) Scanning electron microscope and acoustic emission studies of crack development in rocks. International Journal of Rock Mechanics and Mining Sciences and Geomechanical Abstracts 22:273-289

Fredrich J, Wong T (1986) Micromechanics of thermally induced cracking in three crustal rocks. Journal of Geophysical Research 91:12743-12764

Ghazvinian E, Diederichs M, Labrie D, Martin C (2015) An investigation on the fabric type dependency of the crack damage thresholds in brittle rocks. Geotechnical & Geological Engineering 33:1409-1429

Gong Q, Yin L, Wu S, Zhao J, Ting Y (2012) Rock burst and slabbing failure and its influence on TBM excavation at headrace tunnels in Jinping II hydropower station. Engineering Geology 124:98-108

Gong W, Peng Y, Wang H, He M, Ribeiro e Sousa L, Wang J (2014) Fracture angle analysis of rock burst faulting planes based on true-triaxial experiment. Rock Mechanics and Rock Engineering:1-23

Grassl P, Jirasek M (2006) Damage-plastic model for concrete failure. International Journal for Solids and Structures 43:7166-7196

Grosse C, Ohtsu M (2008) Acoustic Emission Testing. Springer, Germany

Hajiabdolmajid V, Kaiser P, Martin C (2002) Modelling brittle failure of rock. International Journal of Rock Mechanics and Mining Sciences 39:731-741

Hashemi S, Taheri A, Melkoumian N (2015) An experimental study on the relationship between localised zones and borehole instability in poorly cemented sands. Journal of Petroleum Science and Engineering 135:101-117

Hatzor Y, Palchik V (1997) The influence of grain size and porosity on crack initiation stress and critical flaw length in dolomites. International Journal of Rock Mechanics and Mining Sciences 34:805-816

He M, Miao J, Feng J (2010a) Rock burst process of limestone and its acoustic emission characteristics under true-triaxial unloading conditions. International Journal of Rock Mechanics and Mining Sciences 47:286-298

He M, Nie W, Han L, Ling L (2010b) Microcrack analysis of Sanya granite fragments from rockburst tests. Mining Science and Technology 20:238-243

He M, Sousa L, Miranda T, Zhu G (2015a) Rockburst laboratory tests database - Application of data mining techniques. Engineering Geology 185:116-130

He M, Xia H, Jia X, Gong W, Zhao F, Liang K (2012) Studies on classification, criteria and control of rockbursts. Journal of Rock Mechanics and Geotechnical Engineering 4:97-114

He M, Zhao F, Cai M, Du S (2015b) A novel experimental technique to simulate pillar burst in laboratory. Rock Mechanics and Rock Engineering 48:1833-1848

Heo J, Cho H, Lee C (2001) Measurement of acoustic emission and source location considering anisotropy of rock under triaxial compression. In: Sarkka, P, Eloranta, P, editors Rock mechanics - A challenge for society Swets & Zeitlinger Lisse, Espoo Finland:91-96

Hidalgo K, Nordlund E (2013) Comparison between stress and strain quantities of the failure-deformation process of fennoscandian hard rocks using geological information. Rock Mechanics and Rock Engineering 46:41-51

Hoek E, Carranza-Torres C, Corkum B (2002) Hoek-Brown failure criterion - 2002 edition. Paper presented at the Fifth North American Rock Mechanics Symposium (NARMS-TAC), University of Toronto, Toronto,

Hoek E, Martin C (2014) Fracture initiation and propagation in intact rock - A review. Journal of Rock Mechanics and Geotechnical Engineering 6:287-300

Hoskins E (1969) The failure of thick-walled hollow cylinders of isotropic rock. International Journal of Rock Mechanics and Mining Sciences 6:99-125

Huang R, Wang X, Chan L (2000) Triaxial unloading test of rocks and its implication for rockburst. Bulletin of Engineering Geology and the Environment 60:37-41

Hudson J, Brown E, Fairhurst C (1970) Shape of the complete stress-strain curve for rock. Paper presented at the Proc. 13th symp. on Rock Mech., University of Illinois, Hudson J, Crouch S, Fairhurst C (1972) Soft, stiff and servo-controlled testing machines: A review with reference to rock failure. Engineering Geology 6:155-189

ISRM (2007) The complete ISRM suggested methods for rock characterization, testing and monitoring: 1974-2006. Prepared by the commission on testing methods, Ulusay R, Hudson JA, editors. ISRM, Ankara, Turkey

Jacobsson L (2004a) Forsmark site investigation, Borehole KFM01A, Triaxial compression test of intact rock, P-04-227. SP Swedish National Testing and Research Institute, Stockholm, Sweden

Jacobsson L (2004b) Oskarshamn site investigation, Borehole KLX04A, Triaxial compression test of intact rock, P-04-262. SP Swedish National Testing and Research Institute, Stockholm, Sweden

Jaeger J, Cook N, Zimmerman R (2007) Fundamentals of rock mechanics. 4th edn. Blackwell Publishing Ltd.,

Jason L, Huerta A, Pijaudier-Cabot G, Ghavamian S (2006) An elastic plastic damage formulation for concrete: Application to elementary tests and comparison with an isotropic damage model. Computer Methods in Applied Mechanics and Engineering 195:7077-7092

Ji M, Zhang Y, Liu W, Cheng L (2014) Damage evolution law based on acoustic emission and weibull distribution of granite under uniaxial stress. Acta Geodynamics et Geomaterialia 11:269-277

Jiang Q, Feng X-T, Xiang T-B (2010) Rockburst characteristics and numerical simulation based on a new energy index: a case study of a tunnel at 2,500m depth. Bulletin of Engineering Geology and the Environment 69

Jirasek M, Rolshoven S, Grassl P (2004) Size effect on fracture energy induced by non-locality. International Journal for Numerical and Analytical Methods in Geomechanics 28:653-670

Katz O, Reches Z (2004) Microfracturing, damage and failure of brittle granites. Journal of Geophysical Research 109:B01206

Kim J, Lee K, Cho W, Choi H, Cho G (2015) A comparative evaluation of stress-strain and acoustic emission methods for quantitative damage assessments of brittle rock. Rock Mechanics and Rock Engineering 48:495-508

Krajcinovic D (1996) Damage Mechanics. North-Holland, Amsterdam

Labiouse V, Sauthier C, You S (2014) Hollow cylinder simulation experiments of galleries in boom clay formation. Rock Mechanics and Rock Engineering 47:43-55 doi:10.1007/s00603-012-0332-0

Labuz J, Biolzi L (1991) Class I vs Class II stability: A demonstration of size effect. International Journal of Rock Mechanics and Mining Sciences and Geomechanical Abstracts 28:199-205

Lasdon L, Fox R, Ratner M (1974) Nonlinear optimization using the generalized reduced gradient method. Revue Francaise de Automatique, de Informatique et de Recherche Operationnelle 8:73-103

Lee D, Juang C, Chen J, Lin H, Shieh W (1999) Stress paths and mechanical behavior of a sandstone in hollow cylinder tests. International Journal of Rock Mechanics and Mining Sciences 36:857-870

Lee J, Fenves G (1998) Plastic-damage model for cyclic loading of concrete structures. Journal of Engineering Mechanics 124:892-900

Lemaitre J (1992) A course on damage mechanics. Springer-Verlag, Germany

Lemaitre J, Desmorat R (2005) Engineering Damage Mechanics. Springer-Verlag, Berlin

Li X, Du K, Li D (2015) True triaxial strength and failure modes of cubic rock specimens with unloadig the minor principal stress. Rock Mechanics and Rock Engineering 48:2185-2196

Liu D, Li D, Zhao F, Wang C (2014) Fragmentation characteristics analysis of sandstone fragments based on impact rockburst test. Journal of Rock Mechanics and Geotechnical Engineering 6:251-256

Lockner D (1993) The role of acoustic emission in the study of rock fracture. International Journal of Rock Mechanics and Mining Sciences and Geomechanics Abstracts 30:883-899

Lubliner J, Oliver J, Oller S, Onate E (1989) A plastic-damage model for concrete. International Journal for Solids and Structures 25:299-326

Luccioni B, Rougier V (2005) A plastic damage approach for confined concrete. Computers and Structures 83:2238-2256

Lyakhovsky V, Zhu W, Shalev E (2015) Visco-poroelastic damage model for brittle-ductile failure of porous rocks. Journal of Geophysical Research: Solid Earth 120:2179-2199

Ma L, Yang F, Xu H, Xie Z (2017) Post-yield properties of rock salt using the concept of mobilized strength components and the dilation angle. Geotechnical & Geological Engineering 35:2841-2849

Ma T, Tang C, Tang L, Zhang W, Wang L (2015) Rockburst characteristics and microseismic monitoring of deep-buried tunnels for Jinping II hydropower station. Tunnelling and Underground Space Technology 49:345-368

Mansurov V (2001) Prediction of rockbursts by analysis of induced seismicity data. International Journal of Rock Mechanics & Mining Sciences 38:893-901

Martin C (1993) The strength of massive Lac du Bonnet granite around underground openings. PhD Thesis, University of Manitoba, USA.

Martin C (1997) Seventeenth canadian geotechnical colloquium: The effect of cohesion loss and stress path on brittle rock strength. Canadian Geotechnical Journal 34:698-725

Martin C, Chandler N (1994) The progressive fracture of Lac du Bonnet granite. International Journal of Rock Mechanics & Mining Sciences and Geomechanical Abstracts 31:643-659

Mir A, Nguyen G, Sheikh A, Vu V (2016) Modelling dilatant and contractive behaviour in soft rocks. Paper presented at the International conference on geomechanics, geo-energy and geo-resources IC3G, Melbourne, Australia,

Mogi K (1971) Fracture and flow of rocks under high triaxial compression. Journal of Geophysical Research 76:1255-1269

Mukherjee M, Nguyen G, Mir A, Bui H, Shen L, El-Zein A, Maggi F (2017) Capturing pressure and rate-dependent behaviour of rocks using a new damage-plasticity model. International Journal of Impact Engineering 1:1-11

Murakami S (2012) Continuum Damage Mechanics. Springer, London

Nguyen G, Einav I (2009) The energetics of cataclasis based on breakage mechanics. Pure and Applied Geophysics 166:1693-1724

Nguyen G, Houlsby G (2008) A coupled damage-plasticity model for concrete based on thermodynamic principles: Part I: model formulation and parameter identification. International Journal for Numerical and Analytical Methods in Geomechanics 32:353-389

Nicksiar M, Martin C (2012) Evaluation of methods for determining crack initiation in compression tests on low-porosity rocks. Rock Mechanics and Rock Engineering 45:607-617

Oda M, Takemura T, Aoki T (2002) Damage growth and permeability change in triaxial compression tests of Inada granite. Mechanics of Materials 34:313-331

Ortlepp W (2000) Observation of mining-induced faults in an intact rock mass at depth. International Journal of Rock Mechanics & Mining Sciences 37:423-436

Ortlepp W (2001) The behaviour of tunnels at great depth under large static and dynamic pressures. Tunnelling and Underground Space Technology 16:41-48

Ortlepp W RaSiM comes of age—a review of the contribution to the understanding and control of mine rockbursts. In: Sixth International Symposium on Rockburst and Seismicity in Mines, Perth, Australia, 2005.

Ortlepp W, Stacey T (1994) Rockburst mechanisms in tunnels and shafts. Tunnelling and Underground Space Technology 9:59-65

Paterson M, Wong T (2005) Experimental Rock Deformation - The Brittle Field. Springer, Berlin, Germany

Penasa M, Piccolroaz A, Argani S, Bigoni D (2014) Integration algorithms of elastoplasticity for ceramic powder compaction. Journal of the European Ceramic Society 34:2775-2788

Puzrin A (2012) Constitutive Modelling in Geomechanics. Springer-Verlag, Berlin, Germany

Robertson E (1955) Experimental study of the strength of rocks. Bulletin of the Geological Society of America 66:1275-1314

Salari M, Saeb S, William K, Pachet S, Carrasco R (2004) A coupled elastoplastic damage model for geomaterials. Computer Methods in Applied Mechanics and Engineering 193:2625-2643

Schofield A, Wroth P (1968) Critical state soil mechanics. McGraw-Hill, London

Shah K (1997) An elasto-plastic constitutive model for brittle-ductile transition in porous rocks. International Journal of Rock Mechanics and Mining Sciences 34

Stupkiewicz S, Denzer R, Piccolroaz A, Bigoni D (2014) Implicit yield function formulation for granular and rock-like materials. Computational Mechanics 54:1163-1173

Su G, Jiang J, Zhai S, Zhang G (2017) Influence of tunnel axis stress on strainburst: an experimental study. Rock Mechanics and Rock Engineering 50:1551-1567

Summers R, Byerlee J (1977) Summary of results of frictional sliding studies, at confining pressures up to 6.98 kb, in selected rock materials. US Department of Interior Geological Survey:77-142

Tang C, Wang J, Zhang J (2010) Preliminary engineering application of microseismic monitoring technique to rockburst prediction in tunneling of Jinping II project. Chinese Journal of Rock Mechanics and Engineering 2:193-208

Tapponnier P, Brace W (1976) Development of stress-induced microcracks in Westerly granite. International Journal of Rock Mechanics and Mining Sciences and Geomechanical Abstracts 13:103-112

Tarasov B Superbrittleness of rocks at high confining pressure. In: Van Sint Jan M, Potvin Y (eds) Fifth International Seminar on Deep and High Stress Mining, Santiago, Chile, 2010. The Australian Centre for Geomechanics,

Tarasov B, Randolph M (2008) Frictionless shear at great depth and other paradoxes of hard rocks. International Journal of Rock Mechanics and Mining Sciences 45:316-328

Unteregger D, Fuchs B, Hofstetter G (2015) A damage plasticity model for different types of intact rock. International Journal of Rock Mechanics and Mining Sciences 80:402-411

Walton G, Diederichs M (2015a) Dilation and post-peak behaviour inputs for practical engineering analysis. Geotechnical & Geological Engineering 2015:15-34

Walton G, Diederichs M (2015b) A new model for the dilation of brittle rocks based on laboratory compression test data with separate treatment of dilatancy mobilization and decay. Geotechnical & Geological Engineering 33:661-679

Wang J, Park H (2001) Comprehensive prediction of rockburst based on analysis of strain energy in rocks. Tunnelling and Underground Space Technology 16:49-57

Wawersik W (1968) Detailed analysis of rock failure in laboratory compression tests. PhD Thesis University of Minnesota, USA.

Wawersik W, Brace W (1971) Post-failure behavior of a granite and diabase. Rock Mechanics 3:61-85

Wawersik W, Fairhurst C (1970) A study of brittle rock fracture in laboratory compression experiments. International Journal of Rock Mechanics and Mining Sciences 7:561-575

Wen T, Tang H, Ma J, Wang Y (2018) Evaluation of methods for determining crack initiation stress under compression. Engineering Geology 235:81-97

Weng L, Huang L, Taheri A, Li X (2017) Rockburst characteristics and numerical simulation based on a strain energy density index: A case study of a roadway in Linglong gold mine, China. Tunnelling and Underground Space Technology 69:223-232

Wong T (1982) Micromechanics of faulting in Westerly granite. International Journal of Rock Mechanics and Mining Sciences and Geomechanical Abstracts 19:19-49

Yazdani S, Schreyer H (1990) Combined plasticity and damage mechanics model for plain concrete. Journal of Engineering Mechanics 116:1435-1450

Zang H, Wang G (2012) Surrounding rock stability analysis and rock burst prediction of underground cavity in high in-situ stress. Advanced Materials Research 594-597:1174-1181

Zhang C, Chu W, Liu N, Zhu Y, Hou J (2011) Laboratory tests and numerical simulations of brittle marble and squeezing schist at Jinping II hydropower station, China. Journal of Rock Mechanics and Geotechnical Engineering 3:30-38

Zhang H, Tannant D, Jing H, Nunoo S, Niu S, Wang S (2015a) Evolution of cohesion and friction angle during microfracture accumulation in rock. Natural Hazards 77:497-510

Zhang J, Xu W, Wang H, Wang R, Meng Q, Du S (2016) A coupled elastoplastic damage model for brittle rocks and its application in modelling underground excavation. International Journal of Rock Mechanics & Mining Sciences & Geomechanical Abstracts 84:130-141

Zhang Z, Zhang R, Xie H, Liu J, Were P (2015b) Differences in the acoustic emission characteristics of rock salt compared with granite and marble during the damage evolution process. Environmental Earth Sciences 73:6987-6999

Zhao X, Cai M (2014) Influence of specimen height-to-width ratio on the strainburst characteristics of Tianhu granite under true-triaxial unloading conditions. Canadian Geotechnical Journal 52:890-902

Zhao X, Cai M, Wang J, Li P, Ma L (2015) Objective determination of crack initiation stress of brittle rocks under compression using AE measurement. Rock Mechanics and Rock Engineering 48:2473-2484

Zhao X, Cai M, Wang J, Ma L (2013) Damage and acoustic emission characteristics of the Beishan granite. International Journal of Rock Mechanics and Mining Sciences 64:258-269

Zhao X *et al.* (2014) Influence of unloading rate on the strainburst characteristics of Beishan granite under true-triaxial unloading conditions. Rock Mechanics and Rock Engineering 47:467-483

Zhao Y, Wan Z, Feng Z, Yang D, Zhang Y, Qu F (2012) Triaxial compression system for rock testing under high temperature and high pressure. International Journal of Rock Mechanics & Mining Sciences 52:132-138

Zhou C, Zhu F (2010) An elasto-plastic damage constitutive model with double yield surfaces for saturated soft rock. International Journal of Rock Mechanics & Mining Sciences 47:385-395

Zong Y, Han L, Wei J, Wen S (2016) Mechanical and damage evolution properties of sandstone under triaxial compression. International Journal of Mining Science and Technology In Press doi:http://dx.doi.org/10.1016/j.ijmst.2016.05.011